# Metal/ceramic composites from freeze-cast preforms: domain structure and mechanical properties

Zur Erlangung des akademischen Grades

**Doktor der Ingenieurwissenschaften**

**Dr.-Ing.**

der Fakultät für Maschinenbau
Universität Karlsruhe (TH)
genehmigte

**Dissertation**

Von

**M. Tech. Siddhartha Roy**
aus Kolkata, Indien

Tag der mündlichen Prüfung: 21.07.2009

Hauptreferent: Prof. Dr.rer.nat. Dipl.–Ing. Alexander Wanner
Korreferent: Prof. Dr.rer.nat. Michael J. Hoffmann

# Acknowledgements

I am indebted to Prof. Dr.rer.nat. Dipl.–Ing. Alexander Wanner for allowing me to do research at IWKI and for his invaluable guidance and help throughout the course of this work. I am also grateful to him for his constructive criticism of my work as my main supervisor, for correcting my thesis and for acting as the main referee in my Ph.D. examination. Without his constant motivation and encouragement, this work would never have been possible.

I am grateful to Prof. Dr.rer.nat. Michael J. Hoffmann (IKM, Universität Karlsruhe (TH)) for reading the thesis, for acting as the co-referee in my Ph.D. examination and for his valuable suggestions during the course of the quarterly project meetings.

I am thankful to Prof. Dr.-Ing. habil. T. Böhlke (ITM, Universität Karlsruhe (TH)) for acting as the chairman in my Ph.D. examination.

Financial support from German Research Foundation (DFG) is gratefully acknowledged. I also express my thanks to the co-workers at IKM, Universität Karlsruhe (TH) for fabricating the ceramic preform, the co-workers at GTAA and WTAA, FH Aalen for fabricating the metal/ceramic composite by melt infiltration and the co-workers at Fraunhofer-Institut für Werkstoffmechanik, Freiburg. I am also thankful to BESSY, Berlin for providing me with three weeks' beamtime and for allowing me to use the equipment there to carry out the synchrotron experiments.

I convey my heartfelt thanks to Dr.-Ing. J. Gibmeier (IWK I, Universität Karlsruhe (TH)) for his innumerable invaluable suggestions during the course of the synchrotron X-ray experiments and data analysis. His insightful ideas and constructive criticisms always helped me to dig deeper into the vast experimental data and to yield useful information there from. I am particularly grateful to him for always keeping his door open for me for help and suggestions.

I am grateful to Dr.-Ing. K. A. Weidenmann (IWK I, Universität Karlsruhe (TH)) for the priceless suggestions during the group meetings and for extending his help at every possible occasion.

I am thankful to Prof. Dr. D. Gerthsen (LEM, Universität Karlsruhe (TH)) for allowing me to use the laboratory facilities in her institute.

My sincere thanks go to Dipl. Phys. B. Butz (LEM, Universität Karlsruhe (TH)) for helping me with his precious time and knowledge to carry out the in-situ experiments in SEM and for TEM analysis. I convey my gratitude to Dr.-Ing. Dipl.-Math. R. Piat (ITM, Universität

Karlsruhe (TH)) for her interest and suggestions about my overall work. I also thank Dipl.-Ing. V. Kostov (IWK I, Universität Karlsruhe (TH)) for his help and assistance in carrying out the synchrotron experiments at BESSY, Berlin and Dipl.-Ing. M. Zimmermann (IWK I, Universität Karlsruhe (TH)) for his help in translating the abstract of the thesis in German.

In no words can I express my boundless thanks to all the employees and co-workers at IWK I, Universität Karlsruhe (TH) for all their help, cooperation and friendship during the last almost four years. I am particularly grateful to Mrs. C. Rentschler for preparation of my samples, to Mr. R. Rössler for his assistance during the mechanical tests and to Mrs. E. Stahl for her overall non academic help.

I must especially thank Dipl.-Ing. J.-M. Gebert (IWK I, Universität Karlsruhe (TH)) for his priceless friendship and camaraderie. Probably one year's time in the last four year we spent together and I really cherish each of those moments. Apart from being the immediate colleague, he was with me in all my thick and thin and without him my stay in Karlsruhe would never have been so smooth and enjoyable. I also convey my gratitude to Dr.rer.nat. B. Okolo (IWK I, Universität Karlsruhe (TH)) for his help and assistance throughout.

I express my thanks to all the students who helped me as HiWi. These include Mr. D. Berkowitz, Mr. S. Binninger, Miss I. Usandizaga and Miss L. Bruchmüller.

Throughout my stay in Karlsruhe, I have got enormous support and help from Mr. and Mrs. Kunchiwala and Mr. and Mrs. Panchal. I convey my thanks to them.

I must specially thank Prof. P. K. Dutta and Prof. P. K. Mitra (both Department of Metallurgical Engineering, Jadavpur University) for encouraging me when I needed them most and Prof. B. P. Kashyap (Department of Metallurgical Engineering and Materials Science, IIT Bombay) for always motivating me to achieve new heights and to stay focussed.

Utmost credit for what I am today goes to my family. My parents Amal and Arati sacrificed a lot for my well upbringing and proper education. Their desire to see me successful has always fuelled my aims and ambitions. My sister Susmita has been my best friend from my childhood and together we always used to dream to achieve great heights. My brother-in-law Indranil relentlessly provided me with guidance and suggestions from his own research experience. I am also grateful to my in-laws for their help and assistance. Last but not the least, the amount of support, motivation and inspiration that I received from my wife Susmita in the last about one year can probably be expressed by no amount of words.

# Zusammenfassung

Gefriertrocknen von keramischen Suspensionen ist ein innovatives Formgebungsverfahren zur Herstellung von porösen keramischen Materialien. Im Rahmen eines breit angelegten Verbundvorhabens zwischen mehreren Forschungseinrichtungen werden neuartige Metall/Keramik-Verbundwerkstoffe entwickelt, die durch Schmelzinfiltration solcher keramischer Formkörper erzeugt werden. Diese Verbundwerkstoffe weisen eine charakteristische hierarchische Struktur auf. Auf mesoskopischer Ebene liegen lamellare Domänen mit Größen von bis zu mehreren Millimetern vor. Die einzelnen Domänen setzen sich abwechselnd aus keramischen und metallischen Lamellen mit einer Dicke zwischen 20 und 100 µm zusammen.

Das Ziel dieser Arbeit war die experimentelle Charakterisierung der mechanischen Eigenschaften solcher Aluminiumoxid-Aluminium-Verbundwerkstoffe auf unterschiedlichen Größenskalen, d.h. auf der Ebene einzelner Domänen sowie auf der Ebene vieler Domänen.. Das elastische und plastische Verformungsverhalten der einzelnen Domänen wurde mittels Ultraschallmessungen und Druckversuchen an Miniaturproben untersucht, welche aus dem Polydomänenwerkstoff entnommen wurden. Die Schädigungsentwicklung während Druckbeanspruchung wurde mit Hilfe von mikroskopischen in-situ- und ex-situ-Versuchestechniken analysiert. Die herstellungsbedingten Eigenspannungen sowie die innere Lastübertragung unter externer Druckbeanspruchung wurden röntgenographisch mit Hilfe einer energiedispersiven Synchrotron-Experimentiermethode untersucht. Die Untersuchungsergebnisse zeigen, dass die Domänen eine ausgeprägte elastische und plastische Anisotropie aufweisen. Die höchste Steifigkeit wird parallel zur Gefriertrocknungsrichtung beobachtet, die geringste senkrecht dazu. Die elastischen Eigenschaften einzelner Domänen mit unterschiedlicher Orientierung wurden im Lichte eines Modells diskutiert, welches dreidimensionale lamellare Strukturen mit abwechselnden Schichten unterschiedlicher Dicken betrachtet. Die in der Kammer eines Rasterelektronenmikroskops durchgeführte in-situ-Druckversuche an einzelnen Domänen zeigten, dass diese ein ausgeprägt anisotrope elastisch plastisches Verformungsverhalten aufweisen. Bei Beanspruchung parallel zur Gefriertrocknungsrichtung weisen die Domänen eine hohe Festigkeit auf und zeigen ein sprödes Verhalten. Bei Beanspruchung in andere Richtungen wird das Verformungsverhalten von der weichen Metallmatrix dominiert. Die

plastische Anisotropie ist im Vergleich zur Vorhersage mit theoretischen Modellen für Laminate weniger stark ausgeprägt, was auf die Existenz von Brücken zwischen den keramischen Lamellen zurückgeführt werden kann. Die Röntgen-Diffraktionsunstersuchungen zeigen, dass im Herstellungszustand stark fluktuierende phasenspezifische Mikroeigenspannungen vorliegen, welche durch das ungleiche thermische Ausdehnungsverhalten von Metallmatrix und der keramischen Vorform erklärt werden können. Untersuchungen zur inneren Spannungsverteilung unter externer Belastung zeigten, dass der Lastübertrag von der elastisch und plastisch weicheren metallischen Komponente auf die keramische Phase am ausgeprägtesten ist, wenn die Belastung parallel zur Lamellenebene erolft. Auch hier erfolgt der Lastübertrag allerdings nicht vollständig, as auf Schädigungen der keramischen Lamellen und Grenzflächendekohäsionen zurückzuführen ist. Mit den Untersuchungen konnte erstmals ein tiefer Einblick in die Mikromechanik dieser neuartigen Metall-Keramik-Verbundwerkstoffe gewonnen werden.

# Table of contents

# Abbreviations

| | |
|---|---|
| CMC: | Ceramic Matrix Composites |
| PMC | Polymer Matrix Composites |
| MMC | Metal Matrix Composites |
| CIP | Cold isostatic Pressing |
| EMA | Effective Medium Approximation |
| UTS | Ultimate Tensile Strength |
| UPS | Ultrasound Phase Spectroscopy |
| RUS | Resonant Ultrasound Spectroscopy |
| SEM | Scanning Electron Microscope |
| LVDT | Linear Variable Differential Transformer |
| RMS | Root Mean Square |
| GLS | Global Load Sharing |
| LLS | Local Load Sharing |
| TEM | Transmission Electron Microscope |
| μCT | Micro Computed Tomography |
| UPS | Ultrasound Phase Spectroscopy |
| RUS | Resonant Ultrasound Spectroscopy |
| SR | Synchrotron Radiation |
| SSD | Solid State Detector |
| FEM | Finite Element Modeling |
| FOM | Figure of Merit |
| EFTEM | Energy Filtered Transmission Electron Microscopy |

# List of symbols

| | |
|---|---|
| $d_r$ | Reinforcement particle size (μm) |
| $d_c$ | Critical particle size (μm) |
| $d_m$ | Matrix particle size (μm) |
| $V_f$ | Reinforcement volume fraction |
| $R$ | Reduction ratio during secondary processing of powder metallurgy route |
| $l$ | Structural wavelength in freeze-casting (μm) |
| $u$ | Velocity of the ice front in freeze-casting (μm $s^{-1}$) |
| $u_c$ | Critical velocity for particle entrapment in freeze-casting (μm $s^{-1}$) |
| $r$ | Ceramic particle size in freeze-casting (μm) |
| $E$ | Young's modulus (GPa) |
| $G$ | Shear modulus (GPa) |
| $K$ | Bulk modulus (GPa) |
| $v$ | Poisson's ratio |
| $S$ | Compliance |
| $S_c$ | Effective compliance tensor of the composite material |
| $\varphi_s$ | Shape factor of the inclusion used in EMA method |
| $\xi$ | Adjustable parameter in Halpin – Tsai equation |
| $\eta$ | Parameter relating composite and matrix moduli in Halpin – Tsai equation |
| $e^C$ | Constrained strain in the equivalent homogeneous inclusion |
| $e^T$ | Stress-free transformation strain in the equivalent homogeneous inclusion |
| $S_E$ | Eshelby tensor |
| $\rho$ | Density (Mg $m^{-3}$) |
| $V$ | Wave velocity (m $s^{-1}$) |
| $C$ | Elastic constant (GPa) |
| $n$ | Mode number in RUS |
| $fex$ | Measured frequency in RUS (MHz) |
| $fr$ | Fitted frequency in RUS (MHz) |
| $\%err$ | Error in fitting a mode in RUS |
| $k$ | Mode symmetry |

| | |
|---|---|
| $\bar{\varepsilon}$ | Continuum mechanics average lattice microstrain |
| $\alpha_{hkl}$ | Weighting factor for continuum mechanics average lattice microstrain calculation |
| $\varepsilon_{hkl}$ | Individual lattice microstrain |
| $T_{hkl}$ | Texture factor |
| $m_{hkl}$ | Multiplicity factor |
| $E_{hkl}$ | Young's modulus of individual lattice planes (GPa) |
| $\bar{E}$ | Macroscopic Young's modulus of polycrystalline material (GPa) |
| $l_c$ | Critical fiber length for load transfer in short fiber reinforced composites |
| $d_f$ | Diameter of the short fibers |
| $\varepsilon$ | Strain |
| $\tau_d$ | Interfacial shear stress (MPa) |
| $\sigma_u$ | Ultimate tensile/compressive strength |
| $\sigma_{m'}$ | Stress in the matrix at the composite strain equal to fiber tensile strain |
| $m$ | Weibull modulus |
| $\sigma$ | Stress (MPa) |
| $\delta_{ij}$, $\delta_{il}$ | Kronecker's delta |
| $F$ | Externally applied force |
| $s$ | Atomic displacement resulting from external applied force |
| $A$ | Curvature at the bottom of the potential energy vs. atomic distance plot |
| $C_{ijkl}$ | $4^{th}$ order stiffness tensor |
| $S_{ijkl}$ | $4^{th}$ order compliance tensor |
| $d$ | Lattice plane spacing |
| $\theta$ | Angle between the incident X-ray and diffracting plane |
| $\lambda$ | Wavelength |
| $L_i$ | Laboratory co-ordinate system for stress analysis by diffraction |
| $S_i$ | Sample co-ordinate system for stress analysis by diffraction |
| $\psi$ | Angle between the normal to the family of planes to be measured and the normal to the plane of the sample |
| $\phi$ | Azimuthal angle in the plane of the sample |
| $d_{\phi\psi}$ | Lattice plane spacing in stressed condition |

| | |
|---|---|
| $d_0$ | Lattice plane spacing in un-stressed condition |
| $\alpha$ | Thermal expansion coefficient (/°C) |
| $\Delta\alpha$ | Thermal expansion mismatch between matrix and reinforcement |
| $\Delta T$ | Temperature drop |
| $T_{act}$ | Actual temperature where the stress measurement is carried out |
| $T_0$ | Stress-free temperature |
| $I$ | X-ray intensity after attenuation in the object |
| $I_0$ | Initial X-ray intensity |
| $\mu$ | Linear attenuation coefficient for the material being scanned in CT ($cm^{-1}$) |
| $x$ | Length of the X-ray path through the material (cm) |
| $V_i$ | Volume of an arbitrarily shaped free elastic body |
| $S_i$ | Free surface of an arbitrarily shaped free elastic body |
| $L$ | General form of the Lagrangian |
| $KE$ | Kinetic energy |
| $PE$ | Potential energy |
| $\omega$ | Angular frequency |
| $u_i$ | *ith* component of the displacement vector |
| $a_{i\lambda}$ | Expansion coefficients |
| $\Phi_\lambda$ | Basis functions |
| $a$ | Column vector |
| $K$ | Symmetric and positive definite matrix |
| $\Gamma$ | Symmetric matrix |
| $O$ | Order of the matrix |
| $f_{calc}$ | Calculated eigenfrequency in RUS |
| $f_{mea}$ | Measured eigenfrequency in RUS |
| $N_p$ | Number of eigenfrequcies |
| $W_i$ | Weighting factor |
| $d(hkl)$ | Lattice spacing of the (hkl) family of planes (Å) |
| $E(hkl)$ | Energy of the (hkl) family of planes (keV) |
| $h$ | Planck's constant ($6.626068 \times 10^{-34}$ $m^2$ kg / s) |
| $c$ | Velocity of light ($3 \times 10^8$ m $s^{-1}$) |
| $E_0(hkl)$ | Strain free energy (keV) |
| $\Delta E$ | Resolution of the SSD |

| | |
|---|---|
| $\Delta\theta$ | Angular divergence defined by the incident and detecting slit system |
| $k_j$, $k_k$ | Unit wave vectors |
| $\Gamma_{il}$ | Christoffel acoustic tensor |
| $n_j$, $n_k$ | Direction cosines of the normal to the wavefront |
| $\Delta V$ | Estimated error in measuring the wave velocity in a material |
| $dV/df$ | Measure of the material's dispersion |
| $\Delta f$ | Bandwidth of the wave or the pulse in the experiment |
| $\omega t + k_w x$ | Phase function |
| $k_w$ | Wave number |
| $f$ | Frequency (Hz) |
| $V_p$ | Phase velocity |
| $V_g$ | Group velocity |
| $L_s$ | Specimen length in ultrasonic analysis (mm) |
| $N$ | Number of wave periods in the sample |
| $\Delta\phi$ | Phase difference between input and received signals in UPS (rad) |
| $E_L$ | Longitudinal Young's modulus of long fiber reinforced composite |
| $v_{LT}$ | Longitudinal Poisson's ratio of long fiber reinforced composite |
| $K_L^{'}$ | Lateral compression modulus of long fiber reinforced composite |
| $G_{TT'}$ | Transverse shear modulus of long fiber reinforced composite |
| $m'$ | Global slope of the phase-frequency spectra |
| $V_{ij}$ | Shear wave velocity (m $s^{-1}$) |
| $\sigma_{VM}$ | von Mises equivalent stress (MPa) |
| $\sigma_c$ | Composite crushing strength (MPa) |
| $\sigma_{YM}$ | Matrix yield strength (MPa) |
| $\sigma_f$ | Fiber compressive crushing strength (MPa) |
| $\tau_{mu}$ | Ultimate shear stress of the metallic alloy |
| $N_a$ | Number of atoms in a solid |
| $\beta$ | Domain orientation angle |
| $V_p^{'}$ | Pore volume fraction |
| $\rho_p$ | Pore density |
| $\frac{1}{2}S_2^{hkl}$, $S_1^{hkl}$ | Diffraction elastic constants |
| $\Psi^*$ | Strain independent direction |

| | |
|---|---|
| $l_f$ | Load fraction in a phase |
| $\sigma_{appl}$ | Externally applied stress |
| $X$ | Compressive strength along 0 ° domain orientation (MPa) |
| $Y$ | Compressive strength along 90 ° domain orientation (MPa) |
| $\tau_{LT}$ | Compressive shear yield strength (MPa) |
| $\beta$ | Domain orientation angle (°) |
| $\sigma_{xx} = f(\theta)$ | compressive strengths of the single domains at different orientations (MPa) |
| $\theta_t$ | Angle of tilt of a poly domain sample around direction 3 (°) |
| $C_{11}^{'}$ | Off-axis elastic constant along freezing direction for different tilts around 3 direction (GPa) |

## Superscripts

u: Upper bound

l: Lower bound

## Subscripts

f: reinforcement

m: matrix

c: composite

T: transverse

L: longitudinal

TT: transverse – transverse

LT: longitudinal - transverse

# 1 Introduction

Growing demands of aircraft and automobile industries have resulted into continuous search of new materials with light weight and improved structural properties. Composite materials were thus developed because no monolithic material could satisfy all the structural needs [1]. Typically, composite materials contain a reinforcement supported by a binder (matrix) material. As the name suggests, the matrix material in metal matrix composites (MMC) is a metallic material (pure metal or an alloy) while the reinforcement is mostly a ceramic. Over the last few years the MMCs have reached industrial maturity in several different forms and applications and are now widely used in advanced areas like automotive, aerospace, electronic applications etc. In depth surveys depicting the status and future trend of worldwide MMC industry for the period until the end of the year 2001 have been carried out by Mortensen [2] and Evans et al. [3]. Figure 1.1 shows the application area wise actual and predicted annual

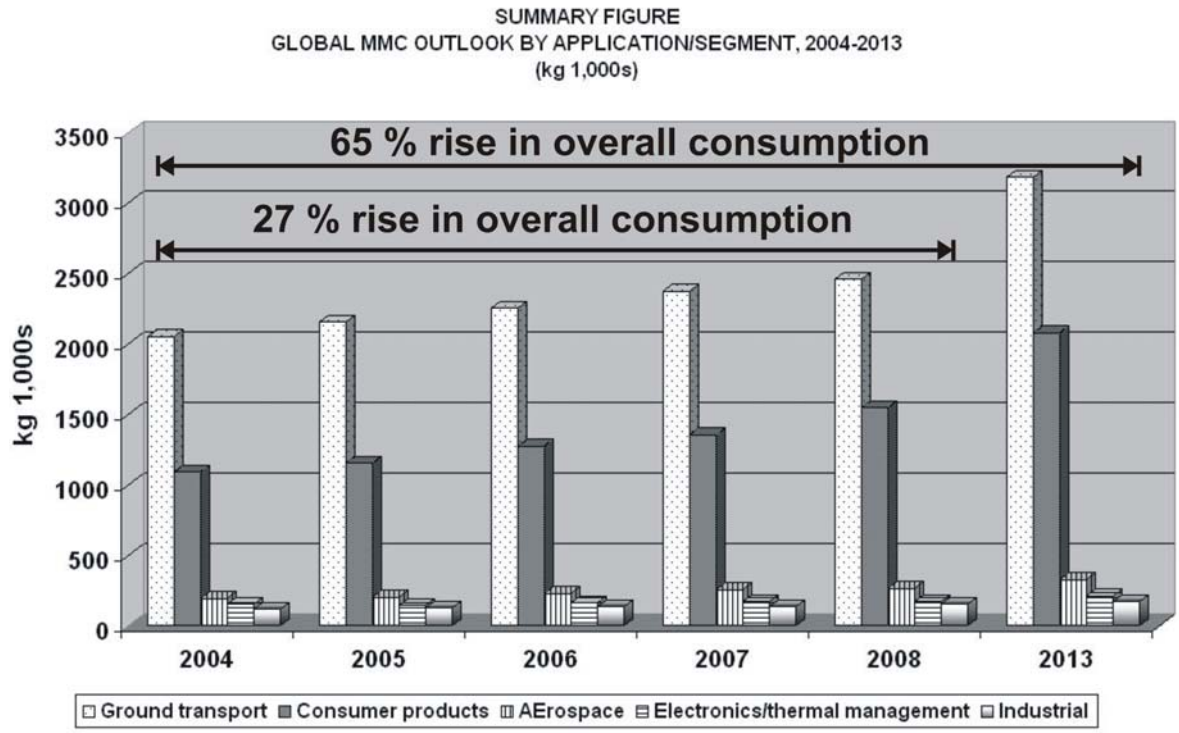


**Figure 1.1: Application area wise annual world market share of MMC for the period of 2004-2013. Data source Ref. [4]**

world market share of MMCs over the time period of 2004-2013. The figure is based on the data obtained from the survey carried out by BCC Research, MA, USA [4]. The diagram clearly shows that there is a continuous rise in the use of MMCs, with the overall consumption in the five main sectors increasing by about 27 % during the period of 2004-2008 and showing a predicted rise of about 65 % during the decade 2004-2013. This increasing interest in MMCs is largely due to their useful combination of properties. MMCs offer several advantages in comparison to unreinforced metals and better known composites such as polymer matrix composites (PMC). Although, in comparison to PMCs, MMCs are relatively difficult to fabricate and are heavier, MMCs offer higher strength, stiffness and conductivity (both thermal and electrical), higher operating temperatures, better transverse properties etc. Advantages over unreinforced metals include higher specific stiffness and strength, better dimensional stability, much improved creep and fatigue resistance etc [5].

Because of their potential applications, MMCs with different properties have been developed in last few decades. Good reviews of the different routes for MMC fabrication are presented in Refs. [6] and [7].Continuous research is however going on to fabricate composites having novel property profiles and more efficient and economic processing routes. A new possibility has recently been opened by the availability of ceramic preforms processed by freeze-casting of ceramic suspensions in a liquid medium. Details about the freeze-casting process can be found in subchapter 2.3. As shown in Ref. [8], ceramic preforms produced by freezing of water based suspensions have a typical hierarchical lamellar domain structure. Preforms produced this way have excellent permeability for liquids and gases along with acceptable mechanical strengths and they are suitable for the fabrication of metal/ceramic composites by infiltration of liquid metal [8].This way it is possible to fabricate composites with intermediate ceramic contents in the range of about 30–70 vol%. This is of particular interest since conventional particle- or fiber-reinforced composites typically contain either a relatively low (5–30 vol. %, e.g. [6]) or a fairly high (50–80 vol. %, e.g. [[9, 10]]) reinforcement content due to processing constraints.

## 1.1 Scope of the work

This work is carried out under the framework of an interdisciplinary project *Neuartige Metallmatrix–Verbundwerkstoffe auf $Al/Al_2O_3$-Basis: Herstellung, Struktur und Eigenschaften* (*Novel metal matrix composite based on $Al/Al_2O_3$: processing, structure and properties*) funded by German Research Foundation (DFG, Bonn). As a first step, ceramic preforms were

produced by freeze-casting at the Institut für Keramik im Maschinenbau (IKM) at Universität Karlsruhe, Germany. Infiltration of the preforms by liquid Al-12Si was carried out by squeeze-casting and die-casting. Squeeze-casting was carried out at the Institute of Surface Technology and Materials Science at Aalen University of Applied Sciences, Germany while die-casting was carried out at the Casting Technology Centre at Aalen University of Applied Sciences, Germany. Finite element based modelling as well as the fracture mechanics study of the composite was carried out at Fraunhofer-Institut für Werkstoffmechanik, Freiburg, Germany. Within the local framework of the work presented in this thesis, study of the structure-mechanical property dependence of the metal/ceramic composite is carried out at mesoscopic level. Elastic analysis of the composite was done at different length scales using non-destructive ultrasonic spectroscopic techniques. Elastic-plastic flow behavior as well as the progressive study of damage evolution was carried out by in-situ compression test in a scanning electron microscope. In depth analysis of the processing induced thermal residual stresses and the internal load transfer behavior under externally applied stresses were performed by synchrotron X-ray energy dispersive diffraction. All the results were discussed using appropriate theoretical models based on fiber reinforced composites and laminates.

## 1.2 Outlook of the thesis

The thesis is subdivided into 7 subchapters. Brief introduction about MMCs in general and motivation behind the work is discussed in this chapter. Chapter 2 presents thorough review of the theoretical background necessary for fundamental understanding of the general aspects of the MMCs. Several relatively new techniques to characterise the mechanical properties were used in this work. Chapter 3 provides brief description of these methods and their fundamental theoretical background. Description of the experiments and the processing as well as the experimental parameters used are discussed in chapter 4. Results obtained from the experimental analysis are described in chapter 5. In chapter 6, detail discussion of the obtained results is carried out on the basis of the theoretical background provided in chapter 2. Finally the conclusions drawn from this work are briefly discussed in chapter 7.

# 2 Literature

This chapter deals with the theoretical background of the work carried out. Subchapter 2.1 gives the definition of a composite material and its various classifications. The studied composite has a metallic alloy and a ceramic as their constituents. As already discussed, this was fabricated by infiltrating the liquid metal into a ceramic preform fabricated by freeze-casting. Subchapter 2.2 discusses the various important processing routes for metal/ceramic composites while subchapter 2.3 describes the process of freeze-casting and the underlying physics in detail. General mechanical properties of composite materials have been discussed in subchapter 2.4.The structure of the composite under study has striking similarity with that of lamellar two phase alloys (e.g. γ–TiAl based alloys). Hence, the mechanical properties of these two phase alloys have been discussed in subchapter 2.5. During this particular work, the problems of elasticity and the residual stress and internal load transfer under external load have been investigated extensively. Hence, the theory of elasticity is described in subchapter 2.6 while diffraction methods for determination of residual stresses are discussed in subchapter 2.7.

## 2.1 Definition of composite materials and their classifications

### 2.1.1 Definition

Several definitions of composites are possible. One such definition suggests that *"A composite material is a combination of two or more materials (reinforcing elements, fillers, and composite matrix binder), differing in form or composition on a macro scale. The constituents retain their identities; that is, they do not dissolve or merge completely into one another although they act in concert. Normally, the components can be physically identified and exhibit an interface between one another"* [1]. They differ from other combination of different materials like metallic alloys in the sense that, in alloys the constituent materials are combined in microscopic scale so that the material as a whole is homogeneous macroscopically [11]. The main advantage of composite materials is that, if designed properly, they show set of mechanical properties more attractive than the component materials considered separately [12].
In the most general case, a composite material has one or more discontinuous phases distributed in a continuous phase. Normally, the continuous phase is soft and compliant and it is called matrix; while the discontinuous phase is harder and stiffer and it is known as rein-

forcement. However, the above statement is not a general one, as in the case of rubber-modified polymers, the discontinuous phase (rubber in this case) is more ductile and more compliant than the polymeric matrix. In this particular example, the presence of rubber enhances the toughness of the resulting material [1, 12].

### 2.1.2 Classifications of composite materials

As has already been mentioned in subchapter 2.1.1, a composite is a combination of two or more materials. A general scheme of classification is shown in Figure 2.1, which combines the classification scheme given in Refs. [12] and [13].

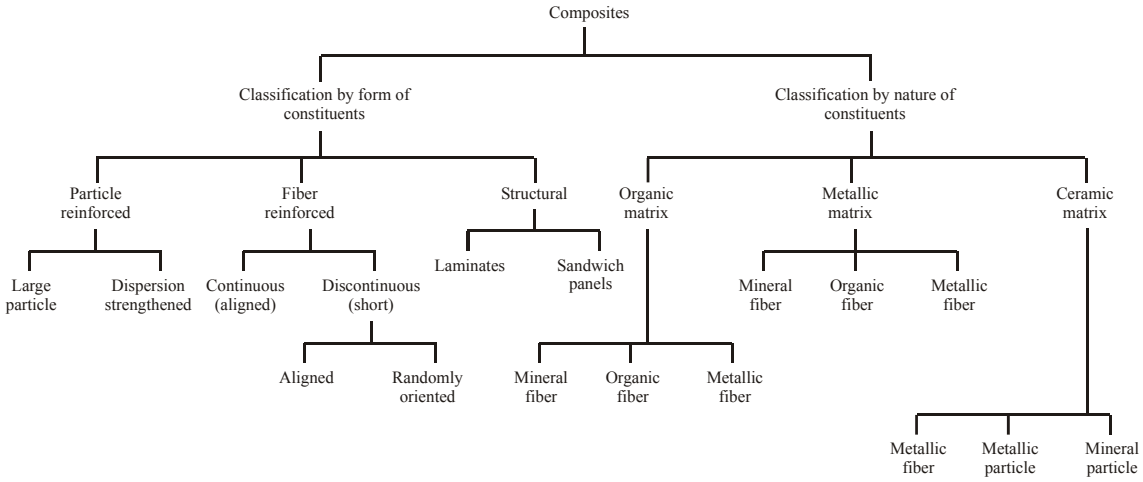


**Figure 2.1: A classification scheme for composite materials [12, 13]**

Composites can be classified either by the geometrical form of the constituents or by their nature.

Classification by form of constituents depends on their geometric shape. As the matrix is the continuous phase, the shape and geometry of the dispersed phase or the reinforcement is the controlling factor. Figure 2.2 shows a classification scheme of the composites based on geometry. In particle reinforced composites, the reinforcement has an aspect ratio[1] close to or equal to unity. Particles are generally used to improve certain properties (e.g. stiffness, strength etc.) of matrices. Because of their low aspect ratio, particulate reinforced composites mostly have isotropic[2] mechanical properties. Fiber reinforced composites have reinforcements with a very high value of aspect ratio (normally more than 1000) [5]. The fibers can be

[1] Aspect ratio is the ratio of length to diameter or thickness

[2] Isotropic materials have properties that are independent of orientation at a point in the body

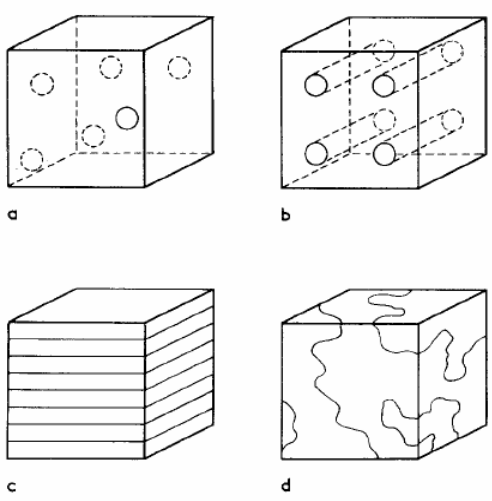


**Figure 2.2: Classification of composites based on geometry: (a) Random dispersion of spheres in a continuous matrix, (b) regular array of aligned filaments, (c) continuous laminate and (d) irregular geometry [14]**

either continuous or discontinuous. Gain in strength and stiffness is the highest when the fibers are continuous and aligned in a direction. Because of the very high aspect ratio of the fibers, the composites reinforced by them show very high anisotropy (excellent combination of properties along the fiber direction and poor properties along directions orthogonal to the fiber direction). Randomly oriented short fiber reinforced composites show mechanical properties inferior to the aligned continuous fiber reinforced composites, but because of the random distribution of the short fibers, the anisotropy is limited. Another way to counter the anisotropy effect of continuous fiber reinforced composites is to produce laminates. A laminate has several layers oriented at different directions with respect to each other, but within a particular lamina the continuous fibers are aligned in a fixed direction.

Composite materials can also be classified according to the chemical nature of the matrices and the reinforcements. In this scheme, the composites are generally named according to the type of matrix material (e.g. metal matrix composites (MMC), polymer matrix composites (PMC), ceramic matrix composites (CMC)). In most PMCs and MMCs, the dispersed phase is used to enhance the strength and stiffness of the weak matrix phase. But, in CMCs, the dispersed phase generally has a different purpose. Ceramics are inherently very stiff and strong but they suffer due to their low toughness. Incorporation of a ductile second phase enhances the toughness of CMCs [15].

The composite material studied in this work has metallic alloy Al–12Si and alumina ceramic as its constituents. Hence, the discussion henceforth will be limited to metal/ceramic composites.

## 2.2 Fabrication routes for metal/ceramic composites

Several processing routes for metal/ceramic composites have become well established in the last few decades. Good reviews of the various processing techniques can be found in Refs. [5, 6, 16]. In the following, only the most important processing techniques will be discussed in brief. In the broadest sense, the two most general processing routes for metal/ceramic composites are powder metallurgy route (solid state processing) and molten metal route (liquid state processing). They both have their inherent features, advantages and disadvantages, which correspondingly control their performance in actual application.

### 2.2.1 Powder metallurgy route

A schematic of the powder metallurgy manufacturing route for MMCs is shown in Figure 2.3.

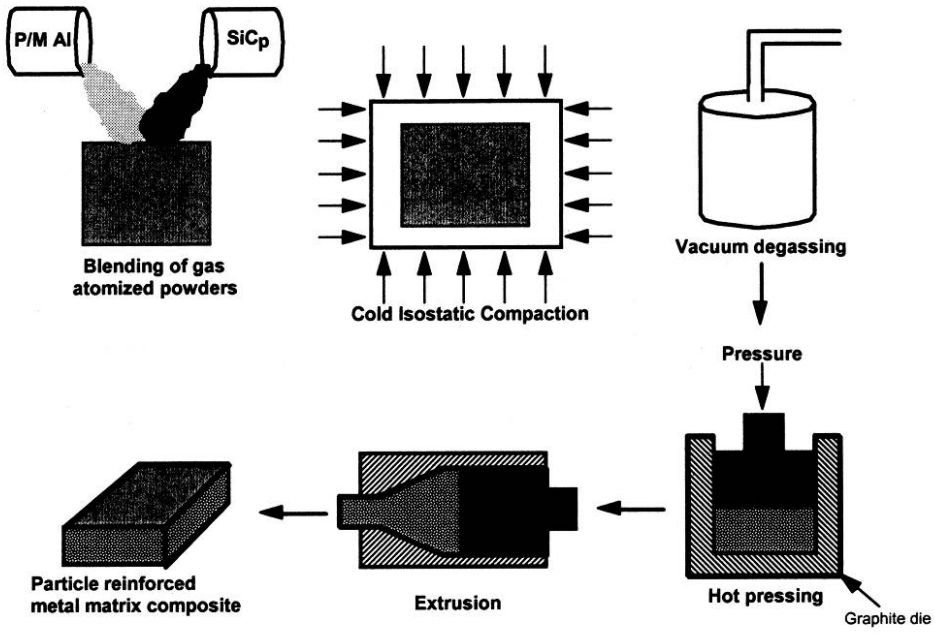


**Figure 2.3: Schematic of the powder metallurgy processing route for MMCs [5]**

Detail description of the methodology can be found in Refs. [5, 6, 17, 18, 19]. The steps involved in the processing route involve:

1) Blending of the metallic and the reinforcement powders
2) Compaction of the blended mixture into a green form, typically by cold iso-static pressing (CIP)
3) Vacuum degassing of the compacted green body. This is mostly done at a temperature high enough for the degassing step.
4) Hot pressing of the compact to form a billet
5) Secondary processing (extrusion, rolling, forging etc.) of the hot pressed and compacted billet into final form.

In the processing of MMCs by powder metallurgy route, the most important variable is the ratio of the reinforcement particle size to matrix particle size. This controls the homogeneous mixture between the two. Tan and Zhang [20] have summarized the condition for non-clustering of the particles of the reinforcement within the matrix. According to them, a uniform distribution of reinforcement particles within the matrix is only possible if the reinforcement particle size $d_r$ is greater than or equal to a critical value $d_c$; which depends upon the matrix particle size $d_m$, reinforcement volume fraction $V_f$ and the reduction ratio during the secondary processing $R$. The secondary processing of the hot pressed billets ensures that the oxide skin between the metal and the powder particles is totally disrupted and a good bonding is generated between them. A high extrusion ratio also enables a good and uniform distribution of the reinforcement particles.

#### 2.2.1.1 Advantages and disadvantages of the powder metallurgical route

The advantages of the powder metallurgical route involve:

1) Possibility to fabricate MMCs with any matrix alloy-reinforcement particle combination.
2) Solid state processing ensures that little or no chemical reaction takes place between the components during processing.
3) MMCs with high reinforcement volume fraction can be fabricated, enabling large gains in stiffness and strength.

The disadvantages of the method are:

1) Processing involves handling of potentially reactive and explosive powders in large quantity.
2) Complex manufacturing route and hence the possible product forms are limited.
3) As a result of the above constraints, the product may be relatively expensive.

### 2.2.2 Molten metal route

In molten metal route of processing of MMCs, the reinforcement is combined with the liquid metal matrix. Different variations of this route are:

1) Casting routes [21, 22, 23]
2) In-situ processes, where the reinforcement phase is formed in-situ during the synthesis itself [24, 25, 26, 27, 28].
3) Spray co-deposition process, where the liquid metal is atomized to form particles and then they are mixed with granular ceramics and finally consolidated to form the metal/ceramic composite [29].
4) Infiltration of liquid metal in ceramic preforms. The infiltration can be carried out without pressure [30] or by applied pressure. Pressure can be applied either by a pressurized inert gas [31, 32] or by a mechanical ram, as in squeeze-casting or squeeze infiltration [33, 34].

Among the routes mentioned above, squeeze-casting has become most popular for the fabrication of metal/ceramic composites via liquid metal route, and it has also been employed to fabricate the composite under study in this work. Hence, brief description of the methodology for squeeze-casting and its features are discussed in subchapter 2.2.2.2.

#### 2.2.2.1 General features of the molten metal route

The molten metal route is attractive because of its ability to produce near net shape components, a faster rate of processing and the possibility to work at relatively low temperatures for most common MMCs having matrices of Al, Mg etc. [5]. A review of the most important factors controlling the fabrication of MMCs by this route can be found in Ref. [7]. These include the viscosity of the molten metal, wettability between the metallic alloy and the ceramic reinforcement and the reaction between the reinforcement and the matrix.

Viscosity is important as it controls the ease of infiltration of the liquid metal within the ceramic preform. As the viscosity increases, the pressure required for melt infiltration increases and correspondingly the processing economics becomes more expensive. Wetting between liquid metals like aluminum and the commonly employed reinforcements is inherently poor. This is mainly caused by the formation of an oxide skin on the liquid metal droplet, which inhibits proper contract between the metal droplet and the ceramic. A good wettability is a must for a good interfacial strength in the final MMC. Refs. [35, 36] discuss in detail about the importance of wettability. Available literature suggests that the factors enhancing wet-

tability include: use of high infiltration temperatures at which the oxide layer disappears [35], heat treatment of the matrix and the reinforcement [37], alloying additions to the matrix material [36, 38], deposition of metallic coatings on the surfaces of the reinforcing solids [36] etc. In some cases the ceramic reinforcement and the metallic matrix react with each other in the absence of any wetting. This is very detrimental as it decreases the final mechanical properties of the MMC (refer to subchapter 2.4.2.3.3 for details). Most efficient ways to reduce the mutual reaction include use of a low processing temperature, use of a short exposure time at the processing temperature (as in squeeze-casting), use of a barrier coating on the reinforcement [39] etc.

#### 2.2.2.2 Squeeze-casting process for the fabrication of metal/ceramic composites

Figure 2.4 shows the schematic of the squeeze-casting process after Ref. [5]. First a specified

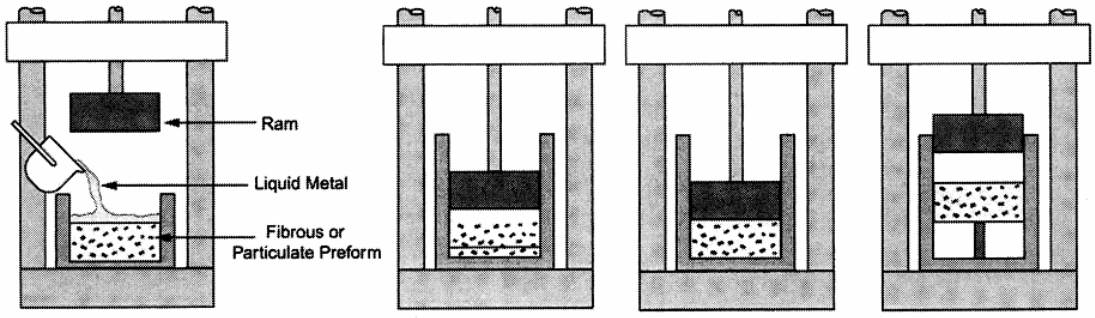


**Figure 2.4: Schematic of the squeeze-casting process [5]**

amount of molten metal is poured into a die cavity placed on a hydraulic ram. The press is then activated very quickly to pressurize the liquid metal so that the molten metal can solidify under pressure. The pressure is applied until the complete metal solidifies, minimizing the chances of gas entrapment. Finally the punch is withdrawn and the composite is ejected from the die cavity.

The dies for squeeze-casting normally experience severe thermal and mechanical loading. Hence the material for the die must be chosen very critically. The choice of the die material again depends upon the alloy to be cast, as the pouring temperature, the die temperature and the thermal properties depend directly on it. Other variables involve the die coat to be used, the time interval over which the pressure is applied (known as dead time) etc. Depending upon the alloy to be cast, the die temperature is normally kept in the range of 200–300 °C and the applied pressure ranges between 50–150 MPa. The pressure can be applied either directly

on the solidifying product (direct mode) or through an intermediate feed system (indirect mode). A good outline of the effect of the processing parameters on the properties of the final squeeze-cast composite can be found in Refs. [40, 41].

Composites fabricated by a squeeze-casting process have superior mechanical properties due to a fine microstructure (because of rapid cooling) and lack of porosity, good surface finish, high productivity etc. The disadvantages include, the process needs high capital cost due to the requirement of high pressure and special die designs and material, products are limited to shapes with relatively low complexity, inability to produce thin sections etc.

The metal/ceramic composite studied in this particular work was processed by squeeze-casting molten Al-12Si in freeze-cast alumina preforms. Freeze-casting is a relatively new technique for the fabrication of ceramic preforms for metal/ceramic composite fabrication. Hence, this technique has been discussed in detail in the next subchapter 2.3.

## 2.3 Freeze-casting

Freeze-casting offers an easy and economic method to produce porous ceramic bodies with aligned pores and having a lamellar microstructure [8, 42, 43, 44, 45, 46, 47]. The process consists of preparing a suspension of ceramic powder in a certain solvent, freezing the suspension to solidify the liquid medium followed by sublimation of the solidified liquid under vacuum to generate a porous body with the porosity being the exact replica of the initial frozen structure. The green body is finally sintered to enhance the inter particle bonding and the mechanical strength. Although, water is almost always used as a liquid medium (also called vehicle for freeze-casting) because of its easy availability and environment friendliness, camphene has also been employed successfully [48]. An up to date review of the current understanding of the process and the controlling parameters is given by Deville [49].

Freezing is carried out by pouring the ceramic suspension into a container designed in such a way that the bottom is made up of a metal having a very high thermal conductivity (e.g. copper) and the sides are made up of thermally insulating materials (like resin or fluoro-resin etc.) (Figure 2.5a). The top of the container is kept open to normal atmosphere at room temperature. The bottom of the container is immersed into a refrigerant (e.g. ethanol) maintained at a fixed subzero temperature. This dictates the growth of the columnar ice crystals (formed by the solidification of water) in a macroscopically vertical direction. The crystal structure of ice allows very little solubility for impurity elements and as a result during freezing the ceramic particles pile up between the growing columns (Figure 2.5b). When the suspension com-

pletely freezes, the container is immediately put under high vacuum to sublimate the ice crystals and hence generating the open porous structure.

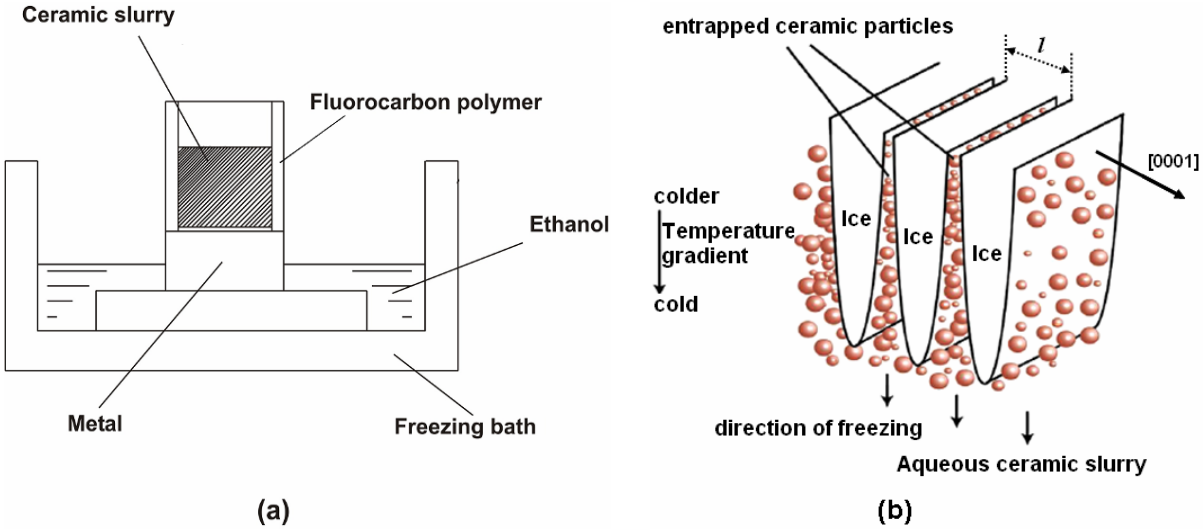


**Figure 2.5: (a) Schematic of the freeze-casting process [44] and (b) Pattern formation and particle segregation during freeze-casting of ceramic slurries. The ice platelets grow in a direction perpendicular to the c-axis of hexagonal ice. The wavelength of the structure is defined by *l* [43]**

The underlying physics behind freeze-casting is extremely complex due to the involvement of several variables and processing conditions. Deville et al. [43] and Mattern [8] have investigated the freezing of ceramic suspensions to identify the controlling factors and to explain the generation of the typical lamellar structure. According to them, the main variables are the initial ceramic content in the suspension, the freezing temperature and the ceramic particle size. Mattern [8] observed that the total porosity in the cast ceramic body is independent of the freezing temperature and is dependent only on the ceramic content in the initial suspension. He observed a direct linear dependence of porosity on the initial ceramic content within a huge porosity range of 15-85 %. The structural wavelength depends upon the speed of the growth of the solidification front (or the freezing kinetics). Figure 2.6 shows the dependence of the structural wavelength on the ice front velocity $u$ in double log axes. The Figure clearly shows that for the same final porosity, the structure wavelength can be varied over a large range by varying the velocity of the growing ice front. As the freezing kinetics increase, the structure becomes correspondingly finer. The interdependence between the wavelength and the ice front velocity parallel to the temperature gradient $u$ can be described in terms of an empirical power law with the exponent depending upon the ceramic particle size.

According to Deville et al. [43], the most important requirements that must be satisfied to ensure a lamellar porous structure are: (1) rejection of the ceramic particles from the advancing ice front and their entrapment between two growing ice crystals and (2) a columnar or lamellar morphology of the ice crystals. The ice front would only reject the ceramic particles

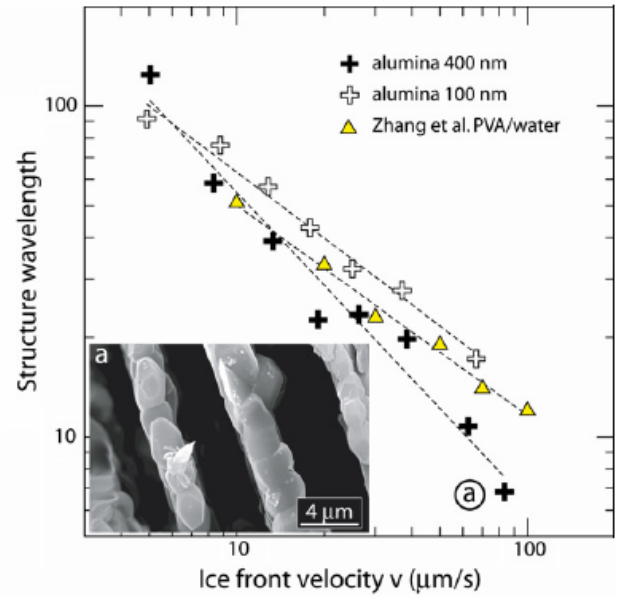


**Figure 2.6: Variation of the structure wavelength with ice front velocity on double log scale for samples with 64% total porosity. The plot shows power law dependence with exponents depending upon the initial ceramic particle size. The micrograph in the inset shows the SEM image of a freeze-cast sample with the cross-section being parallel to the ice front [43]**

if there exists a liquid film of sufficient thickness between the ice front and the particle. If the velocity of the ice front is above a critical value $u_c$, rather than rejecting the particles, the growing ice front would engulf them. This critical velocity again depends upon several factors and it varies inversely with the particle size $r$. Freezing starts by heterogeneous nucleation of ice crystals at the bottom of the sample. Because of the very high cooling rate and correspondingly a very high ice front velocity, the initial ice front is planar and it traps the ceramic particles. This results into a very dense structure at the bottom. As the velocity is decreased below the critical ice front velocity $u_c$, the particles are no longer entrapped, rather they are expelled from the growing ice front and the growth morphology changes from planar to columnar. At even lower cooling rates, the growth morphology is lamellar. At this stage a steady state is reached and the ice crystals become continuous throughout the sample. The ice front velocity is anisotropic and the velocity perpendicular to the crystallographic c-axis is about $10^2$-$10^3$ times higher than that parallel to it. Hence, after the morphological transition to co-

lumnar state takes place, ice crystals with very large anisotropy develop with the growth of the crystals oriented such that their c-axis perpendicular to the macroscopic temperature gradient is favored. Depending upon interfacial kinetics, the growth direction of the ice crystals may be either parallel to the direction of temperature gradient or they may be parallel to the preferred growth direction controlled by the interfacial energy. In the lamellar growth region, if the velocity of the ice front is fast enough, the temperature gradient would be small and it would result into a tilted microstructure. As the velocity decreases, the temperature gradient would increase and this would align the growing ice crystals along that of the temperature gradient with a minimum tilt. Another interesting phenomenon takes place in samples cooled at a slow freezing rate and consisting of suspensions with high ceramic content. As the ceramic concentration increases, the inter-particle interaction becomes very important. This may result into ceramic bridges, shown by Deville et al. [43]. They develop due to localized splitting of the tip of the growing ice crystal to trap the ceramic particles and subsequent healing of the tip. Depending upon the magnitude of this splitting/healing, the entrapped ceramic particles may or may not bridge the gap between two ice crystals completely.

The advantages of freeze-casting include rather small sintering shrinkage, relatively good mechanical strength for subsequent handling, environment friendliness, applicability to a wide range of ceramic/liquid media combination etc. Moreover, as pointed by Mattern [8], freeze-casting provides an opportunity to fabricate ceramic preforms with intermediate ceramic content in the range of 30-70 vol% with pores having an interpenetrating open structure. This along with their sufficient mechanical strength make these preforms suitable for infiltration with a metallic melt to fabricate metal/ceramic composites and hence opening a new possibility to fabricate lightweight hybrid materials in an economic way. This approach has been followed to process the composite material under study.

As has already been mentioned, the goal of the present work is to investigate the structure-mechanical property correlation of the innovative metal/ceramic composite material. Hence, the general mechanical properties of composite materials will be discussed in the next subsection.

## 2.4 General mechanical properties of composites

One of the biggest motivations for the widespread and ever increasing applications of composite materials is their improved mechanical properties over monolithic metals and alloys. Among the various mechanical properties of composites, only the elastic properties and the

elastic-plastic flow behavior (and corresponding damage evolution) under monotonic tension/compression will be discussed here because of their direct relevance to the present work. In case of metal/ceramic composites, processing-induced thermal residual stresses as well as the interfacial strength plays very important roles in controlling their mechanical behavior and hence they would also be discussed.

### 2.4.1 Elastic properties

There are two general approaches to estimate the effective properties of composite materials: approximate solutions based on idealized geometries and determination of rigorous bounds based on actual microstructure having limited knowledge about it [50]. Both these approaches are based on micromechanics[3]. In this particular work the different theories to predict the effective elastic properties of composites will be classified based on the geometry of the reinforcing phase.

#### 2.4.1.1 Discontinuous reinforcement

It is well-known that the elastic modulus of any metal can be increased by dispersing into it a second phase having higher elastic constants than the parent metal. The increase depends upon the volume content and the elastic constant of the added material. This concept is utilized in the design of composite materials. In case of discontinuously reinforced composites the reinforcements are particles or short fibers.

If $E_m$ and $E_f$ are respectively the Young's moduli of the matrix and the reinforcement and if the volume fraction of the reinforcement is denoted by $V_f$, then assuming no porosity (i.e. $V_f + V_m = 1$), the composites Young's modulus $E_c$ (throughout this work subscripts '*m*', '*f*' and '*c*' are used respectively for matrix, reinforcement and the composite, respectively) is strictly bounded by the Equations:

$$E_c = E_m\left(1 - V_f\right) + E_f V_f \tag{2.1}$$

and

$$\frac{1}{E_c} = \frac{V_f}{E_f} + \frac{1 - V_f}{E_m} \tag{2.2}$$

with Equation (2.1) being the Voigt [51] upper bound and Equation (2.2) being the Reuss [52] lower bound, respectively. Although for particle reinforced composites the actual experimen-

[3] Micromechanics is the study of composite material behavior wherein the interaction of the constituent materials is examined in detail as part of the definition of the behavior of the heterogeneous composite material [11].

tally observed Young's modulus always lies within these two bounds, none of them is accurate enough. Hence, effort has been put in for a long time to estimate more accurate expressions. One of the first such expressions was formulated by Paul [53]. He assumed an inclusion of an arbitrary shape in a unit cube and based on strength of materials approach he came up with an expression for the Young's modulus of the particle reinforced composite. For tungsten carbide–cobalt composites excellent match was found between Paul's model and experimental measurements.

For elastic moduli of particle reinforced composites, the most well known bounds were developed by Hashin and Shtrikman (HS bounds) [54]. Their approach was based on variational principles to bound the strain energy and hence the effective elastic moduli. For a two phase composite, Hashin-Shtrikman proposed expressions for the lowest upper bound and the highest lower bounds for the composite shear modulus $G_c$ and composite bulk modulus $K_c$. The distance between these bounds is directly proportional to the difference in stiffnesses of the two phases. In the extreme case of a rigid inclusion, the upper bound goes to infinity while for an empty phase (cavities) the lower bound reaches zero. Thorough analysis of the HS bounds is given in [50]. Walpole [55] generalized the above mentioned HS bounds by relaxing the criteria that the reinforcing phase always has higher moduli compared to the matrix phase and extended it for multiphase materials.

Budiansky [56] developed expressions for overall bulk and shear moduli of multiphase materials composed of a coherent mixture of several isotropic elastic materials. Overall the composite material is assumed to be homogeneous and isotropic. The geometry of individual phases is assumed not to deviate grossly from spherical shapes. He proposed expressions of moduli for a $N$ phase composite. The expressions proposed by Budiansky must be used with caution as they yield unrealistic results for extreme ratios of the stiffness of the involved phases.

More recently Ravichandran [57] proposed upper and lower bounds for discontinuously reinforced composites assuming a periodic arrangement of second phase particles of cubic shape distributed homogeneously within the continuous matrix. The elastic properties are derived by using the basic relationships of elastic properties of parallel and series arrangements of two phases respectively loaded in iso-strain and iso-stress configurations. The matrix and the second phase were assumed to have similar Poisson's ratio. The Ravichandran model claims to improve over the HS bounds and describes the Young's moduli over the complete range of composition and as well as for constituents having largely different elastic moduli.

To summarize the discussions in this subchapter, Figure 2.7 shows the predictions of the above mentioned theoretical models for the Young's modulus of the particle reinforced composites as well some experimental data points for Al-SiC MMC to validate those predictions.

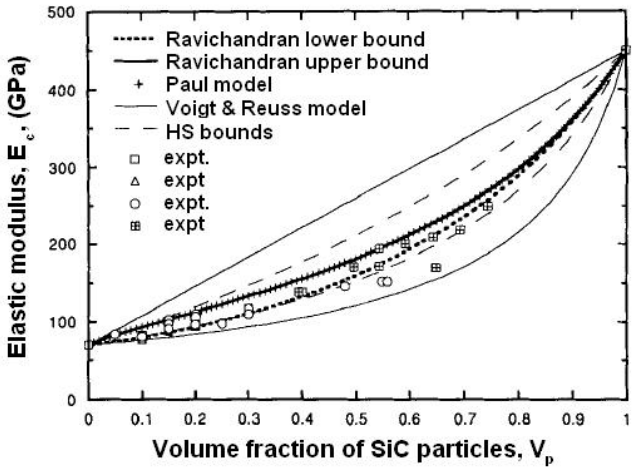


**Figure 2.7: Comparisons of the predictions of the different theoretical models for elastic moduli of particle reinforced composites with experimental data for Al-SiC particle reinforced MMC [57]**

Theories for the elastic behavior of the short fiber reinforced composites take into consideration the aspect ratio of the fibers and their orientation distributions within a plane (aligned, partially aligned or random). A good review of the different theories to estimate the elastic moduli of short fiber reinforced composites has been written by Chou and Kelly [58].

#### 2.4.1.2 Co-continuous reinforcement

The term "matrix" is no more valid in its actual meaning for these composites because both phases are continuous. They typically show better elastic properties in comparison to particle reinforced composites [59]. According to the nomenclature followed by Peng et al. [59], the phase having higher volume fraction is named as the matrix.

Among the models used to predict the elastic moduli of interpenetrating composites, the one developed by Tuchinskii [60] and the theory of effective medium approximation (EMA) are most efficient. The Tuchinskii model [60] considers a two phase interpenetrating skeletal structure (called unit cell) where a cube of the phase 2 is filled within the cavity of a larger cube of the phase 1. Dimensions of these cubes are controlled by the volume fractions of the individual phases. Detail description of the EMA method is given in [61] and a brief description of the method can be found in Refs. [62, 63]. This method considers an isolated randomly oriented ellipsoidal inclusion having compliance *S* surrounded by an effective medium having

the compliance of the total composite $S_c$. By considering the interactions between this inclusion and the surrounding matrix, the EMA method accounts for the average interaction between multiple inclusions. The theory also considers the shape of the inclusion via the shape factor $\varphi_s$. For prolate or needle shaped inclusion $\varphi_s<1$, for spheres $\varphi_s=1$ and for oblate or disc shaped inclusions $\varphi_s>1$.

Apart from compiling the Tuchinskii model and the theory of EMA, Moon et al. [63] also investigated interpenetrating Al-$Al_2O_3$ composites having alumina content between 5–97 vol %. They observed that for interpenetrating composites composed of phases having similar Young's modulus; Tuchinskii model, Ravichandran model (described in 2.4.1.1) and the EMA method predict the Young's modulus over the complete composition range. As the modulus ratio becomes significantly large, only the EMA method with an appropriate shape factor gives accurate predictions. In all cases, the HS bounds (described in 2.4.1.1) serve as the upper and lower bounds.

#### 2.4.1.3 Continuous reinforcement

Long fiber reinforced composites and laminates are typical examples of composites with continuous reinforcement. Because of the long fiber axis, the symmetry changes and the properties of the composite material are no longer isotropic. Rather the composite becomes transversely isotropic with respect to the fiber axis and 5 independent elastic constants are needed to completely describe the composite elastic behavior (details about different symmetries and corresponding elastic behavior are given in subchapter 2.6).

Equations (2.1–2.2) are generally used for the longitudinal and transverse Young's moduli of long fiber reinforced composites. Equation (2.1), based on the iso-strain assumption explains the behavior reasonably well but the equal stress assumption of Equation (2.2) is always very inaccurate because it assumes the matrix to be in series with the reinforcement although a significant proportion of the matrix is in parallel [64]. Halpin and Tsai [65] used empirical methods to propose general equations which give values pretty close to those obtained from experiments for the transverse Young's modulus and axial-transverse shear modulus of the composite. The Halpin-Tsai equation for transverse Young's modulus can be written as:

$$E_T = \frac{E_m\left(1+\xi\eta V_f\right)}{\left(1-\eta V_f\right)} \tag{2.3}$$

where $E_T$ is the transverse Young's modulus of the composite, $\xi$ is an adjustable parameter and $\eta$ is defined as:

$$\eta = \frac{\left(\frac{E_f}{E_m} - 1\right)}{\left(\frac{E_f}{E_m} + \xi\right)} \tag{2.4}$$

For axial-transverse shear moduli $\xi$=1 and for transverse Young's modulus $\xi$=2. Based on the Halpin–Tsai philosophy, Spencer [66] derived a single equation for moduli and thus eliminated the need to use different values of $\xi$ for different moduli. Hewitt and Malherbe [67] observed that the Equation (2.3) with $\xi$=1 gives only a reasonable agreement for fiber volume fractions up to about $V_f$=0.5 and for higher volume fractions the error involved is significantly large. They proposed a general expression for $\xi$ which also involved the volume fraction of fibers and showed that model outcomes matched well with the experiments. Clyne [64] has compiled simple expressions for all independent moduli of a fiber reinforced composite determined on the basis of an argument involving the compressibility of the composite.

Hashin and Rosen [68] predicted the macroscopic elastic behavior of composites consisting of parallel long fibers in terms of the elastic moduli of the constituting materials. The composite was assumed to be statistically homogeneous and transversely isotropic while the constituent materials were assumed to be isotropic. They considered two different cases. In the first case the fibers had equal circular cross-sections and they were arranged in a hexagonal array while in the second case circular fibers of different cross-sections ranging from finite to infinite size were arranged randomly in the transverse plane. They determined expressions for transverse–transverse bulk $K_{TT}$ and shear moduli $G_{TT}$, longitudinal–transverse shear modulus $G_{LT}$, longitudinal Young's modulus $E_L$ and modulus associated with stress or strain in the longitudinal direction, while lateral deformation was being prevented by a rigid enclosure $C_{LL}$.

#### 2.4.1.4 Stiffness tensor of a space filling laminate composite consisting of alternating layers of random thickness

Model to determine the stiffness tensor of laminate composites consisting of alternating layers of random thickness was postulated by Postma [69] and is compiled by Torquato [70]. The subsequent discussion in this subchapter follows from chapter 16 in Ref. [70]. For a laminate in which the layers are oriented along directions 1 and 2 and direction 3 is the transverse direction (as shown in Figure 2.8 for a composite with alternating metal and ceramic layers), the transverse isotropic stiffness matrix is written as:

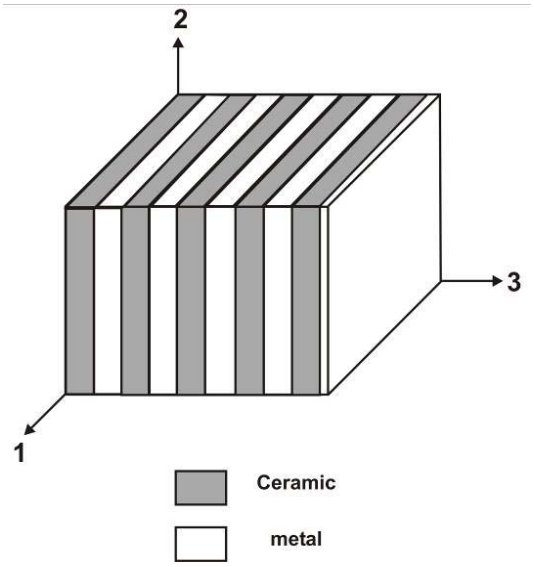


**Figure 2.8: Co-ordinate system for a model 3D laminate composite having alternating layers of random thickness**

$$C = \begin{pmatrix} C_{11} & C_{12} & C_{13} & 0 & 0 & 0 \\ C_{12} & C_{11} & C_{13} & 0 & 0 & 0 \\ C_{13} & C_{13} & C_{33} & 0 & 0 & 0 \\ 0 & 0 & 0 & C_{44} & 0 & 0 \\ 0 & 0 & 0 & 0 & C_{44} & 0 \\ 0 & 0 & 0 & 0 & 0 & C_{66} \end{pmatrix} \tag{2.5}$$

where $C_{66} = \frac{1}{2}\left(C_{11} - C_{12}\right)$ (2.6)

Expressions for the elements of the stiffness matrix are written as:

$$\begin{aligned} C_{11} &= \left\langle \frac{K - 2G/3}{K + 4G/3} \right\rangle \cdot C_{33} + \left\langle K + 4G/3 \right\rangle - \left\langle \frac{\left(K - 2G/3\right)^2}{K + 4G/3} \right\rangle \\ C_{33} &= \left\langle \left(K + 4G/3\right)^{-1} \right\rangle^{-1} \\ C_{13} &= \left\langle \frac{K - 2G/3}{K + 4G/3} \right\rangle \cdot C_{33} \\ C_{44} &= \left\langle G^{-1} \right\rangle^{-1} \\ C_{12} &= \left\langle \frac{K - 2G/3}{K + 4G/3} \right\rangle^2 \cdot C_{33} + \left\langle K - 2G/3 \right\rangle - \left\langle \frac{\left(K - 2G/3\right)^2}{K + 4G/3} \right\rangle \end{aligned} \tag{2.7}$$

$$\langle C \rangle = C_f \cdot V_f + C_m \cdot (1 - V_f)$$

where $$\langle C^{-1} \rangle^{-1} = \frac{C_f \cdot C_m}{C_f \cdot (1 - V_f) + C_m \cdot V_f} \tag{2.8}$$

with $K$ and $G$ being the bulk and shear elastic constants respectively and $V_f$ being the reinforcement volume fraction. Suffixes $f$ and $m$ correspond to reinforcement and matrix, respectively.

Eshelby [71] solved the problem of determining the stresses in an elastic ellipsoidal inclusion embedded in an infinite elastic matrix. The method involved several cutting and welding steps. The stress field in the inclusion was determined by replacing the inclusion with the matrix (called equivalent homogeneous inclusion) but with an appropriate misfit strain (called equivalent transformation strain). Because of the ellipsoidal shape, the stress within the inclusion is uniform. The constrained strain $e^c$ in the equivalent homogeneous inclusion in the composite is related to the stress-free transformation strain $e^T$ according to:

$$e^c = S_E \cdot e^T \tag{2.9}$$

where $S_E$ is the Eshelby tensor, which is dependent only upon the aspect ratio of the inclusion and the Poisson's ratio of the matrix. A complete list of the forms of $S_E$ for different inclusion shapes is given in the appendix of Ref. [16]. The original Eshelby method is valid only for a single inclusion in an infinite matrix (i.e. for infinitely small content of reinforcement). Pedersen [72] has developed the model using mean field approximation to allow for the composites having finite volume fraction of reinforcement. With the help of this approximation and using the Eshelby approach, it is possible to predict the elastic properties of real composites having different shapes of inclusions [73].

### 2.4.2 Elastic–plastic flow behavior under monotonic loading

In comparison to the elastic properties, the prediction of the elastic-plastic flow behavior of composites is less well understood because of the inherently more complex mechanical analysis and due to the fact that the matrix intrinsic post yield behavior is affected by the reinforcement. In comparison, the elastic behavior varies little with composite microstructure and local stresses in different phases [74]. Chawla and Chawla [5] have classified the strengthening of MMCs into direct (due to the load transfer from the weaker metallic matrix) and indirect (due to the change in matrix microstructure and subsequent hindrance to dislocation motion [75]) strengthening. As was done for elastic properties, here also the description will be

classified based on the geometry of the reinforcement. Special emphasis will be put on the monotonic tensile and compressive behavior of continuous fiber reinforced MMCs, as it has relevance with the present work.

#### 2.4.2.1 Particle reinforced MMCs

Addition of hard particles in a soft and compliant matrix results into an increase of the Young's modulus and the yield strength [5]. The mechanisms and theoretical models predicting the increase in Young's modulus have been summarized in sub section 2.4.1.1. Arsenault and Shi [76] attributed this strengthening to the increased dislocation density in the matrix, generated due to the mismatch in thermal expansion coefficients of the matrix and the reinforcement. They proposed a simple model based on dislocation generation by prismatic punching, which successfully estimated a lower bound of the actual dislocation density required to explain the stress increase. In a further work, Arsenault et al. [77] observed that the strength increase in an Al-$SiC_p$ MMC is directly proportional to a decrease in the SiC particle size or an increase in the particle volume fraction. This was attributed to a change in the matrix microstructure (an increased dislocation density and a reduction in matrix sub grain size) caused by the differential thermal expansion coefficients of the two components. Kouzeli and Mortensen [78] as well as Gustafson et al. [79] observed similar trends in different particle reinforced MMCs. Kouzeli and Mortensen [78] attributed the strengthening to a high density of geometrical necessary dislocations generated upon cooling from infiltration temperature. Finer particles as well as a high particle volume fraction lead to a greater strain gradient in the composite matrix, resulting into a higher density of geometrically necessary dislocations and subsequently into a higher composite flow stress. Gustafson et al. [79] analyzed the compressive behavior of a 99.9 % pure aluminum matrix composite reinforced with particles of spinel and processed by powder metallurgical route. Contrary to the discussions of Refs. [76, 77, 78], they inferred that the thermal dislocations did not play any significant role. They explained the observed strengthening with a model which took into consideration the interaction between dislocations in a pile up with the stress field of the low angle boundaries generated due to the impingement of the slip band with the metal ceramic interface. The above mentioned works explained the strengthening based on indirect mechanism, where load transfer from weak matrix took no part. Nardone and Prewo [80] observed that neither the theories based on Orowan strengthening (e.g. in [81]) nor the theories based on dislocation generation due to thermal misfit could explain all aspects of the composite stress-strain behavior. They proposed a modified shear lag theory for particle reinforced composites, taking into consid-

eration the particle aspect ratio and tensile load transfer at particle ends (apart from the shear load transfer along the interface). Bao et al. [82] used finite element method based on a continuum plasticity approach to predict the strengthening in MMCs having particles of different geometry, arrangements and volume fractions. They further proposed simple expressions for the uni-axial stress-strain plot of the composite. Ganesh and Chawla [83] observed that particle reinforced MMCs fabricated by powder metallurgical extrusion showed a pronounced anisotropy in their tensile elastic-plastic behavior, with the modulus and strength along longitudinal direction being significantly higher than that along transverse direction. The increase in anisotropy increased with increasing reinforcement volume fraction. Kouzeli et al. [84] observed that in Al–$B_4C$ MMCs the composites microstructure was dependent upon the time between melt infiltration and solidification. An increased interaction time resulted into a higher effective ceramic content due to bridges forming between adjacent ceramic particles (due to the reaction between matrix and the ceramic), which in turn resulted into a higher tensile modulus and strength as well as a lower strain to failure. Contrary to usual understanding, Manoharan and Lewandowski [85] observed that particle reinforcement in a high strength aluminum matrix resulted in a reduced yield strength, UTS and strain to failure. This was attributed to large stress concentrations near the particles and premature failure of the matrix at those regions.

#### 2.4.2.2 Short fiber reinforced MMCs

In discontinuous fiber reinforced composites the load transfer to the stiff fiber from the compliant matrix takes place by shear stresses along the fiber matrix interface. This mechanism (the so called shear lag phenomenon) was first proposed by Cox [86]. Only a brief description of the shear lag theory will be given here and thorough description can be found in Ref. [58] and chapter 6 of Ref. [15]. In the classical shear lag theory, it is assumed that a round fiber is surrounded by a perfectly bonded cylindrical matrix and load transfer through the fiber ends is neglected. The resulting interfacial shear stress is maximum at the fiber ends while the maximum tensile stress results at the fiber mid point. Provided the lengths of the short fibers are more than a critical length, the tensile stress at and around the fiber mid point reaches the stress predicted by the iso-strain model. This critical length $l_c$ is defined as:

$$l_c = \frac{E_f \cdot \varepsilon_c \cdot d}{2\tau} \tag{2.10}$$

where $E_f$ is the fiber Young's modulus, $\varepsilon_c$ is the strain in the composite, $d$ is the diameter of the short fiber and $\tau_d$ is the interfacial shear stress. This equation at once suggests that the critical length is dependent on the strain in the composite. At low strains all fibers are longer than this critical length and hence they reinforce. As the strain in the composite increases, more and more fibers fail to satisfy this critical length criterion and accordingly the slope of the stress-strain plot progressively decreases as the composite strain increases.

This simple shear lag model, although quite useful, is very inaccurate. This is mainly because of the fact that it neglects any load transfer at the fiber ends. Carrara and Mcgarry [87] showed by finite element calculations that this fiber end stress is about 20% of the maximum fiber stress. Clyne [88] modified the classical shear lag theory by introducing a simple expression for the fiber end stress and observed that the modified model gave very good agreement with Eshelby predictions for composites consisting of components with similar modulus ratios (e.g. MMCs). Tvergaard [89] analyzed the tensile properties of a ductile metal reinforced by aligned short fibers using micro mechanical modeling. His results showed that spacing of the short fiber along the longitudinal direction had a relatively insignificant effect on the tensile strength while fiber aspect ratio and volume fraction were most influential. Towle and Friend [90,91] measured the tensile and the compressive behavior of saffil short fiber reinforced magnesium alloy. Their results showed that the compressive ultimate strengths were always higher in comparison to the tensile ones because of a higher deformability. The proof stress in compression along the fiber direction was significantly higher than that normal to the fiber direction, which was attributed to processing-induced thermal residual stresses.

#### 2.4.2.3 Continuous fiber reinforced MMCs

##### *2.4.2.3.1 Tensile behavior*

In continuous fiber reinforced composites the fibers span the whole length and hence parallel to the fibers strain within the fibers become equal to the strain within the matrix [92]. The main object of fiber strengthening is to transfer the load from the plastically deforming matrix to the stiff fiber, which carries bulk of the load. The matrix has the following functions [93]:

1) To bind the fibers together and to protect their surfaces from damage.
2) To separate the fibers so that a crack cannot propagate catastrophically in a brittle manner.
3) To transfer the load to the strong fibers.

When a fiber reinforced composite is loaded under tension along the fiber direction, four general steps are observed. These are:

1) Initial linear elasticity when both fiber and the matrix deform elastically.
2) Fibers still deform elastically but the matrix deforms plastically.
3) Both the fiber and the matrix deform plastically. This stage is not observed in composites reinforced with brittle fibers.
4) Fracture of the fibers takes place and complete fracture of the composite soon follows.

Thorough detail about the governing equations in the different stages can be obtained from Refs. [92, 93]. More recently, Rossoll et al. [94] studied the progressive damage in long ceramic fiber reinforced MMCs loaded under tension along the fiber direction using acoustic emission. They showed that although fiber fracture occurs in an uncorrelated fashion within the whole sample volume and over the whole lifetime of the sample; damage mainly develops in two stages. First of these two steps take place at intermediate stresses and is attributed to debonding of the embedded fiber ends created during composite processing. Majority of fiber breaks however take place in the second step by individual uncorrelated fiber fracture in accordance with the virgin fiber Weibull statistics. For strengthening to take place, the volume fraction of fibers must exceed a certain minimum value. Provided the fiber content exceeds this minimum value, the ultimate tensile strength[4] of the composite is written as [93]:

$$\sigma_{u,c} = \sigma_{u,f} \cdot V_f + \sigma_{m'} \cdot \left(1 - V_f\right) \tag{2.11}$$

where $\sigma_{u,f}$ is the ultimate tensile strength of the fibers, $V_f$ is the fiber volume fraction and $\sigma_{m'}$ is the stress in the matrix at the tensile strain of the fibers. The main difficulty in using Equation (2.11) arises in choosing an appropriate value for $\sigma_{u,f}$. This is so because ceramic fibers generally exhibit a wide variation in their strength [95]. Curtin and Zhou [96] have shown by numerical simulation that initial fiber damage modifies the entire stress-strain response of the composite, resulting into a smaller tangent elastic modulus, lower tensile strength and reduced strain to failure. The ultimate tensile strength reachable also depends upon whether failure takes place by global load sharing (GLS) or by local load sharing (LLS) conditions. Under GLS, the effect of the local stress concentrations around broken fibers is neglected and load released by the broken fibers is distributed among the intact fibers. In LLS the stress concentration around a broken fiber determines the fracture probability in the neighboring fibers. Curtin [97] proposed expressions for the ultimate tensile strength and failure strain of a bun-

[4] Ultimate tensile strength is defined as the maximum load divided by the initial cross sectional area

dle of fibers following GLS mechanism and assuming that the strength of the fibers in the bundle follow Weibull distribution. González and Llorca [98] developed a model to simulate the deformation and fracture of a composite under LLS condition. Their analysis was based on the stress concentration introduced by the failure of one single or of a cluster of fibers, on its nearest neighbors. Weber et al. [99] treated the expression proposed by Curtin [97] as an upper bound and showed that in SiC reinforced Ti-6Al-4V matrix composites the longitudinal tensile strengths were closer to a lower bound, which was less than that of the upper bound by a factor $2^{1/(m+1)}$, with ($m$) being the Weibull modulus of the fibers. Hu et al. [100] observed that the tensile strength of Al alloys reinforced with continuous alumina fibers could be explained with a crack growth controlled failure mechanism.

Because the tensile behavior of the composite along the fiber direction is controlled by the load carried by the fibers, for a particular fiber volume fraction the tensile stress-strain behavior is independent of fiber distribution. Brockenbrough et al. [101] showed by finite element analysis that composites containing equal fiber content but with various distributions yielded identical axial tensile stress-strain behavior, which also matched extremely well with experimental observations. Fiber distribution though does affect the in-situ matrix work hardening behavior in the second stage of the axial tensile stress-strain curve. Kelly and Lilholt [102] observed that in tungsten fiber reinforced copper composites the in-situ matrix work hardening rate in the second stage of tensile deformation was very high. Mortensen et al. [103] proposed a simple explanation for the observed phenomenon based on fiber clustering during infiltration and subsequent dislocation hardening during cool down.

When loaded along the fiber direction the fibers carry the entire load and the composites display maximum property enhancement. When loaded normal to the fiber axis, stresses are transmitted into the composite by the plastically deforming matrix and the deformation is no longer homogeneous. The stress-strain behavior of the composite is mostly controlled by the matrix, which in turn is strongly affected by the constraint imposed by the fibers and their packing geometries and arrangements. Groh et al. [104] examined the transverse tensile stress-strain behavior of a continuous fiber reinforced composite using a discrete-continuum model and showed that the yield stress increased substantially when the inter fiber distance became smaller than the mean-free path of dislocations. Brockenbrough et al. [101] and Brockenbrough and Suresh [105] studied the effect of fiber shape and fiber distribution on the transverse tensile stress-strain behavior and showed that both these factors strongly affected the deformation response of the composite. Relative strengthening obtained for various ar-

rangements scaled according to the levels of tri-axiality generated within the constrained matrix. Similar results were also obtained by Zahl et al. [106] and they further showed that for significant strengthening to take place the fiber content has to be sufficiently large so that they impinged on the shear plane of the composite. Shetty and Chou [107] characterized tensile properties of continuous FP alumina and tungsten fiber reinforced aluminum composites with fibers oriented at various angles to the loading axis and showed that the samples with fiber orientation 60° resulted into minimum tensile strength.

#### *2.4.2.3.2 Compressive behavior*

Two primary material dependent failure mechanisms are observed in continuous fiber reinforced MMCs loaded under axial compression. These are classified as fiber kinking and fiber crushing [108, 109, 110] respectively.

Failure by kinking takes place by generation of a high shear stress parallel to the fiber length by the applied compressive load. Localized shear failure within a region of misaligned fibers forms a kink band. The stress required to initiate the kink band is significantly higher than the steady state kink band broadening stress and once generated the kink band can propagate across the entire specimen width like a propagating crack [108, 111]. The current understanding behind kinking phenomenon stems from the work of Rosen [112] who proposed a theory based on elastic buckling of initially perfectly aligned fibers. Argon [113] developed an expression for fiber kinking assuming that fibers undergo plastic micro buckling in a band within which fibers are initially misaligned by an initial misalignment angle. The expression proposed by Argon was further extended by Budiansky [114] to a composite following elastic-perfectly plastic behavior. In a subsequent study, Budiansky and Fleck [115] proposed an expression for the kinking stress in a composite with a strain hardening matrix. According to the expression proposed by Budiansky and Fleck, the most important factors controlling the kinking stress are the initial fiber misalignment angle, the shear yield stress and the stress hardening exponent of the matrix. Matrices with a high shear yield strength and a low stress hardening exponent as well as composites with low initial fiber misalignment angle result into a high kinking stress. Effect of these parameters on the compressive behavior of alumina fiber reinforced Al matrix composites has been studied by Dève [116]. Shetty and Chou [107] and Schulte and Minoshima [117] have summarized the steps involved in the development of a kink band. Schulte and Minoshima [117] also identified the preferred locations for kink band formation as: a) matrix rich areas, b) pores, c) regions of fiber misalignment and d) plastically deformed matrix regions.

At the limit of perfect fiber alignment, no shear stresses are induced parallel to the fibers and hence failure by kinking becomes highly unfavorable. Under these circumstances failure of the composite takes place by fiber crushing. This takes place when the stresses in the fibers reach a critical value resulting into a sudden loss of the load carrying capacity of the fibers. This causes the fibers to crush causing extensive plastic deformation in the surrounding matrix. A simple expression to estimate the compressive strength reachable in this failure mode was proposed by Spowart and Clyne [118], considering only the axial stresses and incorporating the effect of thermal residual stresses. Assuming all fibers have the same crushing strength, the expression is similar to Equation (2.11) with the crushing strength of fibers replacing $\sigma_{u,f}$.

Spowart and Clyne [118] compressed SiC monofilament reinforced Ti alloys having different loading axis with respect to the direction of the long fibers and showed that fiber crushing prevailed at very low misalignment angles (less than 2 °) resulting into high compressive strengths. As the initial misalignment increased, the failure mode changed to fiber kinking, resulting into a reduction of compressive strength with increasing misalignment angle. They concluded that the transition between two modes took place at an approximate misalignment of 3.5 °. An increase of the matrix yield strength raises the compressive strength obtainable for both fiber crushing and fiber kinking [108, 116]. Longitudinal compressive strength is also affected by the aspect ratio of the specimen, test method used [107] and use of end plates between the sample and the punches applying the load [107, 119].

Under transverse compression, presence of the fibers increases the Young's modulus and also results into strengthening in the plastic region. Predominant failure modes involve transverse failure of the fiber–matrix interface or the fiber splitting resulting from the tensile stresses induced along a direction perpendicular to the applied stresses and matrix shear failure at 45 ° to loading direction [117, 120]. Fiber arrangement and volume fraction affect the strengthening in the same way as discussed for tensile loading.

#### *2.4.2.3.3 Effect of the interface*

The interface between the fiber and the matrix is of utmost importance because it controls the load transfer from the matrix to the fibers, which in turn controls the overall mechanical behavior of the composite [121]. Most of the subsequent discussion in this subchapter will follow from the excellent work published by Metcalfe [122]. The following definition of interface is proposed: *"An interface is the region of significantly changed chemical composition that constitutes the bond between the matrix and reinforcement for transfer of loads between*

*these members of composite structure."* Interfaces have been classified into three different classes:

1) Class I: fiber and matrix mutually nonreactive and insoluble; e.g. Cu–W, Al–SiC etc.
2) Class II: fiber and matrix mutually nonreactive but soluble; e.g. Ni–C, Ni–W etc.
3) Class III: fiber and matrix react to form compounds at the interface; e.g. Al–C (<700 °C), Ti–SiC etc.

As already mentioned, the primary function of the interface is to transfer the load from the matrix to the fiber reinforcement. This is a mechanical requirement which must be satisfied for all conditions of loading and throughout the lifetime of the composite. Furthermore the generation of the interface should not degrade the intrinsic strength of the fiber and the interface must be stable. Stability of the interface is a physico-chemical requirement, which is most readily satisfied in composites having class I interface. In class II and III systems continued solid state diffusion causes continuous growth of the interface region. Reaction zone theories have been developed to predict the permissible amount of reaction in the class III systems. According to these theories, for very little interaction the cracks in the reaction zone are too small to initiate failure in the fiber and hence the intrinsic fiber strength is not affected. However, for intermediate to higher reaction the crack length in the reaction zone is much longer and hence causes reduction of the intrinsic strength of the fibers. These theories conclude that there is a safe limit of reaction in class III composites below which no loss of longitudinal strength would be obtained. Coatings on fibers have been developed to convert a class III system into a class I system. Six types of interfacial bonding have been proposed for metal matrix composites. They are: i) mechanical bonding, ii) dissolution and wetting bond, iii) oxide bond, iv) reaction bond, v) exchange reaction bond and vi) mixed bond. Pure mechanical bond requires an absence of any chemical source of bonding (even van der Waals forces) and involves only mechanical interlocking. However, absence of any chemical source of bond makes it very weak under transverse loading and this kind of bonding is practically of no use in composites technology. The requirement for an optimum interface has been mentioned by Hibbard [123] as: *"There should be little or no solubility or other reaction between the matrix and the fiber, which should wet each other.*" Strength of the interface can be either its tensile or shear strength. Tensile strength of the interface controls the properties like transverse tensile strength, compressive strength, and crack arrest by tensile delamination etc. Shear strength of the interface controls the properties like critical fiber length for load transfer to take place, fiber pullout after fracture and deformation of the matrix after fracture etc [124].

Depending upon the type of loading, either a weak or a strong interface gives rise to highest strength obtainable. The influences of interfacial bond strength and matrix ductility on the tensile strength of long fiber reinforced composites along the fiber direction have been derived by a Monte Carlo computer simulation method by Ochiai and Osamura [125]. They concluded that both matrix ductility and the interfacial bond strength control the tensile strength of the fiber reinforced composite. For matrices having very high ductility, the strength of the composite increases with increasing interfacial bond strength. For matrices having low ductility there is an optimum interfacial bond strength above which the strength of the composite decreases with further increase of the interfacial strength. A strong interface leads to a LLS regime where lack of fiber debonding leads to a very high stress concentration near fiber breaks leading to failure of the nearest fibers and catastrophic failure at a strain much less than the fiber failure strain. In composites having weak interfaces debonding and sliding at the interface reduce the stress concentrations resulting from broken fibers and the strength of the composite reaches the rule of mixtures tensile stress. In this case the composite

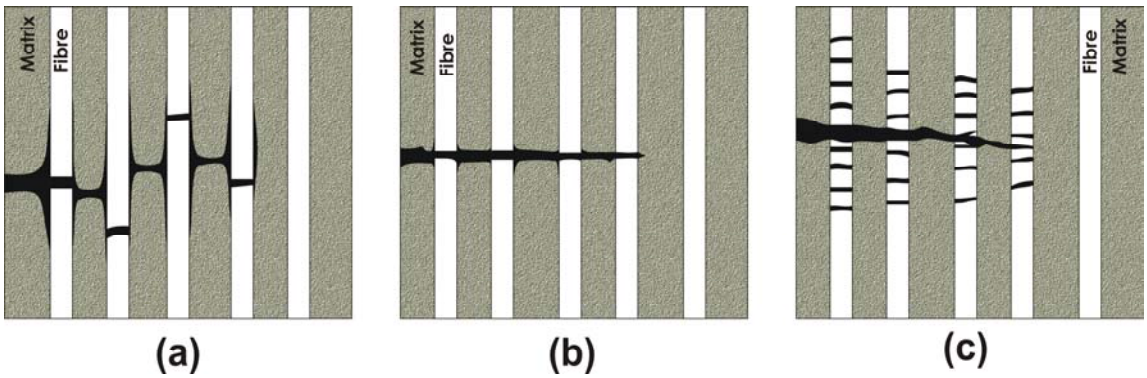


**Figure 2.9: Crack path morphology (schematic) as a result of fiber/matrix bonding: (a) weak bonding, (b) intermediate bonding and (c) strong bonding [117]**

behavior lies in the GLS regime [126]. A matrix having low yield strength and a high ductility shears easily at the interface resulting into GLS regime. Schulte and Minoshima [117] have summarized the different failure mechanisms under longitudinal tension in composites for different interfacial bond strengths. Figure 2.9 shows the crack morphologies for different fiber matrix bond strengths. A weak bonding results into excessive fiber pull out, giving rise to a very irregular fracture surface (Figure 2.9a). For intermediate bonding fracture occurs with a small amount of debonding and the crack propagates from one fiber to another deforming the matrix extensively (Figure 2.9b). In the case of very strong bonding, stress is transferred back to a cracked fiber via the matrix. This causes the fiber to crack at multiple loca-

tions above and below the path of the main propagating crack (Figure 2.9c). The situation is vastly different when tensile load is applied transverse to the fiber direction. Cooper and Kelly [124] used the strength of the matrix or the composite when neither the matrix nor the interface fail as the upper bound and the strength of the matrix for unbounded fibers or when the fibers are replaced by holes as the lower bound for transverse tensile strength. They concluded that when the interfacial tensile strength is less than the above mentioned lower bound, the composite strength is equal to the lower bound. For interfacial strengths between the upper and the lower bounds, transverse tensile strength is a function of the interfacial strength, increasing with increasing interfacial strength. If interfacial strength exceeds the upper bound, failure will take place in the matrix and the transverse strength would be equal to the matrix strength making allowances for the stress concentrations and constraints provided by the rigid fibers. Schulte and Minoshima [117] showed that in transverse tensile test a weak bonding induces failure at the fiber matrix interface. For intermediate bonding a mixture of various failure types take place which include fiber matrix debonding, formation of dimples on the fibers, fiber shear failure etc. In the case of very strong bonding failure may involve tensile or shear failure of the matrix or longitudinal splitting of the fibers.

To summarize, when loaded under tension, a strong fiber-matrix interface results into less anisotropy. From an application point of view the most attractive combination is to have a composite which follows GLS mechanism without undergoing interfacial debonding, as this also imparts substantial transverse strengthening [126]. This can be achieved in aluminum alloys reinforced with alumina fibers if the matrix yield strength lies below 50–80 MPa [127].

So far, this chapter dealt with the various processing techniques and the general mechanical properties of MMCs. Structure of the metal/ceramic composite studied in this work has similarities with lamellar two phase alloys (e.g. γ–TiAl based alloys). Mechanical properties of these alloys are briefly described in the following subchapter.

## 2.5 Mechanical properties of lamellar two phase alloys

Figure 2.10 shows the typical microstructure of a fully lamellar two phase γ–TiAl based alloy. The micrograph in Figure 2.10a shows the grain structure as visible in an optical micrograph. A typical feature of these alloys is the presence of grains with a lamellar structure consisting of alternating lamellae of γ–TiAl with tetragonal $L1_0$ structure and $\alpha_2$–$Ti_3Al$ with hexagonal $D0_{19}$ structure [128, 129, 130]. The micrograph in Figure 2.10b shows the transmission elec-

tron microscope (TEM) image of the lamellar structure. The γ-phase further consists of several ordered domains whose {111} planes overlap on the basal plane of the $\alpha_2$-phase [130].

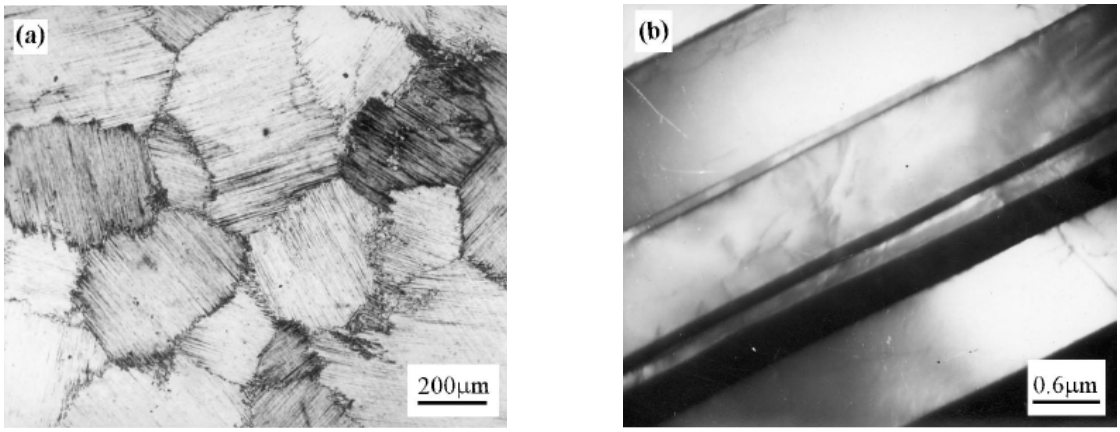


**Figure 2.10: Structure of the two phase γ-TiAl based alloys: (a) optical micrograph showing the grain structure and (b) TEM image showing the lamellar structure [131]**

Because of their two phase structure, these alloys exhibit superior creep resistance [132, 133]. Strength and ductility of these alloys strongly depend on the angle between the lamellae orientation and the loading axis, the volume fraction and thickness of the $\alpha_2$ plates, spacing of the lamellae etc. A finer lamella spacing results into an enhancement of yield stress and ductility. The yield stress enhancement could be explained by a Hall–Petch type relation replacing the lamellae spacing for grain size in the original expression [129, 130]. Furthermore, because of the less deformability of the $\alpha_2$-phase, the hardness and flow stress increases systematically with an increasing volume fraction of this phase [134]. These $\alpha_2$ plates also pin the γ layers at elevated temperatures and thus resulting into a very high thermal stability of the lamellar microstructure [135]. When loaded under compression, the yield stress strongly depends upon the angle between the loading axis and the lamellar planes. An angle of 45 ° results into a minimum yield stress because of easy slip on {111} planes of the γ-phase parallel to the lamellar planes. When stress is applied parallel or perpendicular to the lamellae boundaries, high yield stress results with the 90 ° orientation being the strongest [129, 130]. Cao et al. [136] have identified domain boundary, lamellar interface and grain boundary as the three different types of obstacles to dislocation motion in fully lamellar alloys and showed that the effect of lamellar spacing on yield stress is maximum. For a combination of high strength and good ductility an alloy with both hard and soft deformation orientations within a fine grain structure is optimum.

## 2.6 Theory of elasticity in materials

Fundamental concepts of the theory of elasticity will be discussed very briefly in this sub-chapter. Comprehensive reviews on this can be found in the text books written by Nye [137] and Hearmon [138]. The subsequent discussion mostly follows from chapter 2 in Ref. [139]. Generalized Hooke's law for an anisotropic material is written as:

$$\sigma_{ij} = C_{ijkl} \cdot \varepsilon_{kl} \tag{2.12}$$

or, in the invert form

$$\varepsilon_{ij} = S_{ijkl} . \sigma_{kl} \tag{2.13}$$

In Equations (2.12) and (2.13) $C_{ijkl}$ and $S_{ijkl}$ are the stiffness and compliance tensors while the terms with $\sigma$ and $\varepsilon$ are the stress and strain tensors, respectively. Both stress and strain tensors are second order tensors (having 9 terms in each) and the stiffness and compliance tensors are $4^{th}$ order tensors having 81 terms in each. However, because of symmetry conditions ($C_{ijkl}$=$C_{ijlk}$ and $C_{ijkl}$=$C_{jikl}$ and similar expressions for the compliance tensor) the number of elastic constants are reduced to 36 instead of 81 [137]. Usually elastic constants are written according to a matrix or contracted notation having only 2 suffixes instead of 4. This is done by reducing the first and the second pair of suffixes to single digits following the scheme shown in Table 2.1. Furthermore, strain energy considerations of a crystal shows $S_{ij}$=$S_{ji}$ and $C_{ij}$=$C_{ji}$. This reduces the number of independent elastic constants to 21 in the most anisotropic triclinic system. Stiffness and compliance matrices for the triclinic system are shown in Equation (2.14).

A particular crystal symmetry or atomic arrangement can further reduce the number of independent elastic constants. As the crystal symmetry increases, the number of independent elastic constants decreases and in isotropic systems there are only two independent elastic constants. Most of the engineering materials are polycrystalline and although individual single

**Table 2.1: Scheme followed to cover stiffness and compliance tensors with 4 suffixes to respective matrices with 2 suffixes**

| Tensor notation | 11 | 22 | 33 | 23, 32 | 13, 31 | 12, 21 |
|---|---|---|---|---|---|---|
| Matrix notation | 1 | 2 | 3 | 4 | 5 | 6 |

crystals may have a lower symmetry, because of the random orientation of the grains the polycrystalline aggregates behave as isotropic materials. Particle reinforced composites behave mostly as isotropic solids while a unidirectionally fiber reinforced composite is transversely isotropic with respect to the fiber direction.

$$C_{ij} = \begin{pmatrix} C_{11} & C_{12} & C_{13} & C_{14} & C_{15} & C_{16} \\ C_{12} & C_{22} & C_{23} & C_{24} & C_{25} & C_{26} \\ C_{13} & C_{23} & C_{33} & C_{34} & C_{35} & C_{36} \\ C_{14} & C_{24} & C_{34} & C_{44} & C_{45} & C_{46} \\ C_{15} & C_{25} & C_{35} & C_{45} & C_{55} & C_{56} \\ C_{16} & C_{26} & C_{36} & C_{46} & C_{56} & C_{66} \end{pmatrix} \text{ and } S_{ij} = \begin{pmatrix} S_{11} & S_{12} & S_{13} & S_{14} & S_{15} & S_{16} \\ S_{12} & S_{22} & S_{23} & S_{24} & S_{25} & S_{26} \\ S_{13} & S_{23} & S_{33} & S_{34} & S_{35} & S_{36} \\ S_{14} & S_{24} & S_{34} & S_{44} & S_{45} & S_{46} \\ S_{15} & S_{25} & S_{35} & S_{45} & S_{55} & S_{56} \\ S_{16} & S_{26} & S_{36} & S_{46} & S_{56} & S_{66} \end{pmatrix} \quad (2.14)$$

## 2.7 Residual stress

As reviewed by Eigenmann and Macherauch [140], residual stresses may develop in the absence of external forces and/or moments as well as temperature gradients. All residual stress systems are self-equalizing and the resultant force and moment caused by them are zero. They arise from misfits in the natural shape between different regions (as in shot peening), different parts (such as stresses around a rivet in a plate) or in different phases (as in composites (refer to subchapter 2.7.2)) [141]. They can add to, or subtract from the applied stresses and at times may result into unexpected failure of the structure [142]. Residual stresses can be discussed in terms of a characteristic length, over which they equilibrate to zero. This characteristic length may be long range having dimensions in the scale of the structure (type I stress), may be of intermediate range covering one grain or part of a grain (type II stress) and may be small range covering several atomic distances within a grain (type III stress). Type I stresses are known as macro stresses while types II and III stresses are known as micro stresses [140].

In practice, residual stresses cannot be measured directly and they are calculated from measured elastic lattice strain or some other quantity which can be directly related to stress. Several destructive and non-destructive methods are available for its measurement. Thorough description of the available techniques can be found in Refs. [143, 144]. Figure 2.11 shows the schematic representation of the present capabilities of various available residual stress measurement techniques. Among the techniques available, diffraction based techniques are most popular because of their non-destructive nature and their capability to measure phase

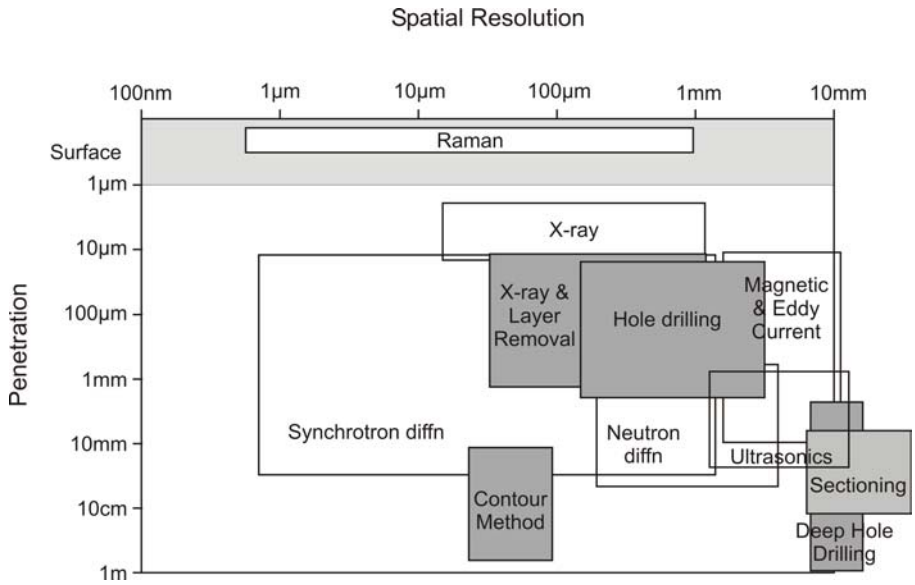


**Figure 2.11: Schematic indicative of the approximate current capabilities of the various techniques. The destructive techniques are shaded grey [145]**

specific stresses. Brief introduction to stress measurement by diffraction using X-rays will be given here and thorough description can be found in Refs. [139, 144, 146, 147].

### 2.7.1 Principle of stress analysis by X-ray diffraction

Detail description of principles of X-ray diffraction is not the aim of this work and that can be found in the text book written by Cullity [148]. When a monochromatic beam of X-ray is incident on a polycrystalline solid, it is scattered by the regularly arranged atoms of the polycrystal. These scattered rays give constructive interference if Bragg's law

$$2d \cdot \sin\theta = \lambda \tag{2.15}$$

is satisfied for the first order of diffraction. Here $d$ is the lattice plane spacing, $\theta$ is the angle between the incident beam and the diffracting plane and $\lambda$ is the X-ray wavelength. In an unstressed condition the lattice spacing $d$ for a particular family of planes does not vary with direction. However, if the lattice is stressed elastically, the lattice spacing varies depending upon the orientation of these planes relative to the direction of stress application. If the suffix *0* refers to unstressed state and absence of any suffix denote stressed state, then the lattice strain can be measured by measuring the diffraction peak shift according to:

$$\varepsilon = \frac{d - d_0}{d_0} = \frac{\Delta d}{d_0} = -\left(\theta - \theta_0\right) \cdot \cot\theta_0 = -\Delta\theta \cdot \cot\theta_0 \tag{2.16}$$

Hence, diffraction methods utilize the lattice spacing as an internal strain gauge. The strain measured by this peak shift method is largely only elastic and the plastic component of the strain present due to the movement of dislocations and other lattice defects cause broadening of the diffraction peaks.

Figure 2.12 shows the orthogonal co-ordinate system used in the stress analysis by diffraction method. $L_i$ and $S_i$ denote the laboratory and sample co-ordinate systems respectively, $\phi$ is the azimuthal angle in the plane of the sample and $\psi$ is the angle between the normal to the family of planes whose line spacing are to be measured and the normal to the plane of the sample. Here onwards the term $d_{\phi\psi}$ will be used in place of $d$ in Equation (2.16) to denote lattice spacing in the stressed condition. Employing suitable expressions for co-ordinate transformations

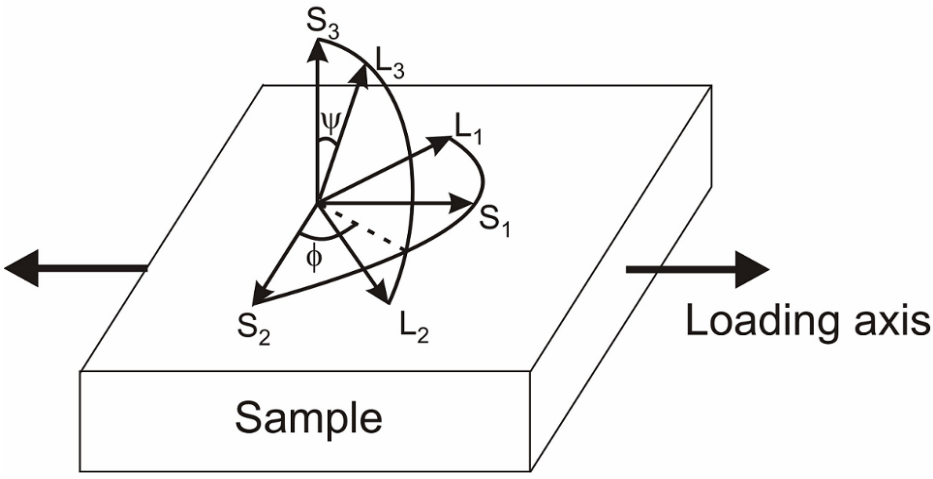


**Figure 2.12: Definition of the laboratory co-ordinate system *L*, sample co-ordinate system *S* and the angles $\phi$ and $\psi$**

(refer to [139] for detail description), the generalized expression for lattice strain in terms of the components of the stress tensor in an isotropic material takes the following form:

$$\frac{d_{\phi\psi}-d_0}{d_0}=\frac{1+\nu}{E}\cdot\left\{\sigma_{11}\cos^2\phi+\sigma_{12}\sin 2\phi+\sigma_{22}\sin^2\phi-\sigma_{33}\right\}\cdot\sin^2\psi$$
$$+\frac{1+\nu}{E}\cdot\sigma_{33}-\frac{\nu}{E}\cdot\left(\sigma_{11}+\sigma_{22}+\sigma_{33}\right)+\frac{1+\nu}{E}\cdot\left\{\sigma_{13}\cos\phi+\sigma_{23}\sin\phi\right\}\cdot\sin 2\phi \qquad (2.17)$$

Equation (2.17) is the fundamental expression for stress analysis by diffraction methods. It has got 6 unknowns and hence it can only be solved exactly if $d_{\phi\psi}$ is measured along 6 independent directions (i.e. at 6 different $\psi$ tilts). In practice more data points are measured for a better statistical accuracy. In case of bi-axial stress tensor and in the absence of any shear stress component, Equation (2.17) takes the simplified form:

$$\frac{d_{\phi\psi} - d_0}{d_0} = \frac{1+\nu}{E} \cdot \left\{ \sigma_{11} \cos^2 \phi + \sigma_{12} \sin 2\phi + \sigma_{22} \sin^2 \phi \right\} \cdot \sin^2 \psi - \frac{\nu}{E} \cdot \left( \sigma_{11} + \sigma_{22} \right) \qquad (2.18)$$

Equation (2.18) suggests a linear relation when measured strain is plotted against $sin^2\psi$. The slope of this straight line is proportional to the stress and the intercept is proportional to the trace of the stress tensor. Accordingly this method is known as "*$sin^2\psi$ method*".

The above discussion is valid for all polycrystalline materials provided that they are homogeneous, macroscopically isotropic, have a small grain size and they are without any stress or composition gradient. However, as has been summarized by Cullity [149], there are some special cases when the residual stress measured by X-ray diffraction give erroneous results.

### 2.7.2 Thermal residual stress in MMCs

Thermal residual stresses are generated in MMCs during fabrication due to the large mismatch in thermal expansion coefficients $\alpha$ between the matrix and the reinforcement. These residual stresses play a significant part in the deformation behavior of MMCs and depending upon the type of application, may enhance or adversely affect the performance of the component. Detail theoretical discussion of this problem starting from physical fundamentals is not possible within the limited scope of this chapter and hence only a brief overview will be given here. Thorough discussion can be found in the comprehensive review written by Delannay [150].

Thermal expansion being a reversible phenomenon, volume averaged thermal residual stresses in matrix and reinforcement can be expressed following elastic analysis according to the formulae [141]:

$$\left\langle \sigma_m \right\rangle_i^{II} = B_{m_{ij}} \cdot \Delta\alpha_{ij} \cdot \Delta T \qquad (2.19a)$$

$$\left\langle \sigma_f \right\rangle_i^{II} = B_{f_{ij}} \cdot \Delta\alpha_{ij} \cdot \Delta T \qquad (2.19b)$$

where $\Delta\alpha\Delta T$ is the strain generated from thermal expansion mismatch between the reinforcement and the matrix and the parameter $B$ reflects the influence of reinforcement volume fraction, phase stiffness and phase geometry on the level of internal stress generated per unit of thermal expansion misfit. $\Delta T$ is written as $\Delta T = T_{act} - T_0$ [151], where $T_{act}$ is the actual temperature where the stress measurement is carried out and $T_0$ is the stress-free temperature. This stress-free temperature is different from the actual fabrication temperature and is taken as the temperature where stress relaxation by viscoelastic deformation is negligible [152]. The

superfix *II* denotes that the thermal residual stresses generated in composites are of type *II*. For a two phase composite in the absence of any applied stress, mechanical equilibrium satisfies the relationship:

$$\left\langle \sigma_m \right\rangle_i^{II} \cdot \left(1 - V_f\right) + \left\langle \sigma_f \right\rangle_i^{II} \cdot V_f = 0 \tag{2.20}$$

Equation (2.20) is valid for all volume averaged stress components including the hydrostatic and deviatoric stresses, but not for the von Mises effective stress (due to the fact that von Mises effective stress is always positive).

The simplest model to estimate the thermal residual stresses in particle reinforced composites considers a sphere of the reinforcement inside a concentric sphere of the matrix. Radii of the spheres depend upon the volume fraction of the reinforcement. An extension of the same model can be used to estimate the stresses in a uni-directional fiber reinforced MMC by considering infinite co-axial cylinders (refer to [150] for details).

For particle reinforced MMCs (throughout the discussion it has been assumed that the matrix co-efficient of thermal expansion is larger than the ceramic reinforcement) where the matrix–particle curvature is convex, the model suggests that the stress states within the particle is pure hydrostatic compressive and equal to the radial stress along the interface. Moreover, the absolute value of the interfacial radial stress is predicted to increase with decreasing particle volume fraction. Experimental evidence also suggests that phase specific mean residual thermal stresses and strains depend strongly on both the reinforcement shape and volume fraction [153, 154].

Predictions of the infinite co-axial cylinder model for fiber reinforced MMCs suggest that all the axial, tangential and the radial stress components within the fiber are compressive and they do not vary along the radial direction within the fiber. The radial and tangential stress components are equal to each other. Assuming a purely elastic matrix this model shows that the axial stresses within the matrix remains constant and tensile along the radial direction. Both the matrix radial and axial stresses vary with distance from the fiber-matrix interface.

Predictions from the above mentioned two models are only valid for a composite having a very low volume fraction of the reinforcement and in which the particle–particle and fiber–fiber interactions are purely isotropic. Moreover, although the above discussion is based on purely reversible elastic behavior, the magnitude of the internal stresses may be so high that they may initiate non-reversible phenomena such as plastic yielding of the matrix, fracture of the reinforcement etc. These non-reversible phenomena counteract the development of resid-

ual stresses and they are termed as relaxation mechanisms because they reduce the overall strain energy of the composite. Chun and Daniel [155] calculated the residual stress state within the fiber and the matrix assuming an elastic–plastic matrix and showed that considering plastic flow of the matrix the residual stresses in the fiber and the matrix were an order of magnitude less than that considering no plastic flow. Thermal residual stresses also depend upon the distribution of the reinforcement within the matrix [156]. Chou et al. [157] have shown that the thermal residual stresses depend upon the ratios of the thermal expansion coefficients and the Young's moduli of the reinforcement and the matrix.

Thermal residual stresses affect the global stress-strain behavior of the MMC [158]. During external straining of the MMC, mismatch of the plastic flow strength between the phases causes the formation of plastic residual stress. As the matrix yields, the relative contribution of the thermal residual stress in comparison to the plastic residual stress decreases with further deformation. In general, the matrix material almost always has a higher thermal expansion coefficient than the reinforcement, resulting in tensile average residual stresses in the matrix and compressive stresses in the reinforcement. This may result into anisotropy in the stress-strain curves under tension and compression. This fact is well documented for MMCs with reinforcements having different geometries. Arsenault and Taya [159] and Hong et al. [160] showed that the tensile thermal residual stresses in the matrix resulted in a higher compressive yield strength than the tensile yield strength in a whisker reinforced MMC. Dutta et al. [161] showed by finite element analysis that this tensile-compressive anisotropy depends upon the volume fraction of whiskers in the MMC and in MMCs with relatively high whisker content the tensile yield strength is higher than the compressive yield strength. Zahl and McMeeking [162] studied the effect of thermal residual stress on the subsequent stress-strain behavior of particle reinforced MMCs. Their results show that prior residual stress results into a transient softening in both tension and compression, whose effect was leveled out at large deformations. They concluded that this behavior also depends upon the particle shape, volume fraction and hardening behavior of the matrix. Nakamura and Suresh [156] studied the effect of thermal residual stress on the macroscopic stress-strain behavior of continuous fiber reinforced MMCs. Their results show that tensile residual stresses in the matrix causes its partial yielding, resulting in a reduced tensile axial stiffness in comparison to a compressive axial stiffness. Effect of thermal residual stress is more prevalent when the same MMCs are tested under transverse tension (similar conclusion has been drawn by Böhm and Rammerstorfer [163]) where the MMC with residual stresses is significantly stronger than the one without it.

Moreover, the difference between the average flow stresses obtained with different fiber arrangements reduces significantly when residual stresses are present. Jensen [164] has shown that the presence of tensile (compressive) residual stresses in the matrix in the loading direction increases (decreases) the critical stress required for kink band formation under axial compression of uni-directional fiber reinforced composites.

# 3 Methodological aspects

## 3.1 Micro Computed Tomography (µCT)

The goal of X-ray CT is to produce 3D internal images of objects non-destructively and with sufficient details. Figure 3.1 schematically shows the operating principle of X-ray CT process.

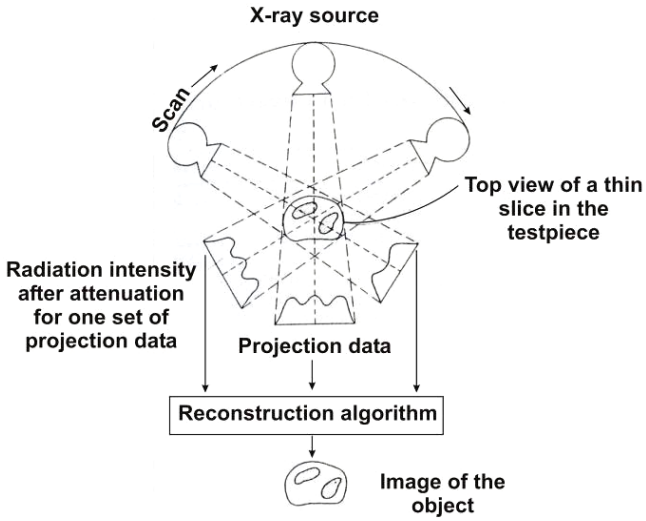


**Figure 3.1: Schematic of a CT process [165]**

This imaging technique was first developed for widespread application in the field of medicine and since then its application has extended to several other fields, including geological sciences [166] and materials science [167, 168]. A very brief description of the CT imaging principle will be given here and details are given in Refs. [165, 169, 170].

At the simplest level, all CT systems consist of an X-ray source, an object to be imaged through which X-rays pass and X-ray detector. A thin slice of the object to be imaged is irradiated by a thin X-ray beam. The X-ray beam is attenuated as it passes through the object. Extent of this attenuation depends on the density of the material, its atomic number and the energy of the incident beam. For any cross sectional plane this information is obtained from many different angles; which are then reconstructed using computer generated algorithms to generate the image.

The capability of the X-ray source depends upon the size of the focal spot, the energy spectrum generated and the X-ray intensity. The energy spectrum defines the penetrative ability of the X-rays. High energy X-rays penetrate more effectively but they are less sensitive to

changes in material density and composition. The energy spectrum is usually described in terms of the peak X-ray energy. X-ray intensity directly affects the signal to noise ratio and thus image clarity.

As X-rays pass through the object, they are attenuated by scattering and absorption within the material following Beer Lambert's law. For monoenergetic X-ray beam this law is written as:

$$I = I_0 \cdot \exp\left[-\mu \cdot x\right] \tag{3.1}$$

where $I$ is the X-ray intensity after traversing through the object, $I_0$ is the initial intensity, $\mu$ is the linear attenuation coefficient of the material and $x$ is the path length traversed within the object. Three dominant mechanisms are responsible for X-ray attenuation within the object. Photoelectric effect is operative at low X-ray energies up to approximately 50–100 keV. Compton scattering is dominant at intermediate energy range of 5–10 MeV and pair production is dominant at still higher energies. Photoelectric effect is proportional to $Z^{4.5}$ where $Z$ is the atomic number of the attenuating material while Compton scattering is proportional to $Z$.

Output of CT imaging procedure strongly depends upon the ability of the detectors to measure the intensity of the transmitted X-rays. Either gas ionization detectors or scintillation detectors are used for this purpose. In ionization detectors the incoming X-rays ionize a noble element which is kept either in a gaseous or in a liquid state. Scintillation detectors work on the principle that certain materials emit visible radiation when exposed to X-rays. Reconstruction is the process of converting this raw data acquired in the detectors into two dimensional slices of images. This process converts the raw intensity data into CT numbers whose range vary upon the computer system used. Modern computers use 16 bit scales and hence these numbers lie in a range within 0 to 65535. These values correspond to the gray value of the image.

Spatial resolution is defined as the smallest separation at which two points can be distinguished as separate entities. This in CT is mainly determined by the size and number of the detector elements, the size of the X-ray focal spot and the distance between the X-ray source and the detector. In absorption contrast tomography, the ability to differentiate between materials depends upon the $\mu$ of the elements. Hence, materials with largely different densities or atomic constituents are easy to differentiate.

Like other imaging techniques, CT is also not free of image artifacts[5]. Common artifacts observed in absorption contrast tomography include beam hardening [171], ring artifacts, partial

[5] An artifact can be defined as the discrepancy between the actual value of some physical property of an object and the map of that property generated by a CT imaging process.

volume effect etc. CT based on absorption contrast performs poorly when the elements in the object to be imaged have similar $\mu$. This can be eliminated in phase contrast tomography [170]. This is based on the principle that the phase of an X-ray beam transmitted through an object is shifted due to its interaction with the electrons in the material. The instrumentation for phase contrast tomography is essentially the same as for absorption contrast tomography, apart from the fact that the sample–detector distance is significantly higher in the former case.

## 3.2 Ultrasonic spectroscopic techniques for determination of elastic constants

Determination of the elastic constants of a body non–destructively using ultrasonic wave is a well established technique [172, 173, 174, 175]. Brief description of the interaction of ultrasound with materials is given in this subchapter. In this work two different ultrasonic techniques have been used. Theoretical background of these two techniques is given in subchapters 3.2.1 and 3.2.2.

Ultrasound is cyclic sound pressure with a frequency greater than the upper limit of human hearing ability (approx. 20 kHz in a healthy young adult [176]). Ultrasonic waves can be generated inside a material by placing a piezoelectric transducer in contact with the surface of the material and subsequently exciting the transducer with an appropriate voltage–time profile. The piezoelectric transducer converts electrical energy into mechanical energy by piezoelectric effect. A couplant material is used between the transducer and the sample to efficiently transmit the ultrasonic wave. The choice of the couplant mostly remains a matter of trial and error. As reported in Ref. [172], several couplant materials have been tried, which include ordinary waxes, beeswax, light machine oils (good for shear waves at temperatures below -10 °C), salol (excellent for shear waves up to about 43 °C), Dow Corning Resin (useful for both longitudinal and shear waves between -80 °C–80 °C) etc. The quality of the couplant seal is of utmost importance. A very thin seal, free of bubbles and prepared between clean surfaces is optimum.

Wave velocity is defined as the velocity at which a disturbance propagates inside a material. Its value depends upon the material, structure and form of the excitation. Closely related to wave velocity is particle velocity. There are two different types of particle velocity in relation to the wave velocity. For a longitudinal wave, the particle velocity vector is in the same direction as the wave velocity vector; while for a shear wave the particle velocity vector is at 90 ° to the wave velocity vector. As the ultrasonic wave propagates within the body, it may get

attenuated or scattered. Ultrasonic attenuation is defined as the rate of decay of mechanical radiation at ultrasonic frequency as it propagates through a material [177]. It is a measure of the relative amplitudes of a wave at two different locations in space. For a nondispersive[6] medium [178] attenuation reduces the magnitude at constant pulse duration while scattering can produce both magnitude reduction and pulse spreading as a result of the interaction of the wave with small obstacles or flaws. Furthermore, as ultrasonic waves propagate within the material, superposition of waves occur, which may lead to constructive or destructive interference. Constructive interference takes place when two waves are completely in phase and the final waveform is a simple sum of the two component waves. Complete destructive interference takes place when the two component waves are out of phase by half a wavelength.

### 3.2.1 Ultrasound Phase Spectroscopy (UPS)

The input waves for the measurement of wave velocity within the material may either be in the form of a pulse or may be continuous waves. Pulses are very broadband in frequency. Continuous waves are essentially narrow band. Although pulse methods are most widely used [179], they suffer from some inherent limitations when applied to dispersive materials. For precise velocity determination using pulse methods, the wave packet must be small in comparison to the specimen length in the direction of wave propagation and the wavelength must be large compared to the pores and other microstructural features to avoid too much of an attenuation [180]. Furthermore, the expected error in the measurement of wave velocity through a material is written as [181]:

$$\Delta V = \left( dV/df \right) \Delta f \tag{3.2}$$

where *dV/df* is a measure of material's dispersion and *Δf* is the bandwidth of the wave or the pulse used. Hence, continuous waves having the narrowest bandwidth, are the automatic choice for determination of wave velocity in a dispersive medium.

Determination of wave velocity by measuring the phase change of a propagating continuous wave was first proposed by Lynnworth et al. [181] and further reviewed by Papadakis [182].

---

[6] Dispersion may be caused by (a) presence of specimen boundaries (geometric dispersion), (b) frequency dependence of material constants like mass density, elastic moduli etc (material dispersion), (c) scattering of waves by densely distributed fine inhomogeneities (scattering dispersion), (d) absorption or dissipation of the wave energy into heat or other form of energy irreversibly (dissipative dispersion) and (e) dependence of wave speed on wave amplitude (nonlinear dispersion).

More recently, Wanner [180] further described this method in detail and used it for the determination of the elastic constants of highly porous ceramics. The subsequent discussion in this subchapter follows the general description given in Refs. [180, 181, 183, 184]. Together, these four papers cover all the important aspects of UPS.

A plane monochromatic wave propagating un-damped in the x–direction can be written as:

$$u(x,t)=u_0 \cdot e^{i(\varpi t+k_w x)} \tag{3.3}$$

where $\omega t+k_w x$ is the phase function, $\omega=2\pi f$ is the circular frequency and $k_w=2\pi/\lambda$ is the wave number. For a specimen of length $L_s$, surfaces of constant phase propagate at the phase velocity $V_p$ defined as:

$$V_p = dx/dt = \varpi/k_w = f\lambda = L_s \cdot \frac{f}{N}. \tag{3.4}$$

A pulse being a superposition of many waves propagates with a group velocity defined as:

$$V_g = d\varpi/dk = \frac{df}{d\left(1/\lambda\right)} = L_s \cdot \frac{df}{dN} \tag{3.5}$$

where $N$ is the number of wave periods in the sample. Furthermore, the phase difference between the received and the input signals $\Delta\phi$ is related to $N$ according to:

$$\Delta\phi = -2\pi N. \tag{3.6}$$

Combining Equations (3.5–3.6), the expression for group velocity is obtained as:

$$V_g = -\frac{2\pi L_s}{\left(d\Delta\phi/df\right)}. \tag{3.7}$$

The denominator on the right hand side of Equation (3.7) is the slope of the phase versus frequency plot. Hence, group velocity is determined by increasing the phase in the specimen by increasing the frequency and then finding the slope of the phase–frequency plot. If the plot turns out to be a straight line with a constant slope within a region of frequency, it suggests that the material is non-dispersive in that region.

While frequency is the independent variable in measuring the group velocity, thickness is the independent variable in measuring phase velocity. Hence, phase velocity measurement can be carried out by either making measurements on samples having different thicknesses or by knowing unambiguously the exact number of wavelengths in the sample and then following Equation (3.4). Group and phase velocities are related according to:

$$V_g = V_p \Big/ \left[1-\left(f/V_p\right)\left(dV/df\right)\right]. \tag{3.8}$$

In a non–dispersive media (*dV/df=0*) and hence group velocity and phase velocity are equal to each other.

The total number of phase periods measured during the experiment is the sum of the number of phase periods within the sample and the transducers. Hence, the number of phase periods within the transducers must be subtracted from the total number of measured phase periods. The number of phase periods within the transducers can be determined by making measurements with the transducers in touch of each other with no sample between them [180, 183]. Once $V_g$ for a particular mode (longitudinal or shear with appropriate propagation and polarizations vectors) of wave propagation is determined, the corresponding elastic constant $C_{ii}$ is determined according to:

$$C_{ii} = \rho V_g^2 . \tag{3.9}$$

In Equation (3.9), $\rho$ is the density; (*i=1-3*) refers to longitudinal elastic constants while (*i=4-6*) corresponds to shear elastic constants. Detail derivation of Equation (3.9) can be found in appendix (A.1).

The accuracy of UPS is limited by two factors, namely bounded specimens and attenuation. The effect of sample boundaries is mostly prevalent in low frequency regimes, where beam spreading fills the entire specimens with sonic waves. This causes the excitation of many modes apart from the principal longitudinal and shear modes. Interference among the modes and the multiple reflections from the sidewalls causes shifts in the apparent phase calculation points, resulting into errors in the computed velocities. Errors from sidewall reflections decrease as attenuation increases as then energy in the spreading part of the beam gets attenuated before it reaches the sidewalls. Attenuation increases and beam spreading decreases at higher frequencies and hence this kind of error is less severe at higher frequencies. However, at very high frequencies high attenuation leads to errors in determining the output phase as it gets affected by the instrument noise level. Hence, the optimum range of operation seems to be at as high frequency as possible without significantly attenuating the input signal.

### 3.2.2 Resonant Ultrasound Spectroscopy (RUS)

RUS involves the study of the eigenfrequencies[7] of solids. These frequencies depend upon the shape, elastic constants, crystallographic orientation, density and dissipation properties of the body. Hence, with this technique the complete stiffness matrix of a body with relatively low symmetry can be obtained non-destructively by measuring its eigenfrequencies [185, 186]. The sample whose elastic constants are to be measured is held lightly between two piezoelectric transducers. One transducer applies a sinusoidal excitement to some point on the sample and its resonance response is measured at some other point by the second transducer. A large response is observed when the frequency of the driving transducer corresponds to one of the sample eigenfrequencies. This procedure is repeated for many frequencies over a large range [187]. A solid with $N_a$ atoms have $6N_a - 6$ eigenfrequencies and of them the lowest $10^4$ or so can be detected as they are isolated. Depending upon the symmetry of the object, accurate measurement of first 100 or less eigenfrequencies is enough for a successful RUS calculation [188].

Maynard [189] has summarized the detail historical development of RUS. During its early days the main stumbling block to the development of RUS was the limited computing power of the available computers. Fraser and LeCraw [190] first used RUS for a sphere of an isotropic material. Demarest [191] solved the problem for a rectangular parallelepiped sample of an anisotropic crystalline material, which was further simplified by Ohno [192]. The current state of the method as well as the computer algorithm used almost universally is described in detail in the book written by Migliori and Sarrao [193].

Essential to the successful implementation of RUS is the ability to determine the eigenfrequencies of a body from its shape, density and elastic constants (known as forward or direct problem). Once these are computed, carefully constructed fitting procedures are used to find the moduli from the measured frequencies (known as backward or inverse problem). The procedure to solve the direct problem is rigorous and mathematically complicated. The underlying theory will be discussed here very briefly and detail description is given in Ref. [186, 187, 193, 194, 195].

For an arbitrarily shaped elastic body with volume $V_i$ and surrounded by a free surface, the general form of the Lagrangian $L$ is written as:

---

[7] A normal mode of an oscillating system is a pattern of motion in which all parts of the system move sinusoidally with the same frequency. The frequencies of the normal modes of a system are known as its natural or eigenfrequencies.

$$L = \int_{V_i} (KE - PE)\, dV \tag{3.10}$$

where *KE* and *PE* are the kinetic and the potential energy densities respectively; written as:

$$KE = \frac{1}{2} \sum_i \rho \cdot \omega^2 \cdot u_i^2 \tag{3.11}$$

$$PE = \frac{1}{2} \sum_{i,j,k,l} C_{ijkl} \frac{\partial u_i}{\partial x_j} \cdot \frac{\partial u_k}{\partial x_l} \tag{3.12}$$

In the above expressions $u_i$ is the *ith* component of the displacement vector, $\omega$ is the angular frequency, $C_{ijkl}$ is a component of the stiffness tensor and $\rho$ is the density. The subscripts *i, j,* etc. refer to the Cartesian co-ordinate system. To find the minimum of the Lagrangian, *L* is differentiated as a function of *u* to yield:

$$\begin{aligned} \delta L = \int_{V_i} \left[ \sum_i \left( \rho \cdot \omega^2 \cdot u_i + \sum_{j,k,l} C_{ijkl} \cdot \frac{\partial^2 u_k}{\partial x_j \partial x_l} \right) \delta u_i \right] dV_i \\ - \int_{S_i} \left[ \sum_i \left( \sum_{j,k,l} \bar{n}_j C_{ijkl} \frac{\partial u_k}{\partial x_l} \right) du_i \right] dS_i \end{aligned} \tag{3.13}$$

For *L* to be stationary for arbitrary $u_i$ in $V_i$ and $S_i$, each of the two terms within square brackets in Equation (3.13) must be individually zero. The displacement vector is further expanded according to:

$$u_i = \sum_\lambda a_{i\lambda} \cdot \Phi_\lambda \tag{3.14}$$

where $a_{i\lambda}$ are the expansion coefficients and $\Phi_\lambda$ are the basis functions. Holland [196] used trigonometric functions while Demarest [191] and Ohno [192] used Legendre polynomials as basis functions. Visscher et al. [197] used a basal function with powers of the Cartesian co–ordinates having the form of $\Phi_\lambda = x^l y^m z^n$, with $\lambda$ = *(l, m, n)* being the function label, a set of three non–negative integers. This choice of the basis function is found to be numerically adequate and very flexible to implement for a wide variety of shapes and symmetries. Substituting this basis function into Equation (3.13) one obtains the following eigenvalue problem:

$$\omega^2 K a = \Gamma a \tag{3.15}$$

with *a* being a column vector and *K* and *Γ* are matrices whose order *O* is determined by the truncation condition

$$l+m+n \le N \tag{3.16}$$

with $O=3\cdot(N+1)\cdot(N+2)\cdot(N+3)/6$. As $N \to \infty$, the solution of the problem becomes exact. In practice a value of *N=10* is chosen as it gives a good compromise between computational accuracy and computing time/memory requirement. This results into an 858×858 matrix. For materials having orthotropic or higher symmetry, Ohno [192] introduced a treatment based on splitting of the original matrix along the mirror planes perpendicular to the x, y and z axes. This transformed the original matrix $\Gamma$ into 8 smaller matrices, thus significantly reducing the computational effort from computing a large 858×858 matrix to that consisting of 8 smaller 100×100 matrices. Each of these 8 matrices corresponds to one vibrational eigenmode.

Solution of Equation (3.15) determines the eigenfrequencies from the elastic moduli. However, computing elastic moduli from the eigenfrequencies is not straightforward as solution of the inverse problem has never been undertaken successfully. In order to overcome this problem, a nonlinear optimization procedure is carried out to determine a set of parameters that produces resonance frequencies that are in the best possible agreement with the measured spectra. In order to determine the best possible parameters, a figure of merit *FOM* is constructed, which provides a measure of how well the calculated and measured resonance frequencies agree. The *FOM* is defined as:

$$FOM = \sum_{i=1}^{N_p} w_i \cdot \left( f_{calc} - f_{mea} \right)^2 \tag{3.17}$$

where $f_{calc}$ and $f_{mea}$ are the calculated and the measured eigenfrequencies respectively, $w_i$ is a weighting factor chosen based on the confidence of the experimenter for the particular frequency and $N_p$ is the number of resonant frequencies. As several eigenfrequencies depend in almost identical way on some of the elastic constants, hence many more resonances than the total number of parameters to be fit must be measured for a meaningful analysis. Migliori and Sarrao [193] suggest that the number of resonant frequencies measured should be at least 5 times and preferably 8–10 times the number of parameters to be determined. Furthermore, the sample for RUS (most preferable sample shape is rectangular parallelepiped, although cylindrical [198] and spherical samples are also used) must have very well defined geometry with face parallelism a few microns per mm and excellent face perpendicularity. Above conditions being fulfilled and using a reasonably good guess for the input parameters, the error bars for compressional moduli in the range of 0.5–1.0 %, for shear moduli in the range of 0.02 % and

for off–diagonal moduli in the range of 2–3 % are achievable [199]. Modern apparatus also permits to carry out RUS for elastic constant measurement at temperatures as high as 1825K [200, 201].

## 3.3 Synchrotron X-ray Energy-dispersive Diffraction

Synchrotron X-ray is generated in particle accelerators when charged particles (electrons or positrons) are accelerated to relativistic velocities and are deflected in magnetic fields to keep them on a circular orbit [202, 203, 204]. In the simplest case, the electrons follow a circular orbit, which is defined by dipole magnets. The emitted radiation covers a range from the infrared to γ–rays. According to Ref. [202], SR was first observed in Schenectady, USA in the year 1947 [205].

SR has found widespread application in the last few decades in a wide variety of applied or fundamental of applied research because of its attractive properties; which include [202]:

1) Continuous spectrum from the infrared to X–rays
2) High intensities
3) Small source size
4) Collimation in forward direction
5) High degree of linear polarization in the orbit plane
6) Elliptical or circular polarization above and below the orbit plane
7) Well defined, pulsed time structure
8) Quantitatively known characteristics
9) Clean environment

The intensities of SR sources are expressed in terms of brilliance[8]. Compared to laboratory X–ray sources, SR provides 5–10 orders of magnitude higher brilliance, which allows to get better signals in shorter time with less sample volume required and/or better energy and spatial resolution. This makes it a perfect tool for in-situ analysis, where measurement time is a serious concern. With laboratory X–rays it is possible to sample only a very shallow surface layer while neutron beams have very low intensities, resulting in slow rates of data acquisition

8

$$Brilliance = \frac{No.of\ \ photons\ per\ unit\ time\left(\mathrm{s}\right)}{per\ source\ size\left(mm^2\right)\times per\ opening\ angle\left(mrad^2\right)\times per\ 0.1\%\ spectral\ bandwidth}$$

and low spatial resolution of about 1 mm. Modern synchrotron sources provide highly intense narrow beams of highly collimating penetrating X–rays and thus overcome the shortcomings of both laboratory X–rays and neutron diffraction.

Three different variations of stress analysis by synchrotron X–ray diffraction have been established, namely (i) *θ/2θ* scanning in either reflection or transmission mode [206, 207], (ii) using high energy monochromatic photons in transmission with 2D detector [208, 209] and (iii) energy-dispersive diffraction using white beams [210, 211, 212, 213, 214]. Among these, synchrotron X–ray energy-dispersive diffraction was used in this work and hence this method is briefly discussed in subchapter 3.3.1.

### 3.3.1 Energy-dispersive diffraction

Together Refs [215, 216, 217] cover most of the methodological aspects of synchrotron X–ray energy-dispersive diffraction. In this method a white beam having a continuous energy spectrum is used. The diffraction angle is defined by two pairs of slits and is kept constant. An energy sensitive solid state detector (SSD) is positioned at this angle with respect to the incoming beam. Constructive interferences from the sample appear as peaks in an energy spectrum, where intensity is plotted against energy. The correlation between the lattice spacing *d(hkl)* and the corresponding energy *E(hkl)* of the *(hkl)* family of planes is obtained from the relation:

$$d(hkl) = \frac{h \cdot c}{2\sin\theta} \cdot \frac{1}{E(hkl)} = \frac{6.199 \quad \text{Å} \cdot keV}{\sin\theta \cdot E(hkl)} \tag{3.18}$$

where *h* is Planck's constant and *c* is the velocity of light. Lattice strain is determined by an expression similar to Equation (2.16) as:

$$\varepsilon(hkl) = \frac{d(hkl) - d_0(hkl)}{d_0(hkl)} = \frac{E_0(hkl) - E(hkl)}{E(hkl)} \tag{3.19}$$

where $E_0(hkl)$ is the strain free energy.

Incoming beam from the source passes through one slit system before impinging on the sample. After being diffracted by the sample, it passes through two other slits before being analyzed by the SSD. The opening of these slits along with their relative distances from the sample controls the shape and volume of the gauge volume within the sample as well as the energy resolution of the setup. Because of the small Bragg angle, the gauge volume always has

the shape of an elongated diamond, with its length being much larger in comparison to its breadth.

Choice of the scattering angle has a large influence on the intensity of the reflections. With increasing $2\theta$ the intensity of the reflections steeply decreases because the atomic scattering factor decreases as scattering angle increases. However, as Equation (3.18) shows, an increase of $\theta$ automatically results into an decrease of $d(hkl)$, suggesting that higher scattering angles lead to a compression of the complete diffraction spectra, resulting into its total shift toward smaller energies. This is a serious concern for materials having low symmetry as in this case identification of individual peaks becomes difficult. Furthermore, with decreasing $\theta$, the asymmetry of the gauge volume also increases. Hence, the actual scattering angle is chosen as a compromise between the above mentioned factors.

In energy-dispersive diffraction one obtains the complete diffraction spectra over a large energy range. This enables one to simultaneously analyze stress and texture. Moreover, as multiple reflections are analyzed, an average stress state of the material can be obtained. Resolution of energy-dispersive diffraction can be obtained by differentiating Equation (3.18) as:

$$\left|\frac{\Delta d}{d}\right| = \left|\frac{\Delta E}{E}\right| + \left|\cot\theta\right| \cdot \Delta\theta \tag{3.20}$$

where $\Delta E$ is the resolution of the SSD and $\Delta\theta$ is the angular divergence defined by the incident and detecting slit systems. Because of the inherently low resolution of the SSD used, this resolution normally lies in the range of about 0.01. However, this resolution denotes the ability to separate different peaks. Strain sensitivity of the method is limited by the minimum measurable shift in energy of a peak of a diffraction profile. Fitting a Gaussian plus quadratic background to each profile, peak positions are obtained to an accuracy of ~1 eV and hence strains as low as $10^{-4}$ can readily be measured.

# 4 Experimental procedures

## 4.1 Specimen materials

The studied material is an interpenetrating composite made of alternating layers of metallic and ceramic lamellae. Because of this interpenetrating structure, the word 'matrix' is inadequate in this context and hence, the terminology metal/ceramic composite will be used throughout the work. Two types of alumina preforms with porosities of about 56 vol% were produced at Institut für Keramik im Maschinenbau (IKM) at Universität Karlsruhe, Karlsruhe, Germany, via freeze-casting of a ceramic suspension and subsequent sintering. Water was used as the liquid vehicle during freeze-casting and the suspension contained 22 vol.% of alumina powder (CT3000SG from Almatis with nominal alumina content of 99.8%, powder particle size 2.5 lm/D90 Cilas and a fired density of 3.90 Mg/m³), 0.5 wt% Dolapix CE64 as dispersant and 10 wt% Optapix PAF60 as a binder. The freeze–casting temperature was either -10°C (Composite Type A) or -30°C (Composite Type B). Freeze-cast ceramic bodies were freeze dried for 48 hours, sintered at 1550°C for 1 hour and then they were brought to room temperature at a cooling rate of 4°C/min [218]. Figure 4.1 shows the typical microstructure of the face perpendicular to the freezing direction for a freeze-cast preform of Composite Type A. Preforms with nominal dimensions 10×44×66 mm³ were infiltrated with a eutectic

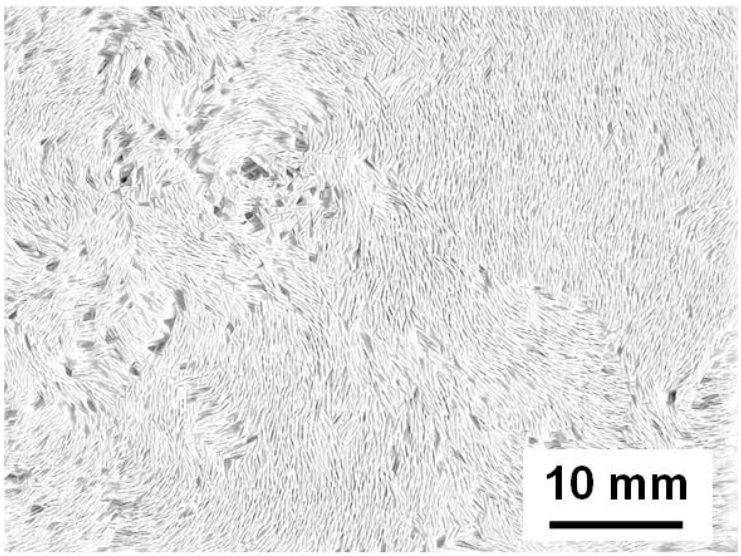


**Figure 4.1: Microstructure of the face perpendicular to the freezing direction for a freeze-cast preform of Composite Type A**

aluminum–silicon alloy (Al–12Si) by squeeze-casting and die-casting. Squeeze-casting was carried out at the Institute of Surface Technology and Materials Science at Aalen University of Applied Sciences, Aalen, Germany while die-casting was done at the Casting Technology Centre at Aalen University of Applied Sciences, Germany. Before squeeze-casting the preforms were preheated to 800°C and the mold was heated up to 400°C. After squeeze-casting, the infiltrated samples were further heat treated to 450 °C, held at that temperature for 2 hours and then were subsequently furnace cooled. To investigate the influence of interfacial properties between the ceramic and metallic component on the mechanical behavior of the composite material, some preforms were additionally coated with Cu and Ni before melt infiltration using an electroless-deposition technique [219]. Commercially available coating solutions (Enthone Inc. USA) were used. Before applying the coating, the substrate surface was activated with Pd/Sn solution containing hydrochloric acid. For coating, the preforms were clamped to a mounting plate made of teflon and the Cu solution was manually pressed into the porous preform with a stamp under appropriate conditions. Some of the Cu coated preforms were additionally heated to 1150 °C for 2 hours to allow the coating to completely oxidize to $Cu_2O$ (this is more a reaction of Cu to $Cu_2O$ in the temperature region of around 600°C. At 1150°C the coating changes to aluminate $CuAlO_2$). Finally the Cu and $Cu_2O$-coated ceramic preforms were infiltrated with Al-12Si melt by squeeze-casting as discussed before. For nickel coating the same procedure followed for Cu coating was followed. Nickel bath Noviganth Ni PA® (Atotech, Germany) was used. Coating took place at 60°C solution temperature [219]. For die-casting, the preform, mold and the melt temperatures were maintained at 800 °C, 200 °C and 750 °C, respectively. The operating pressure was 140 bar [220].

## 4.2 Micro computed tomography (µCT)

Preliminary µCT was carried out to observe the 3D structure of both the uninfiltrated preform and the infiltrated metal/ceramic composite. Tomographic analysis of the preform was carried out at RJL Micro & Analytic GmbH, Karlsdorf-Neuthard, Germany using a desktop CT scanner Skyscan 1072. The source current and source voltage were kept at 98 µA and 100 keV, respectively while the voxel size was 9 µm³. Tomographic analysis of the metal/ceramic composite was carried out at the Casting Technology Center, Aalen University of Applied Sciences, Germany using a CT scanner Ray Scan 200. For the results presented in this work, the voxel size was maintained at 79.5 µm³. The results were analysed with the image analysis software VGStudio Max, developed by Volume Graphics GmbH, Heidelberg, Germany.

## 4.3 Ultrasound Phase Spectroscopy (UPS)

As has already been mentioned in subchapter 3.2, it is a standard approach to determine elastic constants from the velocities of elastic waves propagating through the material of interest. Details about UPS have been discussed in subchapter 3.2.1. In the present study, the measurements were accomplished using an electronic network analyser (Advantest, model R3754A) and two identical broadband ultrasonic transducers from Panametrics (Panametrics, model V122 with nominal central frequency 7.5 MHz and diameter 9.5 mm for longitudinal elastic constants and model V155 with nominal central frequency 5 MHz and diameter 12.7 mm for shear elastic constants). These transducers were attached on opposite sides of the rectangular parallelepiped samples with the help of a water soluble couplant. For longitudinal elastic constants, the phase and amplitude spectra were recorded in the frequency range from 10 kHz to 15 MHz; while for shear elastic constants the same range was from 10 kHz to 10 MHz. Wave velocity measurements were carried out along the three orthogonal specimen axes for all rectangular specimens described above. All measurements were carried out several times and in all cases the velocities determined were repeatable and consistent. Six different measurements were carried out for the three shear elastic constants (a combination of two different measurements for each shear elastic constant as explained in appendix (A.1); e.g. for $C_{66}$ two separate measurements were carried out-one for waves propagating along 1 direction

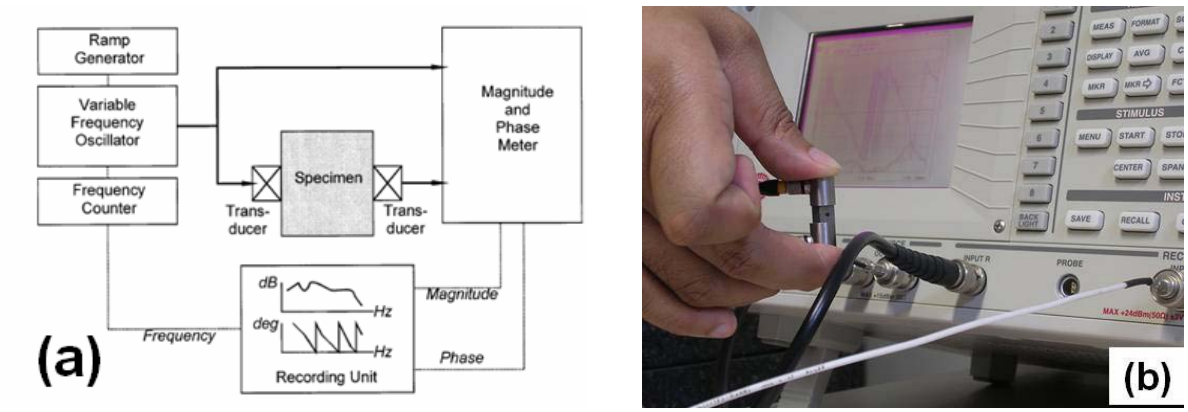


**Figure 4.2: Setup used for UPS: (a) schematic arrangement [180] and (b) actual experimental arrangement**

and polarised along 2 direction and the second for waves propagating along 2 direction and polarised along 1 direction. Average of the velocity obtained from these two measurements was used for the calculation for $C_{66}$. Similarly, directions 1 and 3 were involved for the elastic

constant $C_{55}$ and the directions 2 and 3 were involved for the elastic constant $C_{44}$). Figure 4.2a shows a schematic block diagram of the UPS setup, while Figure 4.2b shows the actual experimental setup with one poly-domain composite sample placed between two transducers. Network analyser used can be seen in the background.

## 4.4 Resonant Ultrasound Spectroscopy (RUS)

For RUS, a sample was placed along its body diagonal between two identical transducers attached to a very rigid stage. The complete stage along with the transducers was manufactured by Quasar (Quasar International Inc., New Mexico, USA). The same network analyzer used for UPS was used to generate the input signal and to record the output signal. A wideband, high speed amplifier [model BA4825 from NF Corporation, Yokohama, Japan with a maximum gain capacity ×50 and maximum output voltage ±250V] was used to amplify the signal

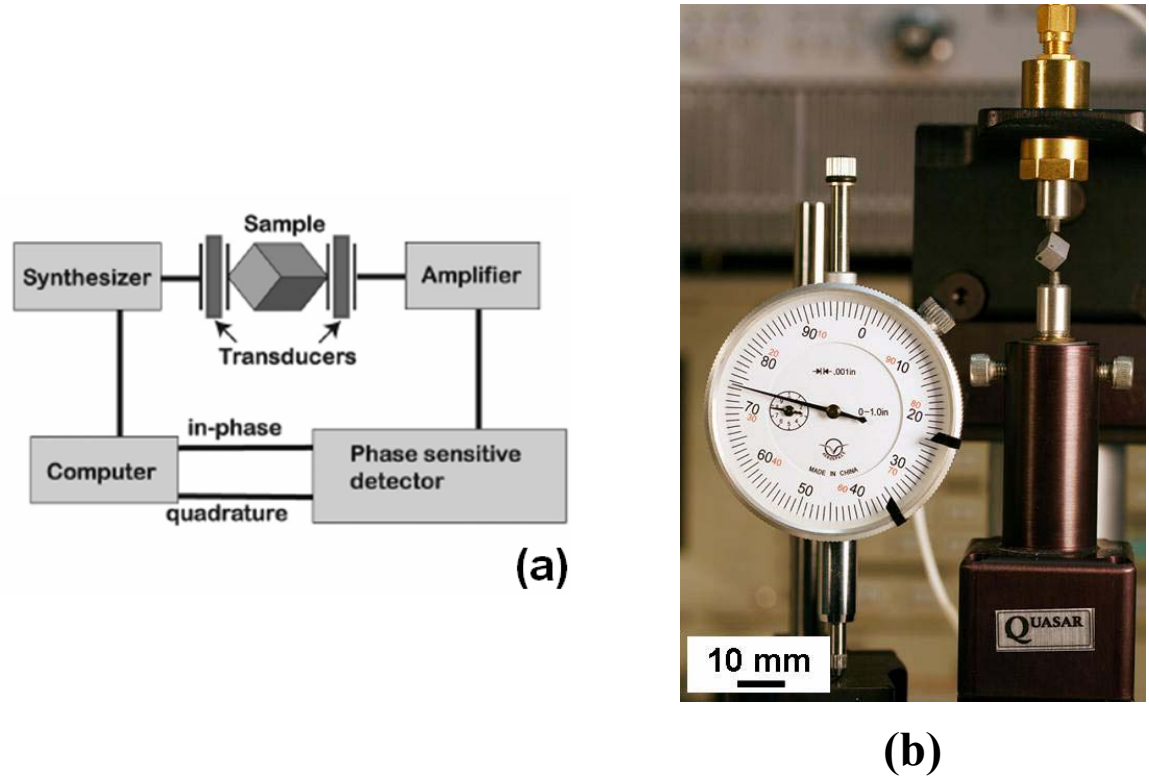


**Figure 4.3: Setup used for RUS: (a) schematic block diagram [221] and (b) actual experimental arrangement**

to the input transducer. Phase and amplitude were measured for each swept frequency. Resonant frequencies were determined from the amplitude spectra. At least four measurements were carried out with different body diagonals of the sample being in touch with the transduc-

ers. This ensured that none of the resonant frequencies was missed. Resonant frequencies for each measurement were determined and the averages of these values were put as input to back calculate the elastic constants based on the input values of the elastic constants and sample mass and dimensions. Figure 4.3a shows a schematic block diagram of the RUS setup, while Figure 4.3b shows the actual experimental setup with the sample positioned along its body diagonal between the transducers of the Quasar stage.

## 4.5 In situ compression test in Scanning Electron Microscope (SEM)

Elastic-plastic flow behavior and damage mechanism of the single-domain samples were determined under compressive load. The compression tests were carried out using a miniature mechanical testing machine manufactured by Kammrath & Weiss GmbH, Dortmund, Germany. The photograph in Figure 4.4 shows a single-domain sample placed between the hardened steel punches in the miniature test setup. 20 μm thick commercially available Al foils were used between the samples and the punches to minimise the sample friction. The total strain was measured with the help of an in-built LVDT (Linear Variable Differential Transformer). All experiments were carried out at a fixed crosshead velocity 2 $\mu m.s^{-1}$ (corresponding to a nominal strain rate of $10^{-3}$ $s^{-1}$). In-situ analyses were carried out in a SEM of type Zeiss EVO 50. This was done by carrying out the compression test while the miniature setup

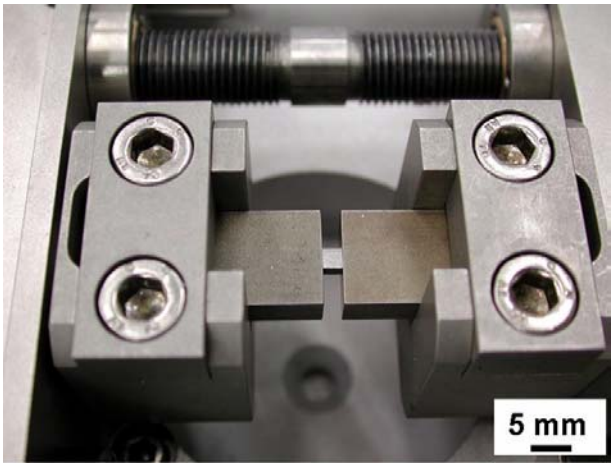


**Figure 4.4: Single-domain sample placed between two flat punches in the miniature mechanical test device**

along with the sample was placed inside the vacuum chamber of the microscope. Damage evolution was directly observed by stopping the test at different loads to take SEM micrographs.

## 4.6 Study of processing-induced thermal residual stresses and internal load transfer under external loading using energy-dispersive synchrotron X-ray diffraction

The diffraction experiments were carried out at beamline EDDI at the Berlin synchrotron storage ring BESSY, Berlin, Germany. A schematic of the beamline components is shown in Figure 4.5 while photograph of the actual beamline setup is shown in Figure 4.6. Detail specifications of the beamline can be found in ref. [222].

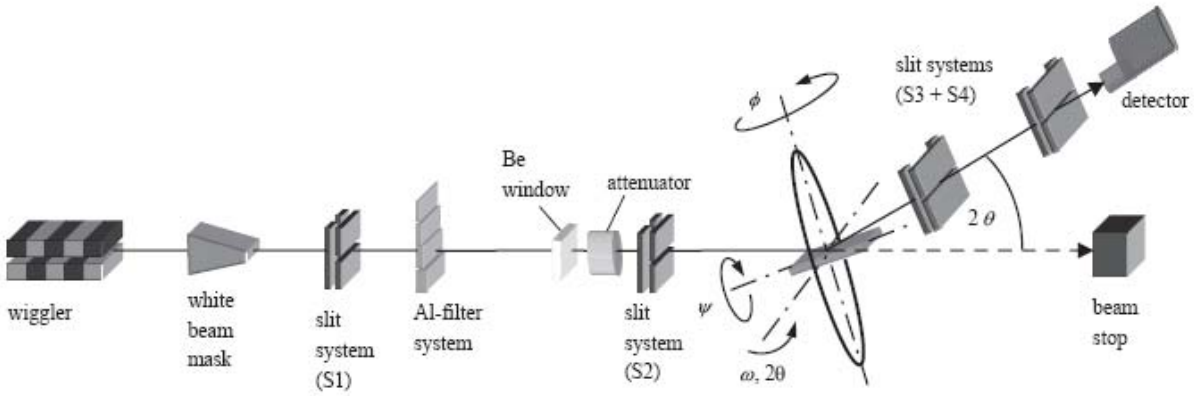


**Figure 4.5: Schematic layout of the main beamline components at materials science beamline EDDI at BESSY, Berlin [222]**

Lattice strain fluctuations along and across the lamellae are determined by stepwise translation of the gauge volume within the sample. For the present study, an energy range between 20–90 keV was selected for analysis and a scattering angle $2\theta = 7$ ° was chosen as it gave good energy separation as well as sufficient peak intensities. For translation scans the slit size S2 was maintained at 200 µm×200 µm while slit system S3 and S4 had dimensions 30 µm×5 mm. Slit system S2 was increased to 1 mm×1 mm for $\sin^2\psi$ measurements. A low-energy germanium detector coupled with a multi channel analyser (MCA) was used to record the diffraction spectra. Diffraction peaks were fitted by a "Pseudo-Voigt" function to determine the positions of the energy peaks. For in-situ analysis of internal load transfer under external compressive loading, the same mechanical test setup along with the Al foils described in

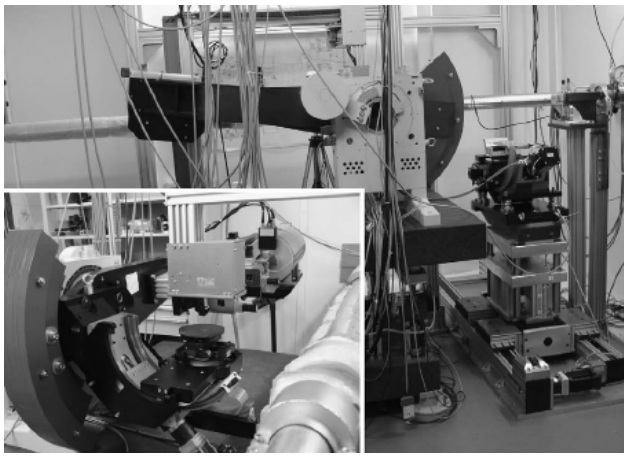

**Figure 4.6: The EDDI experimental hutch showing the y-z stage with the y-y diffractometer and the 4-axis sample positioner directly behind the beamline back end. Inset shows the 5-axes sample positioning unit with the laser and CCD camera system beyond, behind the detector arm with the secondary slit systems**

subchapter 4.5 were used. The testing rig was mounted on the 5-axes sample positioning table of the diffractometer unit. Slit size for the incoming beam (S2 in Figure 5.43) was maintained at 1 mm×1 mm while each of the two slits in the diffracted beam (S3 and S4) had dimensions of 60 μm×5 mm. The sample was aligned so that the centre of mass of the gauge volume was at the centre of the sample. Crosshead velocity during compression was maintained at 2 μm/s, corresponding to a nominal strain rate of $10^{-3}$ $s^{-1}$. Figure 4.7 shows the photograph of the mechanical testing rig mounted on the 5 axis sample positioning table at the EDDI-instrument at BESSY.

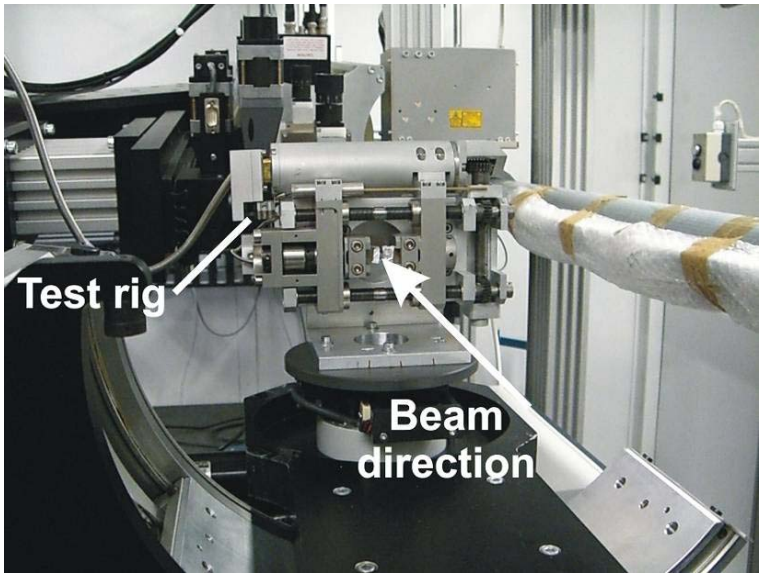


**Figure 4.7: Photograph of the miniature test rig mounted on the 5-axis sample positioning table at EDDI beamline at BESSY, Berlin, Germany.**

# 5 Results

## 5.1 Structural analysis

### 5.1.1 Optical microscopy

If not specifically mentioned, all the subsequent analyses were carried out on metal/ceramic composites fabricated using squeeze-casting for melt infiltration. In Figure 5.1a and b typical metallographic sections of the face perpendicular to the freezing direction for Composite Type A and Composite Type B are shown. In these light-optical micrographs, the ceramic

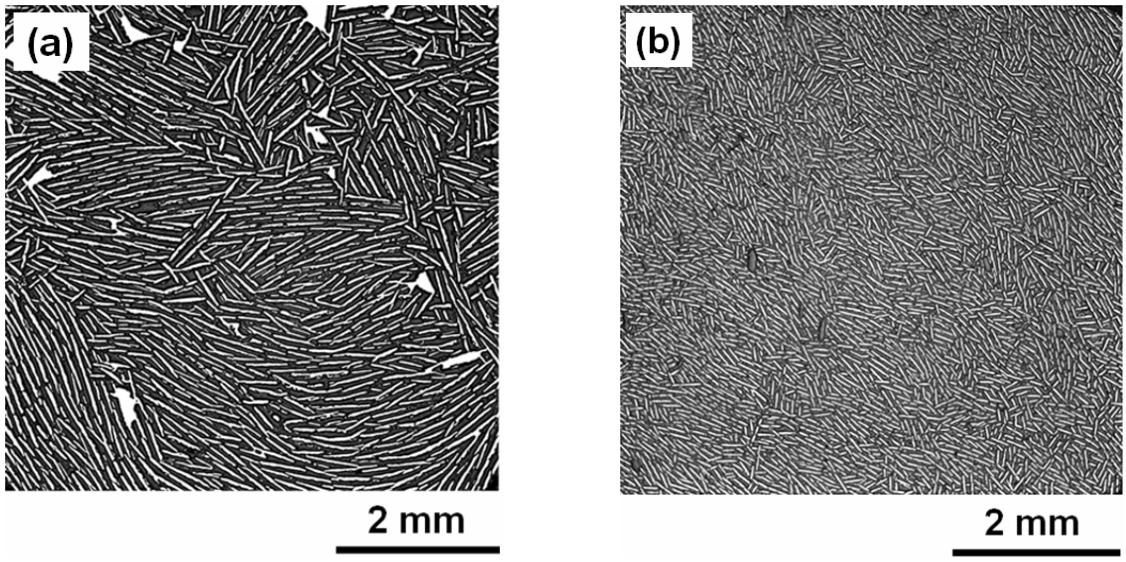


**Figure 5.1: Microstructure of the metal/ceramic composite for the faces perpendicular to the freezing direction of the ceramic preform: (a)** Composite **Type A and (b) Composite Type B**

component appears dark and the metallic alloy appears bright. For Composite Type A (Figure 5.1a) a quite coarse structure exhibiting lamellar domains with sizes up to several millimetres is observed. The material appears fully dense but exhibits some matrix-rich regions which are due to the unwanted removal of individual ceramic lamellae during the grinding of the pre-form prior to metal infiltration. Such matrix-rich regions are therefore only observed near the surface of the composite and have no significant effect on the bulk properties. In comparison, the Composite Type B (Figure 5.1b) has a much finer structure. The domains are considerably smaller and the lamellae are much thinner.

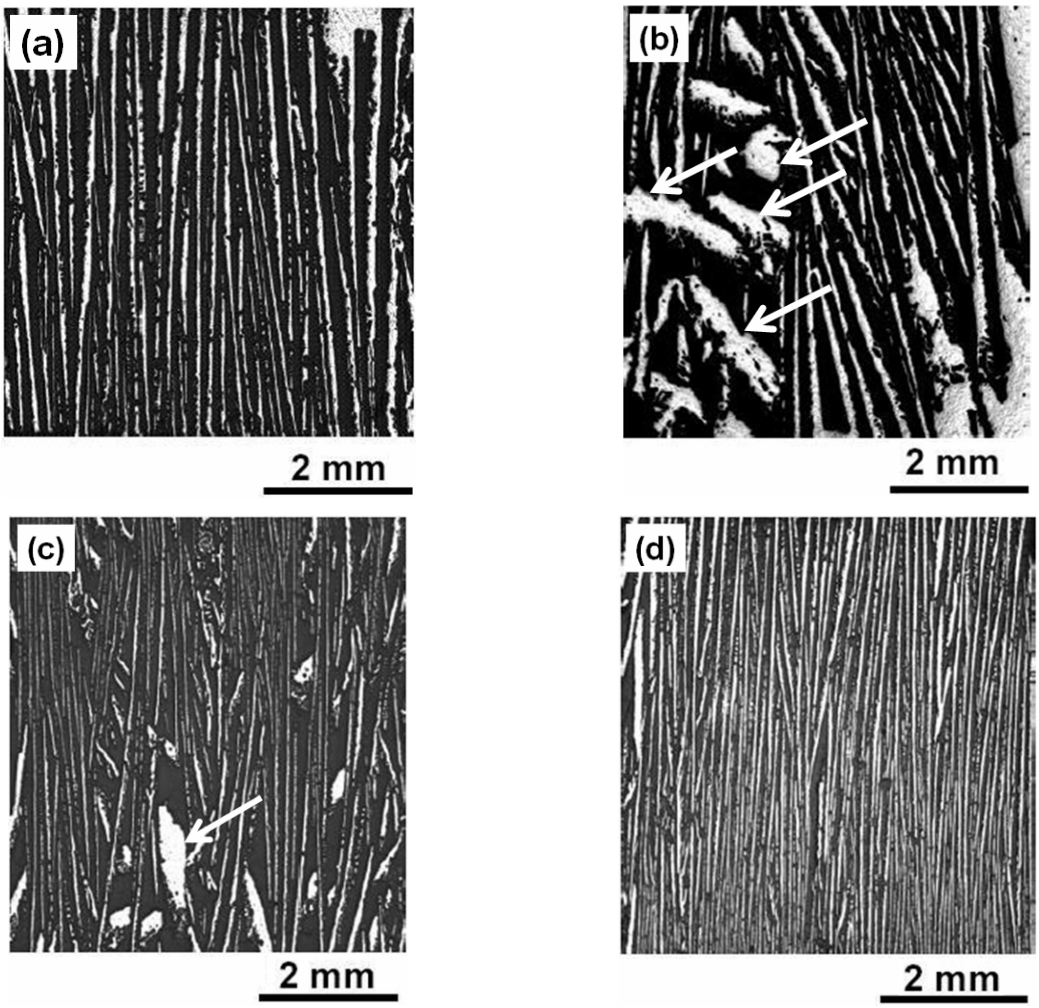


**Figure 5.2: Microstructures of the composites for the two faces parallel to the freezing direction of the preform (a-b): Composite Type A and (c-d): Composite Type B. White arrows denote the irregularities**

In Figure 5.2a–d, sections parallel to the freeze-casting direction are shown for both composite types. It can be seen that the lamellae are predominantly oriented parallel to the freeze-casting direction and they stretch over the whole thickness of the composite plate. In these 'side views', the lamellae appear much thicker and more widely spaced compared to the perpendicular sections because the lamellae are sectioned in a random fashion. The partly irregular patterns, marked with arrows in Figure 5.2b and c, indicate that the lamellae are neither perfectly planar nor perfectly aligned parallel to the macroscopic direction of heat removal. Schematic representation of the specimen co-ordinate system for a poly-domain sample is shown in Figure 5.3. In this figure, direction 1 corresponds to the freezing direction of the

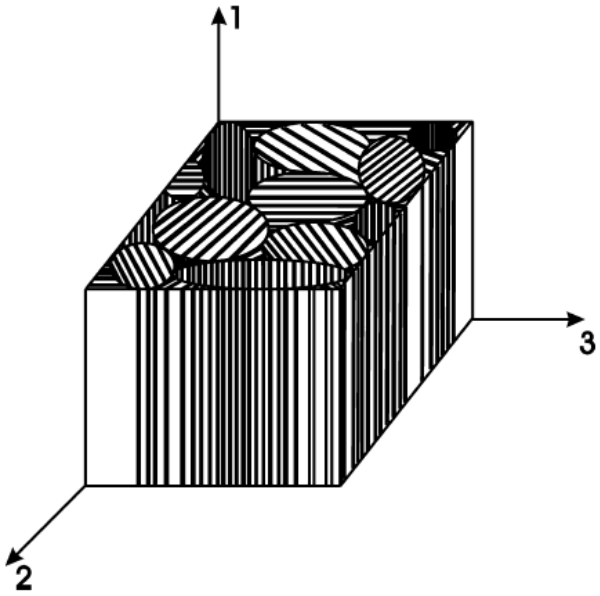


**Figure 5.3: Schematic of the specimen co-ordinate system employed for a poly-domain composite sample**

ceramic preform. This scheme of nomenclature will be followed throughout the work. Figure 5.4 shows a high resolution optical micrograph of the face perpendicular to the freezing direction for Composite Type A. The micrograph was obtained by metallographic polishing and

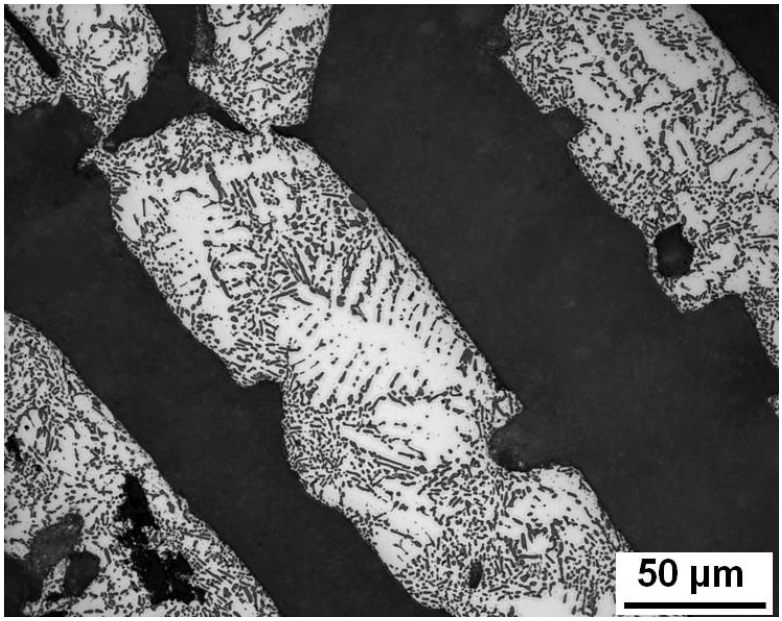


**Figure 5.4: High resolution optical microstructure of the face perpendicular to the freezing direction for Composite Type A.**

subsequent etching with 0.5 % HF solution. In this micrograph the ceramic component is dark while the light regions correspond to the metallic alloy lamellae. Microstructure of the metal-

lic alloy consists of primary dendrites of aluminum solid solution, within which pure silicon particles are distributed. The actual binary phase diagram of Al-Si is given in Ref. [223]. The eutectic point is 577 °C at about 12.6 wt% Si. A typical feature of Al-Si alloys is that the solubility of Al in Si is negligible at all temperatures. Hence, the eutectic structure is composed of aluminum rich alpha solid solution and essentially pure silicon. Silicon has a diamond cubic structure and Figure 5.4 shows that they are distributed mainly in the form of needles or platelets. Hence, this microstructure has poor ductility in comparison to pure aluminum. It may be noted that primary aluminum dendrites can be seen in Al-12Si, although the composition is very close to the eutectic point and an entirely eutectic microstructure might thus have been expected. This is because the sample did not solidify under equilibrium conditions.

Rectangular parallelepiped samples were produced from the composite plates via cutting and grinding for further analysis. The edges of these parallelepipeds were always parallel to the edges of the original composite plates. For composite Type A, samples having two size scales were prepared. Larger samples having more than one domain had nominal dimensions in the range of 6–10 mm. Single-domain samples were further prepared from these poly-domain samples to investigate the mechanical properties at domain level. Samples of composite Type B had a very fine domain structure and so fabrication of single-domain sample from them was not feasible and so only poly-domain samples were prepared for this composite type. The density of each sample was determined from mass and dimensions. The dimensions were measured with a digital calliper and masses of the samples were measured with a high precision laboratory balance (Mettler AE240, Ontario, Canada). The ceramic content in each sample was determined assuming no porosity in the composite and using the rule of mixture:

$$\rho_c = \rho_f \cdot V_f + \rho_m \cdot V_m \tag{5.1}$$

The density of Al-12Si was measured in this work and it was found to be 2.63 $Mg.m^{-3}$. Average density and ceramic content in each composite type (for poly-domain samples) studied is mentioned in Table 5.1.

Fabrication of single-domain samples was done by cutting small samples having dimensions in the range of 1.8–2.5 mm from the poly-domain samples using a diamond coated steel wire having a diameter of 220 μm. These small samples had arbitrary domain orientation in 2-3 plane (refer to Figure 5.3) and their faces were always parallel to the faces of the original poly-domain samples. After subsequent metallographic polishing and observation in optical microscopy, only those samples which had a single-domain or two domains with specific ori-

entations were selected for further analysis. Microstructure of the face perpendicular to the freezing direction for a typical single-domain sample is shown in Figure 5.5. As is apparent

**Table 5.1: Summary of average sample densities and calculated ceramic content in each poly-domain Composite Type studied**

| Composite Type | No. of samples | Average density ($Mg.m^{-3}$) | Average ceramic content (%) |
|---|---|---|---|
| Type A | 27 | 3.121±0.025 | 39±2 |
| Type B | 30 | 3.178±0.036 | 43±3 |
| Type A – Cu coated | 40 | 3.111±0.019 | 38±1 |
| Type A – $Cu_2O$ coated | 9 | 3.111±0.018 | 38±1 |
| Type A – Ni coated | 27 | 3.093±0.026 | 36±2 |
| Type B – Cu coated | 21 | 3.12±0.04 | 39±3 |
| Type B – $Cu_2O$ coated | 28 | 3.14±0.01 | 41±1 |
| Type A – die cast | 19 | 3.107±0.013 | 38±1 |

from this figure, the lamellae are fairly parallel over the whole sample and their orientation can be described by the angle $\beta$ (angle between the lamellae and the specimen axis 2).

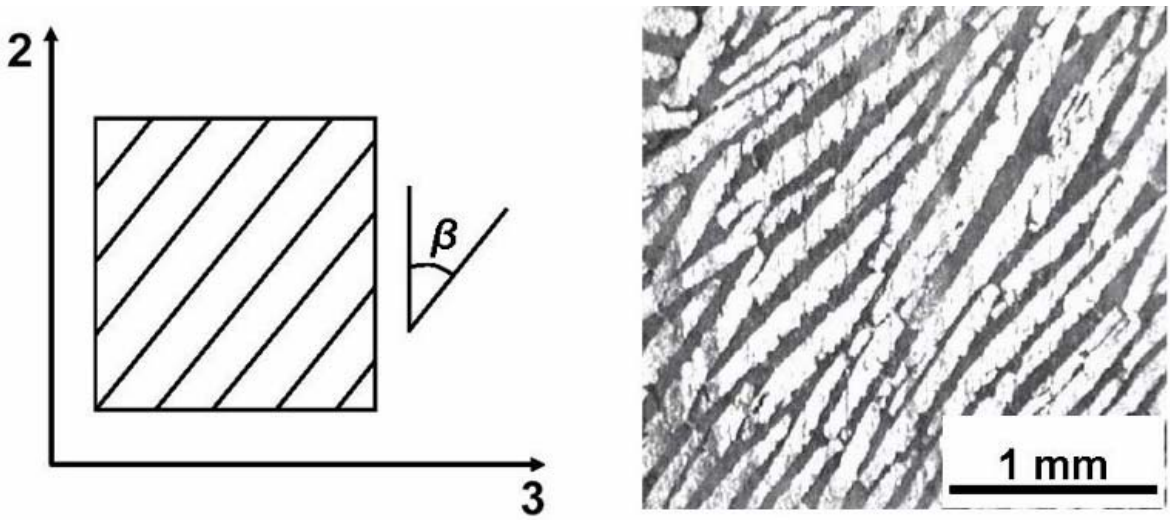


**Figure 5.5: Definition of the angle β, marking the orientation of the single-domain composite sample with respect to the axis 2 of the specimen co-ordinate system**

### 5.1.2 SEM analysis

Figure 5.6 shows one SEM image of the metal/ceramic composite. Prior to analysis, the sample was etched with 5 % HF solution and it was subsequently sputtered with a thin electrically conducting layer of platinum to minimize the charging effect of the ceramic lamellae. Various

features of the microstructure are marked in the image. Only a very small amount of micro-pores are seen within the ceramic lamellae. Hence, for the calculation of volume fractions of

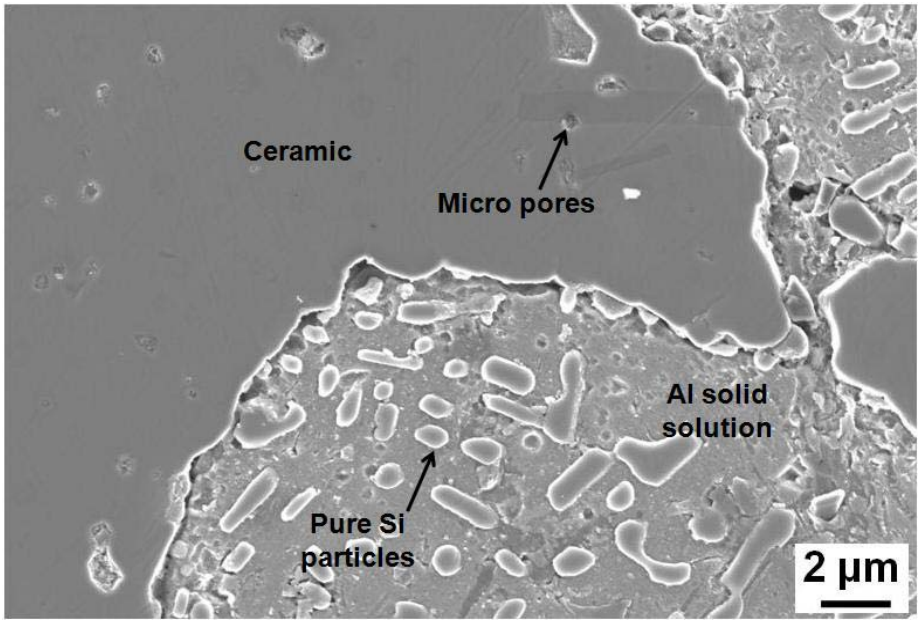


**Figure 5.6: Typical SEM image of the composite**

ceramic in individual samples the samples have been assumed to be pore free. Further estimation of total porosity by mass-dimension analysis and its validation by 3D µCT are discussed in subchapter 5.1.3. The aspect ratios of individual silicon particles are better resolvable in this SEM micrograph.

### 5.1.3 µCT analysis

Figure 5.7 shows the µCT images of the face perpendicular to the freezing direction in the uninfiltrated ceramic preform. The imaged preform had 22 vol% ceramic and it was

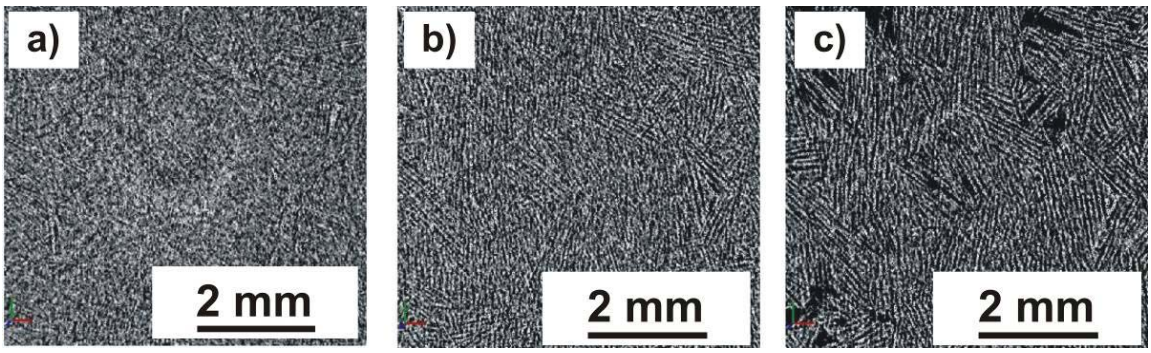


**Figure 5.7: Micro computed tomographic images of the uninfiltrated ceramic preform. Alumina ceramic is bright and porosity is darker**

freeze-cast at -50 °C. In these grey scale images the ceramic is brighter while the pores are dark. The images were taken from three different depths of the preform. Figure 5.7a corresponds to the bottom portion of the preform which was in touch with the cold plate during freeze-casting. Figure 5.7b was taken from the middle region while Figure 5.7c was taken from the upper region of the preform block. The images clearly show that the structure becomes more open and loosely packed as the distance from the cold plate increases. The lamellar domain structure is only visible from the mid portion and it is clearly observed in the image taken from the top region. As has already been discussed in subchapter 2.3, the very dense structure at the bottom of the preform is due to the very fast cooling rate of the ice crystals, which results into a planar ice front. As the distance from the cold plate increases, the cooling rate decreases and the growth morphology changes from planar to columnar and finally to lamellar at the upper most region of the preform.

Figure 5.8 shows the µCT image of the metal ceramic composite. The image shows the face parallel to the freezing direction and the region marked in the figure shows an uninfiltrated channel. The image contrast between alumina and aluminum is inherently poor because of the similar effective atomic numbers and densities of alumina and aluminum, which further results into similar attenuation coefficients. It has already been discussed in subchapter 3.1 that in absorption contrast tomography, features within a microstructure are only identifiable as

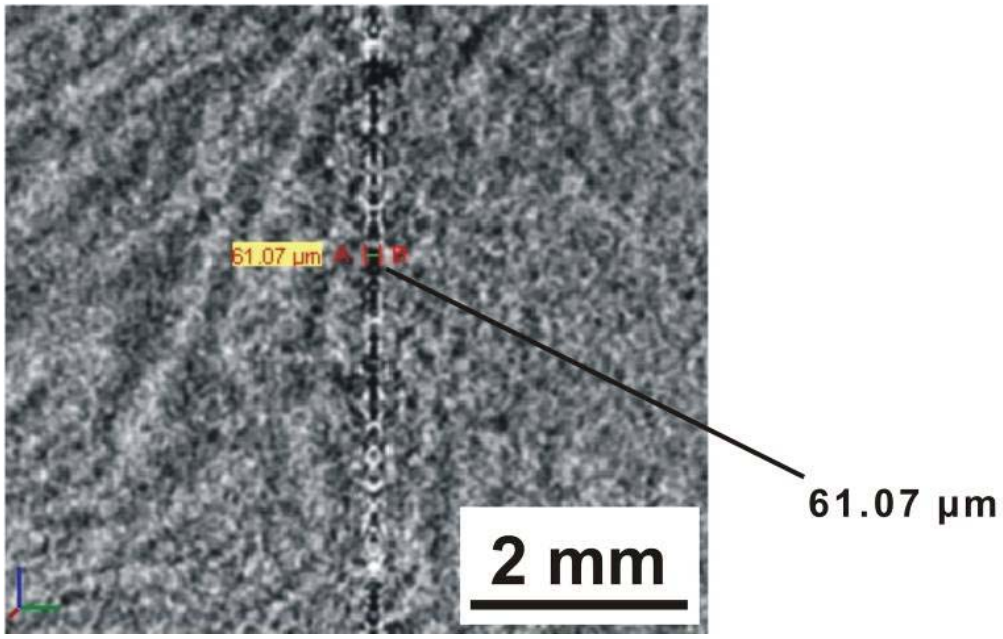


**Figure 5.8: Micro CT image of the infiltrated composite showing an uninfiltrated channel**

separate entities if their absorption coefficients differ significantly. Thickness of the uninfiltrated channel is approximately 61 µm and it runs throughout the sample length. These uninfiltrated pores are important because they may significantly affect the mechanical properties of the composite, when in use. To estimate the amount of porosity in the two composite types, a modified form of Equation (5.1) was used. This expression had the form:

$$\rho_c = \rho_f \cdot V_f + \rho_p \cdot V_p^{'} + \rho_m \cdot V_m \tag{5.2}$$

In Equation (5.2) $V_p^{'}$ and $\rho_p$ corresponds to volume fraction and density of the pores, respectively. Pores, having no mass, only contribute as space filling entity and hence the expression for the ceramic volume content in a composite with pores is written as:

$$V_f = \frac{\rho_m \cdot V_p^{'} + \left(\rho_c - \rho_m\right)}{\rho_f - \rho_m} \tag{5.3}$$

Following Equation (5.3), Figure 5.9 plots the ceramic volume fraction in the two composite types as a function of total porosity in the composite. Mass-density analysis of one bulk uninfiltrated preform of Composite Type A had shown that it had about 44 vol% of alumina ceramic in it. Hence, this has been marked in the plot as the horizontal line. The intersections of this line with the respective lines for the two composite types denote the total amount of porosity in the two composite types. It is seen from the Figure 5.9 that the total porosity in Composite Type B is significantly less than 1 vol% while in Composite Type A the total amount of porosity lies close to 3 vol%.

In a further effort to estimate the total amount of porosity in the studied metal/ceramic composite, one slice of the µCT image obtained from Composite Type A was binarised for different amounts of porosities and the corresponding binary images were visually compared with the original grey scale image of the composite. Figure 5.10 shows the corresponding analysis. In the original image the darker regions correspond to pores while the lighter regions correspond to the metallic alloy and the ceramic, respectively. Binarisation of the image was carried out using the image analysis software VGStudio Max, by assigning different threshold grey values to the pores and calculating the corresponding porosity content. In these binary images the pores are black while the material is white. Visual comparison with the original

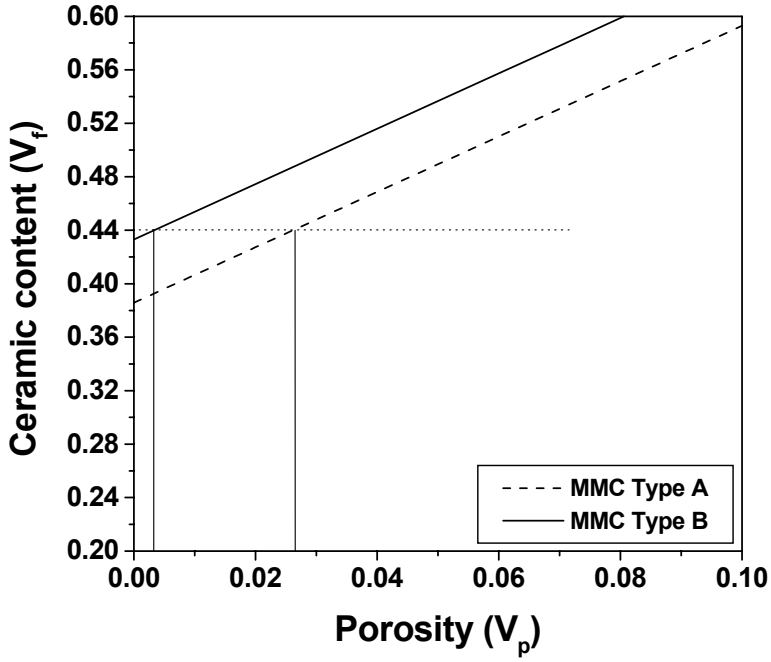


**Figure 5.9: Calculation of total porosity in the two composite types from mass density analysis**

image shows that best match is obtained for range of porosities between 2-4 vol%. Although, resolution of the original and the binary images are quite poor, still porosity estimation from the µCT analysis yields results similar to that obtained from mass density analysis.

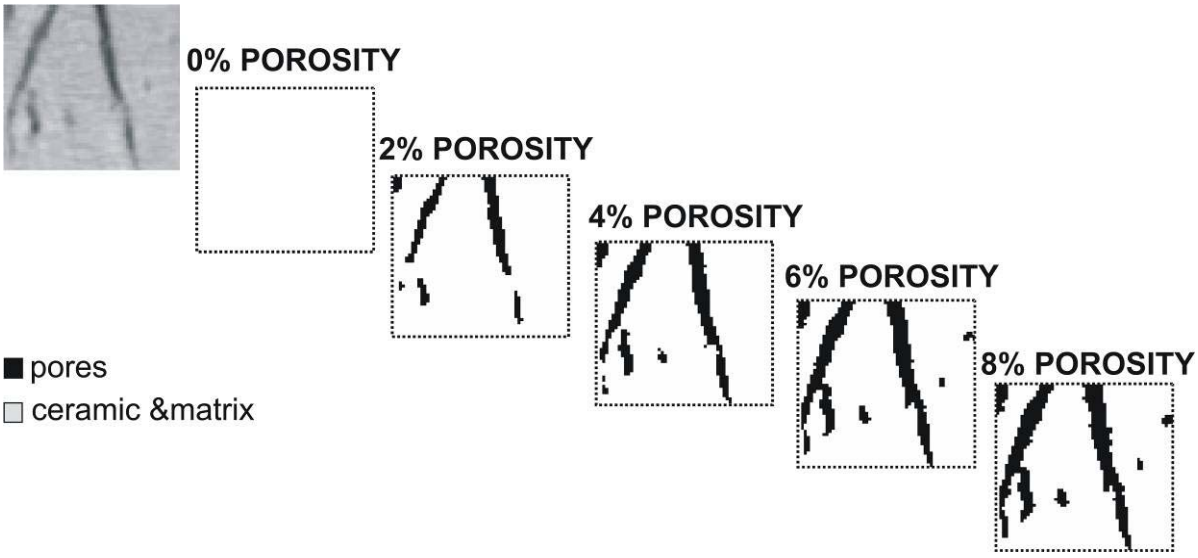


**Figure 5.10: Estimation of total porosity in the composite from µCT analysis**

## 5.2 Analysis of the elastic behavior using UPS

### 5.2.1 Behavior of poly-domain samples

Typical phase and amplitude spectra obtained from the UPS of a poly-domain composite sample using longitudinal transducers are shown in Figure 5.11. The slope of the phase spectrum was found to be fairly constant over a considerable frequency range for all the measurements, indicating that the velocity was in fact independent of frequency (absence of dispersion) and suggesting that elastic constants computed based on the ultrasonic velocities can be assumed to be valid also under static loading conditions. Following the discussion in

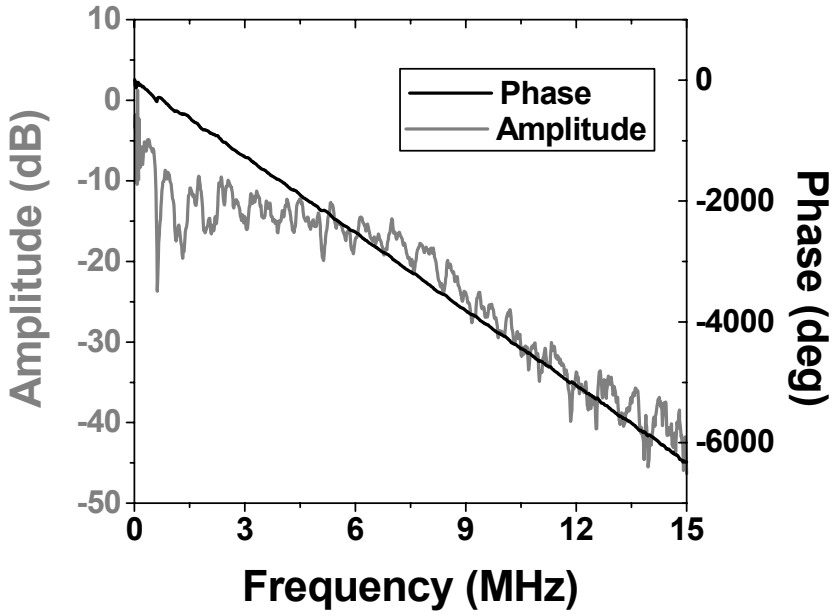


**Figure 5.11: Typical phase and amplitude spectra obtained from the UPS test of a poly-domain sample using longitudinal transducers**

subchapter 4.3, wave velocity can be determined from the global slope *m'* of the phase-frequency spectra according to:

$$V = -2\pi \cdot \frac{L_s}{m'} \tag{5.4}$$

with $L_s$ being the length of the sample. Throughout this work, the co-ordinate system described in Figure 5.3 will be used for poly-domain composite samples. Longitudinal wave velocities along 1, 2 and 3 directions will be denoted as $V_1$, $V_2$ and $V_3$ respectively, while the elastic constants along the same directions will be denoted as $C_{11}$, $C_{22}$ and $C_{33}$ respectively. In Table 5.2 velocities $V_1$, $V_2$ and $V_3$ averaged over all the specimens within a composite type are listed. Experimentally measured wave velocities and elastic constants for each individual

sample are tabulated in appendix A.2. Table 5.2 shows that the averages of $V_2$ and $V_3$ within a particular composite type are not significantly different taking the standard deviations into consideration. Hence, transverse isotropy with respect to 1 direction has been assumed on a macroscopic length scale. Longitudinal elastic constants were calculated for each individual sample from the measured sound velocities and densities according to Equation (3.9). Figure 5.12 shows the variation of $V_1$ against density in individual poly-domain samples, while Figure 5.13 shows the variation of $C_{11}$ against sample density. Variation of $V_2$ and $V_3$ with

**Table 5.2: Average longitudinal wave velocities (±standard deviations) and elastic constants (±standard deviations) determined there from for each poly-domain composite type**

| Composite Type | Average of velocities $V_1$ ($m.s^{-1}$) | Average of velocities $V_2$ ($m.s^{-1}$) | Average of velocities $V_3$ ($m.s^{-1}$) | Average elastic constant $C_{11}$ (GPa) | Average elastic constants ($C_{22} = C_{33}$) (GPa) |
|---|---|---|---|---|---|
| Type A | 8354 ± 242 | 7608 ± 302 | 7372 ± 378 | 218 ± 14 | 176 ± 17 |
| Type B | 8685 ± 179 | 7681 ± 249 | 7841 ± 250 | 240 ± 10 | 192 ± 13 |
| Type A – Cu coated | 8110 ± 108 | 7297 ± 445 | 7492 ± 421 | 205 ± 6 | 170 ± 20 |
| Type A – $Cu_2O$ coated | 8240 ± 139 | 7433 ± 693 | 7505 ± 388 | 211 ± 7 | 174 ± 25 |
| Type A – Ni coated | 8017 ± 103 | 7211 ± 489 | 7179 ± 571 | 199 ± 6 | 161 ± 24 |
| Type B – Cu coated | 8022 ± 67 | 6401 ± 339 | 6634 ± 523 | 201 ± 4 | 133 ± 19 |
| Type B – $Cu_2O$ coated | 8369 ± 65 | 7546 ± 216 | 7568 ± 243 | 220 ± 4 | 180 ± 11 |
| Tape A – die cast | 7742 ± 231 | 7643 ± 401 | 7879 ± 190 | 186 ± 11 | 187 ± 15 |

sample density for poly-domain composite samples is shown in Figure 5.14 while Figure 5.15 shows the corresponding variation of $C_{22}$ and $C_{33}$ with sample density.

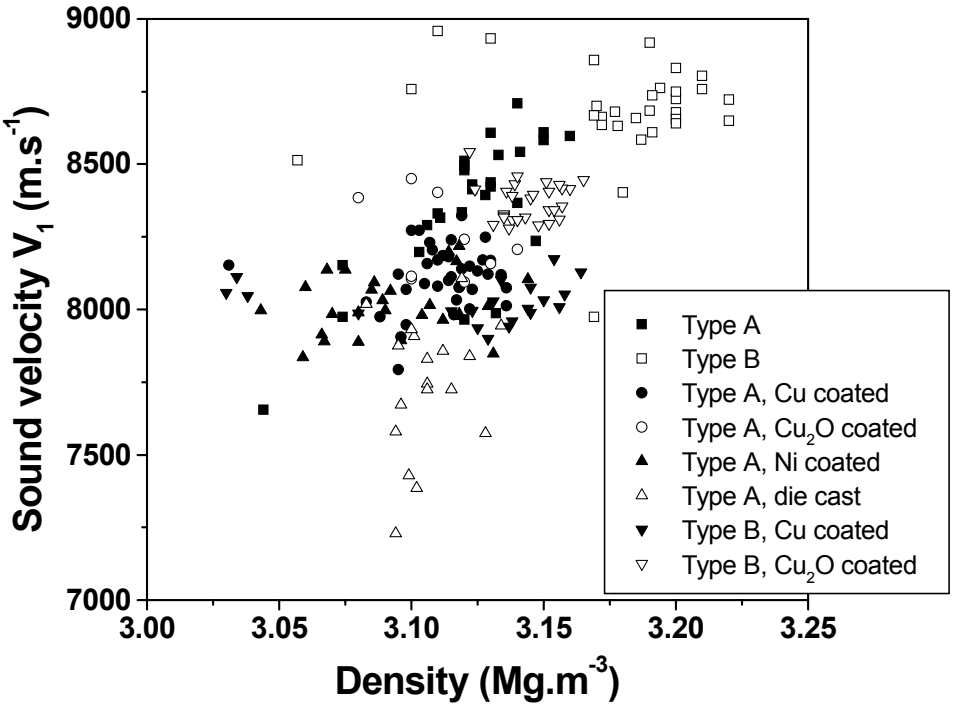


**Figure 5.12: Plot showing the variation of $V_1$ with density for poly-domain composite samples**

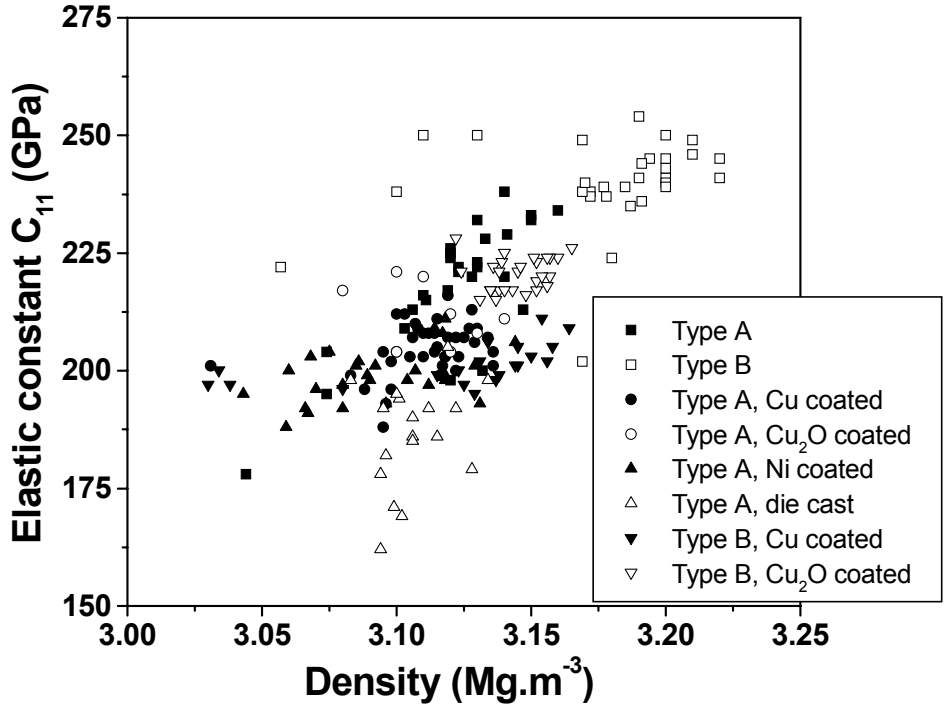


**Figure 5.13: Plot showing the variation of $C_{11}$ with density for poly-domain composite samples**

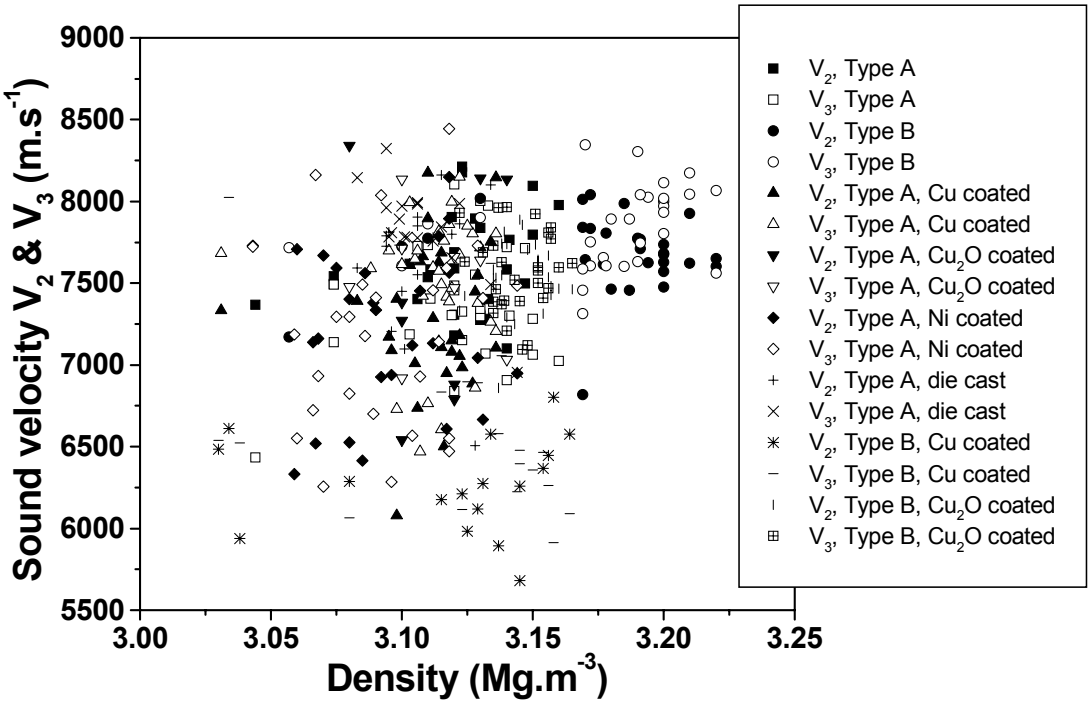


**Figure 5.14: Plot showing the variation of $V_2$ and $V_3$ with density for poly-domain composite samples**

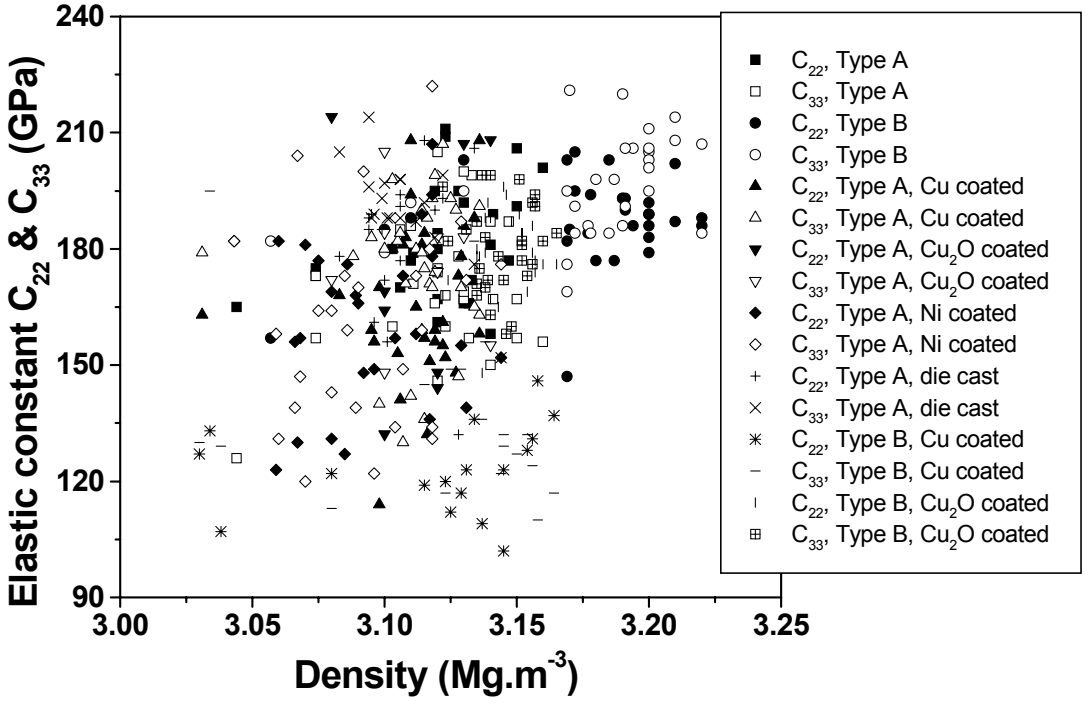


**Figure 5.15: Plot showing the variation of $C_{22}$ and $C_{33}$ with density for poly-domain composite samples**

In Figure 5.16 these elastic constants are compared to the boundaries as predicted based on

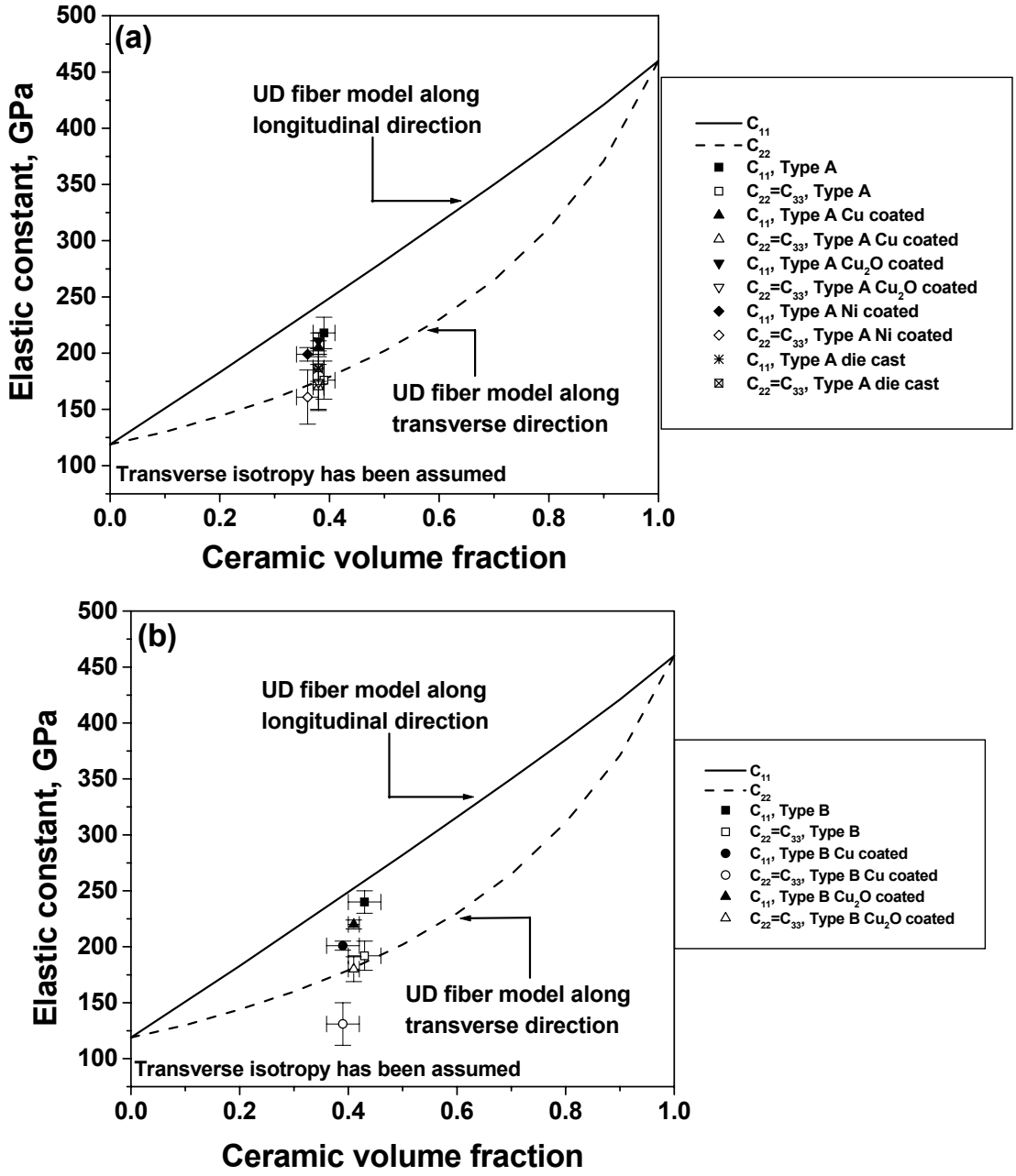


**Figure 5.16: Correlation of the average results obtained from UPS test for individual composite types with the theoretical models for UD fiber reinforced composites: (a) Composite Type A, (b) Composite Type B**

the transverse isotropic models for unidirectional fiber-reinforced composites compiled by Berthelot (Eq. 9.30 in [12]). These bounds are calculated using the following equations:

$$C_{11} = E_L + 4\nu_{LT}^2 K_L^{'}$$
$$C_{22} = C_{33} = G_{TT'} + K_L^{'} \qquad (5.5)$$

where

$$E_L = E_f V_f + E_m\left(1-V_f\right)$$
$$\nu_{LT} = \nu_f V_f + \nu_m\left(1-V_f\right)$$
$$K_L^{'} = K_m^{'} + \frac{V_f}{\frac{1}{K_f - K_m + \frac{1}{3}\left(G_f - G_m\right)} + \frac{1-V_f}{K_m + \frac{4}{3}G_m}} \tag{5.6}$$
$$G_{TT'} = G_m\left(1 + \frac{V_f}{\frac{G_m}{G_f - G_m} + \frac{K_m + \frac{7}{3}G_m}{2K_m + \frac{8}{3}G_m}\left(1-V_f\right)}\right).$$

In Equations (5.5-5.6) $E_L$ is the longitudinal Young's modulus, $\nu_{LT}$ is the longitudinal Poisson's ratio, $G_{TT'}$ is the transverse shear modulus and $K_L^{'}$ is the lateral compression modulus of the long fiber reinforced composite respectively. These equations assume that the long fibers are oriented along direction 1. A more rigorous model should take into consideration the elastic properties of the single-domains and then compute the effective properties of poly-domain aggregates based on their orientation. Still, for a first estimation, the unidirectional fiber model has been used in this study. The Young's modulus, density and Poisson's ratio of alumina were taken as 390 GPa, 3.9 $Mg.m^{-3}$ [1] and 0.24 [224], respectively. The density, Young's modulus and shear modulus of Al–12Si were measured in this study to be 2.63 $Mg.m^{-3}$, 80 GPa and 30 GPa, respectively. The two lines in Figure 5.16 correspond to the elastic constants $C_{11}$ and $C_{22}$=$C_{33}$ of a unidirectionally fiber-reinforced composite where direction 1 is the fiber long axis and directions 2 and 3 are transverse directions. The data points correspond to the elastic constants and the effective reinforcement volume fraction assuming no porosity, averaged over specimens of the same type. Error bars for moduli and reinforcement volume fraction were calculated based on a standard deviation within a particular composite type.

Figure 5.17 shows the typical phase and amplitude spectra obtained from UPS of a poly domain sample and using shear transducers. The slope of the phase spectrum in the region marked by the arrow headed straight line was used to determine the velocity of shear wave propagation for this measurement. In general, in comparison to the measurement of longitudinal elastic constants, the fluctuations of the phase spectrum were relatively higher when shear elastic constants were measured. However, in almost all cases significant frequency range

could be obtained with a constant slope of the phase spectrum (as shown in Figure 5.17). In Table 5.3 the shear wave velocities averaged over all the samples within each composite type

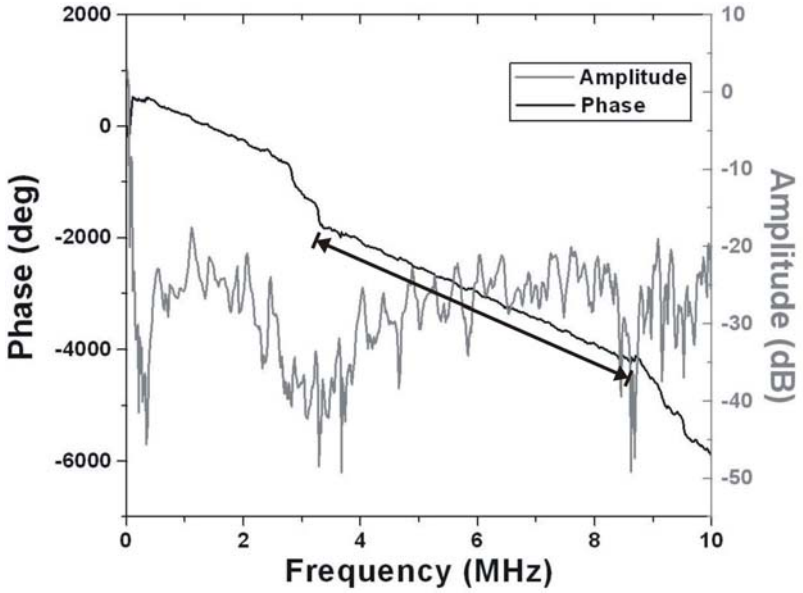


**Figure 5.17: Typical phase and amplitude obtained from a poly domain sample using shear transducers**

**Table 5.3: Average shear wave velocities (±standard deviations) for each composite type**

| Composite Type | Average of velocities $V_{12}$ ($m.s^{-1}$) | Average of velocities $V_{21}$ ($m.s^{-1}$) | Average of velocities $V_{13}$ ($m.s^{-1}$) | Average of velocities $V_{31}$ ($m.s^{-1}$) | Average of velocities $V_{23}$ ($m.s^{-1}$) | Average of velocities $V_{32}$ ($m.s^{-1}$) |
|---|---|---|---|---|---|---|
| Type A | 4424±422 | 4644±247 | 4123±95 | 4356±270 | 4134±105 | 4163±109 |
| Type B | 4263±300 | 4404±158 | 4528±374 | 4618±188 | 4382±125 | 4343±138 |
| Type A – Cu coated | 3966±420 | 4244±272 | 4228±444 | 4401±322 | 3860±226 | 3874±185 |
| Type A – $Cu_2O$ coated | 4506±493 | 4474±478 | 4428±529 | 4400±424 | 4003±171 | 3864±159 |
| Type A – Ni coated | 3977±473 | 4169±405 | 3874±429 | 3995±305 | 3971±545 | 3904±271 |
| Type B – Cu coated | 3619±224 | 4110±390 | 3765±280 | 4200±314 | 3519±275 | 3551±278 |
| Type B – $Cu_2O$ coated | 4052±193 | 4295±163 | 3926±192 | 4357±181 | 4024±151 | 3970±175 |
| Tape A – die- cast | 3926±203 | 4191±271 | 4009±315 | 4210±335 | 3926±294 | 3897±316 |

**Table 5.4: Average shear elastic constant (±standard deviations) for each composite type**

| Composite Type | Average elastic constant $C_{44}$ (GPa) | Average elastic constant $C_{55}$ (GPa) | Average elastic constant $C_{66}$ (GPa) |
|---|---|---|---|
| Type A | 54±2 | 57±4 | 65±9 |
| Type B | 61±4 | 67±7 | 60±5 |
| Type A – Cu coated | 46±4 | 58±10 | 53±8 |
| Type A – $Cu_2O$ coated | 48±4 | 60±13 | 63±13 |
| Type A – Ni coated | 48±8 | 48±7 | 52±9 |
| Type B – Cu coated | 40±6 | 51±7 | 49±8 |
| Type B – $Cu_2O$ coated | 50±3 | 54±5 | 55±4 |
| Tape A – pressure cast | 47±7 | 53±8 | 51±5 |

are shown. As discussed in detail in appendix A.1, each of the three shear elastic constants can be determined by measuring two different shear wave velocities. For $C_{44}$ these two wave velocities are $V_{23}$ and $V_{32}$, for $C_{55}$ the velocities are $V_{13}$ and $V_{31}$ and for $C_{66}$ the velocities are $V_{12}$ and $V_{21}$, respectively. Following the usual nomenclature, shear wave velocity $V_{ij}$ corresponds to a wave polarized along $j$ direction and propagating along $i$ direction. Each shear elastic constant for every sample was determined following Equation (3.9), taking the average of the two different shear wave velocities corresponding to that particular shear elastic constant as the shear wave velocity. Table 5.4 lists the average shear elastic constants for all the samples within a particular composite type.

The experimental observations from Figure 5.12-Figure 5.15 can be summarized as follows:

- The velocity $V_1$ is generally higher than $V_2$ and $V_3$ (correspondingly $C_{11}$ is higher than $C_{22}$ and $C_{33}$) suggesting that the composite is stiffest along the freezing direction of the ceramic preform.
- Except for very few results, $V_1$ (correspondingly $C_{11}$) appears to be strongly correlated to the density.
- For both Composite Type A and Type B (with coated and uncoated preforms), the transverse velocities $V_2$ and $V_3$ (corresponding elastic constants $C_{22}$ and $C_{33}$) exhibit significant scatter which is not correlated to the density.

### 5.2.2 Behavior of single-domain samples

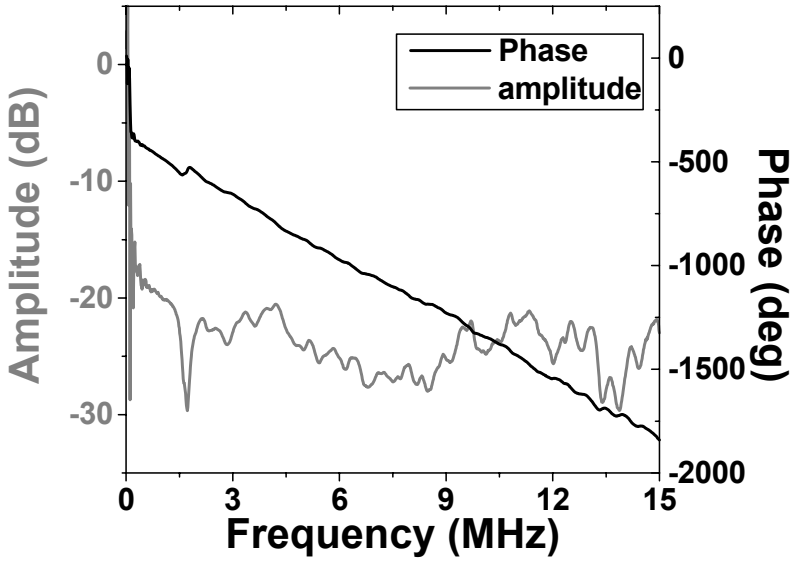


**Figure 5.18: Typical phase and amplitude spectra obtained for a single-domain sample using longitudinal transducers**

As already mentioned, because of the very fine structure of Composite Type B, only poly-domain samples of Composite type A were selected for studying the effect of domain orientation on mechanical properties. Figure 5.18 shows the typical phase and amplitude spectra obtained for single-domain samples using longitudinal transducers. As in Figure 5.11 for poly-domain samples, the global slope of the phase-frequency plot remains fairly constant over the complete frequency range between 2-15 MHz, suggesting that the sample is non-dispersive. However, in comparison to the measurement on the poly-domain sample, in the small single-domain sample the local fluctuations in slope are significantly stronger. This may be attributed to the experimental difficulty in placing the small sample between the two transducers in a stable manner. Moreover, the phase spectrum for the single-domain sample is significantly shallower than that of the poly-domain sample. As will be shown afterwards, the wave velocities in both poly and single-domains are comparable and hence, following Equation (5.4), this lower slope directly results from the smaller dimensions of the single-domain samples.

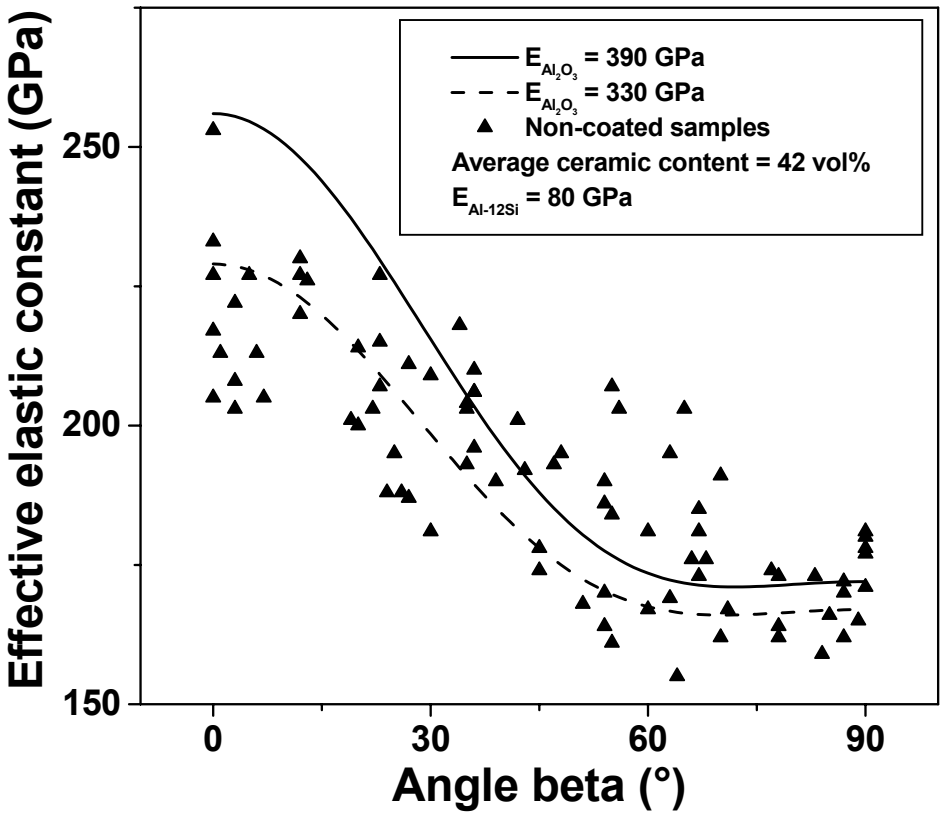


**Figure 5.19: Effect of domain orientation on the effective elastic constant for single-domain samples of Composite Type A**

Figure 5.19 shows the effect of domain orientation $\beta$ on the effective longitudinal elastic constants along 2 and 3 directions (refer to Figure 5.5) in single-domain samples. This effective elastic constant is the quantity $\rho V^2$ (where beta=$\beta$ for $V=V_2$ and beta=(90-$\beta$) for ($V=V_3$) in Figure 5.5). Data points correspond to elastic constants measured experimentally. Only results for composite samples with uncoated preforms are shown. Assuming no porosity, the average ceramic content in these single-domain samples was found to be 42 vol%. Scatter among data points is very pronounced because of the small probed volume and inherent microstructural heterogeneity from sample to sample. In Figure 5.19 the ordinate values obtained from two extremes of the plot (corresponding to beta=0 ° and beta=90 °) are the elastic constants $C'_{22}$ and $C'_{33}$) of the lamellar domains in the domain coordinate system, where direction 2 is parallel to the lamellar plane ($\beta=0$ °) and direction 3 is perpendicular to it ($\beta=90$ °). The figure shows that $C'_{22}$ is in the range of 205–230 GPa while $C'_{33}$ lies in the range of 160–180 GPa.

The model developed by Postma [69] to estimate the transverse isotropic stiffness matrix for a rank 1 composite laminate consisting of alternating layers of random thickness has been briefly discussed in subchapter 2.4.1.4. For a transverse isotropic layered structure the theoretical

predictions for the longitudinal elastic constants ($C'_{11}$=$C'_{22}$) (where direction 1 is the freezing direction) and $C'_{33}$ were calculated with the help of the Postma model and using the elastic constants and the effective volume fractions of alumina and Al–12Si, respectively. This calculation was based on the assumption that direction 1 was always the freezing direction of the preform and the angle $\beta$ was either 0 ° or 90 °. To calculate the elastic constant for any intermediate angle (where $0 \leq \beta \leq 90$), the laminate has to be rotated about the 1-axis by the same angle. The expression for the corresponding transformed modulus is summarized by Berthelot (Table 11.1 in [12]) and for the material co-ordinate system under study this can be written as:

$$C'_{22,\beta} = C'_{22}\cos^4\beta + C'_{33}\sin^4\beta + 2\left(C'_{23} + 2C'_{44}\right)\times\sin^2\beta\cos^2\beta \qquad (5.7)$$

where $C'_{22,\beta}$ is the transformed elastic constant and $C'_{22}$, $C'_{33}$, $C'_{23}$ and $C'_{44}$ are calculated from the theoretical model of Postma. Figure 5.19 shows the theoretical predictions for two different values of the Young's modulus of alumina, keeping all other parameters fixed.
Figure 5.20 shows the longitudinal elastic constant along the freezing direction $C_{11}$ in individual single-domain composite samples plotted against the ceramic content in each sample.

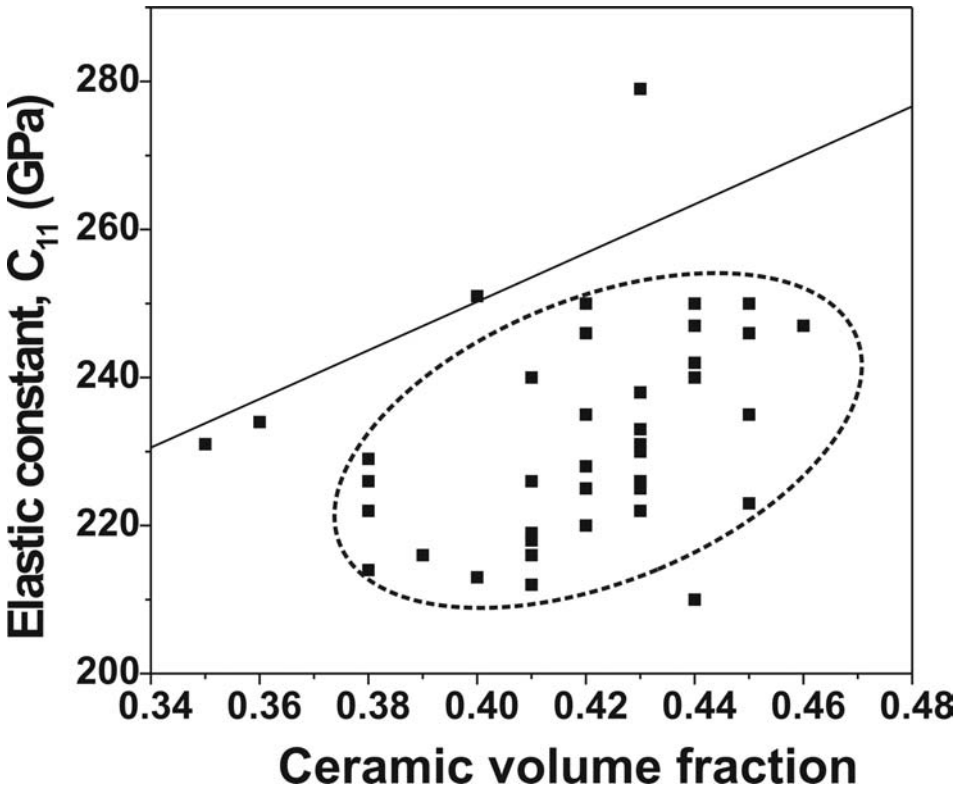


**Figure 5.20: Plot showing the distribution of the longitudinal elastic constant along freezing direction in single-domain samples against ceramic content in each sample calculated assuming no porosity and using the bulk densities of alumina and Al-12Si**

Large scatter in the measured $C_{11}$ for samples having similar ceramic content may be attributed to structural heterogeneity and experimental difficulty because of small measurement volume. The straight line corresponds to the theoretical variation of $C_{11}$ with ceramic content calculated according to Postma model discussed in subchapter 2.4.1.4.

## 5.3 Analysis of the elastic behavior using RUS

One sample of Composite Type B with non-coated preform was selected for RUS to determine the complete stiffness matrix. The sample was assumed to have orthotropic symmetry (9 independent stiffness constants). For RUS, the sample must have parallel faces with very well defined geometry. Hence, all faces of the rectangular parallelepiped sample were polished with SiC emery paper until plane parallelism down to a few microns was attained. The sample had dimensions of 5.221±0.008 mm, 5.439±0.003 mm and 5.897±0.012 mm respectively and its mass was 0.54033 g. UPS was first carried out on this sample to determine the six diagonal elements of the stiffness matrix (3 longitudinal and 3 shear elastic constants). With UPS it was not possible to determine the three off-diagonal stiffness constants and hence initial guesses were made for them based on the theory of uni-directional fiber reinforced composites and using the literature values for the stiffnesses of alumina and Al-12Si and calculating the ceramic content from the measured density and assuming no porosity. These stiffness constants as well as the sample dimensions and mass were put as input (in the rusin.dat file) in the code developed by Migliori and Sarrao [193]. A first run of the code predicted that the first 90 resonant frequencies should be present within the frequency range of 0.3 MHz–1.4 MHz. The above mentioned frequency range was swept in small steps with a step width of 10 Hz and sweep time of 50 ms. Figure 5.21 shows the amplitude spectra obtained from RUS of a poly-domain sample of Composite Type B. Resonant frequencies were determined from the peaks of the amplitude spectra. According to Migliori and Sarrao [193] the number of fitted resonant frequencies should be 5–10 times the number of elastic constants to be determined. As orthotropic symmetry was assumed for the sample, it had 9 independent elastic constants and hence 50–90 resonant frequencies were fitted. Table 5.5 shows the result obtained by fitting the experimentally measured resonant frequencies to the code written by Migliori and Sarrao [193] based on the input values of the elastic constants and sample mass and dimensions. Fit obtained for first 40 resonant frequencies is shown here. The column headers in

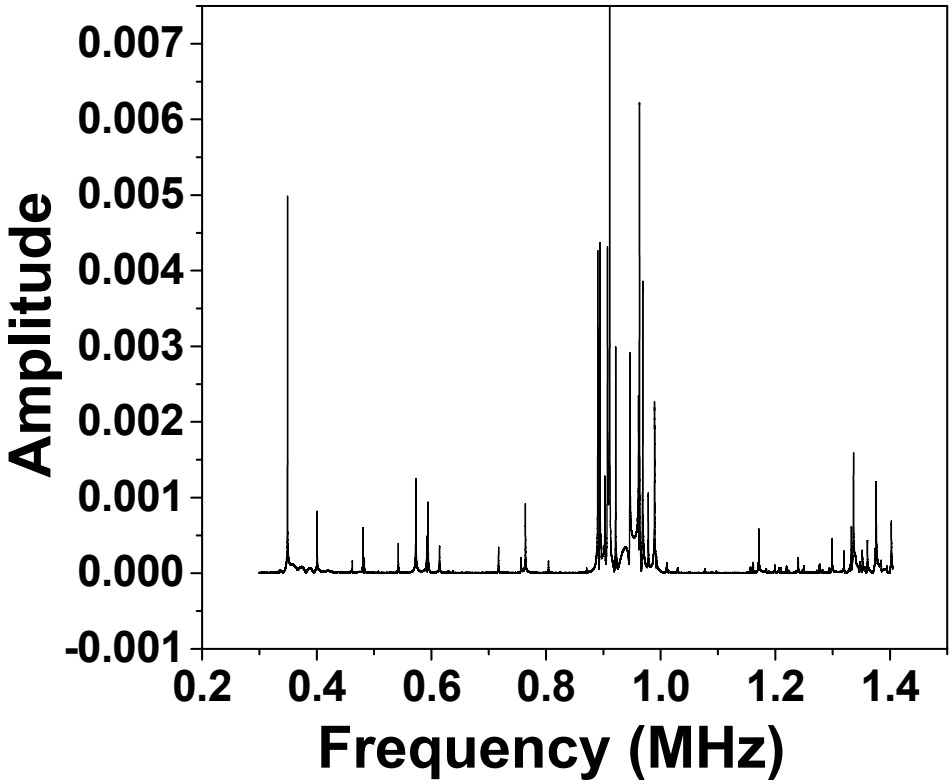


**Figure 5.21: Amplitude spectra obtained from RUS of a poly-domain sample of Composite Type B**

Table 5.5 have the following meanings: *n* corresponds to the number of the mode, *fex* and *fr* are the measured and the fitted frequencies respectively (in MHz) and *%err* is the error in fitting that particular mode. Table 5.6 shows the elastic constants obtained from RUS for various numbers of fitted resonant frequencies ranging from 50–90. The first row also lists the input values of the respective elastic constants. Deviations of the fitted elastic constants from the input values are also shown in the same table. It is clearly observed from Table 5.6 that in all cases the elastic constants which were determined by UPS show very good reproducibility also in RUS (deviations lying in the range of 6-7%). On the contrary, the elastic constants whose values were guessed based on the fiber model show large deviation. The RMS error increases from 0.5825% for 50 fitted resonant frequencies to about 1% for 90 fitted resonant frequencies. Although this increase in RMS error suggests a worsening of the quality of the fit, the confidence level for 90 fitted resonant frequencies is much higher because of the use of almost double the number of fitted frequencies. These RMS errors lie in the same range already observed for composites reinforced by particulate reinforcements (isotropic symmetry) [225] and by fiber reinforcements (transverse isotropic symmetry) [226]. The value of the

**Table 5.5: Comparison between experimentally obtained and fitted frequencies for the first 20 resonant peaks obtained from RUS on a poly-domain sample**

| n | fex (MHz) | fr (MHz) | %err | n | fex (MHz) | fr (MHz) | %err |
|---|---|---|---|---|---|---|---|
| 1 | 0.349025 | 0.347033 | -0.57 | 21 | 0.725113 | 0.724274 | -0.12 |
| 2 | 0.400843 | 0.403743 | 0.72 | 22 | 0.73134 | 0.72658 | -0.65 |
| 3 | 0.462155 | 0.463939 | 0.39 | 23 | 0.751175 | 0.752197 | 0.14 |
| 4 | 0.480615 | 0.481898 | 0.27 | 24 | 0.756433 | 0.752693 | -0.49 |
| 5 | 0.483008 | 0.489053 | 1.25 | 25 | 0.763857 | 0.756511 | -0.96 |
| 6 | 0.507935 | 0.515612 | 1.51 | 26 | 0.768457 | 0.768816 | 0.05 |
| 7 | 0.528040 | 0.524268 | -0.71 | 27 | 0.780653 | 0.784899 | 0.54 |
| 8 | 0.540227 | 0.535400 | -0.89 | 28 | 0.804338 | 0.795677 | -1.08 |
| 9 | 0.542548 | 0.540400 | -0.40 | 29 | 0.82403 | 0.830846 | 0.83 |
| 10 | 0.572800 | 0.567331 | -0.95 | 30 | 0.871038 | 0.870795 | -0.03 |
| 11 | 0.591845 | 0.590179 | -0.28 | 31 | 0.890303 | 0.890195 | -0.01 |
| 12 | 0.594373 | 0.593917 | -0.08 | 32 | 0.893818 | 0.893176 | -0.07 |
| 13 | 0.614453 | 0.614438 | 0.00 | 33 | 0.902815 | 0.90696 | 0.46 |
| 14 | 0.629977 | 0.626010 | -0.63 | 34 | 0.907295 | 0.908284 | 0.11 |
| 15 | 0.637033 | 0.637101 | 0.01 | 35 | 0.910995 | 0.9119 | 0.1 |
| 16 | 0.661293 | 0.668026 | 1.02 | 36 | 0.921683 | 0.929716 | 0.87 |
| 17 | 0.690370 | 0.688507 | -0.27 | 37 | 0.946545 | 0.949751 | 0.34 |
| 18 | 0.694400 | 0.690852 | -0.51 | 38 | 0.961253 | 0.955681 | -0.58 |
| 19 | 0.699050 | 0.695410 | -0.52 | 39 | 0.962803 | 0.961457 | -0.14 |
| 20 | 0.717398 | 0.722718 | 0.74 | 40 | 0.968985 | 0.978338 | 0.97 |

RMS error is considerably higher than that suggested by Migliori and Sarrao [193] (they suggest a value in the range of 0.1-0.2% for a very good measurement with a very well prepared sample). This relatively high RMS error may be attributed to the difficulty in preparation of a sample with very precise geometry and to the inability to obtain good initial guesses for the off diagonal elastic constants.

**Table 5.6: Summary of the elastic constants obtained from RUS for various numbers of fitted modes and their comparison with elastic constants measured via UPS**

| | RMS error (%) | $C_{11}$ (GPa) | $C_{22}$ (GPa) | $C_{33}$ (GPa) | $C_{23}$ (GPa) | $C_{13}$ (GPa) | $C_{12}$ (GPa) | $C_{44}$ (GPa) | $C_{55}$ (GPa) | $C_{66}$ (GPa) |
|---|---|---|---|---|---|---|---|---|---|---|
| Input | - | 242 | 188 | 214 | 90 | 85 | 85 | 64 | 76 | 61 |
| RUS50 | 0.58 | 257 | 200 | 203 | 79 | 65 | 90 | 62 | 74 | 65 |
| Dev50 | | 6% | 6% | 5% | 14% | 24% | 6% | 3% | 3% | 7% |
| RUS60 | 0.67 | 256 | 201 | 196 | 73 | 57 | 90 | 62 | 74 | 65 |
| Dev60 | | 6% | 7% | 8% | 19% | 33% | 6% | 3% | 3% | 7% |
| RUS70 | 0.77 | 255 | 201 | 194 | 72 | 54 | 89 | 62 | 74 | 66 |
| Dev70 | | 5% | 7% | 9% | 20% | 36% | 5% | 3% | 3% | 8% |
| RUS80 | 0.92 | 257 | 200 | 200 | 76 | 60 | 89 | 62 | 75 | 66 |
| Dev80 | | 6% | 6% | 7% | 16% | 29% | 5% | 3% | 1% | 8% |
| RUS90 | 1 | 258 | 200 | 198 | 75 | 57 | 91 | 61 | 76 | 65 |
| Dev90 | | 7% | 6% | 7% | 17% | 33% | 7% | 5% | 0% | 7% |

This knowledge of the complete stiffness matrix is essential to simulate the off-axis loading behavior of the material and to estimate the Young's modulus along any direction in space. Berthelot [12] has compiled the expressions for the elastic constants of an orthotropic material for off-axis loading conditions. According to that, the expression for the longitudinal elastic constant for the studied poly-domain sample along the freezing direction, for different tilts between 0-90 ° around the 3 direction is written as:

$$C_{11}^{'} = C_{11}\cos^4\theta_t + C_{22}\sin^4\theta_t + 2\cdot\left(C_{12} + 2\cdot C_{66}\right)\sin^2\theta_t\cdot\cos^2\theta_t \qquad (5.8)$$

In Equation (5.8), $\theta_t$ is the tilt angle while, $C_{11}^{'}$ is the variation of $C_{11}$ for different tilt angle $\theta_t$. Figure 5.22 shows the variation of $C_{11}$ with the tilt angle, calculated using Equation (5.8). Figure 5.23 shows the 3D plot of Young's modulus for the composite under study computed from the RUS fit for 50 resonant peaks. The calculations were carried out in MATLAB, using the expression proposed by Nye [137].

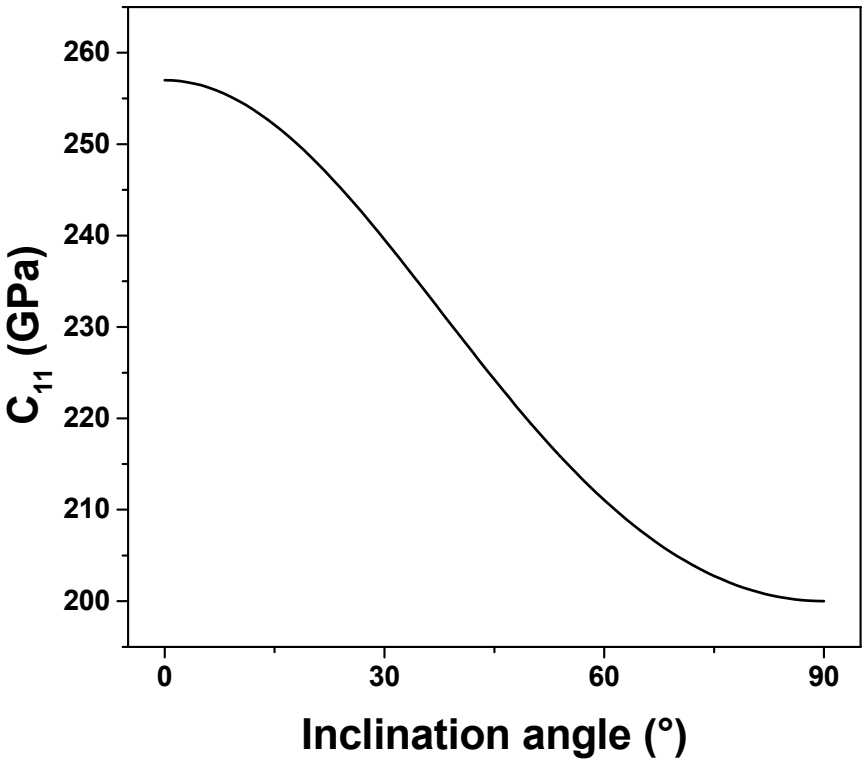


**Figure 5.22: Variation of C11 with tilt angle for different tilts of the poly-domain composite sample around direction 3**

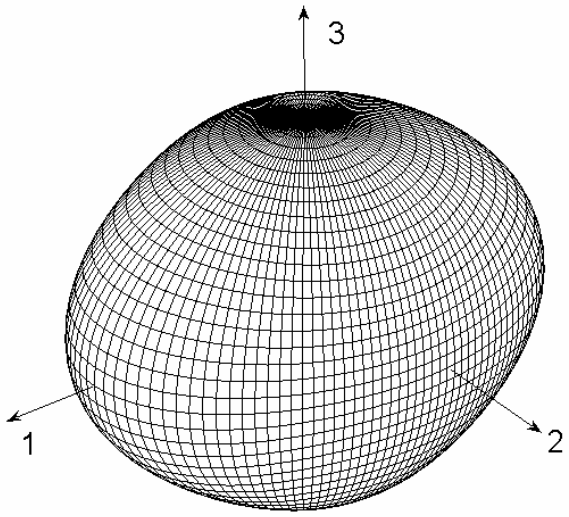


**Figure 5.23: 3D plot of Young's modulus. Direction 1 is the freezing direction**

Figure 5.23 shows that the Young's modulus is highest along the freezing direction (along direction 1) and it is minimum along the 2 direction. The modulus along 1 direction is 211 GPa while that along the 2 direction is 151 GPa. In Figure 5.24 these longitudinal and trans-

verse Young's moduli of the studied composite are compared with the literature data for several MMCs, Al-alloys and alumina ceramic. The literature data is taken from the materials

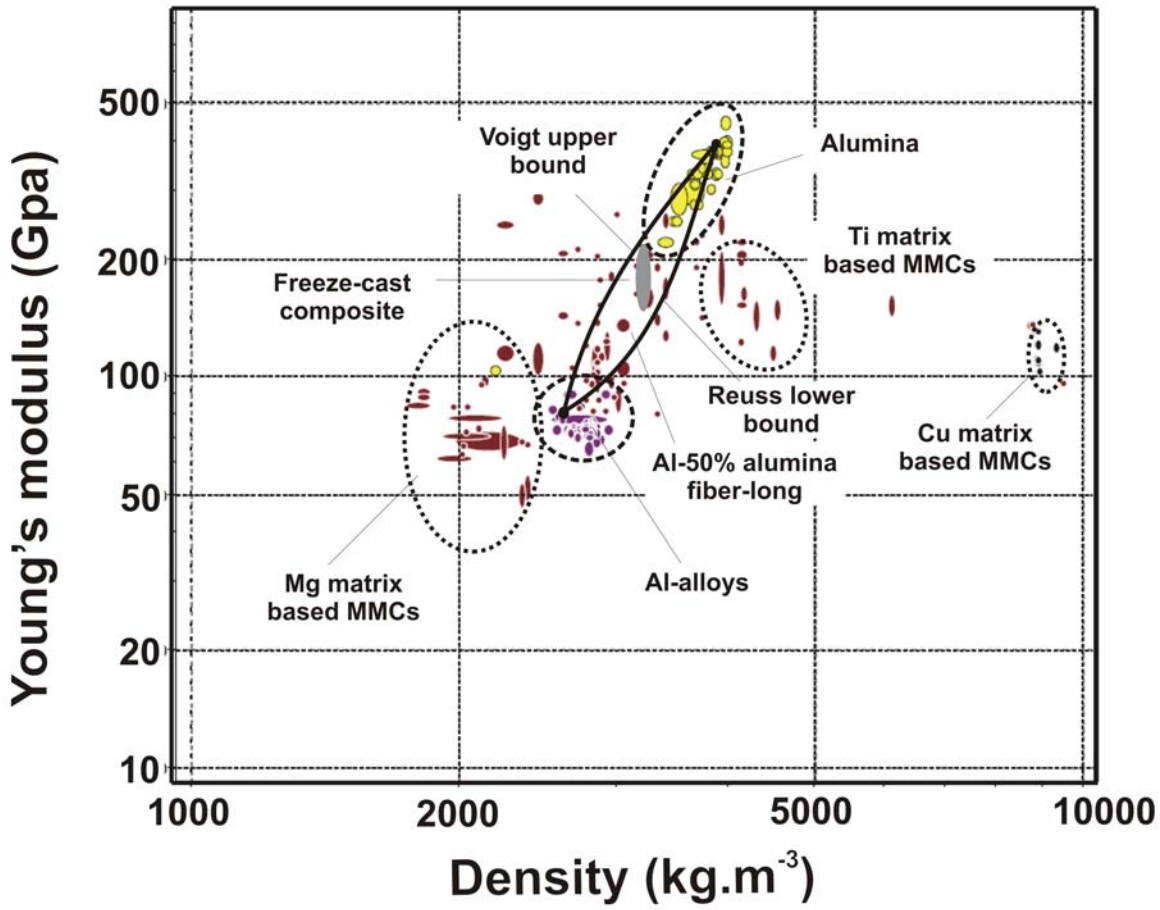


**Figure 5.24: Plot showing the correlation of the Young's modulus of the freeze-cast metal ceramic composite of Type B with alumina, Al-alloys and other MMCs**

database CES EduPack 2008 [227]. Materials of a particular family are enveloped by dotted lines. The freeze-cast metal/ceramic composite is marked by the area shaded in grey. The two solid lines correspond to the predictions according to Voigt and Reuss models discussed in subchapter 2.4.1. These lines are the theoretical upper and lower bounds, respectively. The material parameters for alumina and Al-12Si used to calculate these bounds are the same as the ones used to calculate the bounds shown in Figure 5.16. Figure 5.24 shows that the Young's modulus of the composite studied in this work lies within the envelope bounded by these two theoretical bounds. This satisfies the criterion shown by Ashby [228], that the Young's modulus of any composite composed of any combination of matrix and reinforcement must lie within the envelope formed between these upper and the lower bounds.

## 5.4 Analysis of processing-induced thermal residual stress and strain distribution

In the present study the lattice strain distributions were measured in a single-domain sample using energy-dispersive synchrotron X-ray diffraction. Figure 5.25 shows the microstructure of the face perpendicular to the freezing direction for the actual single-domain sample used in this work. In this figure, direction 1 is the freezing direction and the sample has about 0 °

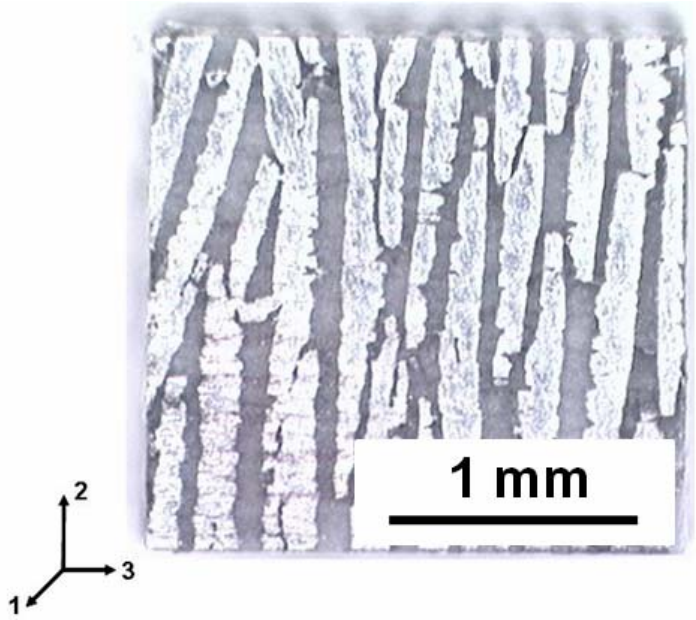


**Figure 5.25: Structure of the single-domain sample used to measure the processing-induced thermal residual stresses using energy-dispersive synchrotron X-ray diffraction. The sample had about 0° domain orientation with 2 direction and direction 1 is the freezing direction**

orientation with 2 direction. Integral as well as spatially resolved measurements were carried out to determine the three principal stress differences in all three phases of the composite (alumina, silicon and Al solid solution) using the well known $\sin^2\psi$–method for X-ray stress analysis (described in detail in subchapter 2.7.1). Figure 5.26 shows a typical energy-dispersive diffraction spectrum, where the individual diffraction peaks for each of the three contributing phases are marked. 8 diffraction peaks of alumina, 4 of aluminum and 3 of silicon were indexed for analysis. Lattice strain fluctuations in the alumina phase for two different orientations were measured. As stated above, the sample had about 0° orientation with the specimen coordinate axis 2, while axis 1 is the freezing direction. As shown schematically

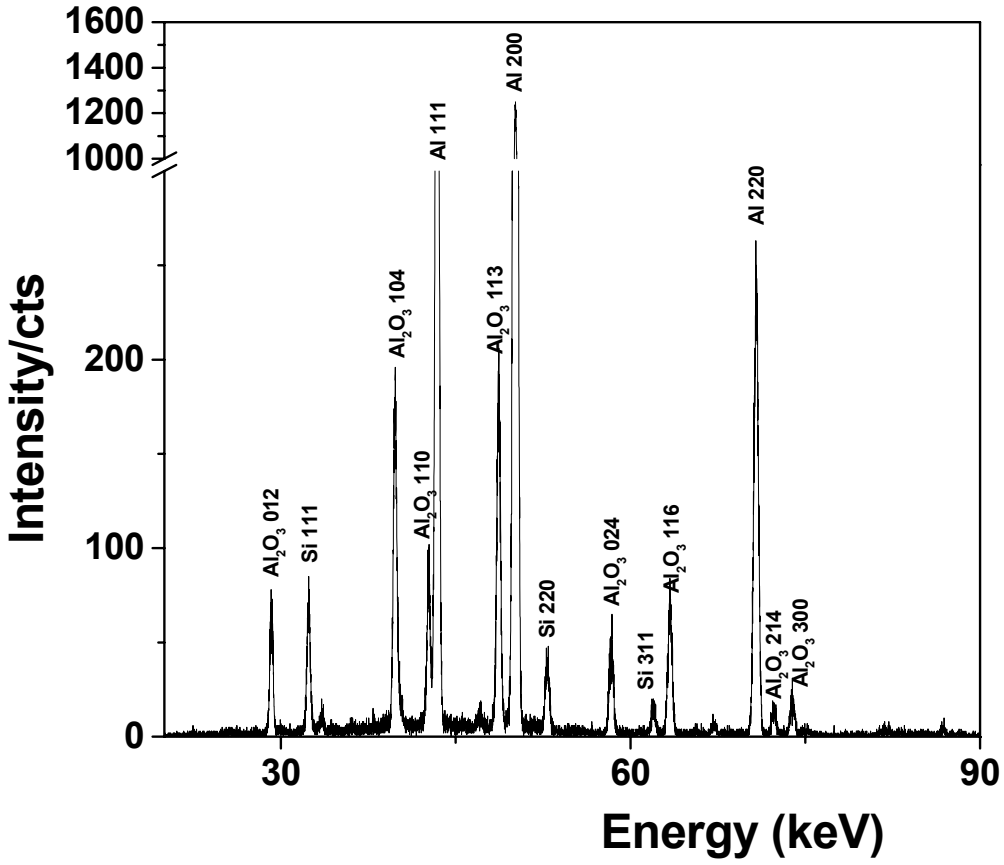


**Figure 5.26: Typical energy-dispersive diffraction spectrum of the composite under study**

in Figure 5.27a and Figure 5.27b, the incident beam in both cases were parallel to axis 2, with the scattering vector being parallel to axis 1 in the first case and it being parallel to axis 3 in the second case. This was carried out by translating the gauge volume through the sample by moving the sample at a step width of 50 μm, while keeping the gauge volume fixed. Strain in the alumina phase was calculated using Equation (3.19), where the energy positions of the stress-free material were determined from diffraction measurements on an uninfiltrated alumina preform. This was done by carrying out $sin^2\psi$ measurements on a sintered alumina block cut from an uninfiltrated preform at 9 different $\psi$ tilts between 0 ° and 63.43 °. Data analysis showed that the residual stresses in the preform range between ±10 MPa and hence the sintered preform was considered to be stress-free. Hence, the average of the energy peak positions over the whole $\psi$-tilt for each alumina diffracting line was taken as the energy positions for the stress-free state. Figure 5.27a and Figure 5.27b show the schematics of the orientation

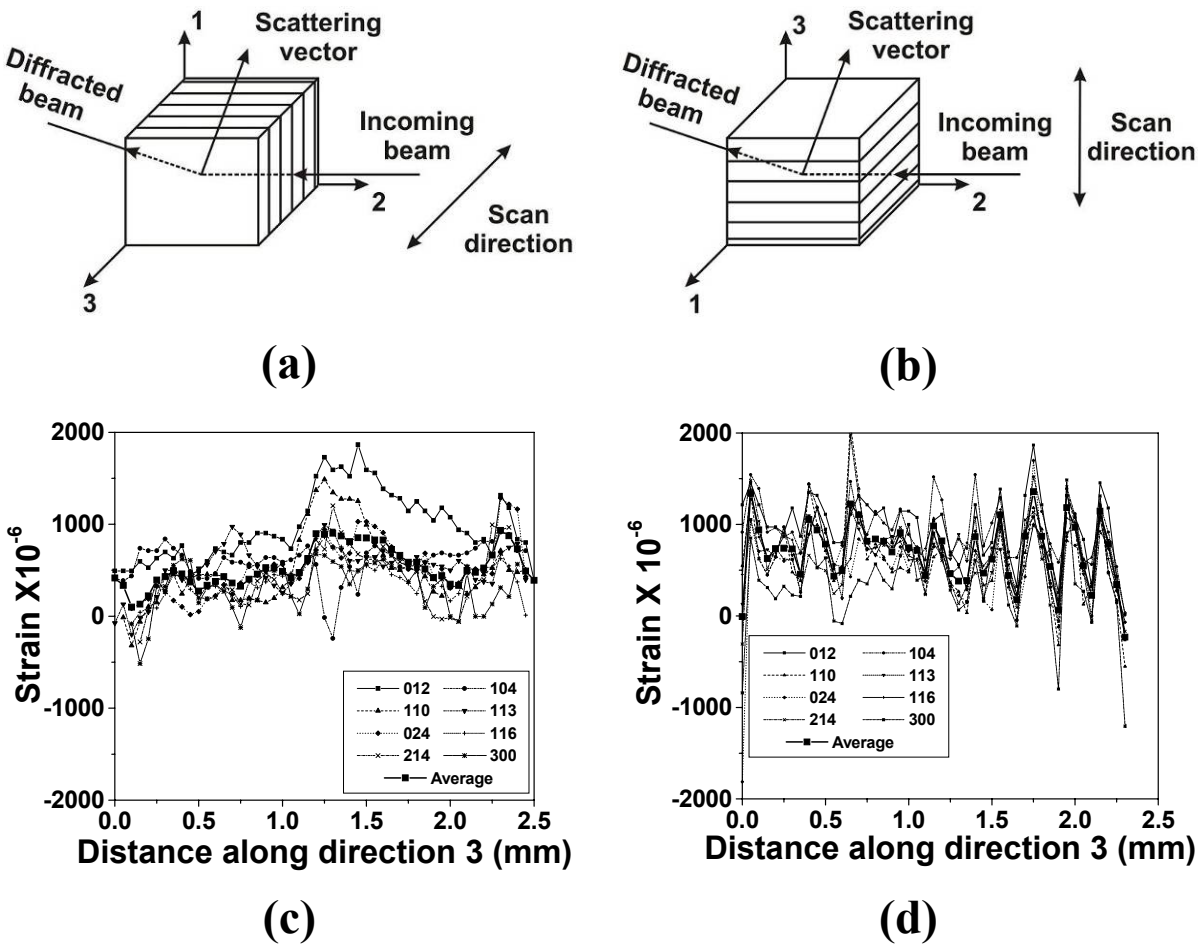


**Figure 5.27: (a) Measurement geometry for scattering vector parallel to the freezing direction; (b): measurement geometry for scattering vector perpendicular to the lamellae orientation; (c): strain fluctuations in the alumina phase for the arrangement shown in (a); and (d): strain fluctuations in the alumina phase for the arrangement shown in (b). The thin lines in (c) and (d) correspond to the individual diffracting planes of alumina while the bold lines represent the continuum mechanics average micro strain.**

of the scattering vector with respect to the freezing direction in the above mentioned two cases. Because of the chosen setup the scattering vector is tilted 3.5 ° with respect to the sample co-ordinate system. In both cases the scanning direction was along specimen coordinate axis 3 (corresponding to 90 ° to lamellae direction; compare Figure 5.25). Corresponding strain distributions are shown in Figure 5.27c and Figure 5.27d. In Figure 5.27c and Figure 5.27d the individual lines correspond to individual diffracting lattice planes of alumina while the bold line corresponds to continuum mechanics average microstrain for the indexed planes of alumina. The continuum mechanics lattice microstrain in Figure 5.27c and in Figure 5.27d was calculated according to the method proposed by Daymond [229] and written as:

$$\bar{\varepsilon} = \frac{\sum_{hkl} \alpha_{hkl} \varepsilon_{hkl}}{\sum_{hkl} \alpha_{hkl}} \tag{5.9}$$

where $\varepsilon_{hkl}$ are the individual plane strains and $\alpha_{hkl}$ are weighting factors defined as:

$$\alpha_{hkl} = T_{hkl} m_{hkl} E_{hkl} / \bar{E} \tag{5.10}$$

where $T_{hkl}$ is the texture factor, $m_{hkl}$ is the multiplicity factor, $E_{hkl}$ is the Young's modulus of individual planes and $\bar{E}$ is the macroscopic Young's modulus of polycrystalline material. As a first approximation, the individual phases were assumed to be texture free (texture factor taken equal to unity); although it has been observed in the course of further analysis that this approximation is very weak for aluminum phase, because of its preferred orientation (large grain size/texture). The shift in the lattice strain distribution for individual diffracting planes observed in Figure 5.27 is due to the inter-planar elastic anisotropy. The figure shows that squeeze-casting produces highly anisotropic thermal residual strains in the alumina phase. There are significant strain fluctuations along the direction transverse to the lamellae which can be explained by the constraint imposed during the solidification and cooling of liquid Al-12Si. Along the freezing direction the ceramic lamellae would be free from such constraints and accordingly less fluctuations of strain are observed here. The individual lamellae in the composite have thicknesses in the range of 20-100 μm, while the slit system for the incoming beam had an opening width of 200 μm. In order to monitor the local fluctuation of the lattice strains more accurately, a gauge volume having dimensions smaller than the lamellae would be ideal. However, this approach was not practicable due to insufficient grain statistics evoked by the small gauge volume.

Integrated line intensities for each energy peak at each scan point were measured. These intensities are plotted in Figure 5.28 as a function of distance traversed for two different orientations of the single-domain sample with respect to the incident beam. Results for {311} family of planes of silicon and {214} family of planes of alumina are shown, as among the planes indexed for the individual phases, they have the highest multiplicity factors. For the plot in Figure 5.28a, the scan direction is parallel to direction 3 in the actual single-domain sample shown in Figure 5.25. As this direction is transverse to the lamella orientation, the gauge volume alternately traverses the ceramic and the metallic lamellae when the sample is shifted stepwise. This results into the alternating peaks of alumina and silicon integrated intensities. Moreover, the number of peaks of alumina and silicon also corresponds to the actual number of ceramic and metallic lamellae in the actual microstructure. For the plot in Figure 5.28b, the

scan direction is parallel to direction 1 (freezing direction). The shape of the plot shows that until about the middle of the sample the integrated intensities of both alumina and silicon almost superimpose on each other. This suggests that the gauge volume covers both ceramic and metallic lamellae. However, afterwards the integrated intensity for alumina shoots up and subsequently the silicon intensity drops down, showing that the gauge volume within this region lies mostly inside one ceramic lamella. This typically indicates to the tilting of the lamellar structure along the freezing direction. Such tilting of the lamellae has already been shown marked with arrows in the microstructures of Figure 5.2.

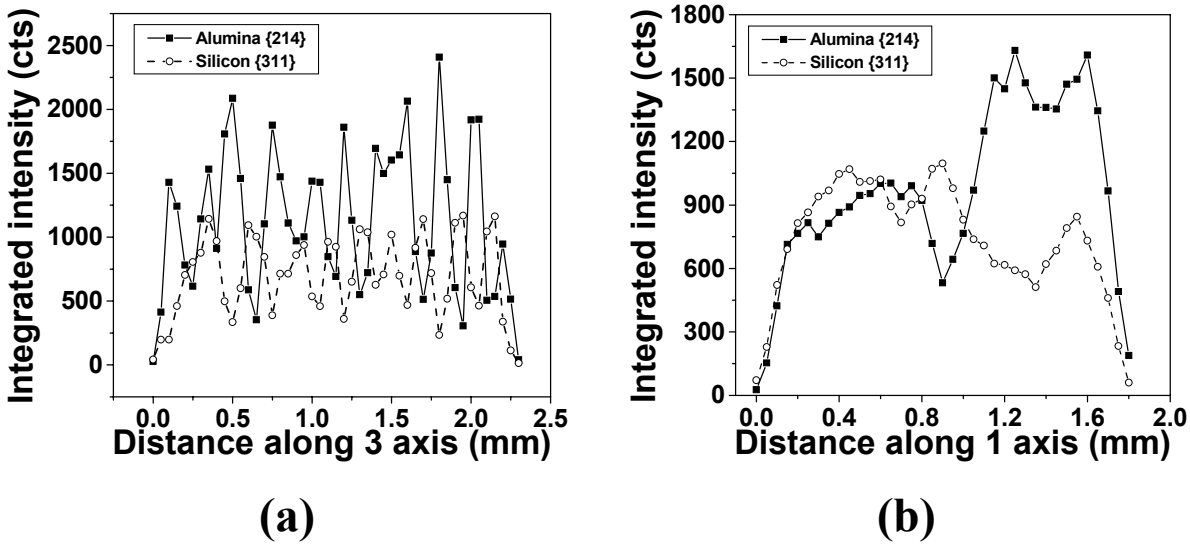


**Figure 5.28: Typical integrated diffracted intensity vs. traversed distance plots for {214} family of planes of alumina and {311} family of planes of Si in the single-domain sample; (a): traverse direction corresponds to direction 3 in Figure 5.25b while in (b) the traverse direction is parallel to direction 1 in Figure 5.25b**

Processing-induced (thermal) residual stresses in all three phases of the composite (alumina, silicon and aluminum solid solution) were determined using the $sin^2\psi$-method of stress analysis described in subchapter 2.7.1. To calculate the absolute phase-specific stresses it is a prerequisite to determine the lattice spacing of the stress-free material for all contributing phases. This requires additional measurements on stress-free materials having the same process history. However, this approach is not feasible for the material under investigation with justifiable effort. To overcome this shortcoming, only the three principal stress differences $\sigma_2$-$\sigma_1$, $\sigma_3$-$\sigma_1$ and $\sigma_3$-$\sigma_2$ were determined for the alumina and for the silicon phase, respectively. This was done according to the $\sin^2\psi$ method for stress analysis by tilting the sample stepwise from 0 °

to 90 ° for the respective planes. From these deviatoric stress components the von Mises equivalent stress was calculated using the following expression:

$$\sigma_{VM} = \frac{1}{\sqrt{2}}\sqrt{(\sigma_1-\sigma_2)^2+(\sigma_2-\sigma_3)^2+(\sigma_3-\sigma_1)^2} \qquad (5.11)$$

It was observed during measurement that $2\theta$ changed slightly with time. This effect can be attributed to the fill level of the liquid nitrogen Dewar vessel necessary for the cooling of the solid state detector. By carrying out measurements on a reference sample before and after filling the Dewar it was observed that in the range of 20-90 keV the shift in the angle $2\theta$ ranges between 0.0042-0.0058 °. This caused an apparent strain change ($\Delta\varepsilon$=1.2-1.6×$10^{-3}$). Since this effect is a long term effect, where the changes will only be seen on a time scale extending over some days, the slight changes in the $2\theta$ angle have a negligible effect on the individual scans but may have a strong effect on the calculated absolute *d-spacings*. To overcome this, only changes in *d-spacing* as a function of $\sin^2\psi$ are shown in Figure 5.29. The measured *d vs.* $\sin^2\psi$ - results were fitted by a straight line and the intersection with ($\psi$=*0*°) was chosen as a reference. This procedure can be followed since only deviatoric stress components in different orientations are of interest and not the absolute *d-spacing*. Among the three phases, the results for aluminum always showed a particularly strong scatter, which can be attributed to the relatively large grain size of this phase. Hence, the further analysis is based on the results for alumina and silicon only. In Figure 5.29 the results obtained for the {214} reflections of alumina and the {311} reflections of silicon are shown. The continuum mechanics average deviatoric stresses were calculated for silicon and alumina using Equations (5.9-5.10). These as well as the von Mises equivalent stress calculated there from using Equation (5.11) are shown in Table 5.7. Table 5.7 clearly illustrates that in both alumina and silicon, the absolute values of the components ($\sigma_3$–$\sigma_1$) and ($\sigma_3$–$\sigma_2$) are similar and also significantly higher than the amounts of ($\sigma_2$–$\sigma_1$), which are near zero in both of the phases. Although from these results it is not possible to determine the absolute values of the individual stress components, they definitely suggest that in both alumina and silicon ($\sigma_{22}\approx\sigma_{11}$). This is due to the fact that the sample makes 0° orientation with axis 2 and hence the processing-induced stresses along axes 1 and 2 are almost similar. Also, the signs of the stress differences are opposite in silicon and alumina. As silicon is present within the aluminum solid solution and also in the form of very fine particulate dispersions, it can be assumed that its behavior images that of the Al-12Si alloy. The opposing signs of the stresses in the alumina and silicon phases are thus due to the different thermal expansion coefficients of the alumina preform and

the infiltrated metallic alloy. The results are thus in agreement with the necessary condition that the overall composite as a whole is free of macroscopic residual stresses.

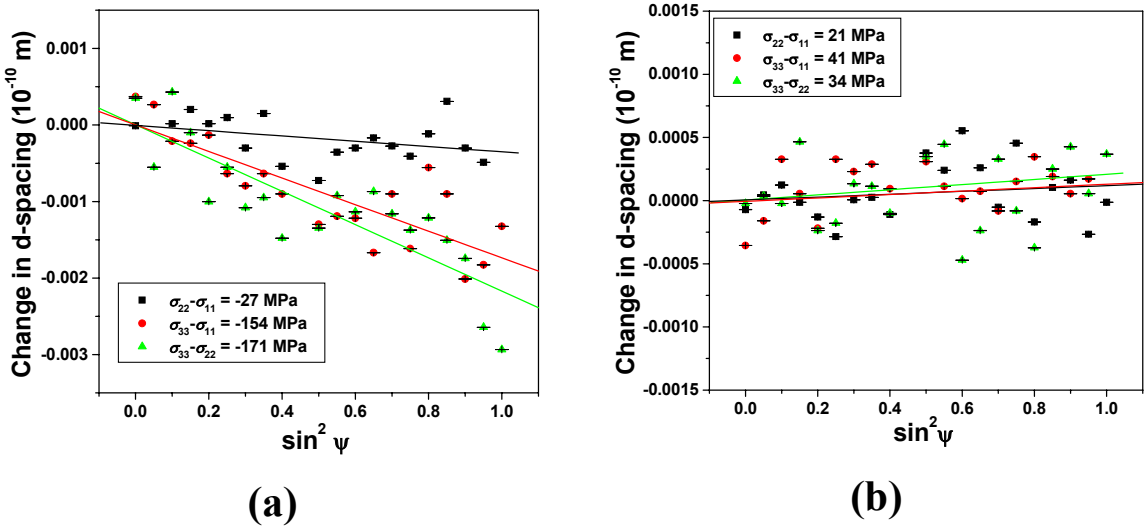


**Figure 5.29: Change in *d-spacing* vs. $\sin^2\psi$ plot for single-domain sample: (a) {311} planes of silicon and (b) {214} planes of alumina**

**Table 5.7: Continuum mechanics equivalent deviatoric stresses and the von Mises equivalent stress in alumina and the silicon phases of the single-domain sample**

| | Alumina | Silicon |
|---|---|---|
| $\sigma_3$-$\sigma_1$ (MPa) | 74 | -154 |
| $\sigma_2$-$\sigma_1$ (MPa) | -7 | -17 |
| $\sigma_3$-$\sigma_2$ (MPa) | 98 | -179 |
| von Mises equivalent stress (MPa) | 87 | -167 |

## 5.5 Elastic-plastic anisotropy and damage evolution in single-domain samples

### 5.5.1 Compressive stress-strain plots along freezing direction in single-domain samples and effect of preform coating

Figure 5.30 shows typical compressive stress-strain diagrams (both stress and strain in absolute scale) for single-domain samples loaded along the freezing direction. For comparison, representative plots for samples whose preforms were coated with Cu and $Cu_2O$ prior to melt infiltration are also shown in the same diagram. In all cases tests were carried out until final fracture of the sample occurred. The initial curved shape of the plots at small applied loads

can be attributed to the deviation of the sample geometry from perfect parallelism and friction between the specimen and the punches. Failure takes place in an almost brittle manner with a

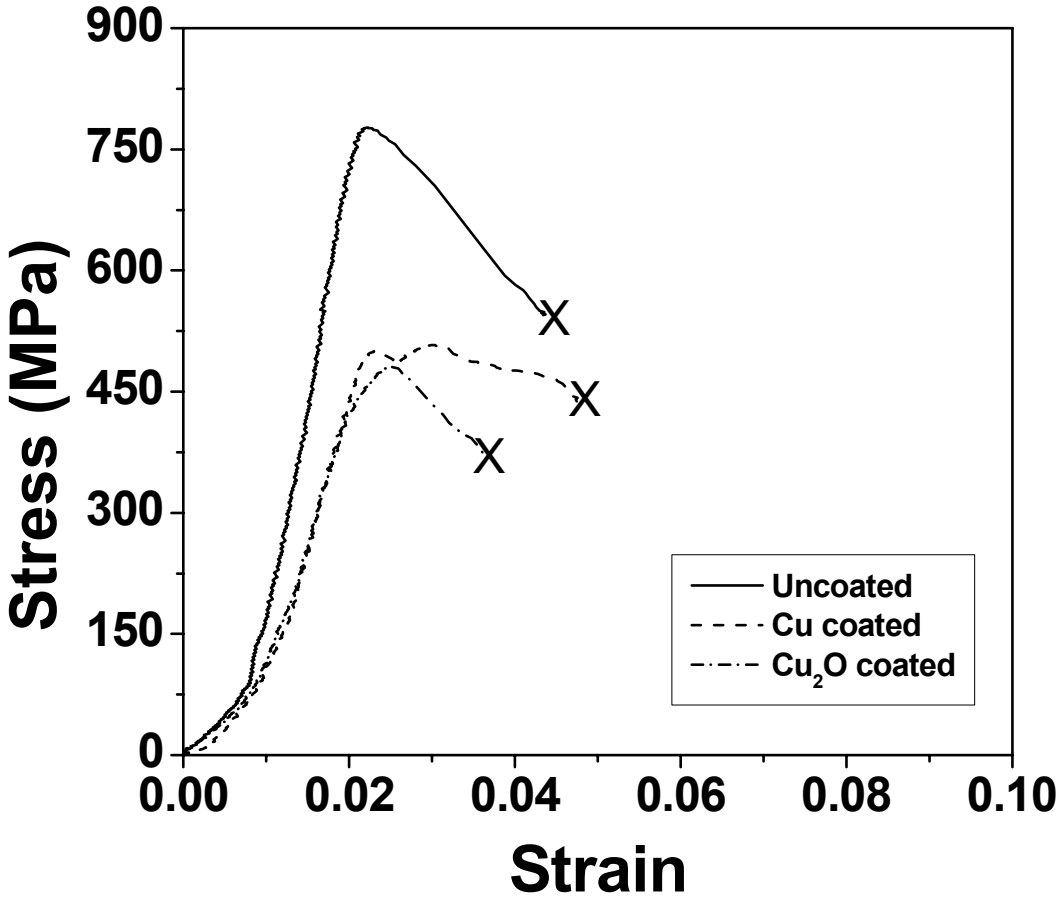


**Figure 5.30: Typical compressive stress-strain diagrams for single-domain samples prepared using un-coated and coated performs, load application along freezing direction**

**Table 5.8: Average compressive strengths and their standard deviations for single-domain samples (un-coated, coated with Cu and $Cu_2O$, respectively) compressed along the freezing directions**

| Batch | No. of samples | Compressive strength (MPa) |
|---|---|---|
| Uncoated | 5 | 688 (67) |
| Cu - coated | 4 | 488 (15) |
| $Cu_2O$ coated | 3 | 455 (51) |

sudden loss of the stored elastic energy. Table 5.8 shows the average compressive strengths (a standard deviation) of several samples for composites with coated or uncoated ceramic pre-forms. The number of samples tested in each batch is also mentioned in the same table. Compressive strength has been taken as the maximum point in the respective stress-strain plots. Table 5.8 clearly shows that the compressive strength of the samples with uncoated preforms

is significantly higher than that with coated preforms. Composites with Cu or $Cu_2O$ coated preforms show similar strengths.

### 5.5.2 Progressive damage mechanism in single-domain samples compressed along the freezing direction

#### 5.5.2.1 Single domain sample with uncoated preform

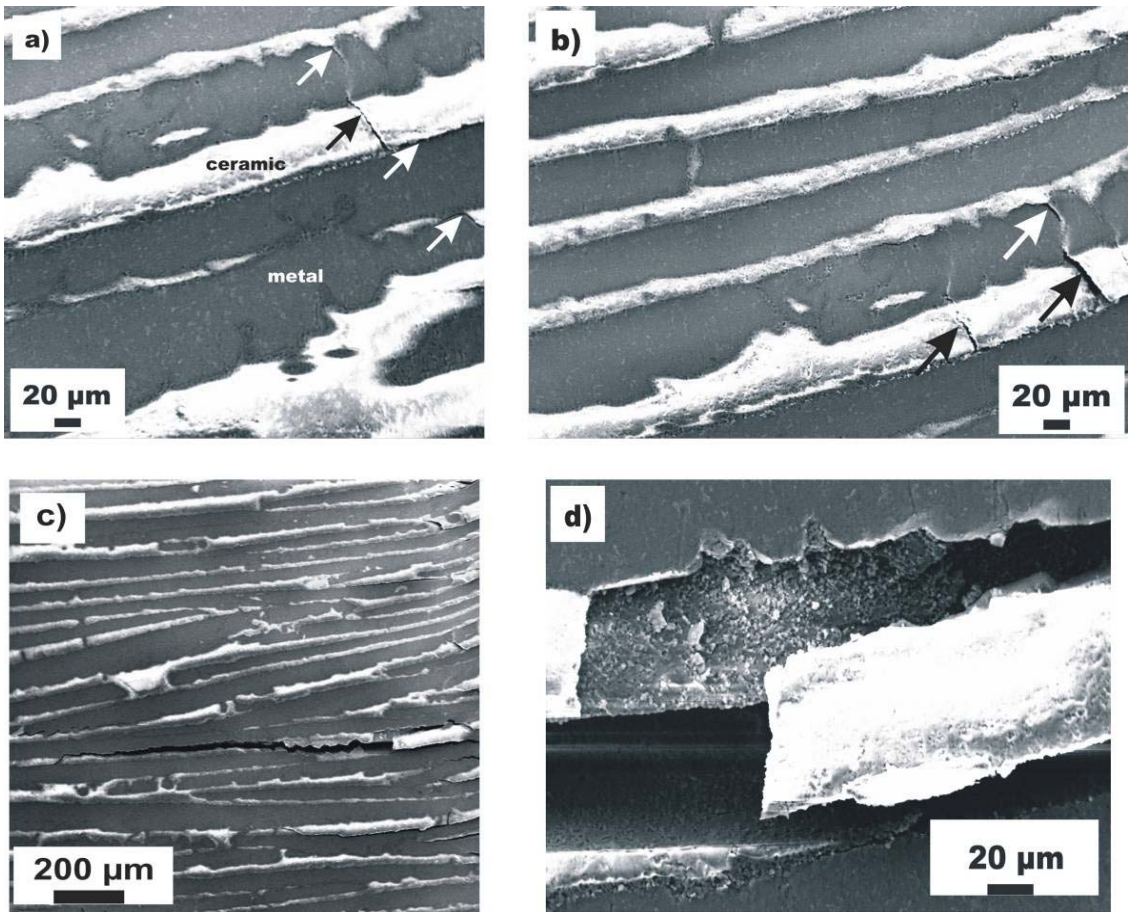


**Figure 5.31: SEM micrographs showing the progressive damage evolution in an uncoated single-domain sample at different loads: compressive load along the freezing direction (= horizontal direction); (a) initial transverse cracking within the ceramic lamellae (σ=422 MPa), (b) generation of more transverse cracks within ceramic lamellae at higher load and propagation of such cracks into the metallic alloy (σ=527 MPa), (c) propagation of one longitudinal crack through a ceramic lamella and hence causing catastrophic failure of the sample (σ=594 MPa) and (d) enlarged view of the region close to the main crack showing ceramic crushing and longitudinal splitting of the metallic lamellae.**

Figure 5.31 shows SEM images of the progressive damage evolution in one single-domain sample with uncoated preform compressed along the freezing direction. In these SEM micro-

graphs the metallic component appears dark, while the ceramic component appears bright due to local charging of this non-conducting compound. No electrically conducting layer was deposited on the samples prior to SEM investigation in order to enhance contrast between the ceramic and the metallic regions. Loading direction corresponds to the horizontal axis. Cracking begins within the ceramic lamellae as transverse cracks which then propagate into the metallic alloy (marked by arrows in Figure 5.31a). Localized debonding at the metal-ceramic interfaces is observed as well. With increasing load more transverse cracks generate within the ceramic lamellae and earlier cracks become longer and wider. Because of the ceramic cracking and subsequent load redistribution, the localized stress in the metallic alloy increases. This causes the transverse cracks in the ceramic lamellae to propagate further as shown by arrows in Figure 5.31b. With further loading, one large crack propagates longitudinally along a single ceramic lamella and the sample fails catastrophically (Figure 5.31c). Damage development is not homogeneous throughout the sample, suggesting that because of the structural heterogeneities in the freeze-cast preform, stress concentration in a localised region causes the ceramic lamellae in that region to fail. Figure 5.31d shows a micrograph taken from the region in the vicinity of the main crack. Apart from ceramic crushing, longitudinal splitting is observed within the metallic lamellae, suggesting that the debonding shear stress $\tau_d$ is greater than the ultimate shear stress of the metallic alloy $\tau_{mu}$.

#### 5.5.2.2 Single domain sample with Cu coated preform

Figure 5.32 shows the compressive stress-strain plot of one single domain sample compressed along the freezing direction. The preform for this sample was coated with Cu prior to melt infiltration by squeeze-casting. Compressive strength is about 500 MPa. Drops in the stress-strain plot correspond to the points where the compression test was stopped to take micrographs to study the propagation of damage. Figure 5.33 shows the progressive damage evolution in this particular sample corresponding to different applied stresses. The micrographs are marked by alphabetical numbers and the same numbers are also shown in the stress-strain plot of Figure 5.32 to show the points where they were taken from. The micrographs in Figure 5.33 show that until about 450 MPa applied stress, no visible sign of any damage can be identified. Damage in the form of separation along the metal/ceramic interface is first observed at an applied compressive stress of about 460 MPa (the micrograph marked with "*b*"). Locations along this separated interface are marked with arrows in the magnified image marked with "*c*". The images marked with "*b*" and "*c*" correspond to the same location and taken at the same applied stress. The image marked with "*d*" shows the complete sample and it was taken

after the sample failed. Regions within this micrograph are shown in the micrographs marked with "*e*" and "*f*". The micrograph marked with "*e*" shows the magnified view of the large

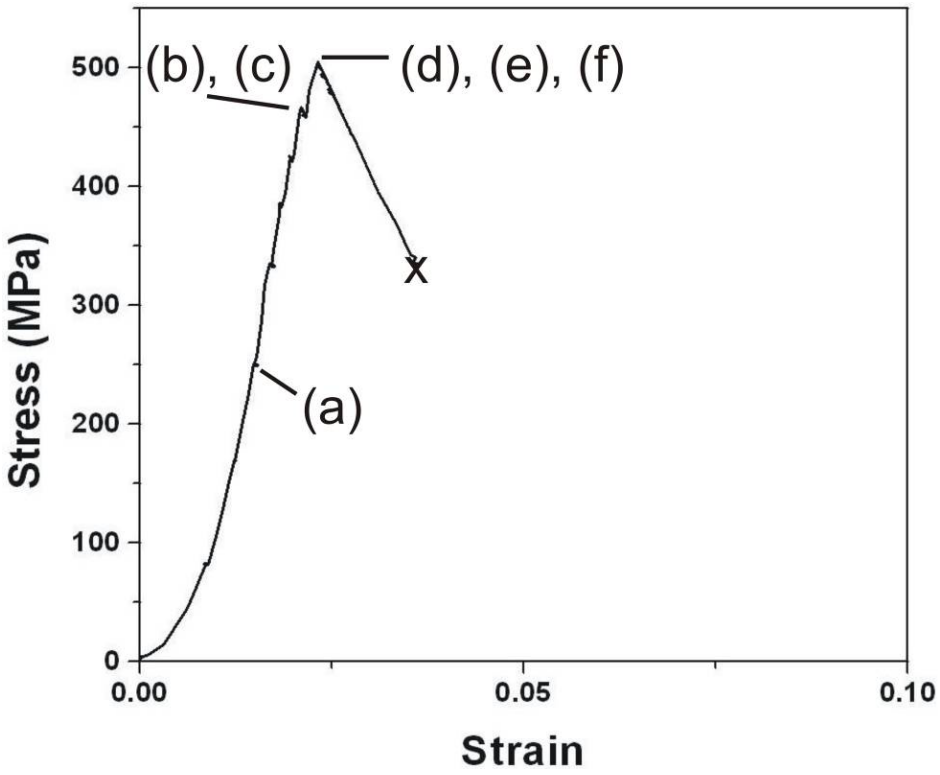


**Figure 5.32: Compressive stress-strain plot for one single domain sample compressed along the freezing direction. The preform was coated with Cu prior to melt infiltration**

crack seen in the upper middle portion of the Figure 5.33d while the micrograph marked with "*f*" shows the magnified view of the crack located at the bottom left hand side of Figure 5.33d. Figure 5.34 shows the damage propagation in single-domain samples whose preform was coated with $Cu_2O$ prior to melt infiltration. Compressive load was applied along the freezing direction (corresponding to the horizontal direction in the micrographs). Both Figure 5.33 and Figure 5.34 show that failure mainly occurs by propagation of cracks along the metal/ceramic interface. Contrary to the samples prepared using uncoated preforms, no cracking of the metallic lamellae could be observed. Although transverse cracking within the ceramic lamellae is observed at some localized regions (much more predominant in the sample with $Cu_2O$ coated preform), actual failure takes place by de-cohesion along the metal/ceramic interface. This suggests that coating the preform prior to melt infiltration weakens the interface, decreasing the interfacial bond strength (reducing $\tau_d$ in comparison to $\tau_{mu}$). Furthermore, non-uniform distribution of the interfacial damage as seen in both the figures is probable due

to non-uniform coating or washing out of the coating during subsequent squeeze-casting. Figure 5.35 shows a TEM bright-field image as well as corresponding element distributions of

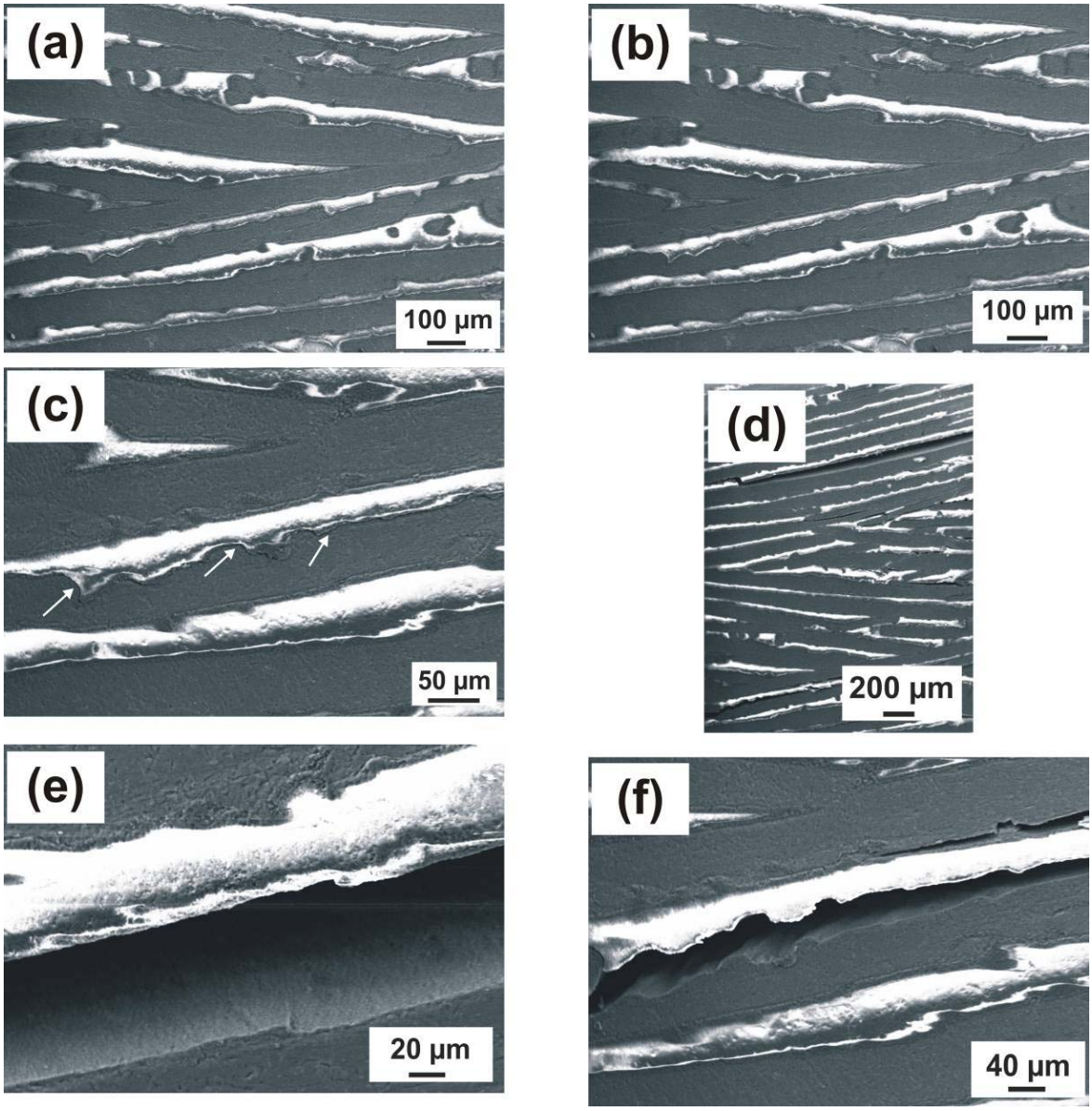


**Figure 5.33: Progressive damage evolution in the single domain sample with Cu coated preform at different externally applied compressive stresses. Compression direction is along the freezing direction (= horizontal direction). Alphabetical numbering of individual microstructures corresponds to the carious stages in the compressive stress-strain plot marked in Figure 5.32**

Al, Cu, and O, respectively, of a representative interfacial region in a specimen prepared from a Cu-coated ceramic preform. TEM was carried out in a 200 keV Zeiss LEO 922 microscope (Oberkochen, Germany) equipped with an Omega filter to perform energy-filtered TEM (EFTEM). EFTEM was applied to analyse the interfacial regions between ceramic and the

metallic alloy in specimens prepared using coated Cu preforms in detail as this method suits to visualize element distributions. The three-window ratio method (power law estimation of the background) with two pre-edge images was used for EFTEM to obtain element

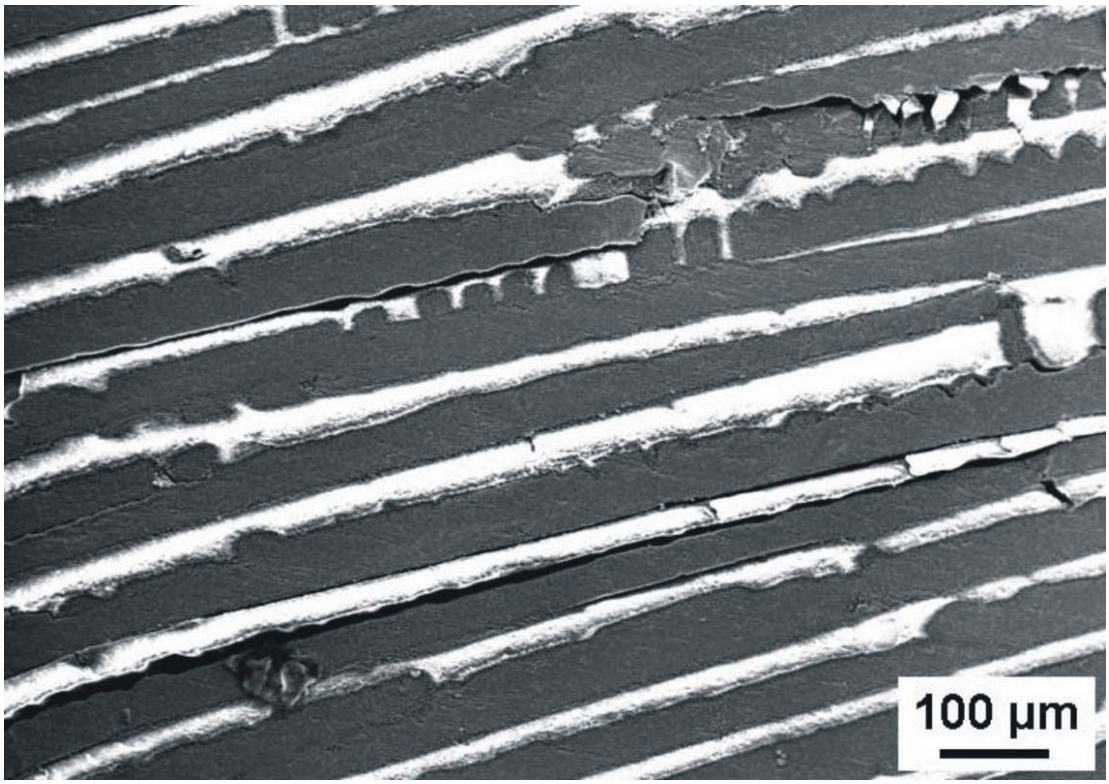


**Figure 5.34: SEM micrograph showing the damage morphology in one composite sample whose preform was coated with $Cu_2O$ prior to infiltration. Compressive load was applied along the freezing direction (= horizontal direction)**

distributions of Al, Cu, and O, respectively. Therefore, electrons with the element specific energy losses of 532 eV (O-K ionization edge), 931 eV (Cu-$L_{23}$ ionization edge) and 1560 eV (Al-K ionization edge), respectively, were selected for the imaging process using a slit with a width of 50 eV or 125 eV (Al-K ionization edge). The Al-$L_{23}$ ionization edge (73 eV), which would normally be preferred due to its much higher intensity, could not be used for analysis, since the Cu-$M_{45}$ ionization edge (74 eV) strongly overlaps. This fact would result in indistinguishable signals of Al and Cu within the obtained energy-filtered image. In addition, electron diffraction analysis was performed to identify the phases present at the interfacial regions. As can be seen in the bright-field micrograph, the Cu coating covers most of the interface between the ceramic and the alloy. Since the atomic density of Al atoms in the matrix is higher compared to $Al_2O_3$, the matrix appears brighter in the Al distribution. The Cu distribution is complementary to the Al distribution which indicates that no reaction takes place at the inter-

face between the coating and the infiltrated alloy. Electron diffraction also did not yield any indication for the formation of intermetallic compounds that are typically known for the Al-

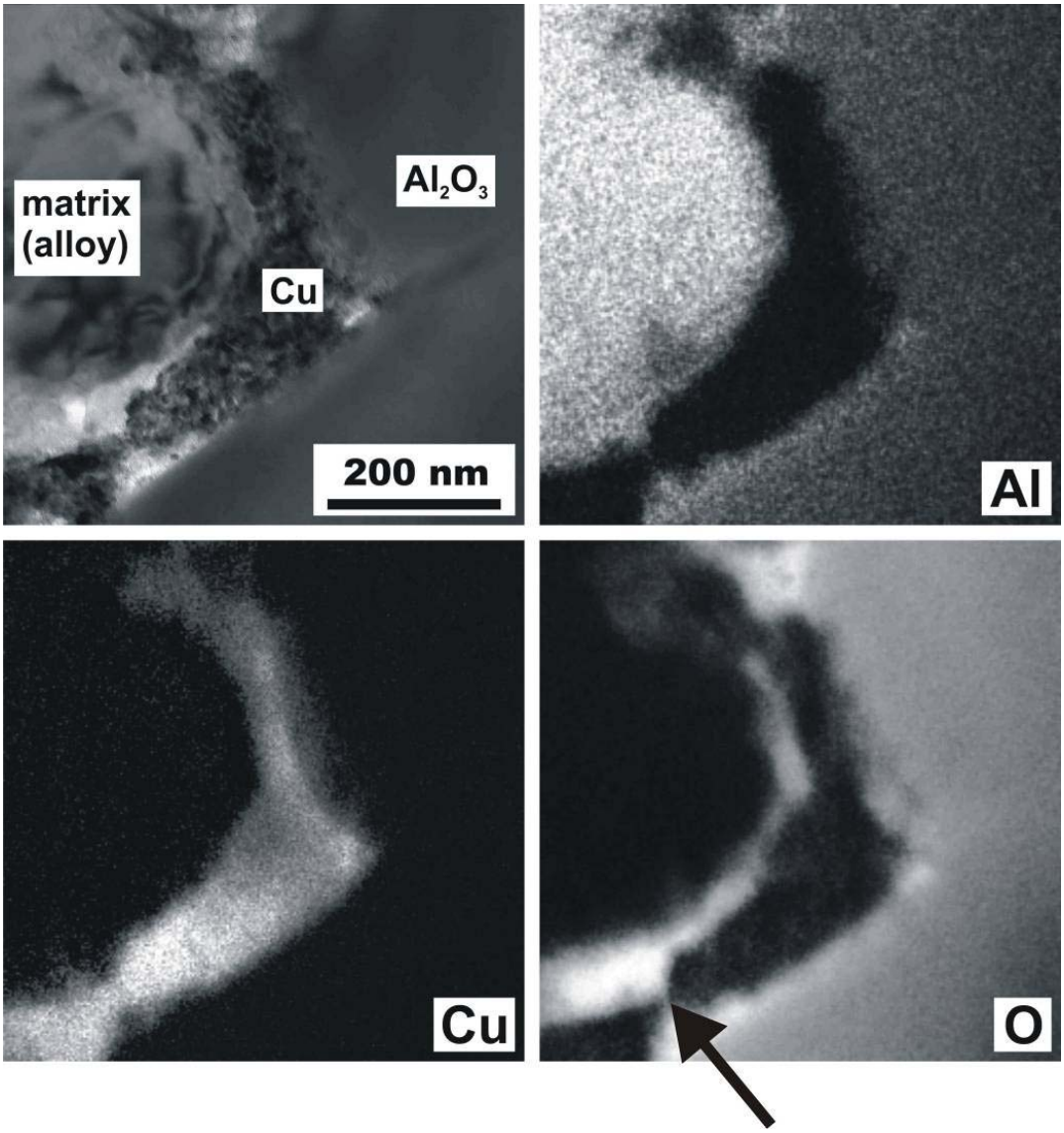


**Figure 5.35: TEM bright-field image with corresponding element distributions of Al, Cu and O of the interfacial region of a metal/ceramic composite whose preform was coated with Cu prior to melt infiltration. The oxidization of the Cu coating prior the infiltration can be recognized (carried out by B. Butz at LEM, University of Karlsruhe)**

Cu-system. This is explained by the low cation diffusivity between Cu coating and matrix which is hindered by a native cupper oxide. As can be recognized in the oxygen distribution, the surface (to air) of the Cu coating as well as the matrix alloy is oxidized during the processing. For the Cu coating oxidation prior to the melt infiltration is assumed. A thin oxygen-rich layer can be recognized in the O distribution (marked by arrow) which clearly indicates the

oxidization of the Cu-alloy interface. Faint additional reflections due to native cupper oxide could additionally be observed in electron diffraction.

### 5.5.3 Effect of domain orientation on the compressive behavior of single-domain samples with uncoated preform

To study the effect of domain orientation on the compressive behavior, uncoated single-domain samples with a large variety of domain orientations ($\beta$ in Figure 5.5) were compressed along one of the alternative directions 2 or 3 in Figure 5.5. Representative stress-strain plots are shown in Figure 5.36. For comparison, a representative compressive stress-strain plot for a block of unreinforced Al-12Si is shown in the same figure (curve marked by bold dashes). This sample was larger than the single-domain samples (nominal dimensions 10×10×10 mm³). The sample with a domain orientation of $\beta$=43 ° (curve marked by bold solid line) was compressed in-situ to observe the progressive damage evolution at different

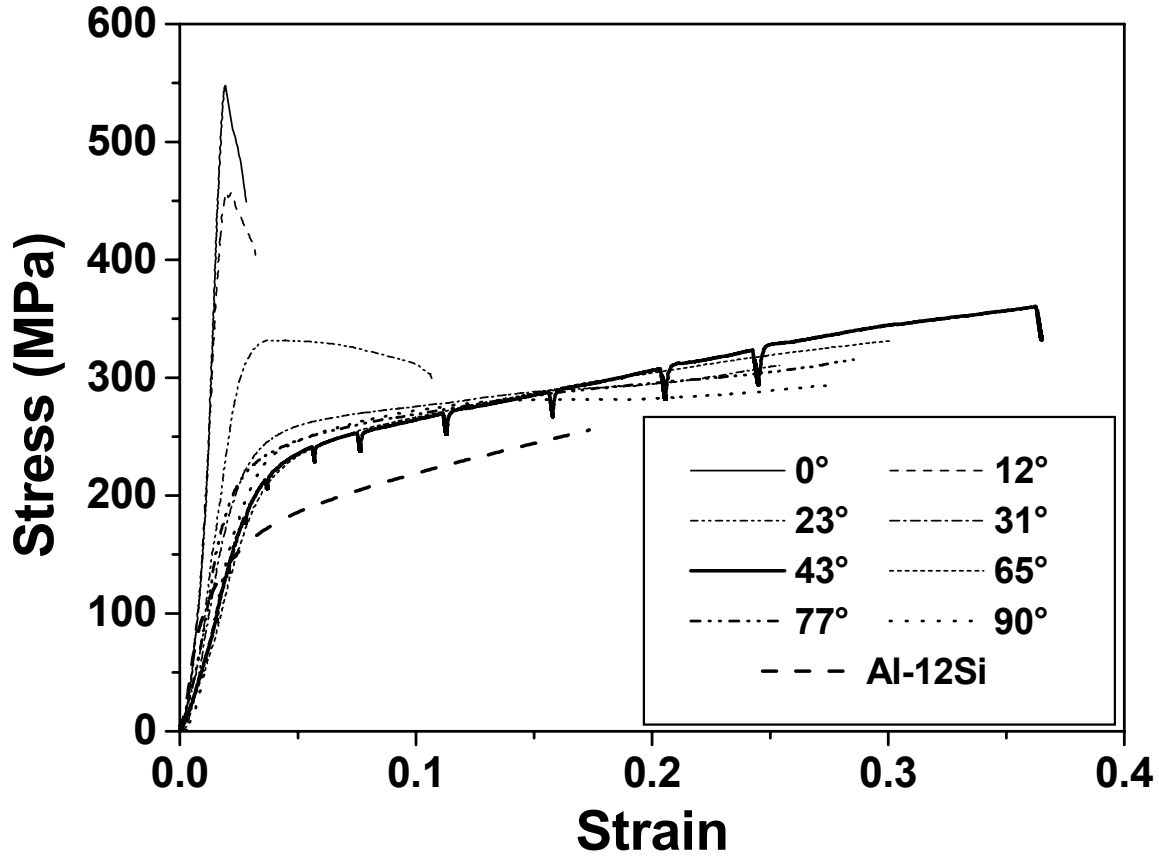


**Figure 5.36: Effect of domain orientation on the compressive stress-strain plots of single-domain samples with uncoated preforms.**

stages of deformation. Drops in this curve correspond to the points when the compression test was stopped to take micrographs of the sample. When loaded along $\beta=0$ °, the composite behaves like a brittle solid, which is similar to that along the freezing direction. The material is strongest along this direction and the freezing direction. As the domain orientation in the samples increases, compressive strength decreases systematically until about $\beta=30$ °. At domain orientations within the range of *30-90* ° ($30° \leq \beta \leq 90°$), the metallic alloy plays the dominant role. No perceptible change in the compressive stress-strain behaviour can be observed in this orientation range. Figure 5.37 shows the effect of domain orientation on the

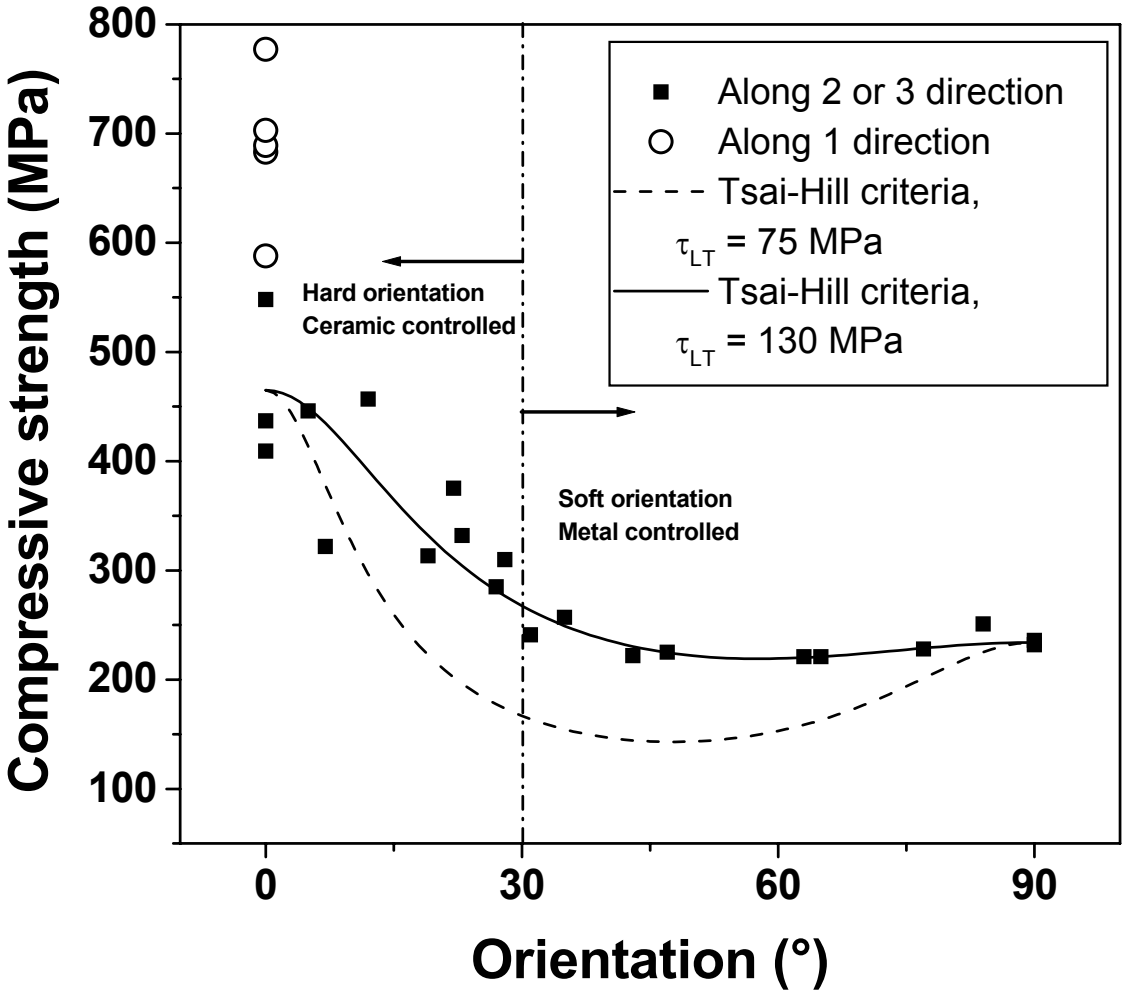


**Figure 5.37: Effect of domain orientation angle on the compressive strength of single-domain samples with uncoated preforms. For comparison the compressive strengths of single-domain samples using uncoated preforms loaded along the freezing direction are shown (open circles). Theoretical predictions for energy-based Tsai-Hill criterion using two different values of composite shear-yield strength are plotted to validate the experimental observations.**

compressive strength of single-domain samples prepared from uncoated preforms. For comparison, compressive strengths of single-domain samples along the freezing direction are additionally presented in the same figure. They are denoted by open circles plotted at the domain orientation of $\beta=0$ °. Due to the difficulty in computing the exact 0.2% composite yield strength for samples showing extensive plasticity ($\beta$ within the range of 30-90 °), strength corresponding to a total strain of 1% has been used as the compressive strength of these samples. Samples having $\beta \leq 30$ ° show a definite maximum in their stress-strain plots and this maximum strength has been taken as their compressive strength. Theoretical predictions for the energy based Tsai-Hill criterion (refer to Equation 12.42 in [12] and also to the next chapter in this work) for two different values of composite shear yield strength are also shown in the same plot. The composite with $\beta$ <30 ° are named as hard orientation. The compressive strength drops systematically with increasing domain orientation angle $\beta$ in this region. The region between $\beta=30$ °-$90$ ° is marked as soft orientation and in this region the compressive strengths of the single-domain samples show no further dependence on domain orientation and remain nearly constant.

### 5.5.4 Damage development in single and double domain samples with different orientations

#### 5.5.4.1 Single domain samples

The scanning electron micrographs in Figure 5.38 show the progressive damage evolution in the single-domain sample with $\beta=43$ °. The stress-strain plot is shown in the same figure to correlate the points where the micrographs were taken from. As already mentioned, the ceramic component appears brighter while the metallic alloy is dark. Damage evolves mainly by transverse cracking within the ceramic lamellae due to the elastic-plastic mismatch of the plastically flowing metallic alloy and the rigid ceramic lamellae. This can clearly be interpreted from the fact that the micrograph taken at the point where global plasticity has not yet set in shows no evidence of any cracks. First cracks are observed within the ceramic lamellae (marked by white arrows in the Figure 5.38b) near the transition point between macroscopic elastic–plastic deformation. At higher strains, extensive transverse cracking of the ceramic lamellae are observed. The metallic alloy undergoes extensive plasticity at these higher strains and thorough shear cracks are seen to be formed within the metallic lamellae oriented at ap-

proximately *45* ° to the direction of compressive load application (marked by white arrow in the Figure 5.38d).

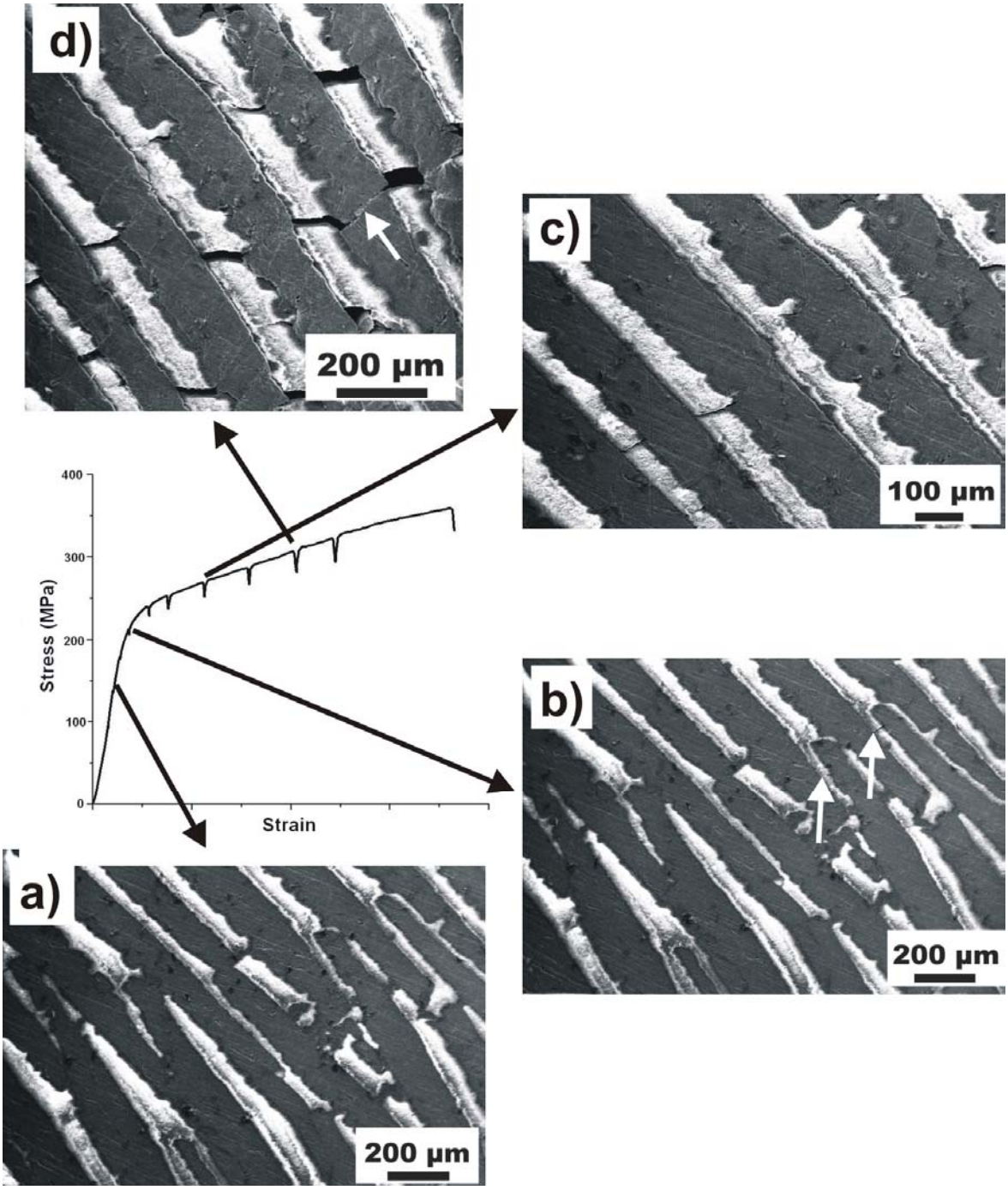


**Figure 5.38: SEM micrographs showing the progressive damage evolution if compressed at *β=43* ° to domain orientation (= horizontal direction in the figure) in a single-domain sample with uncoated preform. The actual stress-strain diagram is shown in the figure. Drops in the plot correspond to the points when the test was stopped for in-situ analysis. Micrographs marked with arrows show the extent of damage evolution at those points. Ceramic component looks bright while the metallic alloy is dark.**

The scanning electron micrographs in Figure 5.39 show the progressive damage evolution in one single-domain sample with *β=84* °. The stress-strain plot is shown in the same figure to correlate the points where the micrographs were taken. As already mentioned, the ceramic

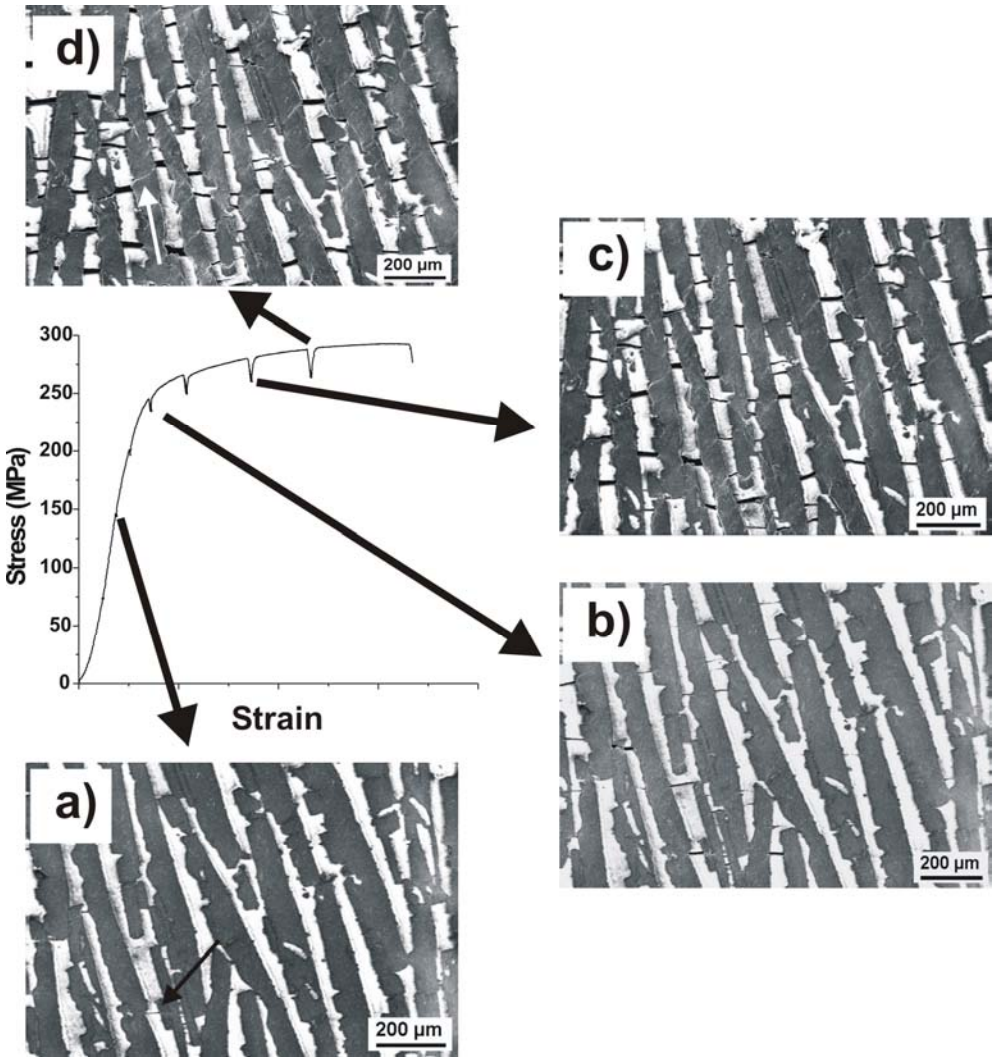


**Figure 5.39: SEM micrographs showing the progressive damage evolution if compressed at *β=84* ° to domain orientation (= horizontal direction in the figure) in a single-domain sample with uncoated preform. The actual stress-strain diagram is shown in the figure. Drops in the plot correspond to the points when the test was stopped for in-situ analysis. Micrographs marked with arrows show the extent of damage evolution at those points. Ceramic component looks bright while the metallic alloy is dark.**

component appears brighter while the metallic alloy is dark. Similar to the sample with about *43* ° domain orientation, damage evolves mainly by transverse cracking within the ceramic lamellae due to the elastic-plastic mismatch of the plastically flowing metallic alloy and the rigid ceramic lamellae. Very limited numbers of such cracks are observed within the ceramic lamellae when macro plasticity has not yet set in. At higher strains, extensive transverse

cracking of the ceramic lamellae are observed. The metallic alloy undergoes extensive plasticity at higher strains and thorough shear cracks are seen to be formed within the metallic lamellae oriented at approximately *45* ° to the direction of compressive load application. Because of the application of compressive load, the sample never really fails even at a very high strain.

#### 5.5.4.2 Double domain sample

One single-domain and one double domain sample were tested in-situ under compression. The single-domain sample had about *27* ° orientation with the 2 direction while in the double domain sample one domain had approximately *63* ° and the other domain had about *26* °

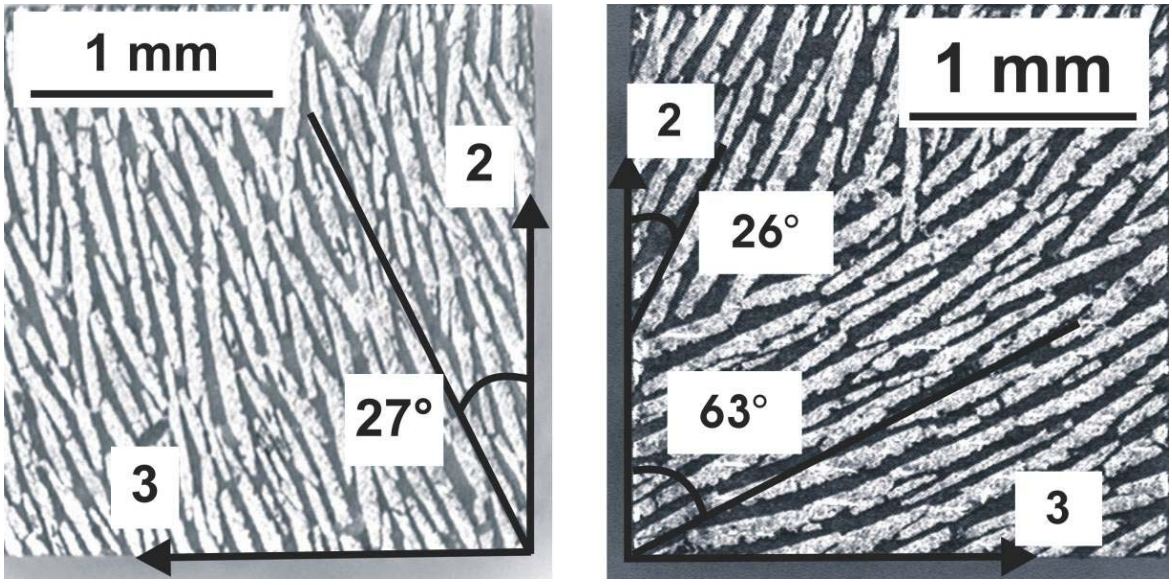


**Figure 5.40: Optical micrographs of the single-domain (on the left) and the double domain sample (on the right)**

orientation with the 2 direction. Figure 5.40 shows the light optical micrographs of the faces perpendicular to the freezing direction in these two samples. The micrograph on the left hand side shows the single-domain sample while the right hand side micrograph corresponds to the double domain sample. As has already been mentioned, in these light optical micrographs the metallic alloy is bright while the ceramic component is dark. The single-domain sample was compressed along 3 direction (corresponding to loading at 63° to the domain orientation) while the double domain sample was compressed along the 2 direction. Figure 5.41 shows the combined compressive stress-strain plots for these two samples. The solid line in this

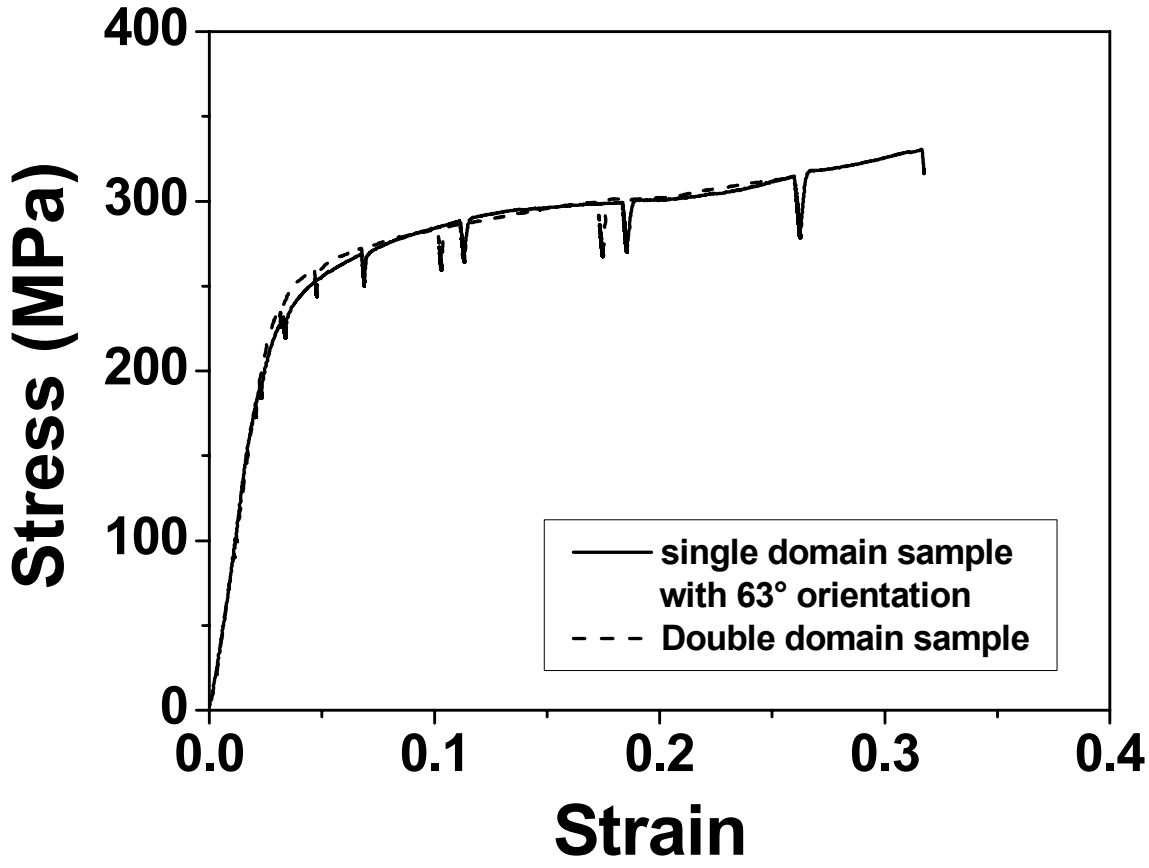


**Figure 5.41: Combined compressive stress-strain plots for a** single-domain **sample having approximately *63* ° orientation with loading direction and one double domain sample having one domain oriented at 63 ° and the other oriented at *26* ° with the loading direction**

figure refers to the single-domain sample while the dashed line corresponds to the double domain sample. As already mentioned, drops in the stress-strain plot correspond to the locations where the test was stopped to observe the damage propagation. At the transition between the macroscopic elastic-plastic regions the compressive stress-strain plot for the double domain sample shows marginally higher strength in comparison to the single-domain sample but otherwise the two curves perfectly superimposes on each other.

Figure 5.42 shows the progressive damage evolution in the double domain sample. The actual compressive stress-strain plot is also marked in the same diagram and alphabets with lines mark the locations where the shown micrographs were taken. Unlike the samples for Figure 5.38 and Figure 5.39, the double domain sample was sputtered with gold prior to observation within the SEM. Hence, the contrast between alumina and aluminum alloy is significantly reduced. Still, the brighter lamellae in the micrographs correspond to the ceramic while the metallic lamellae are darker. Orientations of the two domains are also marked in the

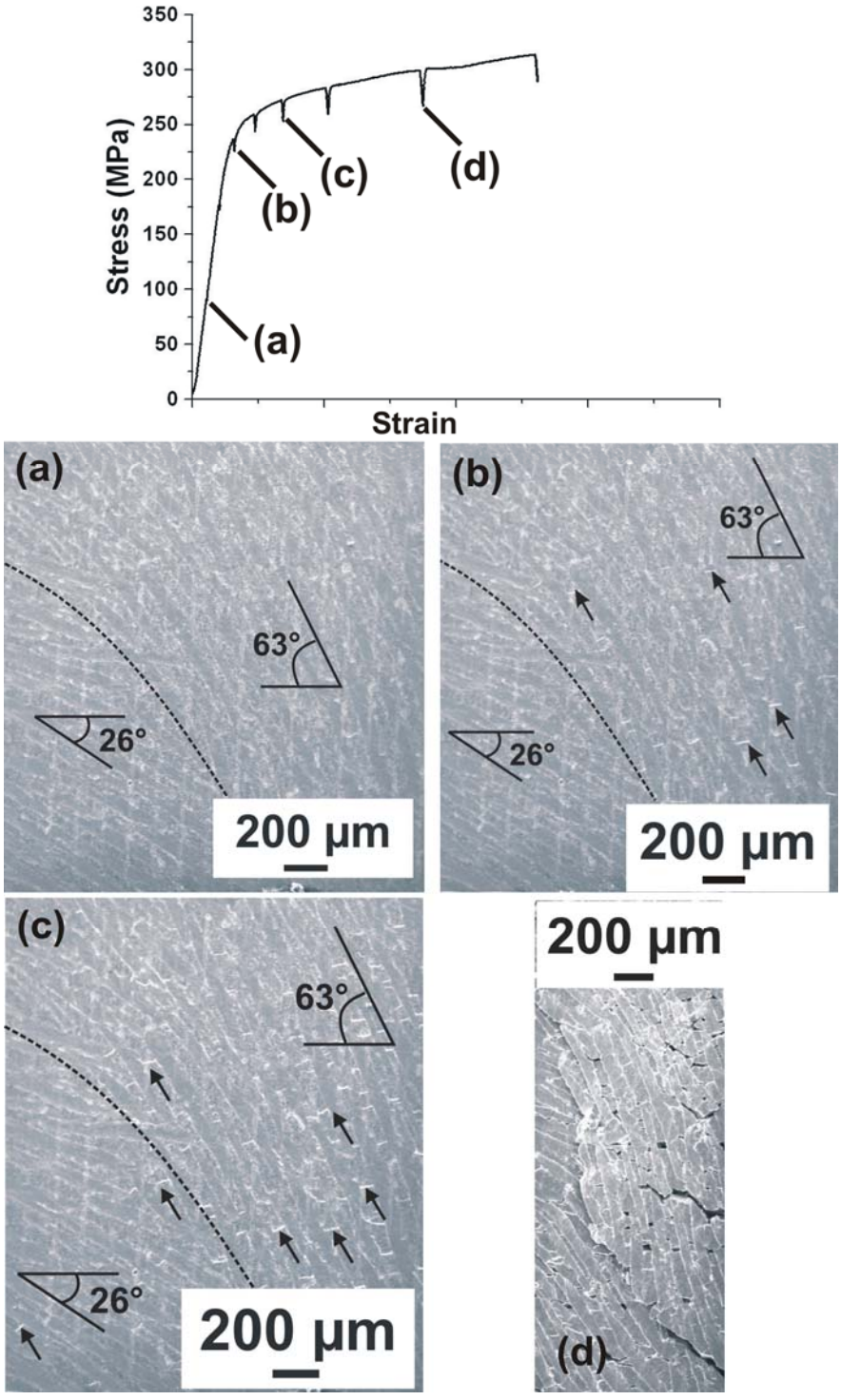


**Figure 5.42: SEM micrographs showing the progressive damage evolution in a double domain sample. Two domains are separated by the dotted black line. Orientation of one domain is approximately 63 ° and the other about 26 ° with the loading direction (= horizontal direction). The actual stress-strain diagram is also shown in the figure. Micrographs show the extent of damage evolution at various points within the stress-strain plot. Some of the cracks within the ceramic lamellae at different load steps are marked .**

micrographs and the black dotted line separates the two domains. The first micrograph marked with *(a)* was taken when the sample was still macroscopically elastic. At this point the sample is essentially free from visible cracks. Extensive damage is first observed at the point marked with *(b)*. The cracks, some of which are marked with black arrows, are mostly transverse cracks within the ceramic lamellae and they are mostly localised within the domain having an orientation of *63* ° with the loading direction. At this point of the stress-strain plot, damage has not yet propagated within the domain with *26* ° orientation. Continued deformation within the plastic range generates many cracks within the domain oriented at *63* ° to the loading direction (micrograph marked with *(c)*). Some cracks are also seen within the *26* ° domain at this point. At still higher plastic strains, extensive cracking and damage take place within the whole sample. As the sample is under compressive load, it does not fail in a catastrophic manner even at this very high strain. The micrograph marked with *(d)* shows that at this very high plastic strain, large cracks can be observed within the *63* ° domain, where apart from transverse cracks within the ceramic lamellae, shear cracks within the metallic lamellae are seen. In comparison, the domain with *26* ° orientation is significantly less damaged. Moreover, one large crack is seen to propagate from the bottom right corner to the top left corner of the micrograph, which approximately traces the boundary between the two domains in the original micrograph.

## 5.6 Synchrotron X-ray energy-dispersive diffraction study of internal load transfer under external compressive loading

### 5.6.1 Monotonic loading of one single domain sample with 0° domain orientation along the freezing direction

To study internal load transfer under external loading, a gauge volume having a nominal volume of 0.12 mm³ was defined by the primary and the secondary slits. The slit system as well as the dimension of the gauge volume within the single domain sample with approximately 0° domain orientation with 2 direction is shown in Figure 5.43. Compressive load was applied along the freezing direction (along direction 1 in Figure 5.43). Compressive load was

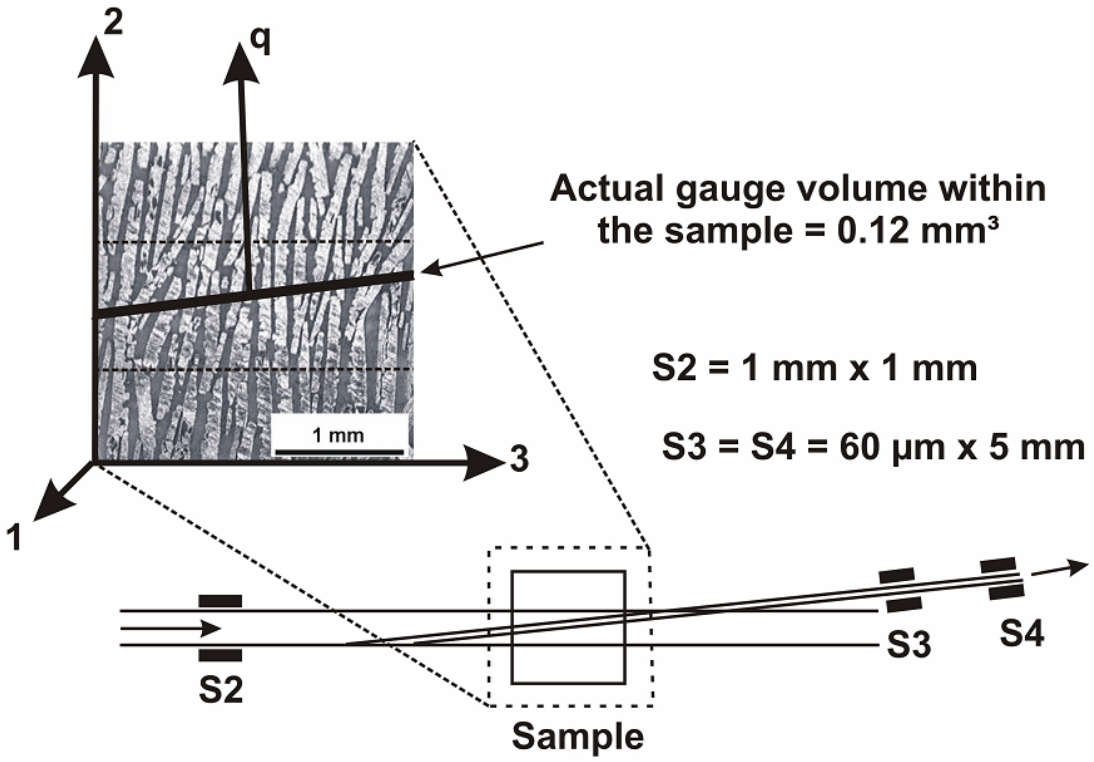


**Figure 5.43: Schematic diagram showing the measurement geometry for energy-dispersive synchrotron X-ray diffraction. The zoomed image shows the microstructure of the face perpendicular to the freezing direction for the actual single-domain sample used in the study. Actual dimensions and shape of the gauge volume are marked within the sample and "*q*" shows the orientation of the scattering vector.**

increased stepwise and at every loading step measurements were carried out according to the $sin^2\psi$ method of X-ray stress analysis by tilting the test rig along with the sample between $\psi$=0–90 ° (definition of the $\psi$ angle is shown in Figure 5.44). After each load application and before the corresponding diffraction measurement, sufficient waiting time (in the range of 5-10 minutes) was maintained to minimize the effects of stress relaxation. At any applied load, for each $\psi$ tilt the acquisition time was 1 minute. In diffraction measurements the lattice strain is always measured parallel to the scattering vector. As shown in Figure 5.44, for $\psi$=0 °, the scattering vector is approximately parallel to 2 direction while for $\psi$=90 ° it is almost parallel to 1 direction. A pre-load in the range of 20–30 N (corresponding to a stress of 3–5 MPa) was first applied to ensure that the sample did not fall down during tilting of the rig and the lattice plane spacing at this initial state was used as the reference value for further calculations. Hence, no effect of processing-induced thermal residual stresses is considered and only the extent of internal load transfer under an applied external compressive load is measured, irrespective of the process history the sample experienced. Here onwards, lattice microstrains

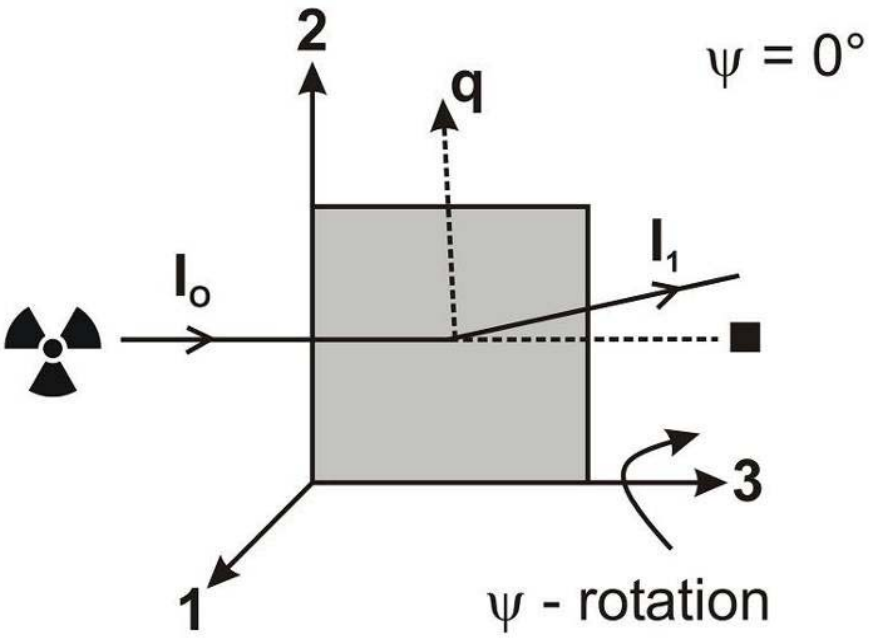


**Figure 5.44: Schematic diagram showing the orientation of the diffraction vector as a function of ψ-tilt. For ψ=0° the scattering vector is along 2 direction while for ψ=90° it is along 1 direction.**

would correspond to changes in lattice microstrains with respect to this reference state. Volume average lattice strain analyses are carried out in all three phases of the composite in transmission mode.

Figure 5.26 shows the typical energy dispersive diffraction spectra obtained from the studied composite material at a diffraction angle 7 °. Figure 5.45 shows the stress-strain plot of the actual single domain sample compressed along the freezing direction. The open circles in the plot correspond to the halt points for in-situ diffraction analysis. The serrations in this plot are due to relaxation (plastic deformation of the metallic alloy, localised damage within the ceramic or interfacial delamination) operative at an externally applied load and before or during the diffraction measurement. The initial curved shape of the plot at small applied loads can be attributed to the deviation of the sample geometry from perfect parallelism and friction between the specimen and the punches. Figure 5.30 has already shown that when compressed along the freezing direction, individual domains show ceramic controlled behavior, displaying high strength with limited or no plasticity.

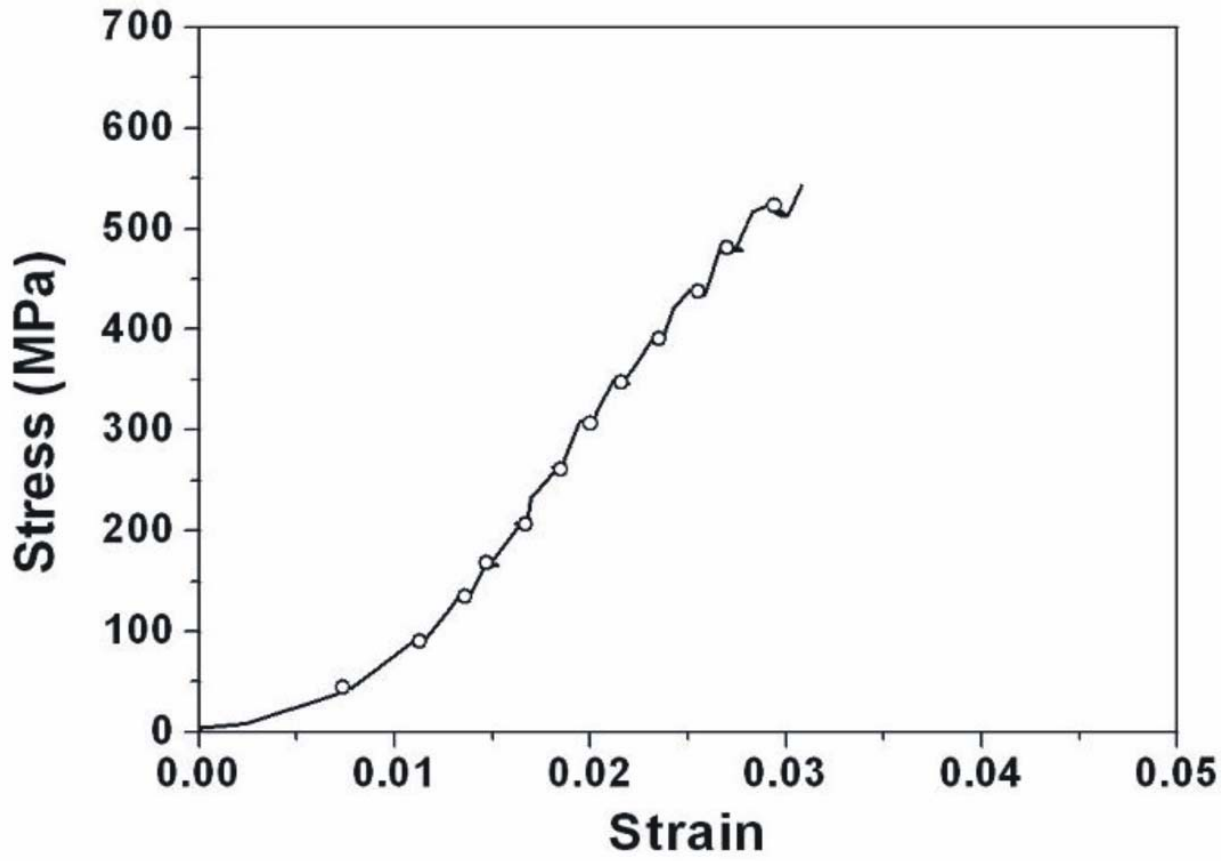


**Figure 5.45: Stress-strain plot of the single domain sample compressed along the freezing direction. Black circles correspond to the points for in-situ analysis**

It is possible to calculate the von Mises equivalent stress by measuring two principal stress differences experimentally and then computing the third principal stress difference there from [230]. In the present study, for a single sample at any particular applied load only one deviatoric stress component $(\sigma_1-\sigma_2)$ could be measured. To measure a second component a different sample loaded to the same applied stresses must be studied. This was not feasible because each sample is structurally different from the other and hence the stress state in different samples is not comparable. Representative plots of lattice spacing $d$ (in $10^{-10}$ m) vs. $sin^2\psi$ for the principal stress difference $(\sigma_1-\sigma_2)$ are shown in Figure 5.46. {311} family of planes of aluminum, {113} family of planes of alumina and {111} family of planes of silicon are shown as

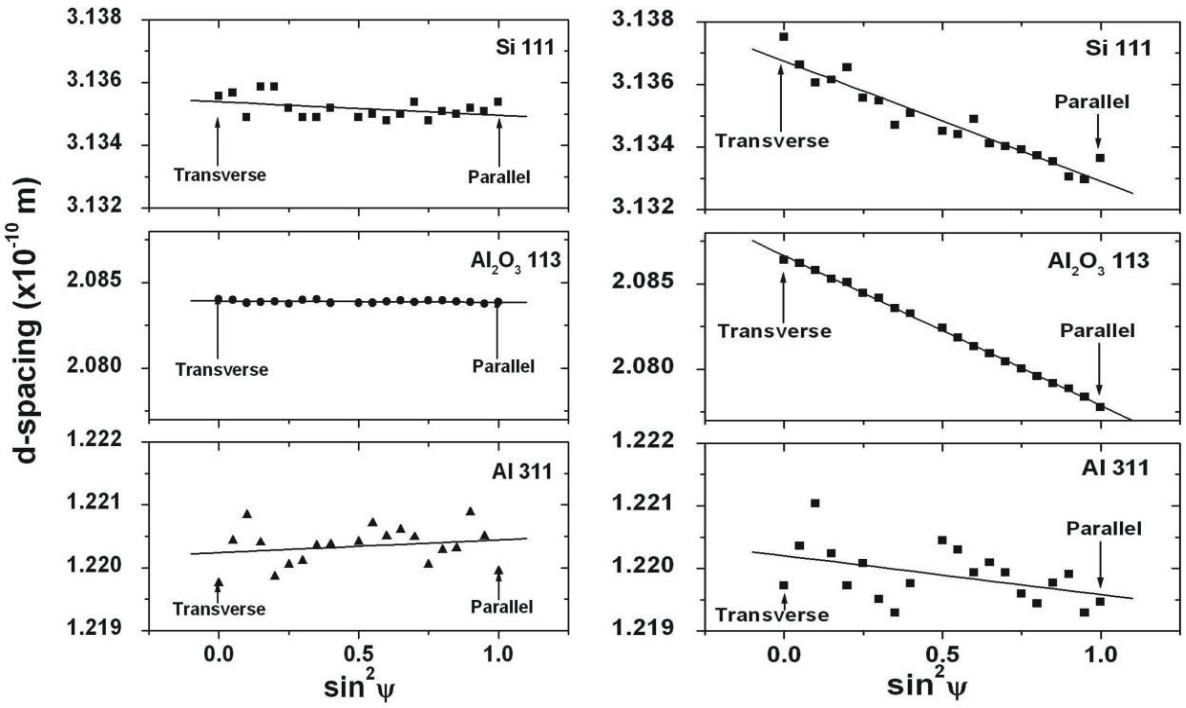


**Figure 5.46: Plots of lattice spacing vs. $sin^2\psi$ for the deviatoric stress component ($\sigma_1$-$\sigma_2$). Representative plots for {111} family of planes of Al, {113} family of planes of alumina and {111} family of planes of Si are shown. (a) at external applied stress 4 MPa and (b) at external applied stress 517 MPa.**

their lattice plane spacings are wide apart; so that they can be plotted in the same figure for visualisation purpose. Figure 5.46a shows the plot when only the initial pre-load was applied while Figure 5.46b corresponds to the maximum stress reached during compression test. Each $d$ vs. $sin^2\psi$ plot was fitted with a straight line and the intersection of this straight line with $\psi$=0 ° and $\psi$=90 ° yielded the lattice spacings of the diffracting planes when the scattering vector was orthogonal and parallel to the direction of load application, respectively. Arrows are shown in the figure at these two extreme $\psi$-tilts. This ensured that the lattice spacings used for strain calculation were much more reliable due to a better statistics, rather than using the experimentally measured lattice spacings at these two extreme $\psi$-tilts. Furthermore the shapes of the $d$ vs. $sin^2\psi$ plots indicate the effect of elastic or plastic anisotropy on the measurement results. Scatter in the results for aluminum is substantially large in comparison to silicon and alumina, which can be clearly attributed to preferred orientation (large grain size/texture effect). Figure 5.47 shows the change in lattice microstrain measured along the loading direction in all three phases of the composite, calculated using Equation (3.19) at different externally applied compressive stresses. The continuum mechanics average lattice microstrain

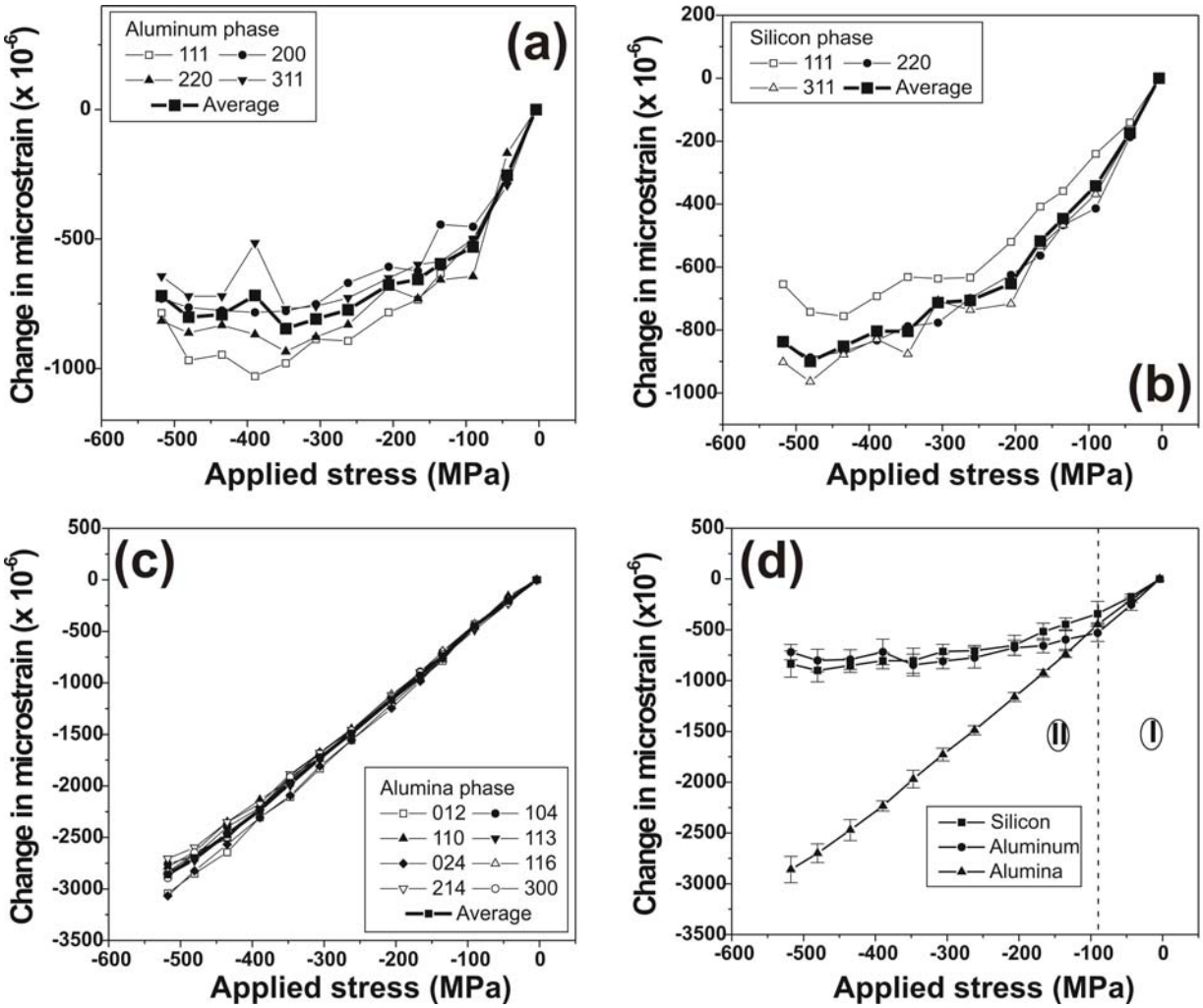


**Figure 5.47: Change in lattice microstrain plotted against applied stress for individual phases of the composite when the measurement direction is parallel to the loading direction (= freezing direction); (a) Al, (b) Si, (c) $Al_2O_3$ and (d) combined plot showing the evolution of continuum mechanics average microstrains for all three phases**

calculated according to the method proposed by Daymond [229](Equation (5.9-5.10) in subchapter 5.4) is also plotted for each phase (marked by the thick line in "*a-c*"). This is calculated using the multiplicity factors and the Young's moduli of each diffracting plane. Considering the interplanar anisotropy, this average strain is more representative of the material behavior in comparison to the information gained from a single diffracting plane. Texture analysis in different phases is yet to be carried out and the phases have been assumed to be texture free as a first approximation. In the plot of Figure 5.47*d* the calculated average lattice microstrain is plotted against the applied compressive stress for all three phases. Error bars in this diagram correspond to the standard deviation of lattice strains for individual diffracting planes and hence it is a measure of the interplanar anisotropy present within each phase.

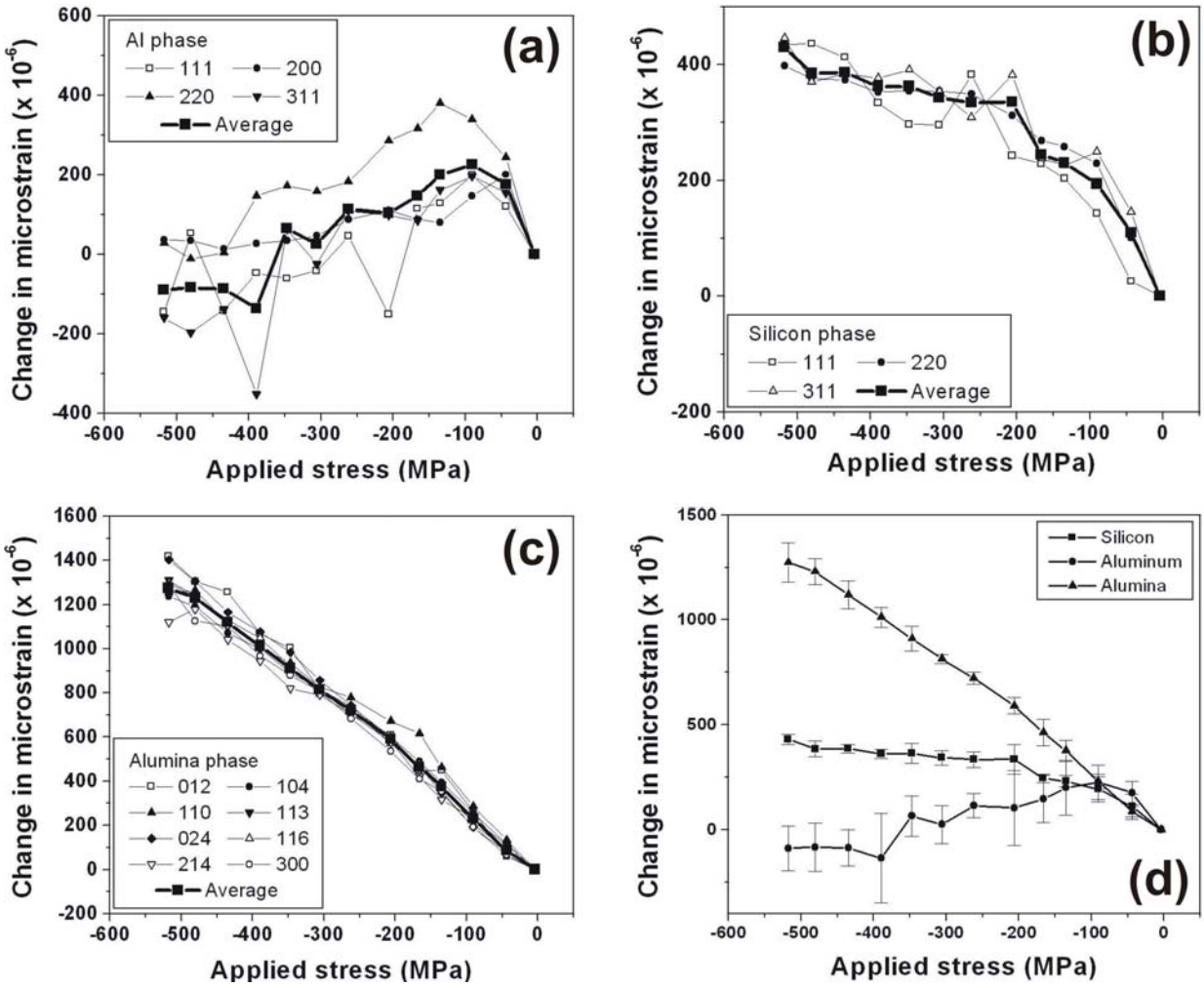


**Figure 5.48: Change in lattice microstrain plotted against applied stress for individual phases of the composite when the measurement direction is perpendicular to the loading direction (= freezing direction); (a) Al, (b) Si, (c) $Al_2O_3$ and (d) combined plot showing the evolution of continuum mechanics average microstrains for all three phases**

Figure 5.48 shows the lattice strain variations when the measurement direction is orthogonal to the direction of load application (measurement direction along 2 axis and loading direction along 1 axis in Figure 5.44). In this orientation the development of lattice microstrains in the alumina phase is tensile as expected. Strain evolution in the aluminum phase is complicated. Microstrain in the aluminum phase is initially tensile until about 100 MPa applied stress. At higher applied stresses it moves into the compressive regime.

The apparent E-modulus (defined as the ratio of the applied stress and the average lattice

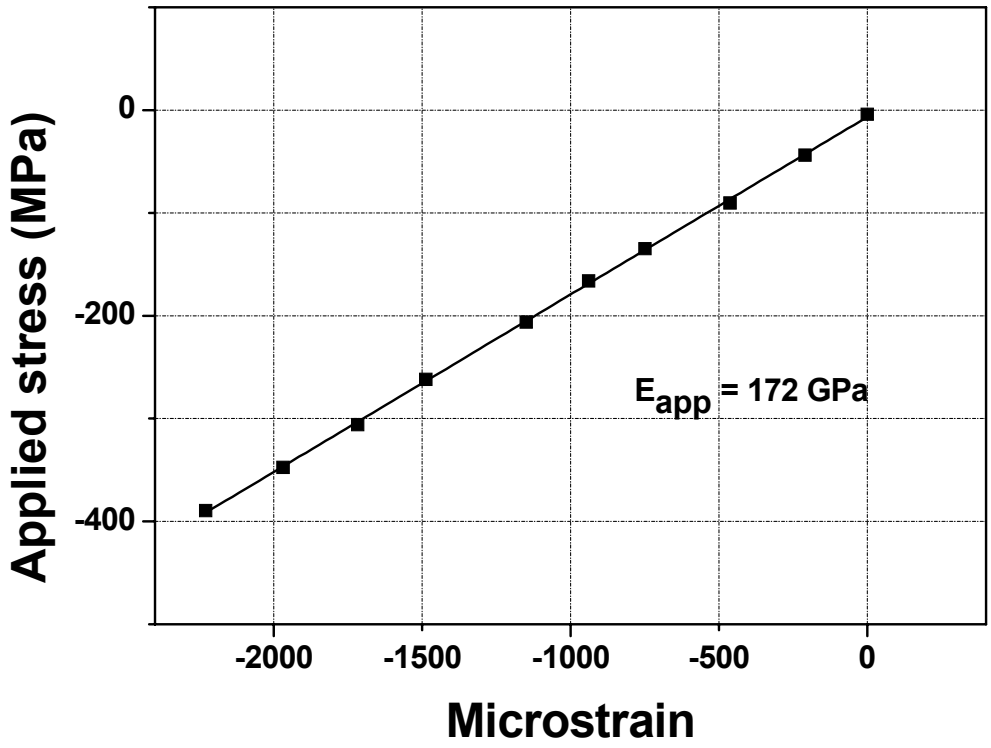


**Figure 5.49: Apparent E-modulus of alumina along the loading direction. Loading direction is parallel to freezing direction**

microstrain measured in the direction of the applied stress [231]) for the alumina phase along the loading direction is calculated from Figure 5.47d for an applied stress upto about 390 MPa. This is equal to the slope of the best fit straight line of applied stress vs. microstrain plot. Figure 5.49 shows that the resulting apparent E-modulus for alumina is approximately 170 GPa, less than half of that of the E-modulus of pure alumina ($E_{alumina}$ = 390 GPa). This drop of the apparent E-modulus of alumina is due to the load transfer taking place from the soft and compliant metallic alloy during externally applied compressive load.

So far, the evolution of lattice microstrain as a function of applied compressive stress has been discussed. However, it is not trivial to directly convert the measured lattice microstrain parallel to loading direction $\varepsilon_1$ to stress along the same direction $\sigma_1$, because although the applied stress is uni-axial, detailed data analysis showed that the actual stress state within the composite studied here is tri-axial. To compute $\sigma_1$, the generalized expression for $sin^2\psi$ method (Equation (2.17)) was used as the starting point. The azimuthal angle $\phi$ was zero for the present experiment. Presence of shear stresses $\sigma_{12}$ and $\sigma_{23}$ cannot be determined only by means of measurements carried out at positive $\psi$ tilts. However, the linear shapes of the $d$ vs. $sin^2\psi$ plots for alumina and silicon in Figure 5.46b clearly show that the distribution can be well fitted with a straight line over the whole $sin^2\psi$ range. As already mentioned, the scatter in

the results for aluminum is due to a poor grain statistics. The linear trend of the *d* vs. $sin^2\psi$ plots clearly indicates that even at very large applied stresses there is no evidence for the occurrence of shear stress components. Hence, shear stress components were neglected for further evaluation ($\sigma_{ij}=0$ *for* $i\neq j$). For the sample co-ordinate system showed in Figure 5.44, the 3 and 1 directions in the original expression (Equation (2.17)) have to be interchanged. With these changes, the governing equation for the calculation of stress along the loading direction ($\sigma_1$) becomes:

$$\frac{d_{\phi\psi}^{hkl}-d_{\phi\psi,0}^{hkl}}{d_{\phi\psi,0}^{hkl}}=\frac{1}{2}S_2^{hkl}\cdot\left(\sigma_1-\sigma_2\right)\sin^2\psi+\frac{1}{2}S_2^{hkl}\sigma_2+S_1^{hkl}\left(\sigma_1+\sigma_2+\sigma_3\right) \qquad (5.12)$$

where $\left(\frac{1}{2}s_2^{hkl}\right)$ and $s_1^{hkl}$ are diffraction elastic constants, which were calculated using the Young's moduli and Poisson's ratios of each indexed diffracting plane {hkl}. Young's moduli and Poisson's ratios of individual diffracting planes were taken from Ref. [232]. Values of the stress free lattice spacing $d_0^{hkl}$ were unknown. However, for alumina, the *d vs.* $sin^2\psi$ for various applied loads passed through or adjacent to one point. According to Ref. [147], the *d-spacing* corresponding to this point may be taken as the strain independent *d-spacing*. This was done by visual observation and was used in place of $d_0^{hkl}$ in Equation (5.9) as the strain independent *d-spacing* for alumina. Figure 5.50 shows the plot for the calculation of strain independent lattice plane spacing for the {024} family of planes of alumina. However, unlike alumina, the d vs. $\sin^2\psi$ distribution for aluminum showed a large scatter because of poor grain statistics and possible texture. Moreover, aluminum undergoes plastic deformation at a quite early stage of deformation and subsequently, the straight line fits of *d vs.* $sin^2\psi$ for aluminum never converged at or near one single point. Hence, theoretical values of the strain independent direction $\psi^*$ were calculated using the relation [147]

$$\sin^2\psi^{*,hkl}=\frac{-2\cdot S_1^{hkl}}{\frac{1}{2}S_2^{hkl}} \qquad (5.13)$$

and *d-spacings* corresponding to this strain independent direction $d_\psi^{*,hkl}$ for each diffracting plane were calculated from the linear fits of the *d* vs. $sin^2\psi$ plots. For each line, $d_\psi^{*,hkl}$ was calculated this way for each applied load and their average was used in place of $d_{\phi\psi,0}^{hkl}$ in

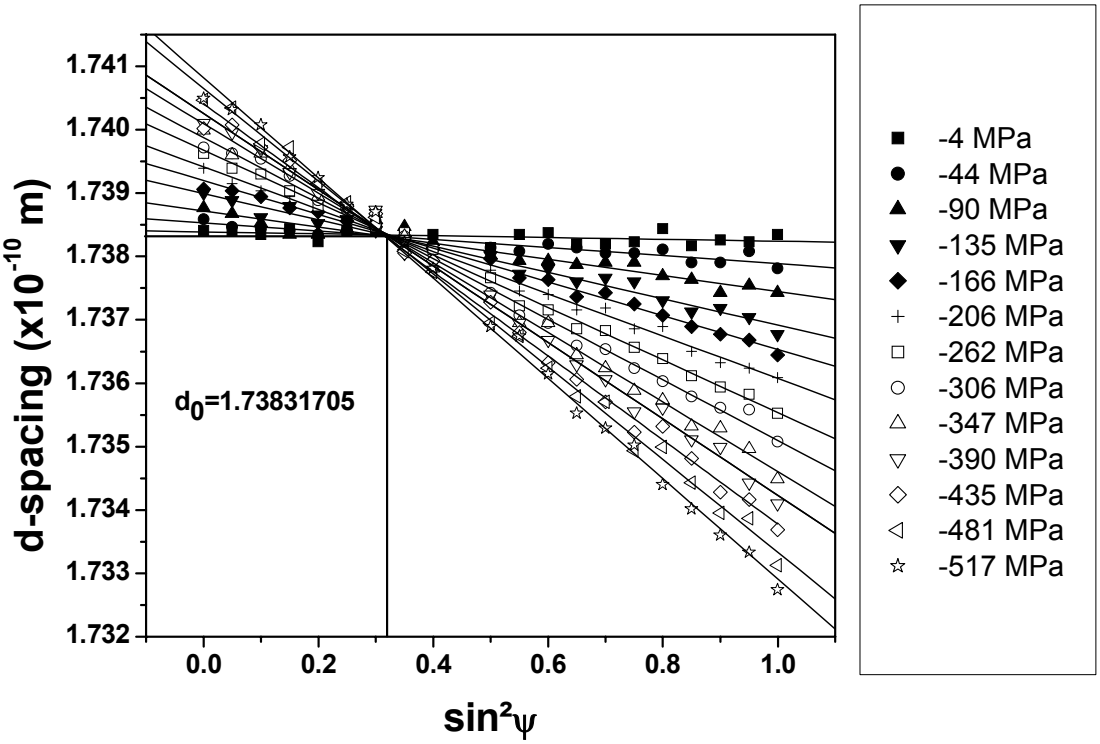


**Figure 5.50: Plot to determine the strain independent lattice plane spacing of {024} family of planes of alumina**

Equation (5.12) for aluminum. Equation (5.12) denotes the expression for a straight line, having

$$\text{slope} = \frac{1}{2} S_2^{hkl} \cdot \left( \sigma_1^{hkl} - \sigma_2^{hkl} \right)$$

and intercept $= \frac{1}{2} S_2^{hkl} \sigma_2 + S_1^{hkl} \left( \sigma_1 + \sigma_2 + \sigma_3 \right)$

The slopes and intercepts of the resulting linear fits and the measured deviatoric stress components were further used to develop a relation between $\sigma_2$ and $\sigma_3$ for each diffracting plane and at each applied load. This expression had the general form:

$$\begin{aligned} \left(1 - \nu_{hkl}\right) \cdot \sigma_2 - \nu_{hkl} \cdot \sigma_3 = E_{hkl} \cdot \left( \frac{1}{2} S_2^{hkl} \sigma_2 + S_1^{hkl} \left( \sigma_1 + \sigma_2 + \sigma_3 \right) \right) \\ + \nu_{hkl} \cdot \frac{1}{2} S_2^{hkl} \cdot \left( \sigma_1 - \sigma_2 \right) \end{aligned} \tag{5.14}$$

where $\nu_{hkl}$ and $E_{hkl}$ are the diffraction elastic constants of the individual {hkl} family of planes. The expression for generalised Hooke's law can be written as [139]:

$$\varepsilon_1 = \frac{\sigma_1}{E} - \frac{\nu}{E}(\sigma_2 + \sigma_3) \tag{5.15}$$

where $\nu$ is the Poisson's ratio. As the single domain sample had almost 0° domain orientation with 2 direction and the compressive load was applied along 1 direction, according to the classical laminate theory the stress component $\sigma_3$ can be assumed to be zero [12] as a first approximation. Moreover, in Figure 5.47 and Figure 5.48 changes in lattice microstrain with respect to the state with only applied preload were plotted. Using the microstrains calculated based on strain independent lattice spacings discussed above, the modified form of Equation (5.15) can be written as:

$$\sigma_1 = E \cdot \varepsilon_1 + \nu \cdot \sigma_2 . \tag{5.16}$$

Equation (5.16) was used to determine the stress component along loading direction in alumina and aluminum phases at each applied load and for each diffracting plane. Average stresses in each phase along the loading direction were calculated according to the method

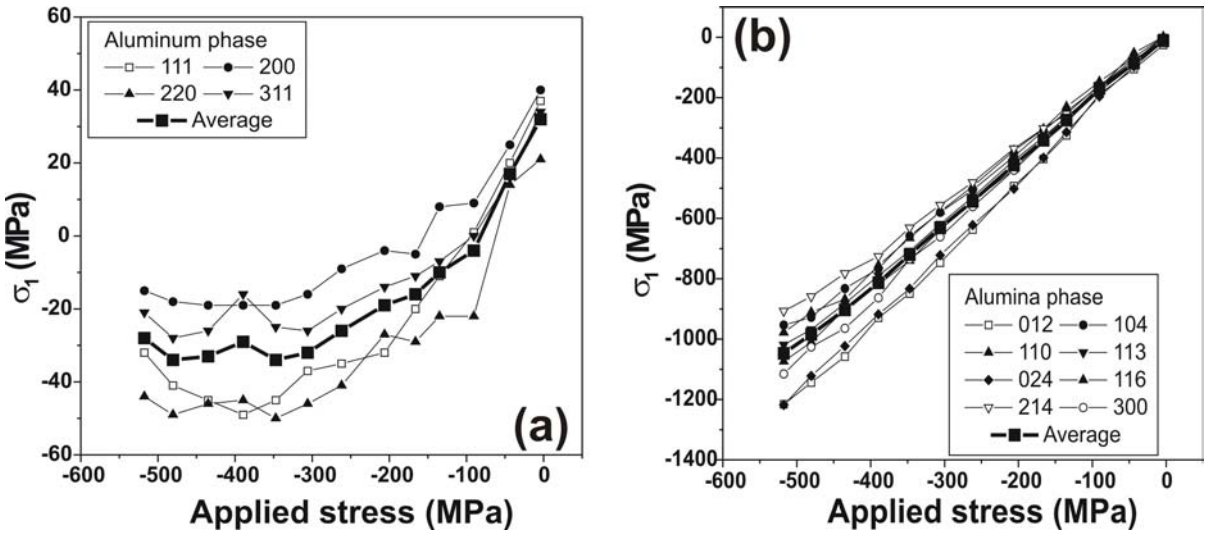


**Figure 5.51: Development of $\sigma_1$ as a function of externally applied stress in individual planes of (a) aluminum and (b) alumina. Bold lines show the average of all the planes.**

followed to calculate the average lattice microstrain. Figure 5.51 shows the development of $\sigma_1$ as a function of applied stress in individual planes of aluminum and alumina while Figure 5.52 shows the average phase specific $\sigma_1$ in aluminum and alumina, plotted against externally applied stress. The trend shown in Figure 5.51 is essentially similar with that shown in Figure 5.47. It is observed from Figure 5.52 that because of stress partitioning, throughout alumina carries most of the load while the stresses in the aluminum phase is only marginal.

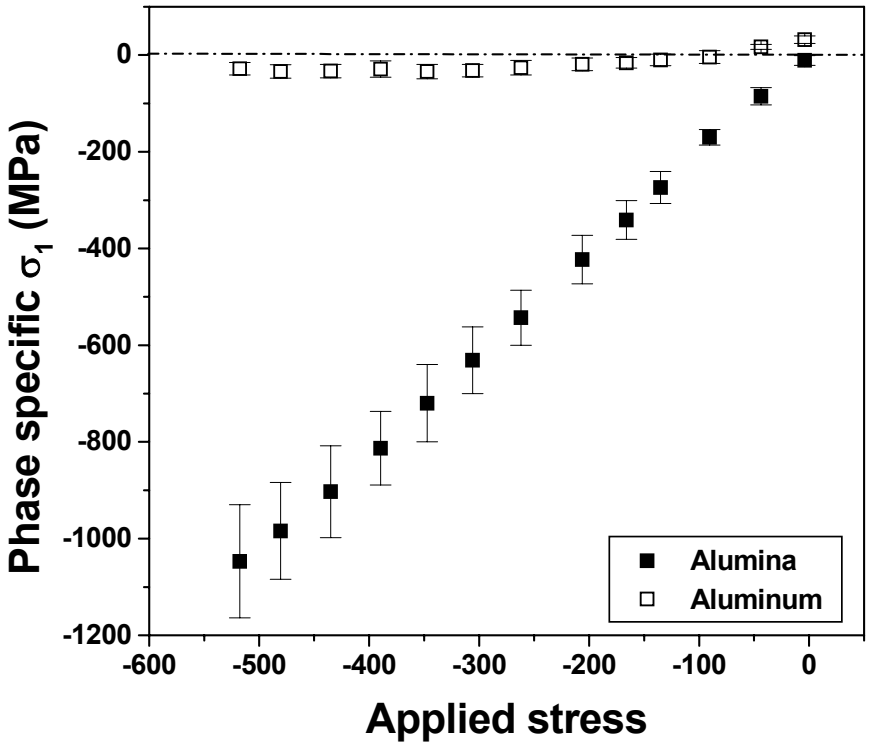


**Figure 5.52: Stress partitioning in aluminum and alumina phases along the loading direction when external compressive load is applied along the freezing direction**

Theoretical prediction of the stress along the loading direction in the alumina phase for different externally applied stresses on the composite was calculated following iso-strain model (Equation (2.11)). For this calculation the alumina content in the composite is taken as 42 vol%, similar to the sample studied in this work. Experimental compressive stress-strain results of Al-12Si were used for aluminum while the stresses for alumina were calculated assuming ideal elastic behavior and using 390 GPa as its Young's modulus. The straight line in Figure 5.53 shows the predicted values of the stress component $\sigma_1$ in the alumina phase for different stress values in the composite along the same direction. Absolute values of the stresses are plotted in this figure. The data points correspond to stress in the alumina phase calculated in this study at different externally applied stress. Figure 5.53 clearly shows that until about 400 MPa applied stress the calculated $\sigma_1$ in the alumina phase fits perfectly to the predictions of the iso-strain model.

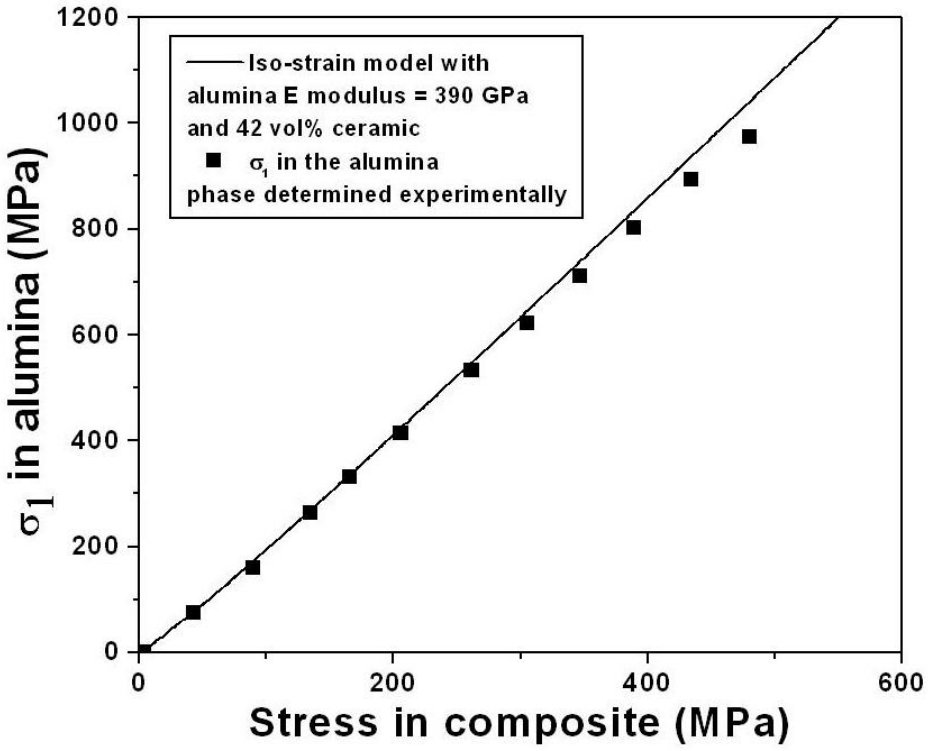


**Figure 5.53: Correlation of the calculated stress along the loading direction in the alumina phase with the stress in alumina phase predicted by iso-strain model**

Load fraction in each phase can be calculated according to the relation given in Ref. [209]:

$$l_f = \frac{\sigma_{1,phase} \cdot V_f}{\sigma_{appl}} \tag{5.17}$$

where $l_f$ is the load fraction, $V_f$ is the volume fraction, $\sigma_{appl}$ is the applied stress and $\sigma_{1,phase}$ is the calculated value of $\sigma_1$ in each phase. Ceramic content in the sample was calculated from the measured mass and dimensions and using the rule of mixtures assuming no porosity in the sample. It was found to be 42 vol%. Minor effect of the silicon phase was neglected and hence, vol% aluminum was taken as 58%. Figure 5.52 shows that at zero applied stress there is marginal tensile residual stress within the metallic phase while the residual stress within the alumina is marginally compressive. For the calculation of load fractions in alumina and aluminum phases, the phase specific stresses in both phases, $\sigma_{1,phase}$, for each externally applied stress were normalised by this initial phase specific residual stresses. The resulting load fractions in each phase thus predict the load partitioning taking place only during the compression test. Figure 5.54 shows the calculated load fraction in the alumina and aluminum phases at different applied stresses. In this figure the macroscopic elastic and the plastic deformation

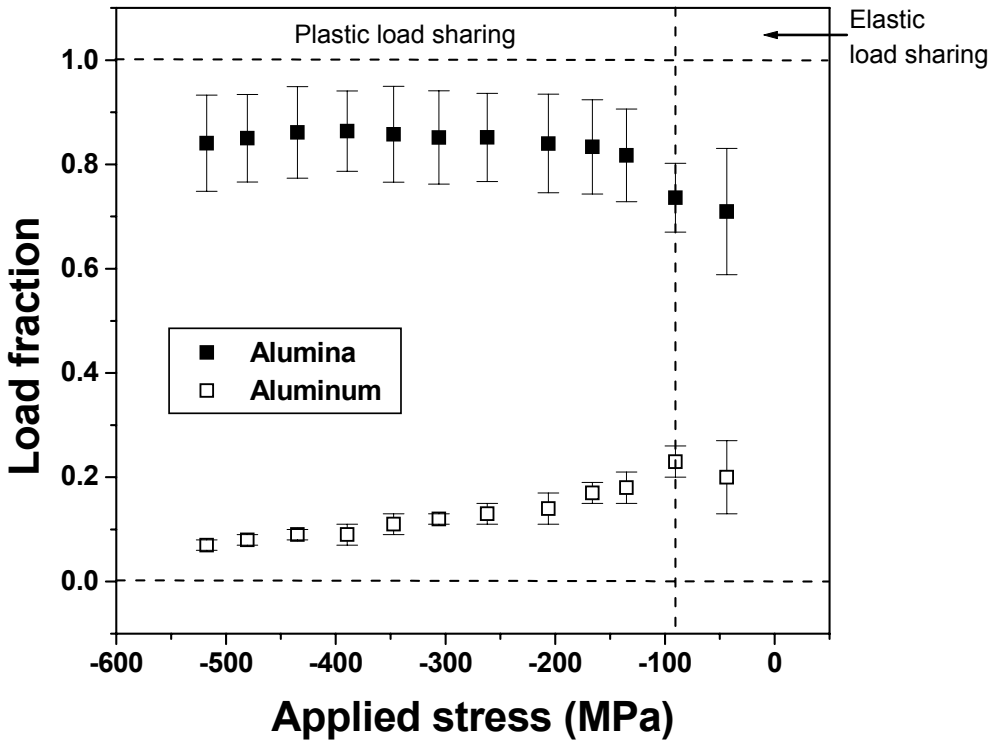


**Figure 5.54: Load fraction vs. applied stress plot for alumina and aluminum phases when loaded along the freezing direction**

regions are separated by the vertical dotted line at an externally applied stress of about 90 MPa. This corresponds to the boundary between regions I and II in Figure 5.47d. The two dotted horizontal lines bound the region between no load sharing (at 0.0) and complete load sharing (at 1.0), respectively. Error bars in the figure correspond to interplanar anisotropy. Figure 5.54 clearly shows that at all applied stresses the alumina phase carries most of the load. In the macroscopic elastic regime the load fraction in each phase simultaneously increases with increasing applied stress. Just after transition to the macroscopic plastic regime the load fraction in the alumina phase displays a strong jump and simultaneously the fraction of load in the aluminum phase decreases. Afterwards, at higher applied stresses the load fraction within the alumina phase remains at this plateau value while the load fraction in the metallic phase progressively decreases towards zero.

### 5.6.2 Study of internal load transfer when loaded at 0 ° to the lamella orientation

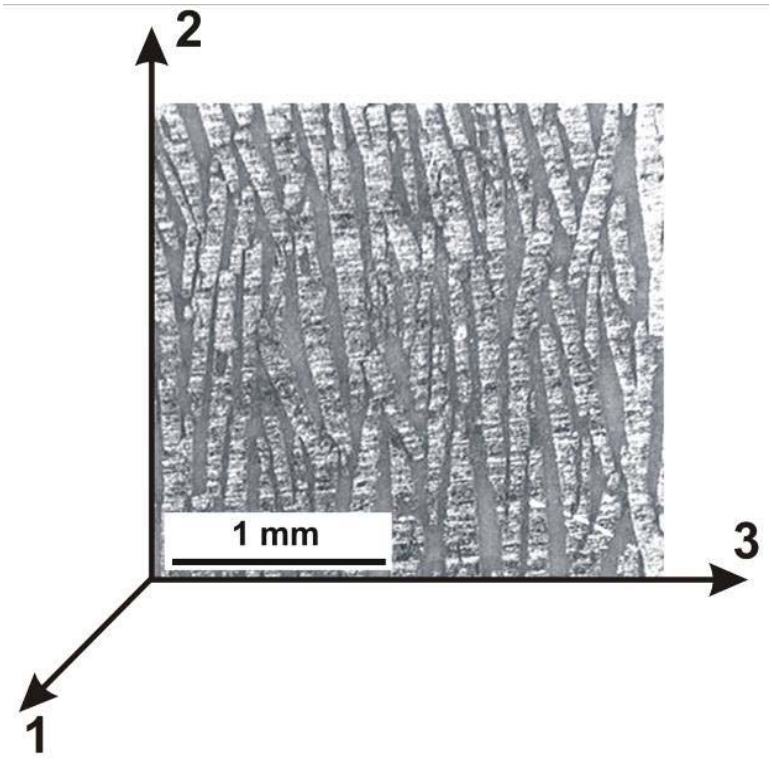


**Figure 5.55: Microstructure of the sample with about 0 ° domain orientation with the 2 direction. The microstructure corresponds to the face perpendicular to the freezing direction**

Figure 5.55 shows the microstructure of the face perpendicular to the freezing direction for the studied sample. The sample had about 0 ° domain orientation with the 2 direction. As has already been mentioned, direction 1 corresponds to the freezing direction. Compressive load was applied along the 2 direction. The loading geometry was such that the incoming beam was parallel to the 3 direction. For $\Psi=0$ ° the scattering vector was almost parallel to the 1 direction while for $\Psi=90$ ° the scattering vector was almost parallel to the 2 direction (1 and 2 directions exchanged in Figure 5.44). Figure 5.56 shows the in-situ stress-strain plot of the single domain sample. Likewise the sample loaded along the freezing direction, the circles on the plot correspond to the points where the test was stopped for data acquisition. The measurement principle as well as the data analysis steps was identical to that already described in subchapter 5.6.1. In Figure 5.57, the change in lattice microstrain along the loading direction is plotted against the externally applied stress. Evolution of lattice microstrain at various applied stresses in all three phases shows trend similar to that observed in Figure 5.47. Until

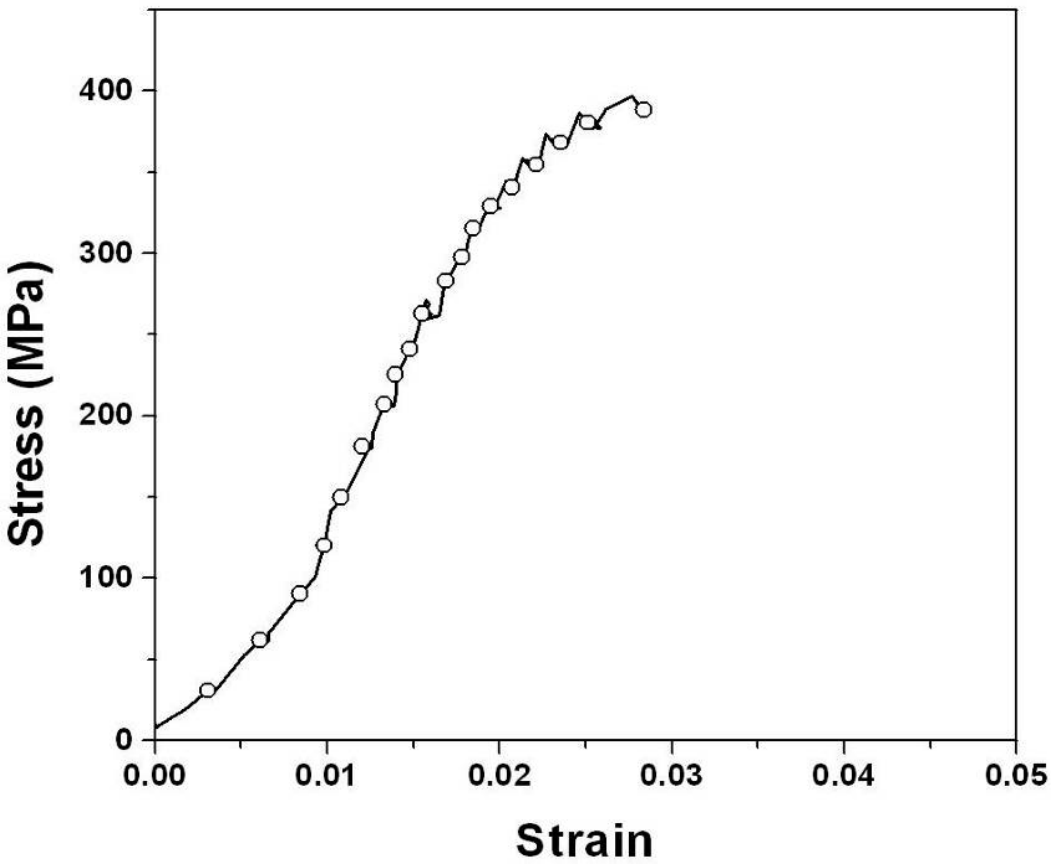


**Figure 5.56: Stress-strain plot of the single domain sample compressed along 0 ° to the domain orientation. Black circles correspond to the points for in-situ analysis**

about 100 MPa applied stress, the lattice microstrains in all three phases increase simultaneously with applied stress; however at higher stresses the lattice microstrain plots of silicon and aluminum reach a plateau while the lattice microstrain in alumina keeps on increasing almost linearly. Figure 5.58 shows the change in lattice microstrain in the individual phases when the measurement direction is orthogonal to the loading direction. Similar to the trend shown in Figure 5.48, the lattice microstrain in the alumina phase is tensile while in aluminum it is initially tensile and then moves into the compressive region because of the constriction posed by the stiff alumina ceramic and the strong interfacial bond between the ceramic and the metallic lamellae. The apparent E-modulus of alumina along the loading direction was calculated for an applied load until 250 MPa. This apparent modulus is taken as equal to the slope of the best fit straight line when applied stress is plotted against lattice microstrains in the alumina phase along the loading direction. Figure 5.59 shows the corresponding plot. It shows that the individual data points can be fitted extremely well with a straight line, suggesting that alumina behaves in a linear elastic way. The apparent E-modulus is about 170 GPa, which is

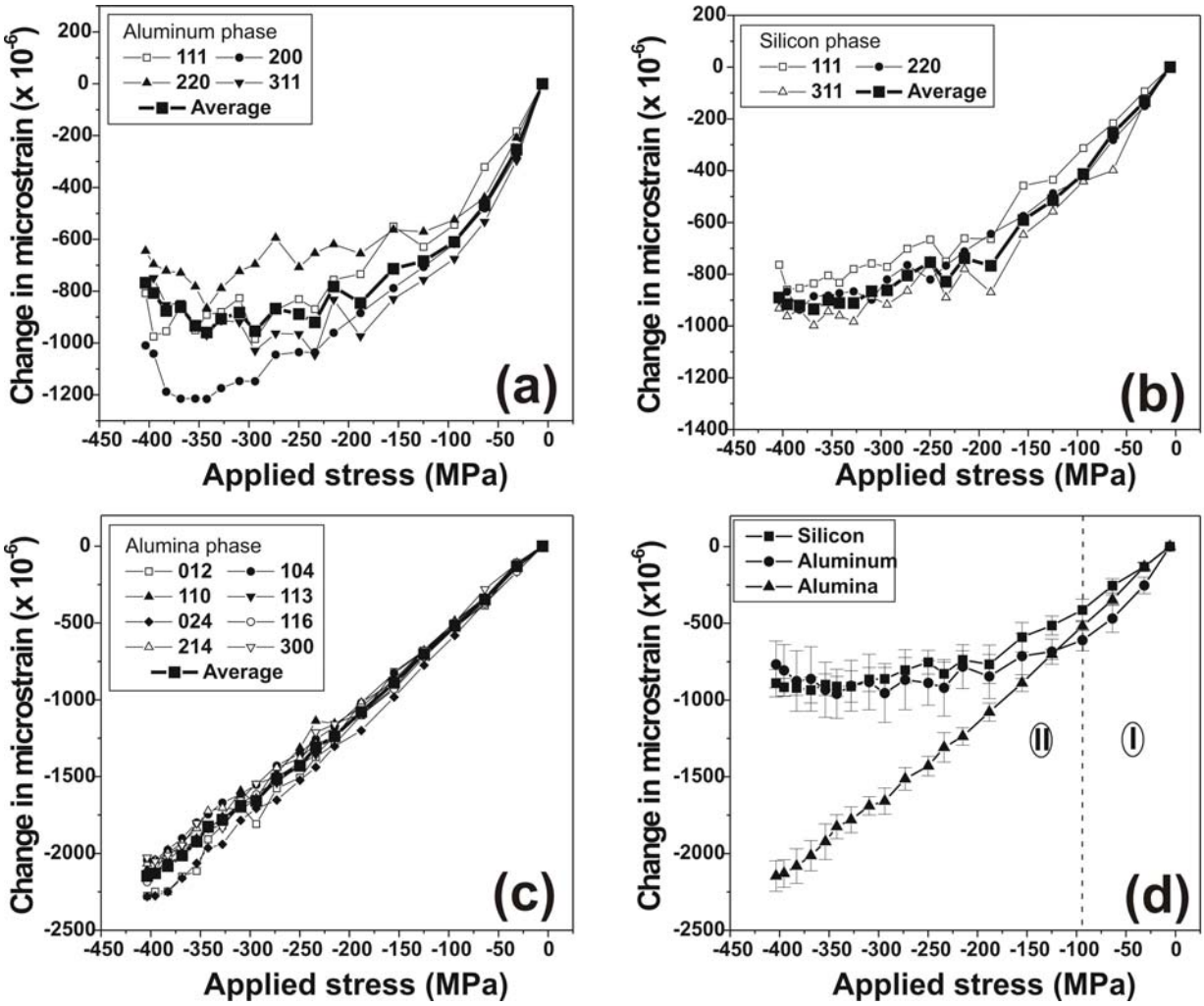


**Figure 5.57: Change in lattice microstrain plotted against applied stress for individual phases of the composite when the measurement direction is parallel to the loading direction (= along 0 ° to domain orientation); (a) Al, (b) Si, (c) $Al_2O_3$ and (d) combined plot showing the evolution of continuum mechanics average microstrains for all three phases**

almost same as that for the single domain sample loaded along the freezing direction. Stresses in the aluminum and alumina phases were calculated from the measured lattice microstrains following the same methodology as discussed in subchapter 5.6.1. The starting point is once again the general expression for *sin²psi* stress analysis, Equation (2.17). Because of the geometry of the present experience, the co-ordinate system of the expression changes in the following way: direction 3 becomes direction 1, direction 1 becomes direction 2 and direction 2 becomes direction 3, respectively. Further, neglecting shear stresses (because of the reason already discussed in subchapter 5.6.1) and for zero azimuthal angle $\phi$, modified form of the expression for stress analysis becomes:

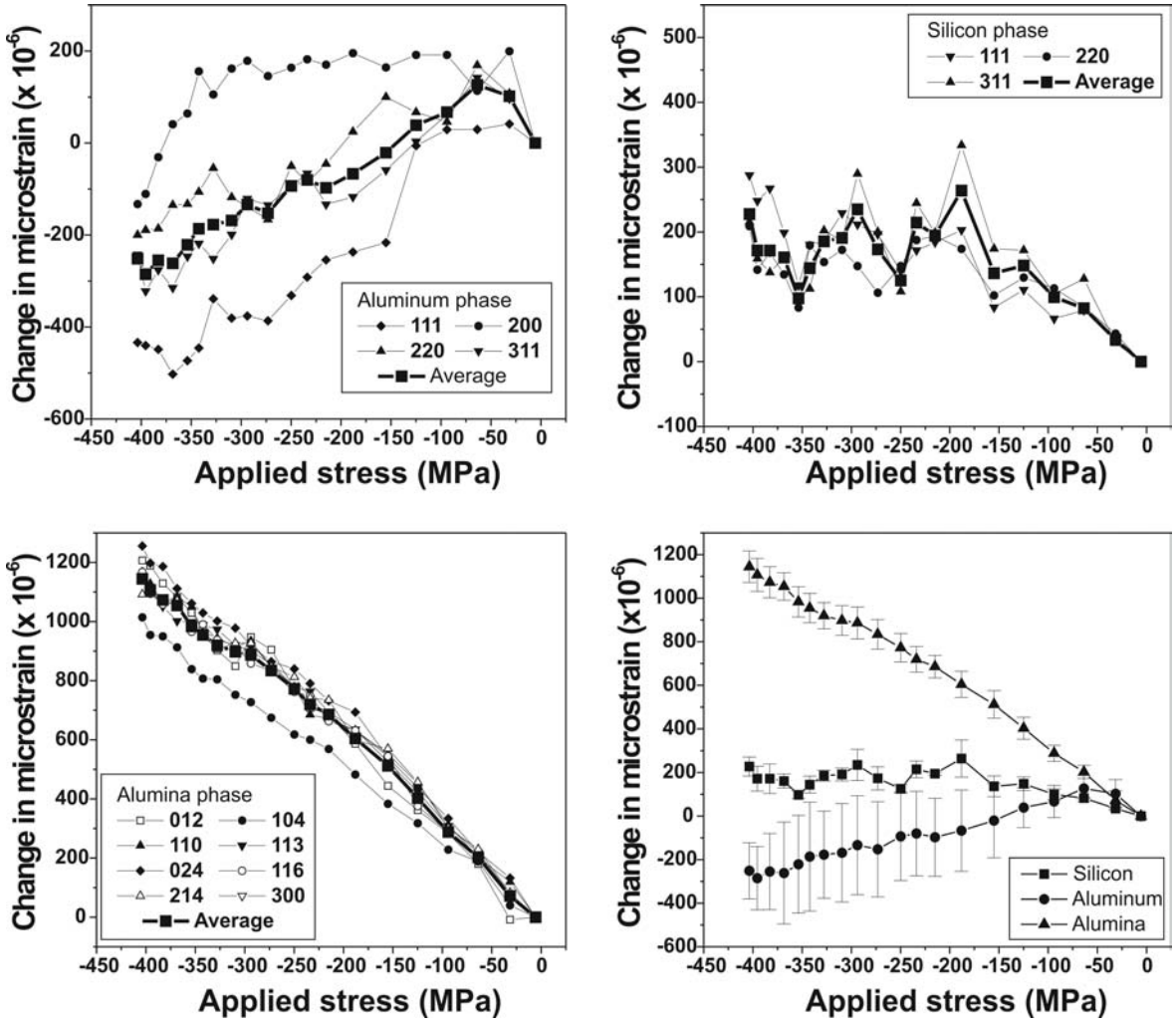


**Figure 5.58: Change in lattice microstrain plotted against applied stress for individual phases of the composite when the measurement direction is transverse to the loading direction (= along 0 ° to domain orientation); (a) Al, (b) Si, (c) $Al_2O_3$ and (d) combined plot showing the evolution of continuum mechanics average microstrains for all three phases**

$$\frac{d_{\phi\psi}^{hkl} - d_0^{hkl}}{d_0^{hkl}} = \frac{1}{2} S_2 \left(\sigma_2 - \sigma_1\right) \cdot \sin^2 \psi + \frac{1}{2} S_2 \sigma_1 + S_1 \left(\sigma_1 + \sigma_2 + \sigma_3\right). \qquad (5.18)$$

Equation (5.18) denotes a straight line with

$$\text{slope} = \frac{1}{2} S_2 \left(\sigma_2 - \sigma_1\right)$$

and intercept $= \frac{1}{2} S_2 \sigma_1 + S_1 \left(\sigma_1 + \sigma_2 + \sigma_3\right)$

Similar to the sample loaded along the freezing direction, it was observed that for alumina the linear fits to the *d vs. sin²psi* plots converged to or near to one point. The *d-spacing* corresponding to this point was taken as $d_0^{hkl}$. However, because of the very early onset of plastic deformation within the aluminum phase, the linear fits never converged and hence the average

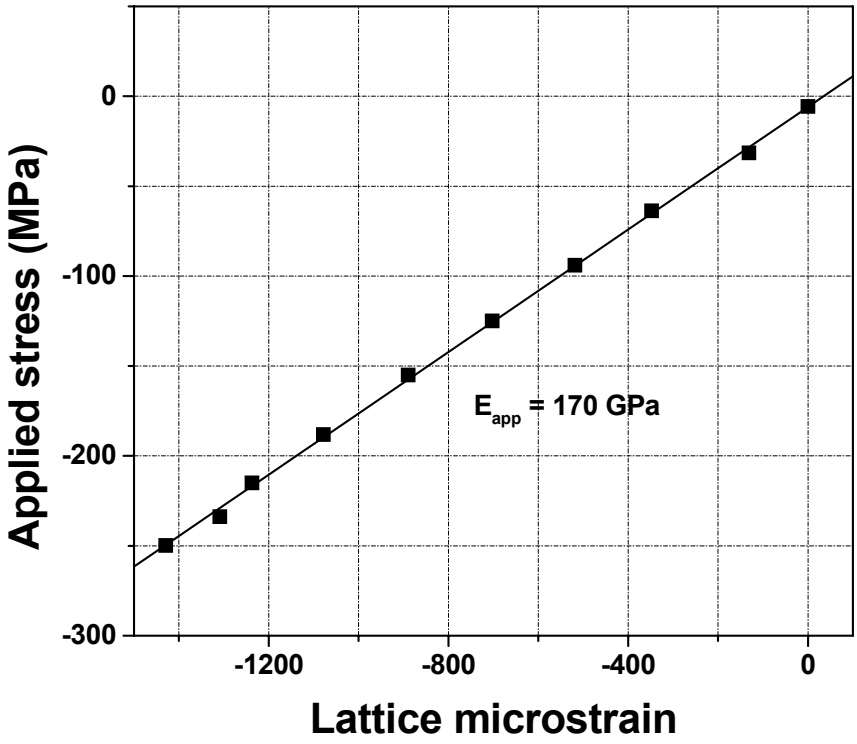


**Figure 5.59: Apparent E-modulus of alumina along the loading direction. Loading direction is at approximately 0 ° to domain orientation**

*d-spacing* corresponding to the theoretical strain independent direction, given in Equation (5.13) was chosen as $d_0^{hkl}$. The slopes and intercepts of the resulting linear fits and the measured deviatoric stress components were further used to develop a relation between $\sigma_1$ and $\sigma_3$ for each diffracting plane and at each applied load. This expression had the general form:

$$\begin{aligned}\left(1-\nu_{hkl}\right)\cdot\sigma_1-\nu_{hkl}\cdot\sigma_3 = E_{hkl}\cdot\left(\frac{1}{2}S_2^{hkl}\sigma_2+S_1^{hkl}\left(\sigma_1+\sigma_2+\sigma_3\right)\right)\\ +\nu_{hkl}\cdot\frac{1}{2}S_2^{hkl}\cdot\left(\sigma_2-\sigma_1\right)\end{aligned} \tag{5.19}$$

As the single domain sample had about 0 ° orientation with the 2 direction, hence following ideal laminate theory it was assumed that the stresses along the 3 direction is negligible. Fur-

ther using the generalized form of Hooke's law, the expression for the stress along the loading direction (direction 2 in this case) becomes:

$$\sigma_2 = E \cdot \varepsilon_2 + \nu \cdot \sigma_1 \tag{5.20}$$

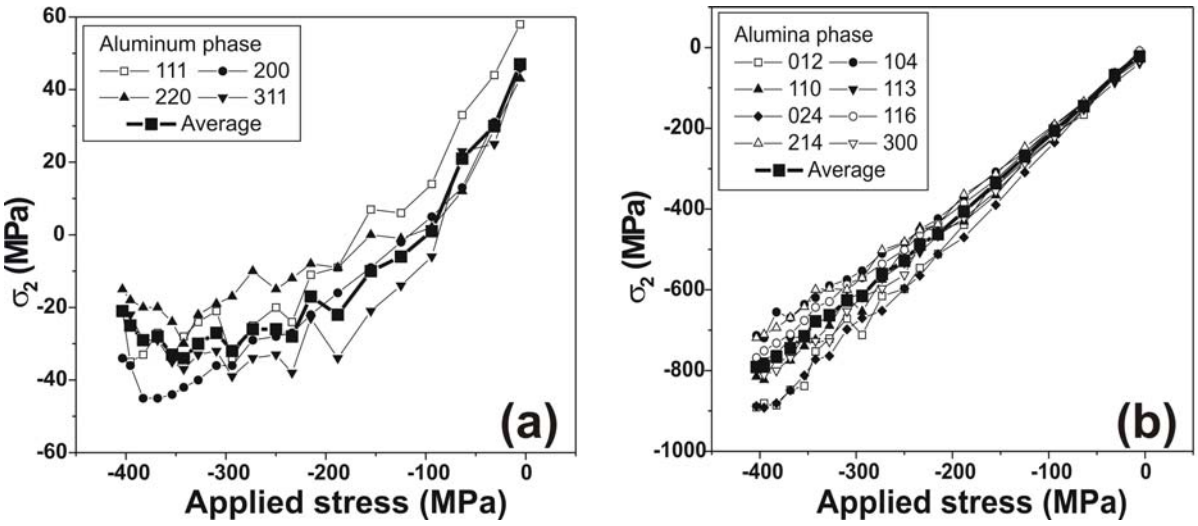


**Figure 5.60: Development of $\sigma_2$ in individual planes of (a) aluminum and (b) alumina as a function of externally applied stress applied along 0 ° to domain orientation. Bold lines show the average of all the planes.**

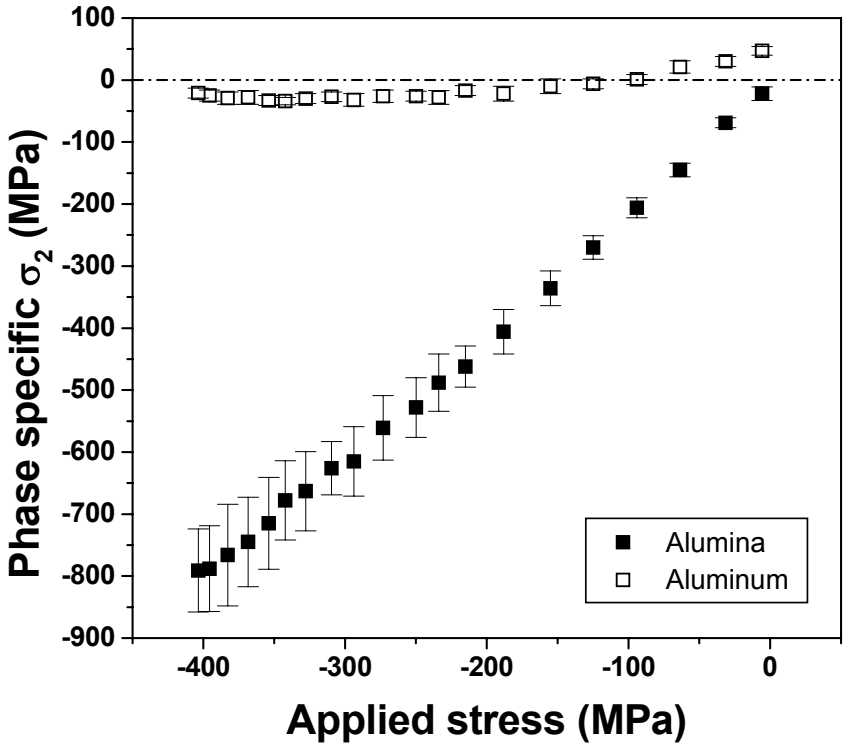


**Figure 5.61: Average $\sigma_2$ in aluminum and alumina phases along the loading direction when external compressive load is applied along 0 ° to the domain orientation**

Figure 5.60 and Figure 5.61 show the evolution of $\sigma_2$ in alumina and aluminum phases for different externally applied stresses. Initially, in the absence of any applied stress, the stresses are tensile in aluminum while they are compressive in the alumina phase. This is due to the thermal residual stresses resulting from the differential thermal expansion coefficients of alumina and aluminum. Figure 5.61 clearly shows that at all stresses alumina carries almost all the load, while the load carried by aluminum is only marginal. From the calculated stresses in the aluminum and the alumina phases along the freezing direction, the fraction of load carried by the two phases at different loads can be calculated in the same way as discussed for the single domain sample loaded along the freezing direction. Following the discussion in subchapter 5.6.1, the phase specific $\sigma_2$ at different externally applied stresses were normalized by the phase specific $\sigma_2$ in the absence of any externally applied stress. This way it is possible to plot the load partitioning taking place only when external load is applied. Volume fraction of

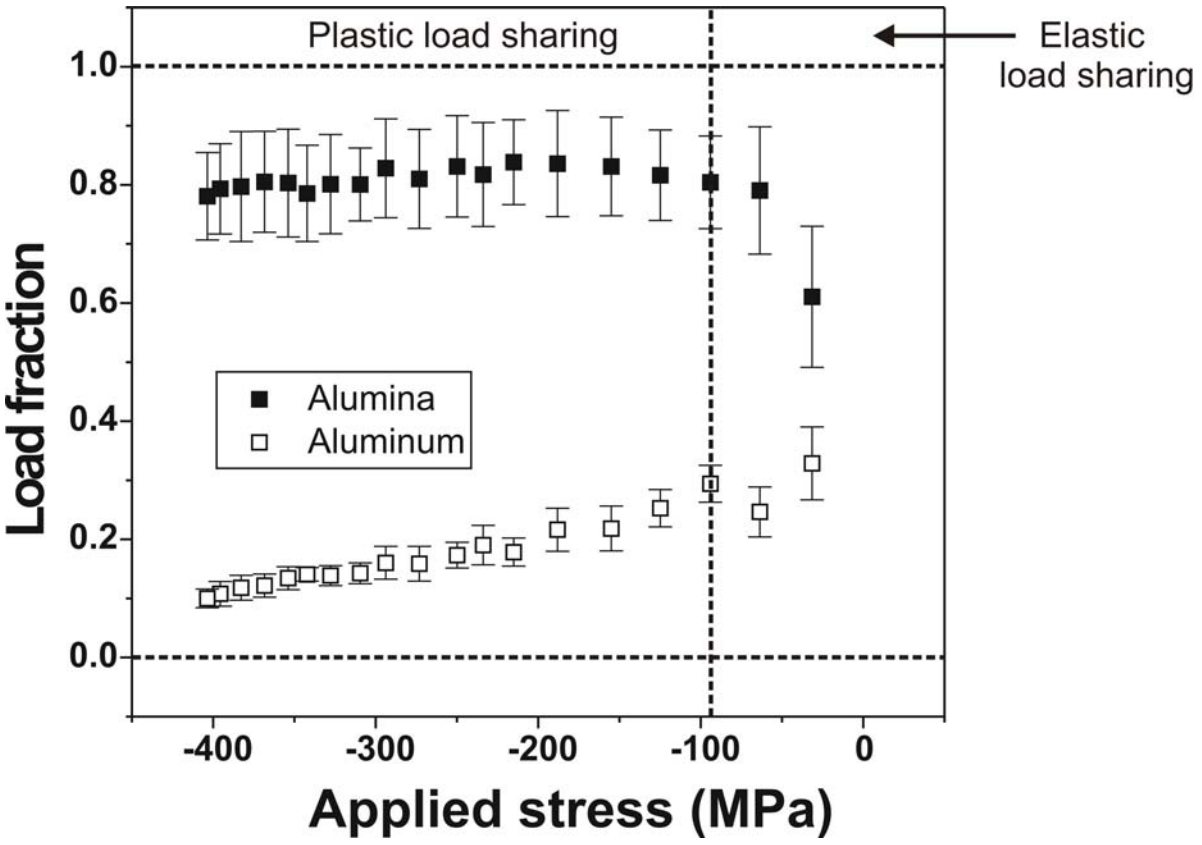


**Figure 5.62: Load fraction vs. applied stress plot for alumina and aluminum when compressed along 0 ° to the freezing direction**

alumina in the sample was calculated by measuring the mass and dimensions of the sample and assuming no porosity. This was found to be 41 vol %. Minor effects of silicon were neglected and hence the volume fraction of aluminum was taken as 59 vol%. Figure 5.62 shows the load fraction in alumina and aluminum phases at different applied compressive stresses. Likewise the sample loaded along the freezing direction, here too for all applied stresses bulk of the load is carried by the alumina phase.

# 6 Discussions

Mechanical properties of a novel metal/ceramic composite material have been studied in this work. At mesoscopic level the composite structure consists of regions (named as domains) within which there is parallel distribution of alternating ceramic and metallic lamellae. This domain like structure has striking similarity with lamellar two phase alloys discussed in sub-chapter 2.5. In these alloys the mechanical properties of the individual domains control their overall mechanical behavior. In the same light, the mechanical properties of the individual domains have been studied in this work to understand the mechanics of this novel composite. Apart from only the domain structure, effects of different processing parameters such as different preform freezing temperatures, modification of the interface between metallic and ceramic lamellae by coating of the preform prior to melt infiltration and use of different melt infiltration techniques (squeeze-casting and die-casting) have also been studied. Detail elastic analysis of poly-domain samples were carried out, while for single-domain samples, apart from the elastic analysis, study of elastic-plastic flow behavior and damage evolution under compressive load, analysis of processing induced thermal residual stress and strain distributions and internal load transfer under external compressive loading were carried out.

According to Mattern [8] and Deville et al. [42, 43], temperature has a strong influence on the structure of the freeze-cast preforms. For the same ceramic content in the starting suspension, a lower freezing temperature generates a higher freezing rate and consequently the extent of supercooling ahead of the solidification front increases, reducing the tip radius of the growing ice crystals and producing a finer microstructure. This is clearly discernible among the composite microstructures shown in Figure 5.1. The preforms for Composite Type A and Composite Type B were freeze-cast at -10 °C and -30 °C, respectively and so the lamella structure of Composite Type A is much coarser.

Coating the preform prior to melt infiltration modifies the interface between the metallic and the ceramic lamellae. In the absence of any coating, alumina forms strong interfacial bonds with alumina [100]. This is also observed in this work from the progressive damage evolution in single domain composite samples with uncoated preform, and compressed along the freezing direction. Figure 5.31 shows that longitudinal splitting is observed within the metallic lamellae, while apart from some localised delamination, the interface remains mostly unaffected. This suggests that the debonding shear stress is greater than the ultimate shear stress of

the metallic alloy. However, Figure 5.33 shows that in single domain composite samples with Cu coated preforms failure takes place by de-cohesion along the metal/ceramic interface. This suggests that coating the ceramic preforms with Cu or $Cu_2O$ weakens the inherently strong interface, hence reducing the interfacial shear strength. This also explains the reduced compressive strength along the freezing direction observed in Table 5.8 in single domain samples with coated preform in comparison to those with uncoated preform. Lankford [110], Dève [116] and McCullough et al. [233] have also shown that a weakening of the interface reduces the compressive strength of uni-directionally reinforced composites along the direction of the reinforcements. Moreover, Figure 5.12 and Figure 5.13 show that for the same density, the composites fabricated by infiltrating uncoated ceramic preforms generally exhibit higher wave velocity along the freezing direction (and correspondingly a higher $C_{11}$ value) in comparison to the composites whose preforms were coated prior to melt infiltration. In Figure 5.16 it is observed that in general the data points for $C_{11}$ with coated preforms lie well below the theoretical predictions for UD fiber reinforced composites. These follow directly from the weak interfacial bonding between alumina and Al-12Si. Apart from reducing the compressive strength along the freezing direction, a weak interfacial bond will also reduce the composite stiffness along this direction. Furthermore, the theoretical UD model assumes a perfect bonding between the matrix and the reinforcement.

Only preliminary study of the effect of die-casting on the elastic properties of the poly-domain composite samples of Composite Type A was carried out in this work. Table 5.2 and

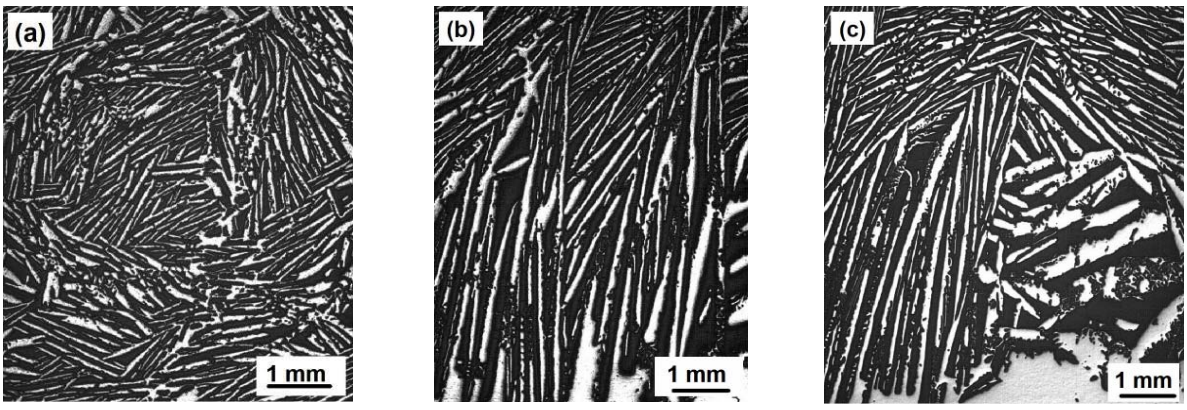


**Figure 6.1: Microstructures of the composite type whose preforms were infiltrated by pressure casting; (a) face perpendicular to 1 direction, (b) face perpendicular to 2 direction and (c) face perpendicular to 3 direction**

Figure 5.16 show that for the Composite Type A, whose preforms were infiltrated by die-casting, the data points for elastic constants along the freezing direction and the average of the elastic constants along the transverse direction superimpose on each other. This suggests that the elastic anisotropy inherent in the composites fabricated by squeeze-casting is no more present in the die-cast composites. Typical microstructures for the three faces of the composite fabricated by die-casting of the melt in freeze-cast preforms are shown in Figure 6.1. These micrographs show that lamellae on the faces parallel to the freezing direction are significantly tilted and fragmented in comparison to those composites whose preforms were infiltrated by squeeze-casting. This tilting and fragmentation would significantly reduce the stiffness along the freezing direction and this would explain the diminished elastic constant along this direction. However, the exact cause of this tilting of the lamellae is not yet known. It is highly unlikely that this was caused during die-casting of the liquid metallic alloy. All the 19 samples of this Composite Type studied in this work were cut from the same composite block and it is possible that the freeze-cast ceramic lamellae were already tilted and fragmented before the infiltration because of a casting defect. To substantiate this and to find out the exact reason behind this anomalous behavior, poly-domain samples cut from a different composite block must be studied.

Results obtained from the UPS of individual poly-domain samples (refer to appendix A.2) using longitudinal transducers show that the difference between the two transverse velocities ($V_2$ and $V_3$) is relatively higher for Composite Type A. This follows from the larger domain size in this composite type, as a result of which the individual samples do not cover representative volumes. The strong increasing correlation between $V_1$ and $C_{11}$ with density, as observed in Figure 5.12 and Figure 5.13 may probably be attributed to two non-distinguishable effects: both an increased ceramic content and a low porosity are expected to increase the density as well as the velocity. However, as shown in Figure 5.14 and Figure 5.15, no such correlation between longitudinal sound velocities and longitudinal elastic constants with sample densities is observed when sound velocities and elastic constants are measured transverse to the freezing direction (along directions 2 and 3). For intermediate ceramic content, the dependence of transverse velocity on the density should be inherently low (denoted by the dashed lines in Figure 5.16a-b). The enormous scatter observed in this study is probably due to the presence of closed cracks in the microstructure since such cracks do affect the stiffness and the wave velocity but have little effect on the density. An example of a closed crack is shown in Figure 6.2. This micrograph shows a single-domain sample of Composite Type A

exhibiting a large crack. Obviously such cracks exist but are rare enough to affect each sample in a different manner. Figure 5.16 shows that the experimentally measured average longitudinal and transverse elastic constants lie close to or within the bounds predicted by the UD fiber model (apart from the data point for transverse elastic constant in Composite Type B whose preforms were coated with Cu; which lies well below the theoretical estimation for $C_{22}$=$C_{33}$). The considerable stretch of the error bars for both longitudinal and transverse moduli below their theoretical estimations can be explained by the presence of pores in the ceramic reinforcement after sintering, which reduce their effective stiffness in comparison to the theoretical values. As Equation (2.1) shows, because of the much higher stiffness of the

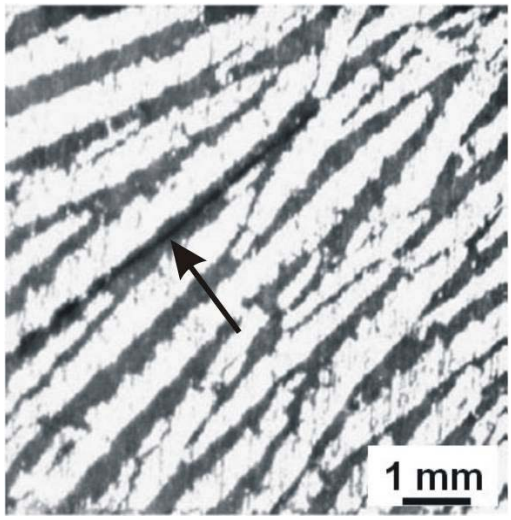


**Figure 6.2: Structure of the face perpendicular to the freezing direction for a single-domain sample of Composite Type A showing the presence of a closed crack**

ceramic with respect to the metallic alloy, stiffness of the composite along the freezing direction is mostly controlled by the stiffness and the volume content of ceramic. The kind of porosities and cracks already mentioned above may significantly reduce the stiffness of the ceramic in comparison to a defect free ceramic. These pores and cracks were not considered in the theoretical calculations and that explains the larger discrepancy between the observed average $C_{11}$ values and the theoretical estimations. Table 5.4 shows that the three average shear elastic constants in each composite type lie relatively close to each other. This follows directly from the layered structure of the material, as a consequence of which, provided the microstructure is large compared to the size of the individual domains, shear takes place with equal ease along all directions. Although a marginal effect, still this is even more prevalent in Composite Type B. This is probably because of its much finer domain structure. Moreover,

Table 5.3 shows that when many poly-domain samples within each composite type are considered, the two shear wave velocities which compose a shear elastic constant are also similar considering their standard deviation. This is a necessary condition for orthotropic or higher material symmetry. However, appendix A.2 shows that in individual poly-domain samples of both composite types the two shear wave velocities for a shear elastic constant mostly differ quite substantially. Following the discussion of Rose [173], this suggests that symmetry of the individual poly-domain samples may probably be better defined by monoclinic symmetry as there the equality of the two shear wave velocities is not implied. Using RUS it was possible to determine the complete stiffness matrix of one poly-domain sample of Composite Type B assuming orthotropic symmetry. This further enabled to determine the maximum and the minimum Young's moduli in this sample. Figure 5.24 shows that the range bounded by this maximum and minimum Young's moduli lie within the theoretical predictions.

Longitudinal elastic constants of the single domain samples with uncoated preform were determined by UPS. Figure 5.20 shows the effect of the ceramic content on $C_{11}$ of single-domain samples. The figure shows that apart from 5 data points, the rest of the experimentally measured values lie within an ellipse, whose principal axis is parallel to the theoretical predictions according to the Postma model discussed in subchapter 2.4.1.4. In general, although the scatter from sample to sample is significantly large, $C_{11}$ increases as the ceramic content increases. Moreover, the measured values lie close to or below the theoretical prediction, suggesting that the Postma model serves as a theoretical upper bound for elastic constants along the freezing direction. Large stretch of the experimental values below the theoretical prediction may be attributed to the presence of cracks and pores within the ceramic lamellae, whose effect have already been discussed. Effect of the domain orientation on the longitudinal elastic constants along 2 and 3 directions in single domain samples is shown in Figure 5.19. The bold line in this figure corresponds to the theoretical predictions according to Postma model when the Young's modulus of alumina is taken as 390 GPa. It shows that the predictions at small $\beta$ are significantly higher than the experimental observations, while the fit is much better at high $\beta$ values. A better match between theory and experiments over the whole range of $\beta$ is obtained assuming a value of 330 GPa for the Young's modulus of alumina, keeping all other parameters fixed. This validates the previously made assumption that the pores present within the ceramic region affect the elastic constant $C'_{22}$ (parallel to the composite layers) much more than $C'_{33}$ (perpendicular to the composite layers). Ziegler et al. [234] predicted the elastic behavior of single-domains by means of micrograph-based Finite Element Modeling

(FEM). They treated the material as a two-phase composite material containing homogeneous phases, i.e. the small Si precipitates in the Al-12Si alloy and the grain structures of both phases were not resolved. FE-meshes were generated from microstructural images of entire surfaces perpendicular to the freezing axis (1-axis). Then a material map was created from the image, in which each pixel was assigned to a material. Finally a first mesh or skeleton consisting of rectangular elements were generated on top of the image. For the calculation of the elastic properties of the composite, the mechanical properties of alumina and Al-12Si were used and the materials were taken to be isotropic and homogeneous. Results showed that the FE model based on the real microstructure gave better agreement with experimental values than the micromechanical models at all domain orientations. This is due to the fact that the irregular shape of the lamellae, which is well represented in the real microstructure mesh, is not considered in the micromechanical models. Micromechanical models assume an ideal structure devoid of any irregularity. At small $\beta$ angles the FE model predictions were very consistent with the experimentally measured elastic constants; however, at large $\beta$ the experimental results show a stiffer response than predicted by the FE model. Tilting of the ceramic lamellae with respect to the freezing direction, presence of ceramic bridges between the lamellae and cracks and pores within the lamellae and possible formation of bridges of silicon between the ceramic lamellae were identified as the probable causes behind the observed small mismatch between model predictions and experimental results. Average ceramic content of the samples shown in Figure 5.20 is 42 vol. % and average of the calculated $C_{11}$ is 232 GPa. This average value of $C_{11}$ is similar to the longitudinal elastic constant measured along 0 ° to domain orientation as shown in Figure 5.19, which lies in the range of 205-230 GPa.

Elastic-plastic flow behavior and mechanism of internal load transfer in single domain samples were studied under externally applied compressive load. The failure mechanism of the single-domains loaded along the freezing direction is complex. Several steps are involved depending upon the individual properties of the ceramic and the metallic alloy as well as the interface in between. Moreover, because of the heterogeneous structure of the ceramic preform and thus the final composite, the structural variation from sample to sample is enormous, resulting in enormous variation of the mechanical properties. Jensen [235] developed models for failure of layered or fiber reinforced materials under compression along the layer axis. For strongly bonded matrix and reinforcement, two primary failure modes were identified as fiber kinking or matrix splitting. Failure by matrix splitting is predominant in fiber reinforced ceramics because of the propagation of microcracks in the brittle, porous matrix. Spowart and

Dève [108] and Dève [116] have identified the different failure modes of continuous fiber reinforced MMCs loaded under compression along the fiber direction. Fiber kinking (in case of poor fiber alignment or high fiber strength) and fiber crushing (for well aligned fibres or low fiber strength) have been identified as the dominant modes. Failure by fiber kinking is a form of a localized shear failure within a region of misaligned fibers forming a kink band, which then propagates catastrophically causing the material to fail [115]. This was identified as the main mode of compressive failure in continuous alumina fiber reinforced Al MMCs [107, 116]. In the case of fiber crushing, as the matrix becomes increasingly plastic, the load bearing capacity of the fibers is exceeded at some point and they crush under the applied compressive load [108]. Spowart and Clyne [118] identified this mechanism as the mode of compressive failure in titanium reinforced with silicon carbide monofilaments. In the present study, detail failure analysis did not show any trace of ceramic kinking in the composite single-domains compressed along the freezing direction and as Figure 5.31 shows, ceramic crushing, due to the inherently low strength of the ceramic preforms after freeze-casting seems to be the dominant failure mode. The compressive yield strength of Al-12Si was additionally measured ex-situ on the sample shown in Figure 5.36 in a universal testing machine Zwick 1494, using a nominal strain rate $10^{-3}$ $s^{-1}$. Its 0.2 % yield strength was found to be 80 MPa. Evolution of lattice microstrain at different externally applied compressive stresses along the freezing direction (refer to Figure 5.47) shows that until about 90 MPa (region I), the lattice microstrains in all three phases increase almost linearly. This limit matches with the compressive yield strength of unreinforced Al-12Si, suggesting that until this point both the metallic and the ceramic phases are macroscopically elastic. At higher applied stresses, the microstrain vs. applied stress plots for the aluminum and silicon phases reach a plateau while the microstrain in the alumina phase keeps on increasing almost linearly. Figure 5.54 shows that at all applied stresses most of the load is carried by the alumina phase. Alumina has a Young's modulus (390 GPa) which is roughly 5 times higher than that of the metallic alloy (Al-12Si has a Young's modulus of 80 GPa). In the macroscopic elastic regime the fraction of load carried by the alumina phase is roughly 4-5 times higher than that carried by aluminum. Figure 5.47 shows that in the region corresponding to macroscopic elastic deformation (marked by region I) the changes in microstrain within the metallic and the ceramic phases are almost similar. Hence, the substantially higher fraction of load carried by alumina within this region is due to its much higher stiffness. At higher stresses, the load fraction in alumina reaches a plateau while the aluminum load fraction slowly tends towards zero. The metallic

component having much lower yield strength, starts deforming plastically and as a consequence it transfers the load to the ceramic component, which carries further load and this way the overall load carrying capacity of the composite increases manifold. This phenomenon has already been shown for particle [209] and short fiber reinforced MMCs [236, 237]. Load carried by the ceramic reinforcement is dependent upon the internal load transfer from the metallic alloy and the already mentioned relaxation mechanisms. In the absence of any damage or stress relaxation, once the lattice microstrain vs. applied stress plots of aluminum and silicon reach a plateau in region II of Figure 5.47d, the corresponding curve for alumina should show a change in slope. Its linear trend may be attributed to the competing effects of load transfer from the plastically deforming metallic alloy and the load relaxation due to localised damage within the ceramic lamellae and at the metal/ceramic interface, which might compensate each other. Figure 5.31 shows that this localised damage may start at a very early stage during compressive loading of the composite. Figure 5.53 further shows that only at very high stresses the calculated $\sigma_1$ values in the alumina phase show a downward deviation from the iso-strain model predictions. This is a further proof of localised damage development which would reduce the load carrying capacity of alumina. Assuming that a pore free composite fails if all fibers reach a single crushing strength $\sigma_f$ and that the metallic matrix behaves as elastic perfectly plastic solid (i.e. neglecting any work hardening), Spowart and Clyne [118] proposed a simple expression for the composite compressive strength $\sigma_c$ written as:

$$\sigma_c = V_f \cdot \sigma_f + \left(1 - V_f\right) \cdot \sigma_{YM} \tag{6.1}$$

In Equation (6.1) $\sigma_{YM}$ is the matrix yield strength and $V_f$ is the fiber volume fraction, respectively. Although, actual damage evolution in the composite under study along the freezing direction is quite heterogeneous and not all ceramic lamellae fail at the same time, Equation (6.1) has been used in this study to estimate crushing strength $\sigma_f$ of the ceramic lamellae. Ceramic content in each sample was determined from mass-dimension analysis. Since no porosity could be detected applying SEM, the porosity of the samples was assumed to be negligible. The estimated volume fraction was found to be between 43–44 vol.%. Using the measured compressive strength of each sample, the calculated ceramic crushing strength lies in the range of 1.26–1.69 GPa. Figure 5.53 shows that the compressive strength of alumina along the freezing direction determined from internal load transfer analysis is approximately 1050 MPa. The marginally reduced compressive strength of alumina along the freezing direction determined from the study of internal load transfer in comparison to the minimum of the

range of compressive stresses determined from the ex-situ analysis is due to the reduced compressive strength of the composite sample studied for internal load transfer analysis. This sample showed a compressive strength of 517 MPa, while the minimum compressive strength of the composite samples studied by ex-situ compression was 588 MPa.The large scatter in the compressive strength of the composite when compressed along the freezing direction (as shown in Figure 5.37) may either be due to the different domain orientations in different samples or due to the variation in the ceramic crushing strengths from sample to sample. Brockenbrough et al. [101] and Brockenbrough and Suresh [105] have shown that, when loaded along the fiber direction, the elastic-plastic flow behavior is controlled by the fibers and for the same fiber content they are insensitive to fiber distribution. This hypothesis should also be valid for single-domain samples having different domain orientations and considering that the ceramic contents in these samples are similar, this scatter is probably due to the scatter in the ceramic crushing strength, probably resulting from inherent defects in the freeze-cast ceramic preform. Bushby [95] has shown that the composite longitudinal tensile strength varies significantly depending on the distribution of flaws in the fiber bundle. The complicated evolution of microstrain within the aluminum phase at different externally applied compressive stresses along the direction transverse to the loading direction (refer to Figure 5.48) may be explained taking into consideration the presence of the stiff ceramic lamellae, the strong metal/ceramic interface and the Poisson's ratio mismatch between the metallic and the ceramic lamellae. The arrows in Figure 6.3 schematically show the directions of the tensile microstrains within the ceramic and the metallic phases when external compressive stresses are applied along the freezing direction (= direction 1 in the diagram). When both the metallic alloy and the ceramic are elastic, metallic alloy having a Poisson's ratio of about 0.3 and the ceramic having a Poisson's ratio of about 0.24, the tensile mismatch between them is less. Hence, they show almost similar behavior. However, as the metallic alloy starts deforming plastically, its Poisson's ratio increases to 0.5. This generates a large mismatch. The metallic lamellae try to expand much more than the ceramic lamellae, which always remain elastic. Because of the much higher stiffness of alumina, the ceramic lamellae effectively constrict the transverse tensile deformation of the metallic lamellae, which as a result of this mechanical interlocking are in effective compression. This is further assisted by the presence of a very strong interface between the metallic and the ceramic lamellae.

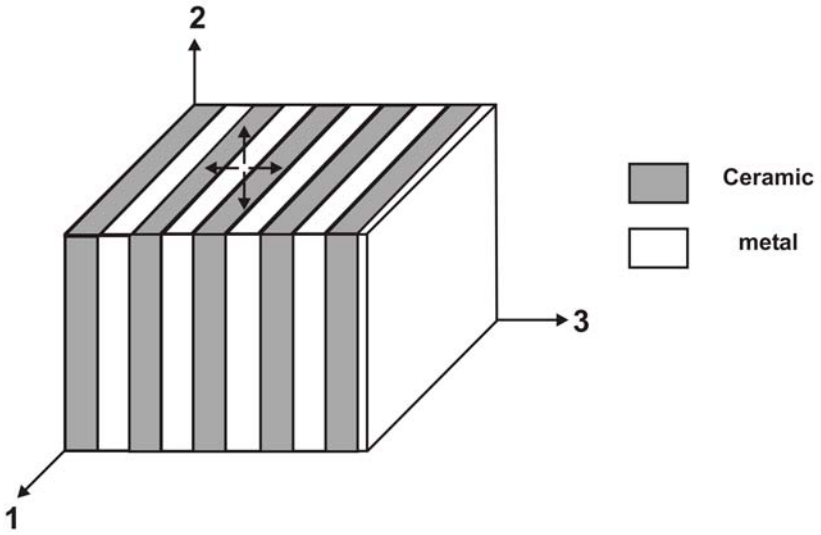


**Figure 6.3: Schematic diagram showing the directions of the transverse tensile strain within the ceramic and the metallic phases when compressed along the freezing direction (= direction 1 in the diagram)**

According to Spowart and Dève [108], the primary factors controlling the transverse compressive strength of fiber reinforced MMCs are the ceramic volume fraction and the distribution of the fibers relative to the loading direction. Effective strengthening requires the ceramic fibres to strongly interrupt the matrix shear bands. Depending on the direction of load application and assuming that the ceramic content is above a critical minimum value, the factor of strengthening lies between 1.15 and 3 with respect to the strength of the metallic alloy [108]. Figure 6.4 schematically shows the propagation of shear bands within the metallic lamellae in composites having idealised laminar structure with three different orientations with the loading direction. In the sample with an orientation of 0 °, the ceramic lamellae carry the load while the metallic alloy merely transfers the load to the ceramic lamellae by plastic deformation. Details about load transfer when loaded along 0 ° to domain orientation have been discussed in subchapter 5.6.2. Subchapters 5.6.1 and 5.6.2 show that in both the sample loaded along the freezing direction and in the sample loaded along 0 ° to domain orientation, the mechanism of internal load transfer under the influence of an externally applied stress is essentially similar and the compressive deformation behavior mostly follows the iso-strain behavior. At low stresses until about 90 MPa the composite behaves in a macroscopically elastic way and all three phases carry the load. At higher stresses the metallic alloy starts to deform plastically and it transfers the load to the ceramic lamellae, which carry further load. Figure 5.54 and Figure 5.62 show that in comparison to the sample loaded along the freezing direction, in the sample loaded along 0 ° to the domain orientation the fraction of load carried by the metallic phase is significantly higher, although both the samples had similar ceramic con-

tent. This can probably be attributed to the higher load carrying efficiency of the ceramic lamellae along the freezing direction. In samples with 45 ° and 90 ° domain orientations, when compressed along the direction shown by the arrows in Figure 6.4, shear within the metallic lamellae should take place along the ABCD and the EFGH planes because at an angle of 45° to the applied compressive load the shear stress in the metallic alloy is expected to be maximal. The dotted lines represent the shear bands within the metallic lamellae. However, in the sample with 90° orientation, shear in both of these planes is expected to be interrupted by the rigid ceramic lamellae. This results in effective strengthening. In the sample with 45° orientation, shear along ABCD will be obstructed while it can easily propagate along the EFGH

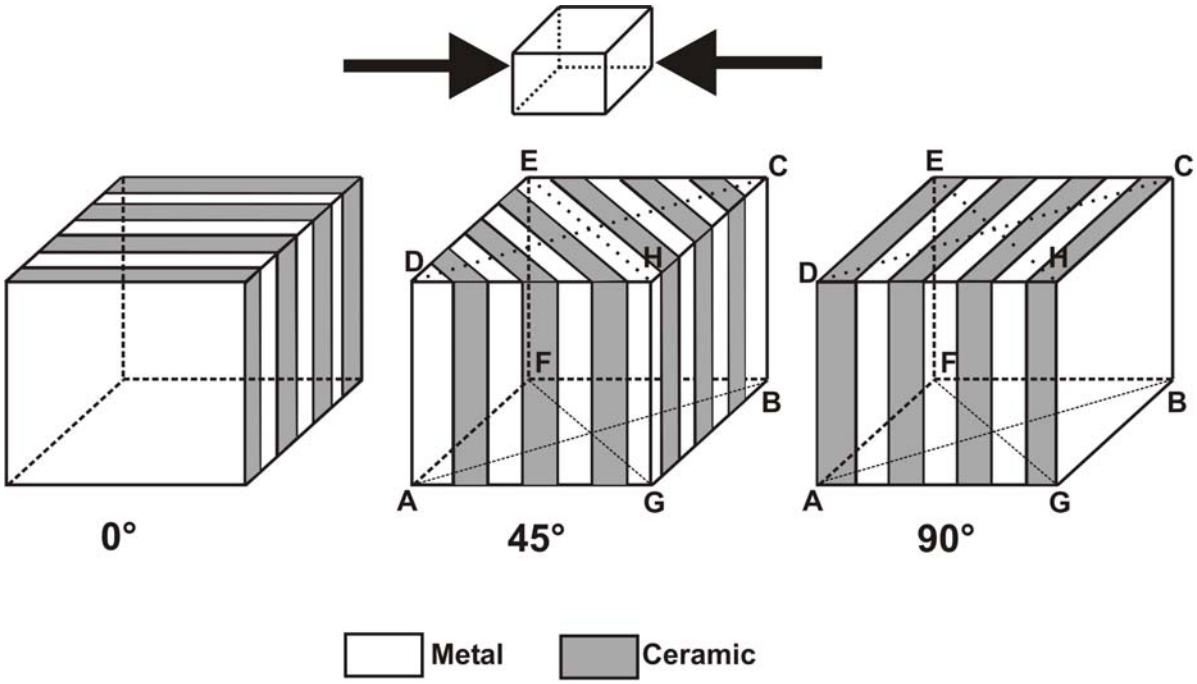


**Figure 6.4: Schematic representation of the shear-band propagation within the metallic lamellae in an idealised laminar metal/ceramic composite having α=45 ° domain orientation. Diagrams for laminates having β=0 ° and β=90 ° are shown for comparison.**

plane. Hence, in an ideal laminate structure the compressive strength at orientations along and close to 45° with the loading direction should be minimal. The influence of loading direction on the transverse compressive strength follows the Tsai-Hill criterion, written as:

$$\frac{1}{\sigma_{xx}^2} = \frac{\cos^4\beta}{X^2} + \left(\frac{1}{\tau_{LT}^2} - \frac{1}{X^2}\right)\sin^2\beta\cdot\cos^2\beta + \frac{\sin^4\beta}{Y^2} \qquad (6.2)$$

In Equation (6.2) $X$ is the compressive strength along 0 ° domain orientation, $Y$ is the

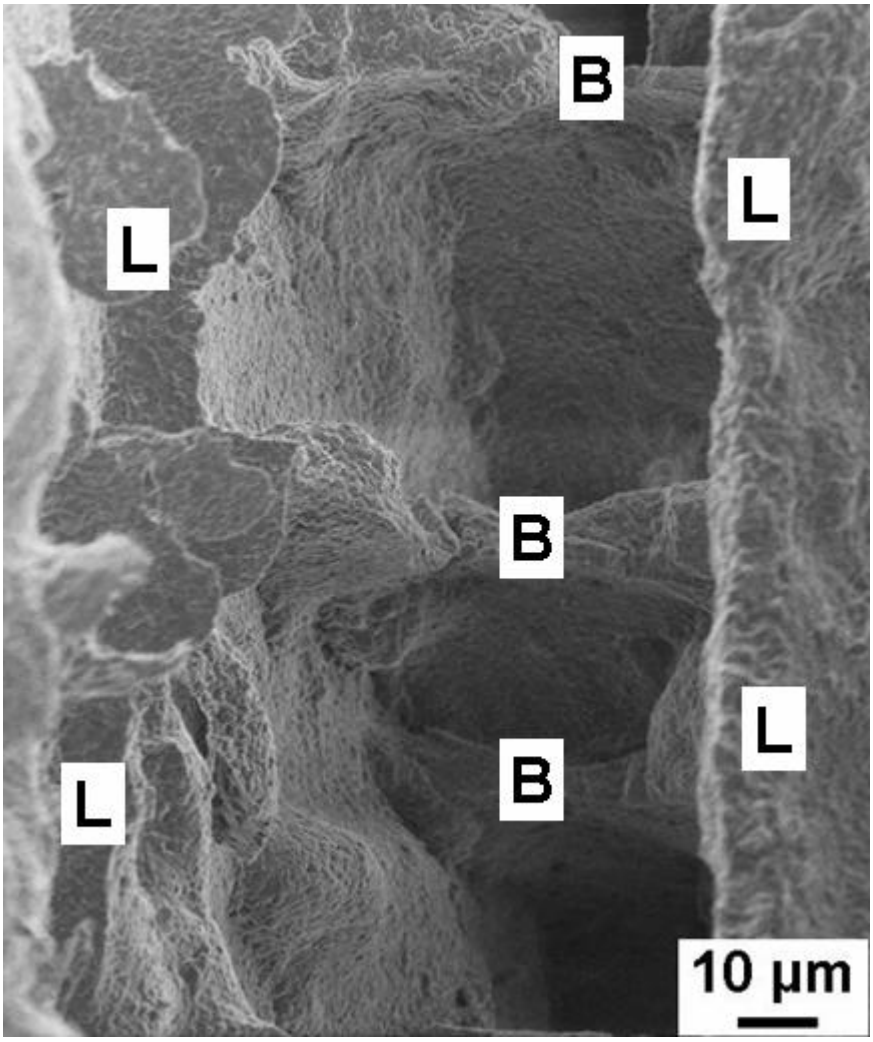


**Figure 6.5: SEM image of the freeze-cast preform showing the ceramic bridges (B) between the lamellae (L) [219]**

compressive strength along 90 ° domain orientation, $\theta$ is the domain orientation angle in degrees, $\tau_{LT}$ is the composite shear yield strength and $\sigma_{xx}=f(\theta)$ are the compressive strengths of the single domains at different orientations. $X$ and $Y$ were determined experimentally. Because of the scatter in the compressive strengths in samples having 0 ° orientation, several (3 in this case) samples having 0 ° domain orientation were compressed and their average was taken as $X$. Two samples having 90 ° domain orientation gave identical values for the compressive strength. Experimental data for the composite shear yield strength was not available. According to Spowart and Dève [108], for composites having well bonded metal-ceramic interface, the matrix shear yield strength can be used as $\tau_{LT}$. Consistent with the methodology followed for composite samples with 30 °$\leq\beta\leq$90 °, stress corresponding to 1% total deformation has been used as the compressive yield strength of Al-12Si. As this strength was 137 MPa, in the

current study a value of 75 MPa (=0.55 times the compressive yield strength of Al-12Si, following page 90 in [238]) was used as $\tau_{LT}$. The corresponding variation is shown by the dashed line in Figure 5.37. As discussed before, it predicts a minimum of the compressive strength at orientations near 45 °. However, the theoretical predictions underestimate the experimental observations. Keeping $X$ and $Y$ fixed at the experimentally determined values, $\tau_{LT}$ was varied to fit the distribution given by Equation (6.2) to the experimental data presented in Figure 5.37. A good match is obtained over the complete range of domain orientations if $\tau_{LT}$ is taken to be 130 MPa. Deville [49] has reported the presence of numerous ceramic bridges between the porous lamellae in freeze-cast alumina fabricated using water-based suspensions. According to him, the presence of such bridges might prevent Euler buckling of the ceramic lamellae and this fact is assumed to explain the enhanced compressive strength of the freeze-cast body. Figure 6.5 shows the typical SEM image of the freeze-cast ceramic preform used to fabricate the composites in this work. The regions marked with "L" correspond to the lamellae while those marked with "B" show the ceramic bridges between the lamellae. These ceramic bridges are numerous and they range over macroscopic depths to act as effective barrier to the shear flow within the metallic lamellae along the EFGH planes in composite samples with 45 ° orientation as discussed in Figure 6.4. As a result, domain orientation has no effect over the compressive strength at intermediate to high domain orientations because in all cases the shear bands within the metallic lamellae are effectively obstructed either by the ceramic lamellae or by the bridges between the lamellae. In the studied double-domain sample one domain had hard orientation while the second domain had soft orientation and accordingly it can be called a hard/soft sample. Comparison of the stress-strain plot of this double-domain sample with one single-domain sample having a similar soft orientation clearly shows that for most of the deformation they superimpose on each other. This along with the observation that the population of cracks within the ceramic lamellae within the region with soft domain orientation is significantly higher suggests that the domain with soft orientation controls the deformation of the whole sample. This is due to the fact that the compressive strength of the domain with hard orientation is even higher than the maximum stress reached in the experiment (refer to Figure 5.37). The above observations suggest that in a sample with more than one domain, the compressive stress-strain behavior is controlled by the deformation behavior of the domain having lower compressive strength. However, for a complete and thorough understanding of the damage mechanism in double-domain samples, samples having domains

with similar orientations (say hard/hard and soft/soft) and with varying area fraction of the domains must be studied.

The variations in lattice strain among different diffracting planes of a single phase observed in Figure 5.47 and Figure 5.57 are due to the interplanar anisotropy, which leads to the development of intergranular stresses [239]. Both the figures show that as the material behavior deviates from elasticity (either due to plastic deformation or damage) the relation between applied stress and lattice microstrain becomes non-linear and very complicated. Figure 5.47a shows that in aluminum in the plastic region,{200} (which is one of the elastically softest for cubic materials) behaves as one of the stiffest while {111} (which is elastically stiffest for cubic materials) behaves as one of the most compliant. Similar behavior for aluminum has been reported by Clausen et al. [240]. However, this trend is absent in Figure 5.57. This difference in behavior shown in different samples may probably be attributed to preferred orientation (texture or large grain size). In both silicon and alumina, the interplanar variation in lattice microstrains with applied stress show similar trend in both the samples. This suggests that silicon and alumina are free from the probable preferred orientation effects observed in aluminum. For silicon the {111} family of planes are the stiffest, which is common for materials having cubic symmetry. For alumina, the {024} and {012} families of planes behave as the most compliant while the {214} family of planes behaves as the stiffest. Figure 5.47d and Figure 5.57d also show that the average lattice microstrain curve for the silicon phase almost superimposes on that of the aluminum phase. The microstructure of the metallic alloy shows that silicon is distributed within the aluminum as very small particles (particle size 1-5 μm) and also within aluminum solid solution. The exact amount of silicon present within the aluminum solid solution is not known. Furthermore, the pure silicon particles are either spherical or they are rod shaped having very small aspect ratios (less than 10). Because of their small aspect ratio, the load transfer from the compliant aluminum phase to the hard and stiff silicon phase by shear lag is not very effective and hence silicon images the behavior of the phase in which it is distributed. Figure 5.54 and Figure 5.62 show that at all applied stresses the summation of load fractions in aluminum and alumina slightly deviates from unity. In the sample loaded along the freezing direction, this sum of load fractions lies in the range of 0.95-1, while in the sample loaded along 0 ° to domain orientation, the total load fraction lies in the range of 0.9-1.1. These observed deviations may probably be attributed to the following reasons:

I. Stress components $\sigma_1$ and $\sigma_2$ have been calculated assuming the transverse stress $\sigma_3$=0. As shown in Figure 6.5, in the structure of the freeze cast bodies, there are numerous ceramic bridges between the ceramic lamellae and they would alter the stresses in direction 3 and hence the assumption that $\sigma_3$=0 may be too simplistic.

II. The volume fraction of alumina was calculated from mass dimension measurements in the complete sample and this was used to determine the load fraction in each phase. The gauge volume consisted of only a very small region of the sample and considering the heterogeneous structure of the composite, it is possible that the ceramic content within the local gauge volume is different from the measured ceramic content within the sample.

III. The actual values of the strain free lattice spacings of aluminum were not known and hence the *d-spacings* corresponding to the strain independent direction have been used for strain free lattice spacing. It is possible that the actual strain free lattice spacing is slightly different from this quantity. This strain free lattice spacing has no effect on the measured deviatoric stress component, but it strongly influences the hydrostatic stress component, and hence may also affect the stress calculations in this work. Furthermore, because of the probable preferred orientation in the aluminum phase, error involved in the aluminum data analysis was always significant.

IV. Minor effects of silicon phase were neglected.

Both Figure 5.54 and Figure 5.62 show that at very high applied stresses, the load fractions in both alumina and aluminum phases show a decreasing trend. In Figure 5.54 this also coincides with the deviation from the predictions of the iso-strain model shown in Figure 5.53. This deviation from iso-strain model has already been attributed to localised damage evolution within the composite. The decreasing trend shown by both phases at very high applied stresses is difficult to explain because if the load fraction in alumina decreases due to incipient damage, the load fraction in aluminum should show a corresponding increasing trend to maintain the summation at unity. The stresses have been calculated using very simplistic assumptions based on ideal laminate theory. It seems most plausible that prediction of the complex stress state developed because of the localised relaxation mechanisms (ceramic cracking, interfacial separation) are beyond the capabilities of the assumptions used in this work.

# 7 Conclusions

Innovative metal/ceramic composites produced by melt infiltration of ceramic performs prepared by a freeze-casting technique have been examined for the first time in this study. These composites exhibit a characteristic hierarchical structure: on a mesoscopic level, lamellar domains with sizes up to several millimetres are observed. The individual domains are composed of alternating ceramic and metallic lamellae with thickness in the range from 20 to 100 µm. The aim of the present study is to characterize the mechanical properties of the composite on different size scales. The elastic and plastic behaviour of individual domains were investigated by ultrasonic measurements and compression tests on miniature samples prepared from poly-domain material. The damage evolution during compressive loading was investigated by in-situ and ex-situ microscopic techniques. Study of processing induced thermal residual stress and strain distributions as well as the internal load transfer under external compressive loading was carried out using synchrotron X-ray energy dispersive diffraction. Following conclusions are drawn from the obtained results:

- Individual domains exhibit a pronounced elastic anisotropy. The highest stiffness is observed in the direction parallel to the preform freezing direction, the lowest in the direction perpendicular to it. The elastic constants of poly-domain samples based on the effective ceramic content (assuming no porosity) lie within and near the bounds set by models established for unidirectional fiber-reinforced composites. The elastic properties of individual domains with different orientations were discussed in the light of a model based on 3D laminate structures with alternating layers of random thickness. Good match between experimental observations and model predictions could be obtained at domain orientations in the range of $45\ ° \leq \beta \leq 90\ °$. However, at domain orientations $0\ ° \leq \beta \leq 45\ °$ the model predictions were much higher than the experimental findings. Better match with experimental results were obtained when a significantly low Young's modulus of alumina was assumed. This is probably because of the cracks and pores present within the ceramic lamellae, which would significantly reduce the stiffness of alumina. Microstructure based FE models could predict the elastic constant much better over the complete range of domain orientation. This is due to the fact that the irregular structure of the lamellae, which was not considered in the theoretical model, was considered in these models.

- Study of thermal residual stress and strain distributions showed that strongly fluctuating local phase specific (micro) residual stresses are present in the as-produced state which can be explained taking into account the thermal expansion mismatch of the alloy and the ceramic preform. Analysis of the deviatoric residual stress components show that only small amounts of phase specific stresses are induced by the squeeze-casting process. The results indicate that these phase specific residual stresses show directionality with respect to the freezing direction of the composite. Taking into account the phase contents of the contributing phases the material emerges to be nearly free of macroscopic residual stresses within the measurement uncertainties as expected for the applied manufacturing process.
- In-situ elastic-plastic analyses of single-domain samples showed that the individual domains exhibit a pronounced anisotropy in their mechanical properties. Compressive mechanical tests of single domain samples showed that the domains are strongest along directions parallel to freezing direction and fails in a brittle manner by ceramic crushing. Theoretical models for layered structures identify kinking of ceramic layers as the primary mode of failure. Compressive failure models for continuous fiber reinforced composites identify fiber crushing as the main failure mode at low fiber strengths. As the domains failed by ceramic crushing under compression along the freezing direction, the fiber crushing model for continuous fiber reinforced composites was used to estimate the compressive strength of the ceramic lamellae along the freezing direction. At domain orientations $30\ ° \leq \beta \leq 90\ °$ the behaviour is controlled by the metallic alloy. The dependence of compressive strength on domain orientation is explained in the light of the energy-based Tsai-Hill criterion using the matrix shear yield strength for the composite shear yield strength. The resulting theoretical predictions overtly underestimate the experimental observations at intermediate to high domain orientations. Good correlation between experimental and modelled results is obtained using a fictive, unrealistically high value for the shear yield strength of the metallic alloy. This way the effects of ceramic bridges between the ceramic lamellae can be mimicked, as these ceramic bridges effectively hinder the shear flow within the metallic lamellae and thus strengthen the composite even at soft orientations. This significantly reduces the structural anisotropy. Coating of the ceramic preform with $Cu_2O$ and Cu prior to melt infiltration weakens the metal-ceramic interfaces and reduces the compressive strength along the freezing direction.

- Studies of internal load transfer under externally applied stresses show that the load transfer mechanism for loading along the freezing direction and along 0 ° to domain orientation are essentially similar. In the macroscopic elastic regime, the metallic and the ceramic phases share the load simultaneously. However, once the metallic phase starts to deform plastically, it transfers the load to the ceramic phase and acts only as a supporting material. Evolution of lattice microstrain within the aluminum phase transverse to the loading direction is complicated because of the constriction posed by the stiff ceramic lamellae and because of the mismatch in Poisson's ratios between the ceramic and the metallic components. Average stress in the alumina and aluminum phases along the loading direction was calculated from the measured lattice microstrain using ideal laminate theory and assuming absence of any stress at 90 ° to lamellae orientation. Fraction of load in each phase was calculated using the volume fraction of ceramic in the whole sample. Results show that within the elastic regime, alumina carries 2-4 times more load than the aluminum phase, although the volume content of alumina was about 40 %. This is due to the much higher stiffness of alumina. At higher loads, the load fraction in aluminum continuously decreases towards zero, while the load fraction within alumina reaches a plateau in the range of 80-90 %. The load transfer from the metallic phase to the ceramic phase is significant, but not complete. This may be attributed to the localized damage taking place within the ceramic lamellae and along the interface.

## A.1 General problem of wave propagation in an orthotropic media

The following discussion is taken from the book written by Rose [173]. The Christoffel equation for a general anisotropic media is written as:

$$\left(\rho\omega^2\delta_{il} - C_{ijkl}k_j k_k\right)u_m = 0 \tag{A.1.1}$$

where $\omega$ is the circular frequency, $\delta_{il}$ is the Kronecker delta and $k_j$, $k_k$ are unit wave vectors. The Christoffel acoustic tensor $\Gamma_{il}$ can be written as:

$$\lambda_{il} = \Gamma_{il} = C_{ijkl}n_j n_k \tag{A.1.2}$$

with $n_j$, $n_k$ being the direction cosines of the normal to the wavefront. Since $k_j=kn_j$, $k_k=kn_k$ and $V^2=\omega^2k^2$, the solution leads to the wave velocity $V$. Hence, Equation (A.1.1) leads to

$$\left(\Gamma_{il} - \rho V^2\delta_{il}\right)u_m = 0 \tag{A.1.3}$$

For a nontrivial solution, the determinant of the coefficient matrix must be equal to 0. This leads to:

$$\left|\Gamma_{il} - \rho V^2\delta_{il}\right| = 0 \tag{A.1.4}$$

As $\Gamma_{il}$ depends on crystal symmetry and the orientation of the waves, expansion of Equation (A.1.4) leads to:

$$\begin{vmatrix} \left(\lambda_{11}-\rho V^2\right) & \lambda_{12} & \lambda_{13} \\ \lambda_{21} & \left(\lambda_{22}-\rho V^2\right) & \lambda_{23} \\ \lambda_{31} & \lambda_{32} & \left(\lambda_{33}-\rho V^2\right) \end{vmatrix} = 0 \tag{A.1.5}$$

where $\lambda_{11}$, $\lambda_{12}$, $\lambda_{13}$,… are obtained from the expressions of the acoustic tensor. The acoustic tensor can now be expanded for all elements of the matrix such that the indices $i$ and $l$ are free and $j$ and $k$ are summers. Expansion for the element $\lambda_{11}$ is shown in Equation (A.1.6) and other elements may be obtained in the similar way.

$$\begin{aligned} & j=1 \qquad j=2 \qquad j=3 \\ \Gamma_{11} = \lambda_{11} = & C_{1111}n_1n_1 + C_{1211}n_2n_1 + C_{1311}n_3n_1 \qquad k=1 \\ & C_{1121}n_1n_2 + C_{1221}n_2n_2 + C_{1321}n_3n_2 \qquad k=2 \\ & C_{1131}n_1n_3 + C_{1231}n_2n_3 + C_{1331}n_3n_3 \qquad k=3 \end{aligned} \tag{A.1.6}$$

The four suffix stiffness notation can be further converted to two suffix notation following the scheme followed in Table 2.1. Because of the symmetry of the stiffness matrix, the acoustic tensor matrix is also symmetric and hence $\Gamma_{ij}=\Gamma_{ji}$. Hence, the number of independent compo-

nents in $\Gamma$ reduces to 6. Following the same methodology followed for Equation (A.1.6), they may be written as:

$$\begin{aligned}
\Gamma_{11} &= C_{11}n_1^2 + C_{66}n_2^2 + C_{55}n_3^2 + 2C_{16}n_1n_2 + 2C_{56}n_2n_3 + 2C_{15}n_1n_3 \\
\Gamma_{22} &= C_{66}n_1^2 + C_{22}n_2^2 + C_{44}n_3^2 + 2C_{26}n_1n_2 + 2C_{24}n_2n_3 + 2C_{46}n_1n_3 \\
\Gamma_{33} &= C_{55}n_1^2 + C_{44}n_2^2 + C_{33}n_3^2 + 2C_{45}n_1n_2 + 2C_{34}n_2n_3 + 2C_{35}n_1n_3 \\
\Gamma_{12} &= C_{16}n_1^2 + C_{26}n_2^2 + C_{45}n_3^2 \\
&\quad + \left(C_{12} + C_{66}\right)n_1n_2 + \left(C_{25} + C_{46}\right)n_2n_3 + \left(C_{14} + C_{56}\right)n_1n_3 \\
\Gamma_{13} &= C_{15}n_1^2 + C_{46}n_2^2 + C_{35}n_3^2 \\
&\quad + \left(C_{14} + C_{56}\right)n_1n_2 + \left(C_{36} + C_{45}\right)n_2n_3 + \left(C_{13} + C_{55}\right)n_1n_3 \\
\Gamma_{23} &= C_{56}n_1^2 + C_{24}n_2^2 + C_{34}n_3^2 \\
&\quad + \left(C_{25} + C_{46}\right)n_1n_2 + \left(C_{23} + C_{44}\right)n_2n_3 + \left(C_{36} + C_{45}\right)n_1n_3
\end{aligned} \tag{A.1.7}$$

For propagation of a plane wave in the $x_1$, $x_2$ plane $n_3$=0. Hence, for a material with orthotropic symmetry Equation (A.1.5) becomes:

$$\begin{vmatrix}
C_{11}n_1^2 + C_{66}n_2^2 - \rho c^2 & \left(C_{12} + C_{66}\right)n_1n_2 & 0 \\
\left(C_{12} + C_{66}\right)n_1n_2 & C_{66}n_1^2 + C_{22}n_2^2 - \rho c^2 & 0 \\
0 & 0 & C_{55}n_1^2 + C_{44}n_2^2 - \rho c^2
\end{vmatrix} = 0\,. \tag{A.1.8}$$

The determinant in Equation (A.1.8) can be expanded to yield

$$\left\{C_{55}n_1^2 + C_{44}n_2^2 - \rho c^2\right\}\begin{Bmatrix}\left(C_{11}n_1^2 + C_{66}n_2^2 - \rho c^2\right)\left(C_{66}n_1^2 + C_{22}n_2^2 - \rho c^2\right) \\ -\left(C_{12} + C_{66}\right)^2 n_1^2n_2^2\end{Bmatrix} = 0\,. \tag{A.1.9}$$

Simplification of Equation (A.1.9) (described in detail in Ref. [173]) leads to the following expressions for wave propagation along the $x_1$–axis.

$$\rho V_{13}^2 = C_{55},\ \rho V_{11}^2 = C_{11},\ \rho V_{12}^2 = C_{66} \tag{A.1.10}$$

Similarly for wave propagation along the $x_2$–axis

$$\rho V_{23}^2 = C_{44},\ \rho V_{22}^2 = C_{22},\ \rho V_{21}^2 = C_{66}\,. \tag{A.1.11}$$

Proceeding in the same way as described before, for plane wave propagation along the $x_3$–axis in the ($x_1$, $x_3$) plane

$$\rho V_{32}^2 = C_{44},\ \rho V_{33}^2 = C_{33},\ \rho V_{31}^2 = C_{55}\,. \tag{A.1.12}$$

In Equations (A.1.10 – A.1.12) the shear elastic constants $C_{44}$, $C_{55}$, $C_{66}$ have each been measured twice; e.g. $C_{66}$ has been determined once for a shear wave propagating in the $x_1$ direction and polarized in the $x_2$ direction and vice versa. The equality of these two phase velocities follows the original definition of orthotropy. Hence, if the measured velocities vary significantly, the material cannot be considered to be orthotropic and probably monoclinic symme-

try better models the material behavior. This way, all the elastic constants along the main diagonal of the stiffness matrix are determined. For determination of the three off - diagonal constants $C_{12}$, $C_{13}$, $C_{23}$, the phase velocity of either a quasi–longitudinal or quasi–transverse wave propagating in three non–principal directions (typically at 45° to the main axes) are measured.

## A.2 Detail tabulation of the elastic constants of the poly-domain samples

**Composite Type A, with uncoated preforms**

| Sample | Density ($kg.m^{-3}$) | Ceramic Vol % | $V_1$ $m.s^{-1}$ | $V_2$ $m.s^{-1}$ | $V_3$ $m.s^{-1}$ | $V_{12}$ $m.s^{-1}$ | $V_{21}$ $m.s^{-1}$ | $V_{13}$ $m.s^{-1}$ | $V_{31}$ $m.s^{-1}$ | $V_{23}$ $m.s^{-1}$ | $V_{32}$ $m.s^{-1}$ | $C_{11}$ (GPa) | $C_{22}$ (GPa) | $C_{33}$ (GPa) | $C_{44}$ (GPa) | $C_{55}$ (GPa) | $C_{66}$ (GPa) |
|---|---|---|---|---|---|---|---|---|---|---|---|---|---|---|---|---|---|
| 1 | 3123 | 0.39 | 8430 | 8211 | 7325 | - | - | - | - | - | - | 222 | 211 | 168 | - | - | - |
| 2 | 3123 | 0.39 | 8413 | 8176 | 7150 | - | - | - | - | - | - | 221 | 209 | 160 | - | - | - |
| 3 | 3133 | 0.40 | 8531 | 7401 | 7975 | - | - | - | - | - | - | 228 | 172 | 199 | - | - | - |
| 4 | 3074 | 0.35 | 8153 | 7543 | 7492 | - | - | - | - | - | - | 204 | 175 | 173 | - | - | - |
| 5 | 3119 | 0.39 | 8334 | 7905 | 7304 | - | - | - | - | - | - | 217 | 195 | 166 | - | - | - |
| 6 | 3111 | 0.38 | 8316 | 7582 | 7406 | - | - | - | - | - | - | 215 | 179 | 171 | - | - | - |
| 7 | 3110 | 0.38 | 8330 | 7536 | 7734 | - | - | - | - | - | - | 216 | 177 | 186 | - | - | - |
| 8 | 3128 | 0.39 | 8393 | 7894 | 7552 | - | - | - | - | - | - | 220 | 195 | 178 | - | - | - |
| 9 | 3132 | 0.40 | 7987 | 7283 | 7070 | - | - | - | - | - | - | 200 | 166 | 157 | - | - | - |
| 10 | 3106 | 0.37 | 8290 | 7404 | 7726 | - | - | - | - | - | - | 213 | 170 | 185 | - | - | - |
| 11 | 3120 | 0.39 | 7966 | 7180 | 6841 | - | - | - | - | - | - | 198 | 161 | 146 | - | - | - |
| 12 | 3141 | 0.40 | 8542 | 7764 | 7302 | - | - | - | - | - | - | 229 | 189 | 167 | - | - | - |
| 13 | 3044 | 0.33 | 7656 | 7368 | 6433 | - | - | - | - | - | - | 178 | 165 | 126 | - | - | - |
| 14 | 3103 | 0.37 | 8198 | 7620 | 7188 | - | - | - | - | - | - | 209 | 180 | 160 | - | - | - |
| 15 | 3147 | 0.41 | 8236 | 7497 | 7714 | - | - | - | - | - | - | 213 | 177 | 187 | - | - | - |

| Sample | Density ($kg.m^{-3}$) | Ceramic Vol % | $V_1$ $m.s^{-1}$ | $V_2$ $m.s^{-1}$ | $V_3$ $m.s^{-1}$ | $V_{12}$ $m.s^{-1}$ | $V_{21}$ $m.s^{-1}$ | $V_{13}$ $m.s^{-1}$ | $V_{31}$ $m.s^{-1}$ | $V_{23}$ $m.s^{-1}$ | $V_{32}$ $m.s^{-1}$ | $C_{11}$ (GPa) | $C_{22}$ (GPa) | $C_{33}$ (GPa) | $C_{44}$ (GPa) | $C_{55}$ (GPa) | $C_{66}$ (GPa) |
|---|---|---|---|---|---|---|---|---|---|---|---|---|---|---|---|---|---|
| 16 | 3074 | 0.35 | 7974 | 7494 | 7138 | - | - | - | - | - | - | 195 | 173 | 157 | - | - | - |
| 17 | 3150 | 0.41 | 8609 | 8094 | 7282 | 4229 | 4728 | 4072 | 4043 | 4251 | 3989 | 233 | 206 | 167 | 54 | 52 | 63 |
| 18 | 3120 | 0.39 | 8496 | 7689 | 7486 | 4549 | 4711 | 4115 | 4152 | 4014 | 4224 | 225 | 184 | 175 | 53 | 54 | 67 |
| 19 | 3160 | 0.42 | 8598 | 7976 | 7023 | 4733 | 4972 | 4168 | 4024 | 4376 | 4178 | 234 | 201 | 156 | 58 | 53 | 75 |
| 20 | 3130 | 0.39 | 8608 | 7837 | 7298 | - | - | - | - | - | - | 232 | 192 | 167 | | | |
| 21 | 3130 | 0.39 | 8437 | 7275 | 7342 | 4022 | 4420 | 4262 | 4445 | 4109 | 4177 | 223 | 166 | 169 | 54 | 59 | 56 |
| 22 | 3120 | 0.39 | 8511 | 7306 | 7458 | 4745 | 4862 | 4107 | 4410 | 4116 | 4002 | 226 | 167 | 174 | 52 | 57 | 72 |
| 23 | 3130 | 0.39 | 8423 | 7306 | 8002 | 4026 | 4581 | 3969 | 4446 | 4045 | 4115 | 222 | 167 | 200 | 52 | 56 | 58 |
| 24 | 3150 | 0.41 | 8583 | 7796 | 7064 | 5052 | 4888 | 4166 | 4359 | 4087 | 4122 | 232 | 191 | 157 | 53 | 57 | 78 |
| 25 | 3140 | 0.40 | 8710 | 7584 | 6906 | 4889 | 4710 | 4091 | 4160 | 4112 | 4245 | 238 | 181 | 150 | 55 | 53 | 72 |
| 26 | 3140 | 0.40 | 8367 | 7101 | 7719 | 4160 | 4330 | 4016 | 4654 | 4141 | 4330 | 220 | 158 | 187 | 56 | 59 | 57 |
| 27 | 3120 | 0.39 | 8479 | 7591 | 8105 | 3835 | 4236 | 4261 | 4867 | 4090 | 4252 | 224 | 180 | 205 | 54 | 65 | 51 |

**Composite Type B. with uncoated preforms**

| Sample | Density ($kg.m^{-3}$) | Ceramic Vol % | $V_1$ $m.s^{-1}$ | $V_2$ $m.s^{-1}$ | $V_3$ $m.s^{-1}$ | $V_{12}$ $m.s^{-1}$ | $V_{21}$ $m.s^{-1}$ | $V_{13}$ $m.s^{-1}$ | $V_{31}$ $m.s^{-1}$ | $V_{23}$ $m.s^{-1}$ | $V_{32}$ $m.s^{-1}$ | $C_{11}$ (GPa) | $C_{22}$ (GPa) | $C_{33}$ (GPa) | $C_{44}$ (GPa) | $C_{55}$ (GPa) | $C_{66}$ (GPa) |
|---|---|---|---|---|---|---|---|---|---|---|---|---|---|---|---|---|---|
| 1 | 3172 | 0.43 | 8663 | 7833 | 7607 | - | - | - | - | - | - | 238 | 195 | 184 | - | - | - |
| 2 | 3194 | 0.44 | 8763 | 7624 | 8026 | - | - | - | - | - | - | 245 | 186 | 206 | - | - | - |
| 3 | 3172 | 0.43 | 8635 | 8040 | 7751 | - | - | - | - | - | - | 237 | 205 | 191 | - | - | - |
| 4 | 3185 | 0.44 | 8658 | 7988 | 7603 | - | - | - | - | - | - | 239 | 203 | 184 | - | - | - |
| 5 | 3169 | 0.42 | 8668 | 8011 | 7457 | - | - | - | - | - | - | 238 | 203 | 176 | - | - | - |
| 6 | 3169 | 0.42 | 8859 | 7842 | 7587 | - | - | - | - | - | - | 249 | 182 | 195 | - | - | - |
| 7 | 3191 | 0.44 | 8737 | 7768 | 7747 | - | - | - | - | - | - | 244 | 193 | 191 | - | - | - |
| 8 | 3177 | 0.43 | 8681 | 7616 | 7657 | - | - | - | - | - | - | 239 | 184 | 186 | - | - | - |
| 9 | 3057 | 0.34 | 8513 | 7172 | 7718 | - | - | - | - | - | - | 222 | 157 | 182 | - | - | - |
| 10 | 3191 | 0.44 | 8609 | 7712 | 8042 | - | - | - | - | - | - | 236 | 190 | 206 | - | - | - |
| 11 | 3169 | 0.42 | 7975 | 6817 | 7313 | - | - | - | - | - | - | 202 | 147 | 169 | - | - | - |
| 12 | 3178 | 0.43 | 8632 | 7806 | 7605 | - | - | - | - | - | - | 237 | 194 | 184 | - | - | - |
| 13 | 3190 | 0.44 | 8684 | 7775 | 7631 | - | - | - | - | - | - | 241 | 193 | 186 | - | - | - |
| 14 | 3187 | 0.44 | 8585 | 7455 | 7890 | - | - | - | - | - | - | 235 | 177 | 198 | - | - | - |
| 15 | 3200 | 0.45 | 8678 | 7475 | 8001 | 4399 | 4546 | 4726 | 4827 | 4512 | 4498 | 241 | 179 | 205 | 65 | 73 | 64 |
| 16 | 3220 | 0.46 | 8649 | 7649 | 7561 | 4298 | 4478 | 4690 | 4602 | 4292 | 4256 | 241 | 188 | 184 | 59 | 70 | 62 |
| 17 | 3200 | 0.45 | 8831 | 7682 | 7804 | 4280 | 4437 | 4661 | 4780 | 4643 | 4645 | 250 | 189 | 195 | 69 | 72 | 61 |

| Sample | Density ($kg.m^{-3}$) | Ceramic Vol % | $V_1$ $m.s^{-1}$ | $V_2$ $m.s^{-1}$ | $V_3$ $m.s^{-1}$ | $V_{12}$ $m.s^{-1}$ | $V_{21}$ $m.s^{-1}$ | $V_{13}$ $m.s^{-1}$ | $V_{31}$ $m.s^{-1}$ | $V_{23}$ $m.s^{-1}$ | $V_{32}$ $m.s^{-1}$ | $C_{11}$ (GPa) | $C_{22}$ (GPa) | $C_{33}$ (GPa) | $C_{44}$ (GPa) | $C_{55}$ (GPa) | $C_{66}$ (GPa) |
|---|---|---|---|---|---|---|---|---|---|---|---|---|---|---|---|---|---|
| 18 | 3220 | 0.46 | 8722 | 7603 | 8067 | 4294 | 4254 | 4806 | 4801 | 4331 | 4416 | 245 | 186 | 207 | 62 | 74 | 59 |
| 19 | 3100 | 0.37 | 8758 | 7723 | 7607 | 3305 | 4394 | 3247 | 4358 | 4310 | 4042 | 238 | 185 | 179 | 55 | 45 | 48 |
| 20 | 3200 | 0.45 | 8655 | 7735 | 7970 | 4623 | 4660 | 4679 | 4764 | 4213 | 4306 | 240 | 192 | 203 | 58 | 72 | 69 |
| 21 | 3200 | 0.45 | 8725 | 7572 | 8113 | 4524 | 4560 | 4612 | 4699 | 4319 | 4180 | 243 | 183 | 211 | 58 | 70 | 66 |
| 22 | 3190 | 0.44 | 8919 | 7771 | 8305 | 4357 | 4361 | 4725 | 4634 | 4484 | 4393 | 254 | 193 | 220 | 63 | 70 | 61 |
| 23 | 3110 | 0.38 | 8959 | 7774 | 7863 | 4251 | 4061 | 4664 | 4443 | 4255 | 4216 | 250 | 188 | 192 | 56 | 65 | 54 |
| 24 | 3200 | 0.45 | 8641 | 7675 | 7933 | 4301 | 4506 | 4662 | 4797 | 4451 | 4354 | 239 | 189 | 201 | 62 | 72 | 62 |
| 25 | 3130 | 0.39 | 8933 | 8020 | 7900 | 4463 | 4409 | 4475 | 4162 | 4338 | 4440 | 250 | 203 | 195 | 61 | 59 | 62 |
| 26 | 3180 | 0.43 | 8402 | 7462 | 7890 | 4069 | 4480 | 4158 | 4637 | 4261 | 4395 | 224 | 177 | 198 | 60 | 62 | 59 |
| 27 | 3210 | 0.46 | 8804 | 7623 | 8174 | 4490 | 4521 | 4740 | 4745 | 4539 | 4413 | 249 | 187 | 214 | 65 | 72 | 66 |
| 28 | 3210 | 0.46 | 8758 | 7925 | 8044 | 4184 | 4262 | 4590 | 4488 | 4384 | 4322 | 246 | 202 | 208 | 61 | 67 | 57 |
| 29 | 3170 | 0.43 | 8701 | 7643 | 8345 | 4019 | 4394 | 4490 | 4464 | 4266 | 4323 | 240 | 185 | 221 | 59 | 64 | 56 |
| 30 | 3200 | 0.45 | 8749 | 7628 | 8020 | 4348 | 4146 | 4515 | 4681 | 4511 | 4296 | 245 | 186 | 206 | 62 | 68 | 58 |

**Composite Type A. with $Cu_2O$ coated preforms**

| Sample | Density ($kg.m^{-3}$) | Ceramic Vol % | $V_1$ $m.s^{-1}$ | $V_2$ $m.s^{-1}$ | $V_3$ $m.s^{-1}$ | $V_{12}$ $m.s^{-1}$ | $V_{21}$ $m.s^{-1}$ | $V_{13}$ $m.s^{-1}$ | $V_{31}$ $m.s^{-1}$ | $V_{23}$ $m.s^{-1}$ | $V_{32}$ $m.s^{-1}$ | $C_{11}$ (GPa) | $C_{22}$ (GPa) | $C_{33}$ (GPa) | $C_{44}$ (GPa) | $C_{55}$ (GPa) | $C_{66}$ (GPa) |
|---|---|---|---|---|---|---|---|---|---|---|---|---|---|---|---|---|---|
| 1 | 3100 | 0.37 | 8106 | 7269 | 6916 | 4877 | 5011 | 3957 | 4308 | 4034 | 3842 | 204 | 164 | 148 | 48 | 53 | 76 |
| 2 | 3080 | 0.35 | 8385 | 8340 | 7477 | 4973 | 4964 | 3997 | 4207 | 3955 | 3782 | 217 | 214 | 172 | 46 | 50 | 76 |
| 3 | 3120 | 0.39 | 8094 | 6879 | 7470 | 4410 | 4244 | 4620 | 4424 | - | - | 204 | 148 | 174 | - | 64 | 59 |
| 4 | 3100 | 0.37 | 8115 | 7379 | 8133 | 3996 | 4292 | 5336 | 5162 | 4327 | 4073 | 204 | 169 | 205 | 55 | 85 | 53 |
| 5 | 3120 | 0.39 | 8242 | 6787 | 7659 | 3954 | 3931 | 4928 | 4495 | 3945 | 3962 | 212 | 144 | 183 | 49 | 69 | 48 |
| 6 | 3110 | 0.38 | 8403 | - | - | 4969 | 4851 | 4209 | 3662 | 3706 | 3593 | 220 | - | - | 41 | 48 | 75 |
| 7 | 3100 | 0.37 | 8450 | 6537 | 7712 | 3913 | 3777 | 4898 | 4653 | 4071 | 3897 | 221 | 132 | 184 | 49 | 71 | 46 |
| 8 | 3140 | 0.40 | 8206 | 8132 | 7030 | 4960 | 4721 | 3981 |  | 3992 | 3740 | 211 | 208 | 155 | 47 | 50 | 74 |
| 9 | 3130 | 0.39 | 8158 | 8138 | 7639 | - | - | 3925 | 4291 | 3990 | 4025 | 208 | 207 | 183 | 50 | 53 | - |

**Composite Type A. with Cu coated preforms**

| Sample | Density ($kg.m^{-3}$) | Ceramic Vol % | $V_1$ $m.s^{-1}$ | $V_2$ $m.s^{-1}$ | $V_3$ $m.s^{-1}$ | $V_{12}$ $m.s^{-1}$ | $V_{21}$ $m.s^{-1}$ | $V_{13}$ $m.s^{-1}$ | $V_{31}$ $m.s^{-1}$ | $V_{23}$ $m.s^{-1}$ | $V_{32}$ $m.s^{-1}$ | $C_{11}$ (GPa) | $C_{22}$ (GPa) | $C_{33}$ (GPa) | $C_{44}$ (GPa) | $C_{55}$ (GPa) | $C_{66}$ (GPa) |
|---|---|---|---|---|---|---|---|---|---|---|---|---|---|---|---|---|---|
| 1 | 3116 | 0.38 | 7982 | 6502 | 7758 | 3960 | 3869 | 4660 | 4556 | 3885 | 3822 | 199 | 132 | 188 | 46 | 66 | 48 |
| 2 | 3095 | 0.37 | 7793 | 7172 | - | 3170 | 3855 | 4263 | 4432 | 3946 | 3729 | 188 | 159 | - | 46 | 59 | 39 |
| 3 | 3127 | 0.39 | - | - | - | - | - | - | - | - | - | - | - | - | - | - | - |
| 4 | 3096 | 0.37 | 7905 | 7089 | - | 4698 | 4426 | 3612 | 3923 | - | 3742 | 193 | 156 | - | 43 | 44 | 64 |
| 5 | 3086 | 0.36 | - | - | - | - | - | - | - | - | - | - | - | - | - | - | - |
| 6 | 3112 | 0.38 | 8185 | 7285 | 7597 | 3707 | 4068 | 3788 | 4324 | - | 3890 | 208 | 165 | 180 | 47 | 51 | 47 |
| 7 | 3119 | 0.39 | 8139 | 7148 | 7995 | 4011 | 3911 | 4771 | 4748 | 4131 | 4248 | 207 | 159 | 199 | 55 | 71 | 49 |
| 8 | 3130 | 0.39 | 8168 | 7718 | - | 4680 | 4526 | 4029 | 4073 | 3936 | 3814 | 209 | 186 | - | 47 | 51 | 66 |
| 9 | 3136 | 0.40 | 8075 | 8146 | 7206 | 4792 | 4776 | 3900 | 3989 | 3972 | 3962 | 204 | 208 | 163 | 49 | 49 | 72 |
| 10 | 3110 | 0.38 | 8170 | 8175 | 6764 | 4605 | 4380 | 3475 | 3842 | 3805 | 3720 | 208 | 208 | 142 | 44 | 42 | 63 |
| 11 | 3107 | 0.38 | 8230 | 7630 | 6469 | 4561 | 4502 | 4014 | 3692 | 3912 | 3766 | 210 | 181 | 130 | 46 | 46 | 64 |
| 12 | 3119 | 0.39 | 8323 | 7077 | 7470 | 3948 | 4596 | 4778 | 4690 | 3379 | 3972 | 216 | 156 | 174 | 42 | 70 | 57 |
| 13 | 3103 | 0.37 | 8272 | 7608 | 7992 | 3834 | 4341 | 3827 | 4646 | 3649 | 3854 | 212 | 180 | 198 | 44 | 56 | 52 |
| 14 | 3129 | 0.39 | 8121 | 7549 | 7378 | 3837 | 4337 | 3812 | 4177 | 4405 | 4081 | 206 | 178 | 170 | 56 | 50 | 52 |
| 15 | 3134 | 0.40 | 8119 | 7753 | 7262 | 4665 | 4484 | 3951 | 4058 | 3946 | 3974 | 207 | 188 | 165 | 49 | 50 | 66 |
| 16 | 3083 | 0.36 | 8026 | 7389 | - | 3857 | - | 3717 | - | 3378 | - | 199 | 168 | - | 35 | 43 | 46 |
| 17 | 3110 | 0.38 | 8079 | 7895 | - | 4446 | 4459 | 3634 | 3954 | - | 3832 | 203 | 194 | - | 46 | 45 | 62 |

| Sample | Density ($kg.m^{-3}$) | Ceramic Vol % | $V_1$ $m.s^{-1}$ | $V_2$ $m.s^{-1}$ | $V_3$ $m.s^{-1}$ | $V_{12}$ $m.s^{-1}$ | $V_{21}$ $m.s^{-1}$ | $V_{13}$ $m.s^{-1}$ | $V_{31}$ $m.s^{-1}$ | $V_{23}$ $m.s^{-1}$ | $V_{32}$ $m.s^{-1}$ | $C_{11}$ (GPa) | $C_{22}$ (GPa) | $C_{33}$ (GPa) | $C_{44}$ (GPa) | $C_{55}$ (GPa) | $C_{66}$ (GPa) |
|---|---|---|---|---|---|---|---|---|---|---|---|---|---|---|---|---|---|
| 18 | 3100 | 0.37 | 8272 | - | 7616 | 3629 | 4077 | 3974 | 4344 | - | 3685 | 212 | - | 180 | 42 | 54 | 46 |
| 19 | 3095 | 0.37 | 8121 | - | 7697 | 3800 | - | 4439 | 4526 | - | 3751 | 204 | - | 183 | 44 | 62 | 45 |
| 20 | 3088 | 0.36 | 7974 | - | 7591 | 3915 | - | 4701 | 4723 | 3978 | 3623 | 196 | - | 178 | 45 | 69 | 47 |
| 21 | 3136 | 0.40 | 8012 | 7103 | 7804 | 3477 | 3895 | 4441 | 4517 | 3885 | 4093 | 201 | 158 | 191 | 50 | 63 | 43 |
| 22 | 3115 | 0.38 | 8113 | 7106 | 7490 | 3753 | 4292 | 3688 | 4421 | 4139 | 4210 | 205 | 157 | 175 | 54 | 52 | 51 |
| 23 | 3105 | 0.37 | 8089 | 7009 | 7647 | - | 4106 | 4735 | 4598 | - | 3787 | 203 | 153 | 182 | 45 | 68 | 52 |
| 24 | 3114 | 0.38 | 8181 | 7627 | 7816 | - | 4500 | 4560 | 4395 | 3858 | 3982 | 208 | 181 | 190 | 48 | 62 | 63 |
| 25 | 3108 | 0.38 | 8205 | 7663 | 7423 | 3555 | 4259 | 3511 | 4428 | - | 3864 | 209 | 183 | 171 | 46 | 50 | 48 |
| 26 | 3122 | 0.39 | 8002 | 7054 | 7674 | 3943 | 4332 | 4648 | 4995 | 3996 | 3914 | 200 | 155 | - | 49 | 73 | 54 |
| 27 | 3098 | 0.37 | 8069 | 7403 | 6728 | 3764 | 4223 | 3650 | 4112 | 3840 | 4071 | 202 | 170 | 140 | 49 | 47 | 50 |
| 28 | 3118 | 0.38 | 8077 | - | 7861 | 3591 | 4234 | 4686 | 4741 | - | 3859 | 203 | - | 193 | 46 | 69 | 48 |
| 29 | 3115 | 0.38 | 8240 | 7684 | 6606 | 4719 | 4531 | 3718 | - | 3752 | 3457 | 211 | 184 | 136 | 41 | 43 | 67 |
| 30 | 3128 | 0.39 | 8249 | 7446 | 6858 | 4452 | 4674 | 3804 | 3941 | 3722 | 3772 | 213 | 173 | 147 | 44 | 47 | 65 |
| 31 | 3114 | 0.38 | 8099 | 7141 | 7575 | 3701 | 4408 | 4568 | 4607 | 3846 | 3883 | 204 | 159 | 179 | 47 | 66 | 52 |
| 32 | 3117 | 0.38 | 8032 | 6949 | 7416 | 3740 | 3823 | 4649 | 4432 | 3836 | 3646 | 201 | 151 | 171 | 44 | 64 | 45 |
| 33 | 3127 | 0.39 | 8170 | 6886 | 7802 | 3961 | 4188 | 4784 | 4805 | 3556 | 3835 | 209 | 148 | 190 | 43 | 72 | 52 |
| 34 | 3125 | 0.39 | 8133 | - | 7850 | 3765 | 3848 | 4725 | 4835 | 3943 | 3593 | 207 | - | 193 | 44 | 71 | 45 |

| Sample | Density ($kg.m^{-3}$) | Ceramic Vol % | $V_1$ $m.s^{-1}$ | $V_2$ $m.s^{-1}$ | $V_3$ $m.s^{-1}$ | $V_{12}$ $m.s^{-1}$ | $V_{21}$ $m.s^{-1}$ | $V_{13}$ $m.s^{-1}$ | $V_{31}$ $m.s^{-1}$ | $V_{23}$ $m.s^{-1}$ | $V_{32}$ $m.s^{-1}$ | $C_{11}$ (GPa) | $C_{22}$ (GPa) | $C_{33}$ (GPa) | $C_{44}$ (GPa) | $C_{55}$ (GPa) | $C_{66}$ (GPa) |
|---|---|---|---|---|---|---|---|---|---|---|---|---|---|---|---|---|---|
| 35 | 3118 | 0.38 | 8077 | - | 7385 | 3529 | 4022 | 4461 | 4239 | 3729 | - | 203 | - | 170 | 43 | 59 | 45 |
| 36 | 3122 | 0.39 | 8148 | 7179 | 8148 | 3822 | 4149 | 4546 | 4899 | 3914 | 4082 | 207 | 161 | 207 | 50 | 70 | 50 |
| 37 | 3031 | 0.32 | 8153 | 7334 | 7683 | 3766 | 4441 | 4692 | 4432 | 4234 | 4296 | 201 | 163 | 179 | 55 | 63 | 51 |
| 38 | 3123 | 0.39 | 8069 | 6982 | - | 3615 | 4012 | 4583 | 4558 | 4034 | 4034 | 203 | 152 | - | 51 | 65 | 46 |
| 39 | 3106 | 0.37 | 8157 | 6737 | 7698 | 3826 | 4322 | 4425 | 4303 | 3608 | 3827 | 207 | 141 | 184 | 43 | 59 | 52 |
| 40 | 3098 | 0.37 | 7947 | 6077 | - | 3699 | 3679 | 4452 | 4485 | 3596 | 3797 | 196 | 114 | - | 42 | 62 | 42 |

**Composite Type A with Ni coated preforms**

| Sample | Density ($kg.m^{-3}$) | Ceramic Vol % | $V_1$ $m.s^{-1}$ | $V_2$ $m.s^{-1}$ | $V_3$ $m.s^{-1}$ | $V_{12}$ $m.s^{-1}$ | $V_{21}$ $m.s^{-1}$ | $V_{13}$ $m.s^{-1}$ | $V_{31}$ $m.s^{-1}$ | $V_{23}$ $m.s^{-1}$ | $V_{32}$ $m.s^{-1}$ | $C_{11}$ (GPa) | $C_{22}$ (GPa) | $C_{33}$ (GPa) | $C_{44}$ (GPa) | $C_{55}$ (GPa) | $C_{66}$ (GPa) |
|---|---|---|---|---|---|---|---|---|---|---|---|---|---|---|---|---|---|
| 1 | 3118 | 0.38 | 7983 | 8149 | 6471 | - | 3772 | 4613 | - | 3484 | 3694 | 199 | 207 | 131 | 40 | 66 | 44 |
| 2 | 3118 | 0.38 | 7977 | 7564 | 6550 | 4216 | 3824 | 3974 | 4051 | 3708 | 3777 | 198 | 178 | 134 | 44 | 50 | 51 |
| 3 | 3114 | 0.38 | 8197 | 7788 | 7143 | 4642 | 4653 | 3588 | 4311 | 3325 | 4221 | 209 | 189 | 159 | 45 | 49 | 67 |
| 4 | 3104 | 0.37 | 7980 | 7120 | 6566 | 4586 | 4508 | 3584 | 4222 | 3565 | 3717 | 198 | 157 | 134 | 41 | 48 | 64 |
| 5 | 3112 | 0.38 | 7964 | 7132 | 7456 | 4406 | 4421 | 3680 | 3931 | 3623 | 3690 | 197 | 158 | 173 | 42 | 45 | 61 |
| 6 | 3090 | 0.36 | 7997 | 7335 | 7413 | 3739 | 4675 | 4613 | 3856 | 4074 | 4646 | 198 | 166 | 170 | 59 | 56 | 55 |
| 7 | 3144 | 0.40 | 8104 | 6949 | 7485 | 3797 | 3766 | 3951 | 4444 | 4042 | 4107 | 206 | 152 | 176 | 52 | 56 | 45 |
| 8 | 3080 | 0.35 | 7989 | 6525 | 7295 | 3796 | 4250 | 4441 | 4550 | 3876 | 3863 | 197 | 131 | 164 | 46 | 62 | 50 |
| 9 | 3089 | 0.36 | 8030 | 7380 | 6699 | 4592 | 4611 | 3974 | 4252 | 4087 | 4140 | 199 | 168 | 139 | 52 | 52 | 65 |
| 10 | 3070 | 0.35 | 7983 | 7668 | 6257 | 4190 | 4799 | 3797 | 3996 | 3702 | 4019 | 196 | 181 | 120 | 46 | 47 | 62 |
| 11 | 3066 | 0.34 | 7912 | 7139 | 6722 | 3592 | 3916 | 3521 | 3687 | 4265 | 4011 | 192 | 156 | 139 | 53 | 40 | 43 |
| 12 | 3096 | 0.37 | 7893 | 6938 | 6284 | 4299 | 4344 | 3155 | 3950 | 4371 | 3507 | 193 | 149 | 122 | 49 | 40 | 58 |
| 13 | 3129 | 0.39 | 8011 | 7042 | 7730 | BAD | 3946 | 4622 | 3822 | 4749 | 4110 | 201 | 155 | 187 | 62 | 56 | 49 |
| 14 | 3085 | 0.36 | 8068 | 6415 | 7492 | 4700 | 3874 | 4646 | 3745 | 4596 | 3884 | 201 | 127 | 173 | 56 | 55 | 57 |
| 15 | 3068 | 0.34 | 8137 | 7161 | 6932 | 4551 | 4256 | 3707 | 3631 | 4470 | 3919 | 203 | 157 | 147 | 54 | 41 | 60 |
| 16 | 3060 | 0.34 | 8077 | 7707 | 6550 | 3023 | 4532 | 3879 | 4073 | 3858 | 2686 | 200 | 182 | 131 | 34 | 48 | 45 |
| 17 | 3043 | 0.33 | 7997 | 7730 | 7724 | 3479 | 4501 | 3167 | 3956 | 4143 | 3700 | 195 | 182 | 182 | 47 | 39 | 49 |

| Sample | Density ($kg.m^{-3}$) | Ceramic Vol % | $V_1$ $m.s^{-1}$ | $V_2$ $m.s^{-1}$ | $V_3$ $m.s^{-1}$ | $V_{12}$ $m.s^{-1}$ | $V_{21}$ $m.s^{-1}$ | $V_{13}$ $m.s^{-1}$ | $V_{31}$ $m.s^{-1}$ | $V_{23}$ $m.s^{-1}$ | $V_{32}$ $m.s^{-1}$ | $C_{11}$ (GPa) | $C_{22}$ (GPa) | $C_{33}$ (GPa) | $C_{44}$ (GPa) | $C_{55}$ (GPa) | $C_{66}$ (GPa) |
|---|---|---|---|---|---|---|---|---|---|---|---|---|---|---|---|---|---|
| 18 | 3131 | 0.39 | 7847 | 6667 | 7408 | 3676 | 3837 | 3914 | 3533 | 4305 | 3399 | 193 | 139 | 172 | 47 | 44 | 44 |
| 19 | 3117 | 0.38 | 8166 | 6609 | 7594 | 3820 | 3597 | 4122 | 3750 | 4655 | 4008 | 208 | 136 | 180 | 59 | 48 | 43 |
| 20 | 3092 | 0.36 | 8064 | 6925 | 8037 | 3685 | 3741 | 3720 | 3806 | 4835 | 4047 | 201 | 148 | 200 | 61 | 44 | 43 |
| 21 | 3075 | 0.35 | 8137 | 7593 | 7293 | 3931 | 4499 | 3200 | 3722 | 4466 | 388 | 204 | 177 | 164 | 31 | 37 | 55 |
| 22 | 3080 | 0.35 | 7888 | 7404 | 6824 | - | 4336 | 3663 | - | - | 3940 | 192 | 169 | 143 | 48 | 41 | 58 |
| 23 | 3059 | 0.34 | 7834 | 6332 | 7188 | - | 3336 | 3811 | - | - | 3426 | 188 | 123 | 158 | 36 | 44 | 34 |
| 24 | 3067 | 0.34 | 7890 | 6519 | 8163 | 3331 | 3675 | 3820 | 3495 | 3367 | 3850 | 191 | 130 | 204 | 40 | 41 | 38 |
| 25 | 3118 | 0.38 | 8217 | 7894 | 8444 | 3727 | 3834 | 4145 | 4311 | 2483 | 3753 | 211 | 194 | 222 | 32 | 56 | 45 |
| 26 | 3107 | 0.38 | 8015 | 7452 | 6929 | 3429 | 4573 | 3794 | 4445 | 3429 | 3748 | 200 | 173 | 149 | 40 | 53 | 51 |
| 27 | 3086 | 0.36 | 8093 | 7562 | 7177 | 4260 | 4496 | 3488 | 4342 | 3784 | 4123 | 202 | 176 | 159 | 48 | 48 | 59 |

**Composite Type B with Cu coated preforms**

| Sample | Density ($kg.m^{-3}$) | Ceramic Vol % | $V_1$ $m.s^{-1}$ | $V_2$ $m.s^{-1}$ | $V_3$ $m.s^{-1}$ | $V_{12}$ $m.s^{-1}$ | $V_{21}$ $m.s^{-1}$ | $V_{13}$ $m.s^{-1}$ | $V_{31}$ $m.s^{-1}$ | $V_{23}$ $m.s^{-1}$ | $V_{32}$ $m.s^{-1}$ | $C_{11}$ (GPa) | $C_{22}$ (GPa) | $C_{33}$ (GPa) | $C_{44}$ (GPa) | $C_{55}$ (GPa) | $C_{66}$ (GPa) |
|---|---|---|---|---|---|---|---|---|---|---|---|---|---|---|---|---|---|
| 1 | 3034 | 0.32 | 8110 | 6613 | 8026 | - | - | - | - | - | - | 200 | 133 | 195 | - | - | - |
| 2 | 3123 | 0.39 | 7995 | 6211 | 6115 | - | - | - | - | - | - | 200 | 120 | 117 | - | - | - |
| 3 | 3145 | 0.41 | 8074 | 6259 | 6395 | 3884 | 4543 | 3832 | 4526 | 3699 | 3694 | 205 | 123 | 129 | 43 | 55 | 56 |
| 4 | 3154 | 0.41 | 8172 | 6367 | 6467 | - | - | - | - | - | - | 211 | 128 | 132 | - | - | - |
| 5 | 3145 | 0.41 | 7988 | 5681 | 6479 | - | 4556 | - | 4645 | 3736 | 3538 | 201 | 102 | 132 | 42 | 68 | 65 |
| 6 | 3137 | 0.40 | 7940 | 5895 | 6580 | - | 4429 | 3870 | 4882 | 3578 | 3581 | 198 | 109 | 136 | 40 | 61 | 62 |
| 7 | 3115 | 0.38 | 7993 | 6176 | 6834 | 3463 | 4205 | 3623 | 4506 | 3817 | 4268 | 199 | 119 | 145 | 51 | 52 | 46 |
| 8 | 3030 | 0.31 | 8057 | 6485 | 6538 | 3564 | 3551 | 3693 | 3836 | 3121 | 3332 | 197 | 127 | 130 | 32 | 43 | 38 |
| 9 | 3080 | 0.35 | 7986 | 6287 | 6064 | 3186 | 3873 | 3593 | 4099 | 3649 | 3563 | 196 | 122 | 113 | 40 | 46 | 39 |
| 10 | 3158 | 0.42 | 8051 | 6803 | 5912 | 3384 | 4022 | 3512 | 4015 | 3272 | 3348 | 205 | 146 | 110 | 35 | 45 | 44 |
| 11 | 3164 | 0.42 | 8127 | 6578 | 6091 | 3748 | 4329 | 3405 | 4073 | 3686 | 3143 | 209 | 137 | 117 | 37 | 45 | 52 |
| 12 | 3150 | 0.41 | 8031 | - | 6356 | 3727 | 4776 | 4242 | - | 3229 | 3643 | 203 | - | 127 | 37 | 57 | 58 |
| 13 | 3138 | 0.40 | 7958 | - | 7055 | 3565 | 4586 | - | 4398 | 3986 | - | 199 | - | 156 | 50 | 61 | 53 |
| 14 | 3131 | 0.39 | 8028 | 6275 | 6673 | - | 3535 | 3632 | 4320 | 3695 | 3674 | 202 | 123 | 139 | 43 | 50 | 39 |
| 15 | 3055 | 0.33 | 8030 | 6483 | 6835 | - | 3617 | 3620 | 3917 | 3213 | 3414 | 197 | 128 | 143 | 34 | 43 | 40 |
| 16 | 3107 | 0.38 | 7947 | 6558 | 7474 | 3871 | 4521 | 3971 | 3641 | 3906 | 3774 | 196 | 134 | 174 | 46 | 45 | 55 |
| 17 | 3103 | 0.37 | 8014 | 6388 | 6321 | 3792 | 4083 | 3256 | 4131 | 3944 | 3321 | 199 | 127 | 124 | 41 | 43 | 48 |

| Sample | Density ($kg.m^{-3}$) | Ceramic Vol % | $V_1$ $m.s^{-1}$ | $V_2$ $m.s^{-1}$ | $V_3$ $m.s^{-1}$ | $V_{12}$ $m.s^{-1}$ | $V_{21}$ $m.s^{-1}$ | $V_{13}$ $m.s^{-1}$ | $V_{31}$ $m.s^{-1}$ | $V_{23}$ $m.s^{-1}$ | $V_{32}$ $m.s^{-1}$ | $C_{11}$ (GPa) | $C_{22}$ (GPa) | $C_{33}$ (GPa) | $C_{44}$ (GPa) | $C_{55}$ (GPa) | $C_{66}$ (GPa) |
|---|---|---|---|---|---|---|---|---|---|---|---|---|---|---|---|---|---|
| 18 | 3153 | 0.41 | 8075 | 6834 | 6271 | - | 4148 | - | 3766 | 3436 | 3010 | 206 | 147 | 124 | 33 | 45 | 54 |
| 19 | 3127 | 0.39 | 8129 | 7003 | 7346 | 3717 | 3984 | 4167 | 4597 | - | 3940 | 207 | 153 | 169 | 49 | 60 | 46 |
| 20 | 3038 | 0.32 | 8045 | 5937 | 6523 | 3321 | 3175 | - | 4162 | 3218 | 3416 | 197 | 107 | 129 | 33 | 53 | 32 |
| 21 | 3125 | 0.39 | 7934 | 5982 | 6896 | 3370 | 3886 | 3930 | 4001 | 3465 | 3593 | 197 | 112 | 149 | 39 | 49 | 41 |
| 22 | 3144 | 0.40 | 8001 | 6955 | 6225 | 3562 | 4202 | 3630 | 4031 | 3294 | 3597 | 201 | 152 | 122 | 37 | 46 | 48 |
| 23 | 3156 | 0.41 | 8007 | 6445 | 6261 | 3650 | 4186 | 3474 | 4108 | 3398 | 3221 | 202 | 131 | 124 | 35 | 46 | 49 |
| 24 | 3129 | 0.39 | 7898 | 6120 | 6890 | - | 4257 | 4060 | 4132 | 3173 | 3728 | 195 | 117 | 149 | 37 | 52 | 57 |
| 25 | 3134 | 0.40 | 8100 | 6578 | 7623 | 3693 | 3921 | 4213 | 4551 | 3231 | 3823 | 206 | 136 | 182 | 39 | 60 | 45 |

**Composite Type B with $Cu_2O$ coated preforms**

| Sample | Density ($kg.m^{-3}$) | Ceramic Vol % | $V_1$ $m.s^{-1}$ | $V_2$ $m.s^{-1}$ | $V_3$ $m.s^{-1}$ | $V_{12}$ $m.s^{-1}$ | $V_{21}$ $m.s^{-1}$ | $V_{13}$ $m.s^{-1}$ | $V_{31}$ $m.s^{-1}$ | $V_{23}$ $m.s^{-1}$ | $V_{32}$ $m.s^{-1}$ | $C_{11}$ (GPa) | $C_{22}$ (GPa) | $C_{33}$ (GPa) | $C_{44}$ (GPa) | $C_{55}$ (GPa) | $C_{66}$ (GPa) |
|---|---|---|---|---|---|---|---|---|---|---|---|---|---|---|---|---|---|
| 1 | 3145 | 0.41 | 8381 | 7887 | 7391 | 4594 | 4578 | 3468 | - | - | 3860 | 221 | 196 | 172 | 47 | 38 | 66 |
| 2 | 3152 | 0.41 | 8404 | 7644 | 7500 | 4014 | - | 3722 | 4155 | 4005 | 3939 | 223 | 184 | 177 | 50 | 49 | 51 |
| 3 | 3136 | 0.40 | 8405 | 7534 | 7462 | 4062 | - | 3545 | 3954 | 3756 | 3853 | 222 | 178 | 175 | 45 | 44 | 52 |
| 4 | 3124 | 0.39 | 8412 | 7421 | 7630 | 3860 | 4144 | 4158 | 4190 | 4004 | 3913 | 221 | 172 | 182 | 49 | 54 | 50 |
| 5 | 3139 | 0.40 | 8431 | 7814 | 7393 | 4030 | 4414 | 4018 | 4344 | 4014 | 3868 | 223 | 192 | 172 | 49 | 55 | 56 |
| 6 | 3131 | 0.39 | 8291 | 7707 | 7687 | 4166 | 3981 | 3914 | 4305 | 4142 | 3940 | 215 | 186 | 185 | 51 | 53 | 52 |
| 7 | 3135 | 0.40 | 8326 | 7531 | 7386 | 4099 | 4149 | 3992 | 4569 | 4010 | 3846 | 217 | 178 | 171 | 48 | 58 | 53 |
| 8 | 3152 | 0.41 | 8294 | 7631 | 7597 | 4301 | 4279 | 3570 | 4257 | 4158 | 4073 | 217 | 184 | 182 | 53 | 49 | 58 |
| 9 | 3135 | 0.40 | 8320 | 7585 | 7728 | 3943 | 4298 | 3873 | 4474 | 4193 | 4042 | 217 | 180 | 187 | 53 | 55 | 53 |
| 10 | 3138 | 0.40 | 8391 | 7549 | 7627 | 4154 | 4267 | 3921 | 4396 | 4048 | 4240 | 221 | 179 | 183 | 54 | 54 | 56 |
| 11 | 3160 | 0.42 | 8414 | 7465 | 7596 | 4166 | 4396 | 4096 | 4269 | 4317 | 4114 | 224 | 176 | 182 | 56 | 55 | 58 |
| 12 | 3156 | 0.41 | 8308 | 7535 | 7468 | 4277 | 4342 | 4301 | 4371 | 4228 | 4003 | 218 | 179 | 176 | 54 | 59 | 59 |
| 13 | 3138 | 0.40 | 8307 | 7742 | 7371 | 3906 | - | 3991 | 4121 | 3800 | - | 217 | 188 | 170 | 45 | 52 | 48 |
| 14 | 3152 | 0.41 | 8341 | 7635 | 7577 | 3834 | 4294 | 4099 | 4396 | 3952 | 4198 | 219 | 184 | 181 | 52 | 57 | 52 |
| 15 | 3157 | 0.42 | 8353 | 7481 | 7772 | 3870 | 4308 | 4097 | 4467 | 4203 | 3983 | 220 | 177 | 191 | 53 | 58 | 53 |
| 16 | 3157 | 0.41 | 8416 | 7427 | 7841 | 3858 | 4265 | 4011 | 4316 | 3963 | 4089 | 224 | 174 | 194 | 51 | 55 | 52 |
| 17 | 3156 | 0.41 | 8428 | 7668 | 7808 | 4035 | 4485 | 3845 | 4279 | 4247 | 3816 | 224 | 186 | 192 | 51 | 52 | 57 |

| Sample | Density ($kg.m^{-3}$) | Ceramic Vol % | $V_1$ $m.s^{-1}$ | $V_2$ $m.s^{-1}$ | $V_3$ $m.s^{-1}$ | $V_{12}$ $m.s^{-1}$ | $V_{21}$ $m.s^{-1}$ | $V_{13}$ $m.s^{-1}$ | $V_{31}$ $m.s^{-1}$ | $V_{23}$ $m.s^{-1}$ | $V_{32}$ $m.s^{-1}$ | $C_{11}$ (GPa) | $C_{22}$ (GPa) | $C_{33}$ (GPa) | $C_{44}$ (GPa) | $C_{55}$ (GPa) | $C_{66}$ (GPa) |
|---|---|---|---|---|---|---|---|---|---|---|---|---|---|---|---|---|---|
| 18 | 3137 | 0.40 | 8277 | 6860 | 7963 | 3926 | 3849 | 3933 | 4678 | 3763 | 4392 | 215 | 148 | 199 | 52 | 59 | 47 |
| 19 | 3146 | 0.41 | 8394 | 7856 | 7093 | 3953 | 4477 | 3954 | 4162 | 4015 | 3621 | 222 | 194 | 158 | 46 | 52 | 56 |
| 20 | 3135 | 0.40 | 8315 | 7476 | 7318 | 4458 | 4209 | 3896 | 4325 | 4016 | 4120 | 217 | 175 | 168 | 52 | 53 | 59 |
| 21 | 3165 | 0.42 | 8445 | 7463 | 7623 | 4098 | 4358 | 4119 | 4552 | 4132 | 3790 | 226 | 176 | 184 | 50 | 60 | 57 |
| 22 | 3122 | 0.39 | 8541 | 7331 | 7931 | 3919 | 4216 | 3714 | 4461 | 3974 | 3697 | 228 | 168 | 196 | 46 | 53 | 52 |
| 23 | 3151 | 0.41 | 8437 | 7737 | 7923 | 3923 | 4278 | 4077 | 4751 | 4138 | 3779 | 224 | 189 | 198 | 49 | 62 | 53 |
| 24 | 3143 | 0.40 | 8315 | 7250 | 7520 | 3889 | 4250 | 3840 | 4329 | 4013 | 3974 | 217 | 165 | 178 | 50 | 53 | 52 |
| 25 | 3140 | 0.40 | 8307 | 7738 | 7210 | 4072 | 4419 | 3871 | 4377 | 3931 | 3968 | 217 | 188 | 163 | 49 | 54 | 57 |
| 26 | 3148 | 0.41 | 8288 | 7705 | 7121 | 4270 | 4561 | 4024 | 4174 | 3972 | 3993 | 216 | 187 | 160 | 50 | 53 | 61 |
| 27 | 3154 | 0.41 | 8342 | 7314 | 7408 | 3968 | 4345 | 3826 | 4336 | 3829 | 3752 | 220 | 169 | 173 | 45 | 53 | 55 |

**Composites Type A fabricated by pressure casting**

| Sample | Density ($kg.m^{-3}$) | Ceramic Vol % | $V_1$ $m.s^{-1}$ | $V_2$ $m.s^{-1}$ | $V_3$ $m.s^{-1}$ | $V_{12}$ $m.s^{-1}$ | $V_{21}$ $m.s^{-1}$ | $V_{13}$ $m.s^{-1}$ | $V_{31}$ $m.s^{-1}$ | $V_{23}$ $m.s^{-1}$ | $V_{32}$ $m.s^{-1}$ | $C_{11}$ (GPa) | $C_{22}$ (GPa) | $C_{33}$ (GPa) | $C_{44}$ (GPa) | $C_{55}$ (GPa) | $C_{66}$ (GPa) |
|---|---|---|---|---|---|---|---|---|---|---|---|---|---|---|---|---|---|
| 1 | 3122 | 0.39 | 7838 | 7862 | 7987 | 4058 | 3556 | 3710 | 4220 | 3969 | 3869 | 192 | 193 | 199 | 48 | 49 | 45 |
| 2 | 3101 | 0.37 | 7907 | 7098 | 7784 | 4011 | 4493 | 4143 | 4149 | 3842 | 3735 | 194 | 156 | 188 | 45 | 53 | 56 |
| 3 | 3102 | 0.37 | 7384 | - | 7779 | 3759 | 3949 | - | 3960 | 3164 | 3692 | 169 | - | 188 | 37 | - | 46 |
| 4 | 3083 | 0.36 | 8018 | 7592 | 8147 | 3809 | 4030 | 4235 | 4219 | 3843 | 3948 | 198 | 178 | 205 | 47 | 55 | 47 |
| 5 | 3134 | 0.40 | 7943 | 8102 | 7490 | 4053 | 4234 | 4437 | 4409 | - | 4180 | 198 | 206 | 176 | - | 61 | 54 |
| 6 | 3120 | 0.39 | - | - | - | 3805 | 4305 | 4315 | 4680 | 3926 | 3778 | - | - | - | 46 | 63 | 51 |
| 7 | 3094 | 0.37 | 7579 | 7791 | 7961 | 4274 | 4110 | 3808 | 3974 | 4238 | 4526 | 178 | 188 | 196 | 59 | 47 | 54 |
| 8 | 3106 | 0.37 | 7744 | 7849 | 7778 | 3425 | 4257 | 4402 | 4591 | 3841 | 3393 | 186 | 191 | 188 | 41 | 63 | 46 |
| 9 | 3128 | 0.39 | 7574 | 6507 | - | 4057 | 4209 | 3884 | 4053 | 3658 | 3514 | 179 | 132 | - | 40 | 49 | 53 |
| 10 | 3112 | 0.38 | 7856 | 7779 | 7757 | 3836 | 3801 | 4219 | 4571 | 4392 | - | 192 | 188 | 187 | - | 60 | 45 |
| 11 | 3106 | 0.37 | 7724 | 7905 | 7983 | 3985 | 4456 | 3765 | 4276 | 3878 | 3480 | 185 | 194 | 198 | 42 | 50 | 55 |
| 12 | 3096 | 0.37 | 7672 | 7205 | 7808 | - | 4199 | 4064 | 4528 | 3885 | 4186 | 182 | 161 | 189 | 50 | 57 | - |
| 13 | 3115 | 0.38 | 7724 | 8162 | 7845 | - | 4434 | 3864 | 3547 | 3918 | 3874 | 186 | 208 | 192 | 47 | 43 | - |
| 14 | 3094 | 0.37 | 7229 | 7725 | 8324 | 4060 | 4457 | - | 4059 | 3821 | - | 162 | 185 | 214 | - | - | 56 |
| 15 | 3119 | 0.39 | 8107 | 7798 | 7658 | 4066 | 4738 | 4366 | 4416 | 4433 | 4319 | 205 | 190 | 183 | 60 | 60 | 61 |
| 16 | 3106 | 0.37 | 7830 | 7553 | 7993 | 3692 | 4114 | 4024 | 4629 | 4116 | 3923 | 190 | 177 | 198 | 50 | 58 | 47 |
| 17 | 3100 | 0.37 | 7931 | 7451 | 7971 | 4164 | 4004 | 4036 | 4089 | - | 3755 | 195 | 172 | 197 | - | 51 | 52 |

| Sample | Density ($kg.m^{-3}$) | Ceramic Vol % | $V_1$ $m.s^{-1}$ | $V_2$ $m.s^{-1}$ | $V_3$ $m.s^{-1}$ | $V_{12}$ $m.s^{-1}$ | $V_{21}$ $m.s^{-1}$ | $V_{13}$ $m.s^{-1}$ | $V_{31}$ $m.s^{-1}$ | $V_{23}$ $m.s^{-1}$ | $V_{32}$ $m.s^{-1}$ | $C_{11}$ (GPa) | $C_{22}$ (GPa) | $C_{33}$ (GPa) | $C_{44}$ (GPa) | $C_{55}$ (GPa) | $C_{66}$ (GPa) |
|---|---|---|---|---|---|---|---|---|---|---|---|---|---|---|---|---|---|
| 18 | 3095 | 0.37 | 7875 | 7812 | 7784 | 3869 | 4229 | 3292 | 3476 | - | - | 192 | 189 | 188 | - | 35 | 51 |
| 19 | 3099 | 0.37 | 7428 | 7734 | 7890 | 3822 | 4045 | 3591 | 4147 | 3896 | 4183 | 171 | 185 | 193 | 51 | 47 | 48 |

# Publications from the present work

Based on this thesis, following papers have already been published or submitted for publication:

**Peer reviewed scientific journals**

- S. Roy, B. Butz, A. Wanner, Damage evolution and domain level anisotropy in metal/ceramic composites exhibiting lamellar microstructures, Acta Materialia, communicated
- R. Piat, S. Roy, A. Wanner, Material parameter identification of interpenetrating metal-ceramic composites, Key Engineering Materials, 417-418, 53-56, 2010
- S. Roy, J. Gibmeier, A. Wanner, Residual stresses in novel metal/ceramic composites exhibiting a lamellar microstructure, Powder Diffraction Suppl., 24(S1), S59-S64, 2009
- S. Roy, J. Gibmeier, A. Wanner, In situ study of internal load transfer in a novel metal/ceramic composite exhibiting lamellar microstructure using energy dispersive synchrotron X-ray diffraction, Advanced Engineering Materials, 11, 471-477, 2009
- T. Ziegler, A. Neubrand, S. Roy, A. Wanner, R. Piat, Elastic constants of metal/ceramic composites with lamellar microstructures: finite element modelling and ultrasonic experiments, Composites Science and Technology, 69, 620-626, 2009
- S. Roy, A. Wanner, Metal/ceramic composites from freeze-cast preforms: domain structure and elastic properties, Composites Science and Technology, 68, 1136-1143, 2008

**Conference Proceedings**

- S. Roy, J-M. Gebert, A. Wanner, Complete stiffness characterization of a lamellar metal/ceramic composite using ultrasonic spectroscopy techniques, Paper No. IF19.1, Proceedings of the 17$^{th}$ International Conference on Composite Materials, July 27-31, 2009, Edinburgh, Scotland
- S. Roy, B. Butz, A. Wanner, Damage evolution and anisotropy in freeze cast metal/ceramic composites: an in-situ SEM analysis, Paper No. 303, Proceedings of the

13th European Conference on Composite Materials, June 2-5, 2008, Stockholm, Sweden

**Technical reports**


- S. Roy, J. Gibmeier, A. Wanner, Internal load transfer in a novel metal/ceramic composite exhibiting lamellar microstructure, to appear in BESSY annual report, 2008
- S. Roy, A. Wanner, J. Gibmeier, Residual stresses in novel metal/ceramic composites exhibiting a lamellar microstructure, BESSY annual report, 143-145, 2007

# References

1. Composites. Engineered Materials Handbook vol. 1, ASM International, Metals Park, OHIO, USA, 1987

2. A. Mortensen, Metal matrix composites in industry: an overview, http://mmc-assess.tuwien.ac.at/public/mmc_in_ind.pdf

3. A. Evans, C San Mirchi, A. Mortensen, Metal Matrix Composites in Industry: An Introduction and a Survey. Kluwer Academic Publishers, 2003

4. BCC Research, MA, USA, www.bccresearch.com

5. N. Chawla, K. K. Chawla, Metal Matrix Composites. Springer, 2006

6. D. J. Lloyd, in Composites Engineering Handbook (edited by P. K. Mallick). Marcel Dekker Inc., 1997

7. A. Mortensen, J. A. Cornie, M. C. Flemings, Overview: Solidification processing of metal-matrix composites. Journal of Metals, 12 – 19, Feb 1988

8. A. Mattern, Interpenetrierende Metall-Keramik-Verbundwerkstoffe mit isotropen und anisotropen $Al_2O_3$ – Verstärkungen. Dissertation, Universität Karlsruhe (TH), 2005

9. S. Skirl, M. Hoffman, K. Bowman, S. Wiederhorn, J. Rödel., Thermal expansion behavior and macrostrain of $Al_2O_3$/Al composites with interpenetrating networks, Acta Materialia, 46, 2493-9, 1998

10. H. Prielipp, M. Knechtel, N. Claussen, S. K. Streiffer, H. Müllejans, M. Rühle, Strength and fracture toughness of aluminum/alumina composites with interpenetrating networks, Materials Science and Engineering, A197, 19–30, 1995

11. R. M. Jones, Mechanics of Composite Materials. Taylor & Francis, USA, 1999

12. J M. Berthelot, Composite Materials: Mechanical Behavior and Structural Analysis. Springer, 1997

13. W. D. Callister Jr., Materials Science and Engineering: An Introduction. John Wiley & Sons, Inc., 2007

14. D. K. Hale, Review: The Physical Properties of Composite Materials. Journal of Materials Science, 11, 2105 – 2141, 1976

15. T. H. Courtney, Mechanical Behavior of Materials. McGraw-Hill Higher Education, 2000

16. T. W. Clyne, P. J. Withers, An Introduction to Metal Matrix Composites. Cambridge University Press, 1993

17. D. J. Lloyd, Particle reinforced aluminum and magnesium matrix composites. International Materials reviews, 39 (1), 1 – 23, 1994

18. W. C. Harrigan Jr., Commercial processing of metal matrix composites. Materials Science & Engineering A, A244, 75 – 79, 1998

19. J. H. Tweed, Manufacture of 2014 aluminum reinforced with SiC particulate by vacuum hot pressing. Materials Science & Engineering A, A135, 73 – 76, 1991

20. M. J. Tan, X. Zhang, Powder metal matrix composites: selection and processing. Materials science & Engineering A, A244, 80 – 85, 1998

21. M. K. Surappa, P. K. Rohatgi, Preparation and properties of cast aluminum – deramic particle composites. Journal of Materials Science, 16, 983 – 993, 1981

22. M. D. Skibo, D. M. Schuster, Process for preparation of composite materials containing nonmetallic particles in a metallic matrix, and composite materials thereby. US Patent 4786467, 1988

23. Y. Tsunekawa, M. Okumiya, I. Niimi, K. Yoneyama, Centrifugally cast aluminum matrix composites containing segregated alumina fibers. Journal of Materials Science Letters, 7, 830 – 832, 1988

24. J. M. Brupbacher, L. Christodoulou, D. C. Nagle, Process for forming metal-ceramic composites. US Patent 4710348, 1987

25. I. Gotman, M. J. Koczak, E. Shtessel, Fabrication of Al matrix in situ composites via self-propagating synthesis. Materials Science & Engineering A, A187, 189 – 199, 1994

26. C. Raghunath, M. S. Bhat, P. K. Rohatgi, In situ technique for synthesizing Fe – TiC composites. Scripta Metallurgica et Materialia, 32 (4), 577 – 582, 1995

27. D. C. Nagle, J. M. Brupbacher, L. Christodoulou, Metal - second phase composites by direct addition. US Patent 4915908, 1990

28. M. S. Newkirk, A. W. Urquhart, H. R. Zwicker, E. Breval, Formation of Lanxide™ ceramic composite materials. Journal of Materials Research, 1 (1), 81 – 89, 1986

29. F. A. Feest, P. F. Chesney, J. S. Coombs, Metal matrix composite manufacture. US Patent 4928745, 1990

30. M. K. Aghajanian, M. A. Rocazella, J. T. Burke, S. D. Keck, The fabrication of metal matrix composites by a pressureless infiltration technique. Journal of Materials Science, 26, 447 – 454, 1991

31. C. Garcia-Cordovilla, E. Louis, J. Narciso, Pressure infiltration of packed ceramic particles by liquid metals. Acta Materialia, 47 (18), 4461 – 4479, 1999

32. A. J. Cook, P. S. Werner, Pressure infiltration casting of metal matrix composites. Materials Science & Engineering A, A144, 189 – 206, 1991

33. M. R. Ghomashchi, A. Vikhrov, Squeeze-casting: an overview. Journal of Materials Processing Technology, 101, 1 – 9, 2000

34. R. Saha, E. Morris, N. Chawla, S. M. Pickard, Hybrid and conventional particle reinforced metal matrix composites by squeeze infiltration casting. Journal of Materials Science Letters, 21, 337 – 339, 2002

35. J-G. Li, Wetting of ceramic materials by liquid silicon, aluminum and metallic melts containing titanium and other reactive elements: a review. Ceramics International, 20, 391 – 412. 1994

36. F. Delannay, L. Froyen, A. Deruyttere, Review: The wetting of solids by molten metals and its relation to the preparation of metal-matrix composites. Journal of Materials Science, 22, 1 – 16, 1987

37. B. P. Krishnan, M. K. Surappa, P. K. Rohatgi, The UPAL process: a direct method of preparing cast aluminum alloy – graphite particle composites. Journal of Materials Science, 16, 1209 – 1216, 1981

38. Y. Kimura, Y. Mishima, S. Umekawa, T. Suzuki, Compatibility between carbon fiber and binary aluminum alloys, Journal of Materials Science, 19, 3107 – 3114, 1984

39. K. Phillips, A. J. Perry, G. E. Hollox, E. De Lamotte, The mechanical properties of carbon fibers coated with titanium carbide. Journal of Materials Science Letters, 6, 270 – 273, 1971

40. T. W. Clyne, J. F. Mason, The squeeze infiltration process for fabrication of metal-matrix composites. Metallurgical Transactions A, 18A, 1519 – 1530, 1987

41. C. G. Kang, Y. H. Seo, The influence of fabrication parameters on the deformation behavior of the preform of metal-matrix composites during the squeeze-casting processes. Journal of Materials Processing Technology, 61, 241 – 249, 1996

42. S. Deville, E. Saiz, R. K. Nalla, A. P. Tomsia, Freezing as a path to build complex composites. Science, 311, 515 – 518, 2006

43. S. Deville, E. Saiz, A. P. Tomsia, Ice – templated porous alumina structures. Acta Materialia, 55, 1965 – 1974, 2007

44. T. Fukasawa, Z. –Y. Deng, M. Ando, T. Ohji, Y. Goto, Pore structure of porous ceramics synthesized from water – based suspension by freeze – dry process. Journal of Materials Science, 36, 2523 – 2527, 2001

45. T. Fukasawa, Z. –Y. Deng, M. Ando, T. Ohji, S. Kanzaki, Synthesis of porous silicon nitride with unidirectionally aligned channels using freeze – drying process. Journal of the American Ceramic Society, 85, 2151 – 55, 2002

46. S. W. Sofie, F. Dogan, Freeze-casting of aqueous alumina slurries withy glycerol. Journal of the American Ceramic Society, 84, 1459 – 64, 2001

47. T. Fukasawa, M. Ando, T. Ohji, S. Kanzaki, Synthesis of porous ceramics with complex pore structure by freeze dry processing. Journal of the American Ceramic Society, 84, 230 – 32, 2001

48. Y. –H. Koh, J. –J. Sun, H. –E. Kim, Freeze-casting of porous Ni – YSZ cermets. Materials Letters, 61, 1283 – 1287, 2007

49. S. Deville, Freeze-casting of porous ceramics: a review of current achievements and issues. Advanced Engineering materials, 10, 155 – 169, 2008

50. S. Torquato, C. L. Y. Yeong, M. D. Rintoul, D. L. Milius, I. A. Aksay, Elastic properties and structure of interpenetrating boron carbide/aluminum multiphase composites. Journal of the American Ceramic Society, 82, 1263 – 68, 1999

51. W. Voigt, Lehrbuch der Kristallphysik, B. G. Teubner, Leipzig, Berlin, 1928

52. A. Reuss, Berechnung der Fließgrenze von Mischkristallen auf Grund der Plastizitätsbedingung für Einkristalle. Z. f. Angew. Math. U. Mech., 9, 49 – 58, 1929

53. B. Paul, Predictions of elastic constants of multiphase materials. Transactions of the Metallurgical Society of AIME, 218, 36 – 41, 1960

54. Z. Hashin, S. Shtrikman, A variational approach to the theory of the elastic behavior of multiphase materials. Journal of the Mechanics and Physics of Solids, 11, 127 – 140, 1963

55. L. J. Walpole, On bounds for the overall elastic moduli of inhomogeneous systems – I. Journal of the Mechanics and Physics of Solids, 14, 151 – 162, 1966

56. B. Budiansky, On the elastic moduli of some heterogeneous materials. Journal of the Mechanics and Physics of Solids, 13, 223 – 227, 1965

57. K. S. Ravichandran, Elastic properties of two phase composites. Journal of the American Ceramic Society, 77, 1178 – 84, 1994

58. T. W. Chou, A. Kelly, Mechanical properties of composites. Annual Review of Materials Science, 10, 229-259, 1980

59. H. X. Peng, Z. Fan, J. R. G. Evans, Bi-continuos metal matrix composites. Materials Science & Engineering A, 303, 37 – 45, 2001

60. L. I. Tuchinskii, Elastic constants of pseudoalloys with a skeletal structure. Poroshk. Metall., 7 [247], 85, 1983 (Translated in Powder Metallurgy and Metal Ceramics, 1983)

61. W. Kreher, W. Pompe, Internal stresses in heterogeneous solids. Akademie Verlag, 1989

62. M. T. Tilbrook, R. J. Moon, M. Hoffman, On the mechanical properties of alumina - epoxy composites with an interpenetrating network structure. Materials Science and Engineering A, 393, 170 – 178, 2005

63. R. J. Moon,. M. Tilbrook, M. Hoffman, A. Neubrand, Al – Al2O3 composites with interpenetrating network structures: composite modulus estimation. Journal of the American Ceramic Society, 88, 666 – 674, 2005

64. T. W. Clyne, A compressibility- based derivation of simple expressions for the transverse Poisson's ratio and shear modulus of an aligned long fiber composite. Journal of Materials Science Letters, 9, 336 – 339, 1990

65. B. C. Halpin, S. W. Tsai, Environmental factors in composite design. Airforce Materials Laboratory Technical Report (AFML-TR-67-423), 1967

66. A. Spencer, The transverse moduli of fiber composite material. Composites Science and Technology, 27, 93 – 109, 1986

67. R. L. Hewitt, M. C. de Malherbe, An approximation for the longitudinal shear modulus of continuous fiber composites. Journal of Composite materials, 4, 280 – 282, 1970

68. Z. Hashin, B. W. Rosen, The elastic moduli of fiber – reinforced materials. Journal of Applied mechanics, 223 – 232, June 1964

69. G. W. Postma, Wave propagation in a stratified medium, Geophysics, 20, 780-806, 1955

70. S. Torquato, Random Heterogeneous Materials: Microstructure and Macroscopic Properties, Springer, 2002

71. J. D. Eshelby, The determination of the elastic field of an ellipsoidal inclusion, and related problems. Proceedings of Royal Society, A241, 376- 396, 1957

72. O. B. Pedersen, Thermoplasticity and plasticity of composites – I. Mean field theory. Acta Metallurgica, 31, 1795 – 1808, 1983

73. P. J. Withers, W. M. Stobbs, O. B. Pedersen, The application of the Eshelby method of internal stress determination to short fiber metal matrix composites. Acta Metallurgica, 37, 3061 – 3084, 1989

74. J. A. Isaacs, A. Mortensen, Structure and room-temperature deformation of alumina fiber-reinforced aluminum. Metallurgical Transactions A, 23A, 1207 – 1219, 1992

75. K. K. Chawla, M. Metzger, Initial dislocation distributions in tungsten fiber – copper composites. Journal of Materials Science, 7, 34 – 39, 1992

76. R. J. Arsenault, N. Shi, Dislocation generation due to differences between the coefficients of thermal expansion. Materials Science and Engineering, 81, 175 – 187, 1986

77. R. J. Arsenault, L. Wang, C. R. Feng, Strengthening of composites due to microstructural changes in the matrix. Acta Metallurgica et Materialia, 39, 47 – 57, 1991

78. M. Kouzeli, A. Mortensen, Size dependent strengthening in particle reinforced aluminum. Acta Materialia, 50, 39 – 51, 2002

79. T. W. Gustafson, P. C. Panda, G. Song, R. Raj, Influence of microstructural scale on plastic flow behavior of metal matrix composites. Acta Materialia, 45, 1633 – 1643, 1997

80. V. C. Nardone, K. M. Prewo, On the strength of discontinuous silicon carbide reinforced aluminum composites. Scripta Metallurgica, 20, 43 – 48, 1986

81. R. J. Lederich, S. M. L. Sastry, Materials Science and Engineering, 55, 143, 1982

82. G. Bao, J. W. Hutchinson, R. M. McMeeking, Particle reinforcement of ductile matrices against plastic flow and creep. Acta Metallurgica et Materialia, 39, 1871 – 1882, 1991

83. V. V. Ganesh, N. Chawla, Effect of reinforcement-particle-orientation anisotropy on the tensile and fatigue behavior of metal-matrix composites. Metallurgical and Materials Transactions, 35A, 53 – 61, 2004

84. M. Kouzeli, C. San Marchi, A. Mortensen, Effect of reaction on the tensile behavior of infiltrated boron carbide – aluminum composites. Materials Science and Engineering, A337, 264 – 273, 2002

85. M. Manoharan, J. J. Lewandowski, Effect of reinforcement size and matrix microstructure on the fracture properties of an aluminum metal matrix composite. Materials Science and Engineering, A150, 179 – 186, 1992

86. H. L. Cox, The elasticity and strength of paper and other fibrous materials. British Journal of Applied Physics, 3, 72 – 79, 1952

87. A. S. Carrara, F. J. Mcgarry, Matrix and interface stresses in a discontinuous fiber composite model. Journal of Composite Materials, 2, 222 – 243, 1968

88. T. W. Clyne, A simple development of the shear lag theory appropriate for composites with a relatively small modulus mismatch. Materials Science and Engineering, A122, 183 – 192, 1989

89. V. Tvergaard, Analysis of tensile properties for a whisker – reinforced metal – matrix composite. Acta Metallurgica et Materialia, 38, 185 – 194, 1990

90. D. J. Towle, C. M. Friend, Effect of reinforcement architecture on mechanical properties of a short fiber/magnesium RZ% MMC manufactured by preform infiltration. Materials Science and Engineering, A188, 153 – 158, 1994

91. D. J. Towle, C. M. Friend, Comparison of compressive and tensile properties of magnesium based metal matrix composites. Materials Science and Technology, 9, 35 – 41, 1993

92. G. S. Holister, C. Thomas, Fiber Reinforced Materials. Elsevier Publishing Co. Ltd., 1966

93. A. Kelly, G. J. Davies, The principles of the fiber reinforcement of metals. Metallurgical Reviews, 10, 1 – 77, 1965

94. A. Rossoll, C. Otto, B. Moser, L. Weber, A. Wanner, A. Mortensen, Measurement of damage evolution in continuous ceramic fiber-reinforced metals by acoustic emission. Scripta Materiaila, 59, 842-845, 2008

95. R. S. Bushby, Evaluation of continuous alumina fiber reinforced composites based upon pure aluminum. Materials Science and Technology, 14, 877 – 886, 1998

96. W. A. Curtin, S. J. Zhou, Influence of processing damage on performance of fiber reinforced composites. Journal of the Mechanics and Physics of Solids, 43, 343 – 363, 1995

97. W. A. Curtin, Ultimate strengths of fiber reinforced ceramics and metals. Composites, 24, 98 – 102, 1993

98. C. González, L. Llorca, Micromechanical modeling of deformation and failure in Ti-6Al-4V/SiC composites. Acta Materialia, 49, 3505 – 3519, 2001

99. C. H. Weber, X. Chen, S. J. Connell, F. W. Zok, On the tensile properties of a fiber reinforced titanium matrix composite – I. Unnotched behavior. Acta Metallurgica et Materialia, 42, 3443 – 3450, 1994

100. M. –S. Hu, J. Yang, H. C. Cao, A. G. Evans, R. Mehrabian, The mechanical properties of Al alloys reinforced with continuous $Al_2O_3$ fibers. Acta Metallurgica et Materialia, 40, 2315 – 2326, 1992

101. J. R. Brockenbrough, S. Suresh, H. A. Wienecke, Deformation of metal-matrix composites with continuous fibers: geometrical effects of fiber distribution and shape. Acta Metallurgica et Materialia, 39, 735 – 752, 1991

102. A. Kelly, H. Lilholt, Philosophical Magazine, 20, 311, 1969

103. A. Mortensen, O. B. Pedersen, H. Lilholt, On the work hardening of fiber reinforced copper. Scripta Materialia, 38, 1109 – 1115, 1998

104. S. Groh, B. Devincre, L. P. Kubin, A. Roos, F. Feyel, J. –L. Chaboche, Size effects in metal matrix composites. Materials Science and Engineering, A400-401, 279 – 282, 2005

105. J. R. Brockenbrough, S. Suresh, Plastic deformation of continuous-fiber reinforced metal-matrix composites: effects of fiber shape and distribution. Scripta Metallurgica et Materialia, 24, 325 – 330, 1990

106. D. B. Zahl, S. Schmauder, R. M. McMeeking, Transverse strength of metal matrix composireinforced with strongly bonded continuous fibers in regular arrangements. Acta Metallurgica et Materialia, 42, 2983 – 2997, 1994

107. H. R. Shetty, T. –W. Chou, Mechanical properties and failure characteristics of FP/aluminum and W/aluminum composites. Metallurgical Transactions, 16A, 853 – 864, 1985

108. J. E. Spowart, H. E. Dève, Compressive failure of metal matrix composites in Comprehensive Composite materials edited by A. Kelly and C. Zweben, Vol. 3, 2000

109. P. M. Jelf, N. A. Fleck, Compression failure mechanisms in unidirectional composites. Journal of Composite Materials, 26, 2706 – 2726, 1992

110. J. Lankford, Compressive failure of fiber-reinforced composites: buckling, kinking and the role of the interphase, Journal of Materials Science, 30, 4343 – 4348, 1995

111. H. M. Jensen, Analysis of compressive failure of layered materials by kink band broadening. International Journal of Solids and Structures, 36, 3427 – 3441, 1999

112. B. W. Rosen, Mechanics of composite strengthening: fiber composite materials. American Society of Metals, 37 – 45, 1964

113. A. S. Argon, Fracture of Composites: Treatise of Materials Science and Technology, vol 1, cademic Press New York, 1972

114. B. Budiansky, Micromechanics. Computers and Structures, 16, 3 – 12, 1983

115. B. Budiansky, N. A. Fleck, Compressive failure of fiber composites. Journal of the Mechanics and Physics of Solids, 41, 183 – 211, 1993

116. H. E. Dève, Compressive strength of continuous fiber reinforced aluminum matrix composites. Acta Materialia, 45, 12, 5041 – 5046, 1997

117. K. Schulte, K. Minoshima, Damage mechanisms under tensile and fatigue loading of continuous fiber - reinforced metal – matrix composites. Composites, 24, 197 – 208, 1993

118. J. E. Spowart, T. W. Clyne, The axial compressive failure of titanium reinforced with silicon carbide monifilaments. Acta Materialia, 47, 671 – 687, 1999

119. M. Guden, I. W. Hall, Quasi static and dynamic compression behavior of an FP$^{TM}$ alumina reinforced aluminum metal matrix composite. Journal of Materials Science, 33, 3285 – 3291, 1998

120. B. J. weng, S. T. Chang, S. E. Hsu, Microfracture mechanisms of fiber reinforced aluminum composites. Materials Science and Engineering, A156, 143 – 152, 1992

121. A. M. Waas, Effect of interphase on compressive strength of unidirectional composites. Journal of Applied Mechanics, 59, S183 – S188, 1992

122. A. G. Metcalfe, Interfaces in Metal Matrix Composites, Academic Press, 1974

123. W. R. Hibbard. Jr., An introductory review in Fiber Composite materials, American Society of Metals, ASM, Metals Park Ohio, 1 – 10, 1964

124. G. A. Cooper, A. Kelly, Role of the interface in the fracture of fiber - composite materials in “Interfaces in Composites”, STP 452 Amer. Soc. Test. Mater., Philadelphia, Pennsylvania, 90 – 106, 1968

125. S. Ochiai, K. Osamura, Influence of matrix ductility, interfacial bonding strength and fiber volume fraction on tensile strength of unidirectional metal matrix composite. Metallurgical Transactions, 21A, 971 – 977, 1990

126. H. E. Deve, C. McCullough, Continuous – fiber reinforced Al composites: a new generation. Journal of and materials Society, 33 – 37, 1995

127. Z. –Z. Du, R. M. McMeeking, Control of strength anisotropy of metal matrix fiber composites. Journal of Computer – Aided Materials Design, 1, 243 – 264, 1993

128. M. Riemer, H. G. Jentsch, H. Biermann, H. Mughrabi, The internal stress state in lamellar PST – crystals of the intermetallic alloy TiAl after compressive deformation. Intermetallics, 7, 241 – 249, 1999

129. Y. Umakoshi, T. Nakano, T. Yamane, The effect of orientation and lamellar structure on the plastic behavior of TiAl crystals. Materials Science and Engineering, A152, 81 – 88, 1992

130. Y. Umakoshi, T. Nakano, The role of ordered domains and slip mode of $\alpha_2$ phase in the plastic behavior of TiAl crystals containing oriented lamellae. Acta Metallurgica et Materialia, 41, 1155 – 1161, 1993

131. C. E. Wen, K. Yasue, J. G. Lin, Y. G. Zhang, C. Q. Chen, The effect of lamellar spacing on the creep behavior of a fully lamellar TiAl alloy. Intermetallics, 8, 525 – 529, 2000

132. C. Schuh, D. C. Dunand, A. Wanner, H. Clemens, Thermal – cycling creep of $\gamma$ – TiAl – based alloys. Intermetallics, 8, 339 – 343, 2000

133. A. Dlouhý, K. Kuchařová, Creep and microstructure of near – gamma TiAl alloys. Intermetallics, 12, 705 – 711, 2004

134. J. Chrapoński, The effect of lamellar separation on the properties of a Ti – 46Al – 2Nb – 2Cr intermetallic alloy. Materials Characterization, 56, 414 – 420, 2006

135. Y. Yamamoto, M. Takeyama, Physical metallurgy of single crystal gamma titanium aluminide alloys: orientation control and thermal stability of lamellar microstructure. Intermetallics, 13, 965 – 970, 2005

136. G. Cao, L. Fu, J. Lin, Y. Zhang, C. Chen, The relationships of microstructure and properties of a fully lamellar TiAl alloy. Intermetallics, 8, 647 – 653, 2000

137. J. F. Nye, Physical Properties of Crystals, Oxford Science Publications, 1985

138. R. F. S. Hearmon, An Introduction to Applied Anisotropic Elasticity, Oxford University Press, 1961

139. I. C. Noyan, J. B. Cohen, Residual Stress: Measurement by Diffraction and Interpretation, Springer – Verlag, 1987

140. B. Eigenmann, E. Macherauch, Röntgenographische Untersuchung von Spannubgszuständen in Werkstoffen, Mat. – wiss. U. werkstofftech., 26, 148-160, 1995

141. P. J. Withers, H. K. D. H. Bhadeshia, Residual stress part 2 – nature and origins. Materials Science and Technology, 17, 366 – 375, 2001

142. P. J. Withers, Residual stress and its role in failure. Reports on Progress in Physics, 70, 2211 - 2264, 2007

143. P. J. Withers, H. K. D. H. Bhadeshia, Residual stress part 1 – measurement techniques. Materials Science and Technology, 17, 355 – 365, 2001

144. Handbook of Measurement of Residual Stresses edited by J. Lu, The Fairmont Press, Inc. Lilburn, GA, USA, 1996

145. P. J. Withers, M. Turski, L. Edwards, P. J. Bouchard, D. J. Buttle, Recent advances in residual stress measurement. International Journal of Pressure Vessels and Piping, 85, 118 – 127, 2008

146. J. Lu, D. Retraint, A review of recent developments and applications in the field of X-ray diffraction for residual stress studies. Journal of Strain Analysis, 33, 127 – 136, 198

147. V. Hauk, Structural and Residual Stress Analysis by Non - destructive Methods, Elsevier, 1997

148. B. D. Cullity, Elements of X-ray Diffraction, Addison-Wesley Publishing Company Inc., 1978

149. B. D. Cullity, Sources of error in X-ray measurements of residual stress. Journal of Applied Physics, 35, 1915 – 1917, 1964

150. F. Delannay, Thermal stresses and thermal expansion in MMCs in Comprehensive Composite materials edited by A. Kelly and C. Zweben, Vol. 3, 2000

151. M. Kuntz, B. Meier, G. Grathwohl, Residual stresses in fiber-reinforced ceramics due to thermal expansion mismatch. Journal of the American Ceramics Society, 76, 2607 – 2612, 1993

152. M. Vedula, R. N. Pangborn, R. A. Queeney, Fiber anisotropic thermal expansion and residual thermal stress in a graphite/aluminum composite. Composites, 19, 55 – 60, 1988

153. K. Seol, A. D. Krawitz, J. W. Richardson, C. M. Weisbrook, Effects of WC size and amount on the thermal residual stress in WC – Ni composites. Materials Science and Engineering, A398, 15 – 21, 2005

154. D. L. Coats, A. D. Krawitz, Effect of particle size on thermal residual stress in WC – Co composites. Materials Science and Engineering, A359, 338 – 342, 2003

155. H-J. Chun, I. M. Daniel, Residual thermal stresses in a filamentary SiC/Al composite. Composites Engineering, 5, 425 – 436, 1995

156. T. Nakamura, S. Suresh, Effects of thermal residual stresses and fiber packing on deformation of metal matrix composites. Acta Metallurgica et Materialia, 41, 1665 – 1681, 1993

157. T. W. Chou, A. Kelly, A. Okura, Fiber reinforced metal matrix composites. Composites, 16, 187 – 206, 1985

158. G. K. Hu, G. J. Weng, Influence of thermal residual stresses on the composite macroscopic behavior. Mechanics of Materials, 27, 229 – 240, 1998

159. R. J. Arsenault, M. Taya, Thermal residual stress in metal matrix composite. Acta Metallurgica, 35, 651 – 659, 1987

160. S-K. Hong, H. Tezuka, A. Kamio, Effects of thermal residual stress on mechanical properties of SiC whisker reinforced Al-Mg and Al-Li alloys composites. Materials Transactions JIM, 37, 975 – 982, 1996

161. I. Dutta, J. D. Sims, D. M. Seigenthaler, An analytical study of residual stress effects of uniaxial deformation of whisker reinforced metal matrix composites. Acta Metallurgica et Materialia, 41, 885 – 908, 1993

162. D. B. Zahl, R. M. Mcmeeking, The influence of residual stress on the yielding of metal matrix composites. Acta Metallurgica et Materialia, 39, 1117 – 1122, 1991

163. H. J. Böhm, F. G. Rammerstorfer, Micromechanical investigation of the processing and loading of fiber reinforced metal matrix composites. Materials Science and Engineering, A135, 185 – 188, 1991

164. H. M. Jensen, Residual stress effects on the compressive strength of uni-directional fiber composites. Acta Materialia, 50, 2895 – 2904, 2002

165. M. J. Dennis, Industrial computed tomography in Metals Handbook Vol. 17 on Non - destructive Evaluation and Quality Control, ASM International, Metals Park Ohio

166. R. A. Ketcham, W. D. Carlson, Acquisition, optimization and interpretation of X-ray computed tomographic imagery: applications to the geosciences. Computers & Geosciences, 27, 381 – 400, 2001

167. E. Maire, J. –Y. Buffière, P. Cloetens, W. Ludwig, G. Peix, High resolution X-ray tomography applied in the observation of the micro-structure of materials. Prakt. Metallogr., 39, 155 – 169, 2002

168. J. C. Elliott, P. Anderson, G. Davis, S. D. Dover, S. R. Stock, T. M. Breunig, A. Guvenilir, S. D. Antolovich, Application of X-ray microtomography in materials science illustrated by a study of a continuous fiber metal matrix composite. Journal of X-ray Science and Technology, 2, 249 – 258, 1990

169. ASTM Designation E1441-00, Standard Guide for Computed Tomography (CT) Imaging in Annual Book of ASTM Standards 2005

170. J. Baruchel, J-Y Buffière, E. Maire, P. Merle, G. Peix, X-ray Tomography in Materials Science, Hermes Science Publications, Paris, 2000

171. R. A. Brooks, G. D. Chiro, Beam hardening in X-ray reconstructive tomography. Phys. Med. Biol., 21, 390 – 398, 1976

172. E. Schreiber, O. L. Anderson, N. Soga, Elastic Constants and Their Measurement, McGraw – Hill Book Company, 1973

173. J. L. Rose, Ultrasonic Waves in Solid Media, Cambridge University Press, 1999

174. M. Mah, D. R. Schmitt, Determination of the complete elastic stiffnesses from ultrasonic phase velocity measurements. Journal of Geophysical Research, 108, 6-1 – 6-11, 2003

175. P. W. A. Stijnman, Determination of the elastic constants of some composites by using ultrasonic velocity measurements. Composites, 26, 597 – 604, 1995

176. D. Meschede, Gerthsen Physik, Springer, 2003

177. E. P. Papadakis, The measurement of ultrasonic attenuation. Physical Acoustics, XIX, 107 – 155, 1990

178. W. Sachse, Y. –H. Pao, On the determination of phase and group velocities of dispersive waves in solids. Journal of Applied Physics, 49, 4320 – 4327, 1978

179. E. P. Papadakis, The measurement of ultrasonic velocity. Physical Acoustics, XIX, 81 – 106, 1990

180. A. Wanner, Elastic moduli measurements of extremely porous ceramic materials by ultrasonic phase spectroscopy. Materials Science and Engineering, A248, 35 – 43, 1998

181. L. C. Lynnworth, E. P. Papadakis, W. R. Rea, Ultrasonic measurement of phase and group velocity using continuous wave transmission techniques. AMMRC Report CTR 73 – 2, January 1973

182. E. P. Papadakis, Ultrasonic velocity and attenuation: measurement methods with scientific and industrial applications. Physical Acoustics, XII, 277 – 374, 1976

183. C. S. Ting, W. Sachse, Measurement of ultrasonic dispersion by phase comparison of continuous harmonic waves. Journal of the Acousric Society of America, 64, 852 – 857, 1978

184. L. C. Lynnworth, W. R. Rea, E. P. Papadakis, Continuous wave transmission techniques for measuring ultrasonic phase and group velocities in dispersive materials and composites. Journal of the Acoustic Society of America, 70, 1699 – 1703, 1981

185. J. L. Sarrao, S. R. Chen, W. M. Visscher, M. Lei, U. F. Kocks, A. Migliori, Determination of the crystallographic orientation of a single crystal using resonant ultrasound spectroscopy. Review of Scientific Instruments, 65, 2139 – 2140, 1994

186. R. G. Leisure, F. A. Wills, Resonant ultrasound spectroscopy. Journal of Physics - Condensed Matter, 9, 6001 – 6029, 1997

187. B. J. Zadler, J. H. L. Le Rousseau, J. A. Scales, M. L. Smith, Resonant ultrasound spectroscopy: theory and application. Geophysics Journal International, 156, 154 – 169, 2004

188. A. Migliori, T. W. Darling, Resonant ultrasound spectroscopy for materials studies and non – destructive testing. Ultrasonics, 34, 473 – 376, 1996

189. J. Maynard, Resonant ultrasound spectroscopy. Physics Today, 49, 26 – 31, 1996

190. D. B. Fraser, R. C. LeCraw, Novel method of measuring elastic and anelastic properties of solids. The Review of Scientific Instruments, 35, 1113 – 1115, 1964

191. H. H. Demarest, Cube – resonance method to determine the elastic constants of solids. The Journal of the Acoustical Society of America, 49, 768 – 775, 1971

192. I. Ohno, Free vibration of a rectangular parallelepiped crystal and its application to determination of elastic constants of orthorhombic crystals. Journal of Physics of the Earth, 24, 355 – 379, 1976

193. A. Migliori, J. L. Sarrao, Resonant Ultrasound Spectroscopy: Applications to Physics, Materials Measurements and Nondestructive Evaluation, John Wiley & Sons, Inc., 1997

194. J. D. Maynard, The use of piezoelectric film and ultrasound resonance to determine the complete elastic tensor in one measurement. Journal of the Acoustic Society of America, 91, 1754 – 1762, 1992

195. A. Migliori, J. L. Sarrao, W. M. Visscher, T. M. Bell, M. Lei, Z. Fisk, R. G. Leisure, Resonant ultrasound spectroscopic techniques for measurement of the elastic moduli of solids. Physica B, 183, 1 – 24, 1993

196. R. Holland, Resonant properties of piezoelectric ceramic rectangular parallelepipeds. The Journal of the Acoustic Society of America, 43, 988 – 997, 1968

197. W. M. Visscher, A. Migliori, T. M. Bell, R. A. Reinert, On the normal modes of free vibration of inhomogeneous and anisotropic elastic objects. The Journal of the Acoustic Society of America, 90, 2154 – 2162, 1991

198. P. Heyliger, A. Jilani, H. Ledbetter, R. G. Leisure, C – L. Wang, Elastic constants of isotropic cylinders using resonant ultrasound. Journal of the Acoustic Society of America, 94, 1482 – 1487, 1993

199. R. B. Schwarz, J. F. Vuorinen, Resonant ultrasound spectroscopy: applications, current status and limitations. Journal of Alloys and Compounds, 310, 243 – 250, 2000

200. O. L. Anderson, Rectangular parallelepiped resonance – a technique of resonance ultrasound and its applications to the determination of elasticity at high temperatures. Journal of the Acoustic Society of America, 91, 2245 – 2253, 1992

201. T. Goto, O. L. Anderson, Apparatus for measuring elastic constants of single crystals by a resonance technique up to 1825 K. Review of Scientific Instruments, 59, 1405 – 1408, 1988

202. R. Treusch, Production and properties of synchrotron radiation, in Neutrons and Synchrotron Radiation in Engineering Materials Science edited by W. Reimers, A. R. Pyzalla, A. Schreyer, H. Clemens, Wiley – VCH, 2008

203. M. E. Fitzpatrick, A. Lodini, Analysis of Residual Stress by Diffraction using Neutron and Synchrotron Radiation, Taylor & Francis, 2003

204. Webpage: http://www.bessy.de/?idcat=163&changelang=5

205. F. R. Elder, A. M. Gurewitsch, R. V. Langmuir, H. C. Pollock, Radiations from electrons in a synchrotron. Physics Review, 71, 829 – 830, 1947

206. P. J. Webster, L. D. Oosterkamp, P. A. Browne, D. J. Hughes, W. P. Kang, P. J. Withers, G. B. M. Vaughan, Synchrotron X – ray residual strain scanning of a friction stir weld. Journal of Strain Analysis, 36, 61 – 70, 2001

207. M. Lee, Y. Xiao, D. E. Wittmer, T. J. Graber, S. M. Mini, Residual stresses in particle – reinforced ceramic composites using synchrotron radiation. Journal of Materials Science, 37, 4437 – 4443, 2002

208. A. wanner, D. C. Dunand, Methodological aspects of the high – energy synchrotron X – ray diffraction technique for internal stress evaluation. Journal of Neutron Research, 9, 495 – 501, 2001

209. A. Wanner, D. C. Dunand, Synchrotron X – ray study of bulk lattice strains in externally loaded Cu – Mo composites. Metallurgical and Materials Transactions, 31A, 2949 – 2961, 2000

210. A. M. Korsunsky, S. P. Collins, R. A. Owen, M. R. Daymond, S. Achitoui, K. E. James, Fast residual stress mapping using energy-dispersive synchrotron X – ray diffraction on station 16.3 at the SRS. Journal of Synchrotron Radiation, 8, 77 – 81, 2002

211. T. A. Kuntz, H. N. G. Wadley, D. R. Black, Residual strain gradient determination in metal matrix composites by synchrotron X – ray energy-dispersive diffraction. Metallurgical Transactions, 24A, 1117 – 1124, 1993

212. A. R. Pyzalla, B. Reetz, A. Jacques, J. P. Feiereisen, O. Ferry, T. Buslaps, W. Reimers, In – situ investigation of strain relaxation in an Al/Si – MMC using high energy synchrotron radiation. Zeitschrift für Metallkunde, 95, 624 – 630, 2004

213. W. Reimers, A. Pyzalla, M. Broda, G. Brusch, D. Dantz, T. Schmackers, K. D. Liss, T. Tschentscher, The use of high – energy synchrotron diffraction for residual stress analysis. Journal of Materials Science Letters, 18, 581 – 583, 1999

214. W. Reimers, M. Broda, G. Brusch, D. Dantz, K. D. Liss, A. Pyzalla, T. Schmackers, T. Tschentscher, Evaluation of residual stresses in the bulk of materials by high energy synchrotron diffraction. Journal of Nondestructive Evaluation, 17, 129 – 140, 1998

215. D. R. Black, C. J. Bechtoldt, R. C. Placious, M. Kuriyama, Three dimensional strain measurements with X – ray energy-dispersive spectroscopy. Journal of Nondestructive Evaluation, 5, 21 – 25, 1985

216. A. Pyzalla, Methods and feasibility of residual stress analysis by high – energy synchrotron radiation in transmission geometry using a white beam. Journal of Nondestructive Evaluation, 19, 21 – 31, 2000

217. C. Genzel, Residual stress analysis by white high energy X – rays, in in Neutrons and Synchrotron Radiation in Engineering Materials Science edited by W. Reimers, A. R. Pyzalla, A. Schreyer, H. Clemens, Wiley – VCH, 2008

218. T. Waschkies, R. Oberacker. M. J. Hoffmann, Control of lamellae spacing during freeze-casting of ceramics using double-side cooling as a novel processing route. Journal of the American Ceramic Society, 92, S79 – S84, 2009

219. O. Lott, A. Nagel, Fakultät Maschinenbau Oberflächentechnik und Werkstoffkunde, Hochschule Aalen, Germany, *personal communication*

220. W. Leis, L. H. Kallein, Gießereitechnik der Fachhochschule Aalen (GTAA), Germany, *personal communication*

221. A. Migliori, J. D. Maynard, Implementation of a modern resonant ultrasound spectroscopy system for the measurement of the elastic moduli of small solid specimens. The Review of Scientific Instruments, 76, 121301, 2005

222. Ch. Genzel, I. A. Denks, J. Gibmeier, M. Klaus, G. Wagener, The materials science synchrotron beamline EDDI for energy-dispersive diffraction analysis. Nuclear Instruments & Methods in Physics Research: Section A, A578, 23 – 33, 2007

223. ASM Specialty Handbook on aluminum and aluminum alloys edited by J. R. Davis and Davis & Associates, ASM International, 1996

224. J. F. Shackelford, W. Alexander, Materials Science and Engineering Handbook, CRC Press, 2001

225. M. Koopman, K. K. Chawla, C. Coffin, B. R. Patterson, X. Deng, B. V. Patel, Z. Fang, G. Lockwood, Determination of Elastic Constants in WC/Co Metal Matrix Composites by Resonant Ultrasound Spectroscopy (RUS) and Impulse Excitation, Advanced Engineering Materials, 4, 37 – 42, 2002

226. J. E. Vuorinen, R. B. Schwarz, C. McCullough, Elastic constants of an aluminum – alumina unidirectional composite, Journal of the Acoustic Society of America, 108, 574 – 579, 2000

227. CES EduPack 2008, Granta Design Limited, Cambridge, UK, www.grantadesign.com

228. M. F. Ashby, Criteria for selecting the components of composites, Acta Metallurgica et Materialia, 41, 1313-1335, 1993

229. M. R. Daymond, The determination of a continuum mechanics equivalent elastic strain from the analysis of multiple diffraction peaks, Journal of Applied Physics, 96, 4263 – 4272, 2004

230. G. Garces, G. Bruno, A. Wanner, Residual stresses in deformed random-planar aluminum/Saffil® short-fibre composites, Mater Sci. Eng. A, A417, 73-81, 2006

231. M. L. Young, J. D. Almer, U. Lienert, D. R. Haeffner, R. Rao, J. A. Lewis, D. C. Dunand, Diffraction measurements of load transfer in interpenetrating phase $Al_2O_3$/Al composites, Materials Science & Technology Proceedings, 225-233, 2003

232. Landolt-Börnstein, Band 1, Springer-Verlag, 1966

233. C. McCullough, H. E. Deve, T. E. Channel, Mechanical response of continuous fiber-reinforced $Al_2O_3$-Al composites produced by pressure infiltration casting. Materials Science and Engineering, A189, 147-154, 1994

234. T. Ziegler, A. Neubrand, S. Roy, A. Wanner, R. Piat, Elastic constants of metal/ceramic composites with lamellar microstructures: finite element modeling and ultrasonic experiments. Composites Science and Technology, 69, 620-626, 2009

235. H. M. Jensen, Models of failure in compression of layered materials. Mechanics of Materials, 31, 553-564, 1999

236. G. Garces, G. Bruno, A. Wanner, Internal stress evolution in a random-planar short fiber aluminum composite, Scripta Materialia, 55, 163-166, 2006

237. G. Garces, G. Bruno, A. Wanner, Load transfer in short fiber reinforced metal matrix composites, Acta Materialia, 55, 5389-5400, 2007

238. A. D. Deutschman, W. J. Michels, C. E. Wilson, Machine Design Theory and Practice. Macmillan Publishing Co., Inc., 1975

239. E. Macherauch, K. H. Kloos, in Proc. 1st Int. Conf. On Residual Stresses, ed. E. Macherauch and V. Hauk, 3, 1986

240. B. Clausen, T. Lorentzen, T. Leffers, Self-consistent modelling of the plastic deformation of the fcc polycrystals and its implications for diffraction measurements of internal stresses, Acta Materialia, 46, 3087-3098, 1998